

Award Number:

W81XWH-04-1-0249

TITLE:

Improved Sensitivity and Specificity for Detection of Prostate Cancer

PRINCIPAL INVESTIGATOR:

PI: Rao P. Gullapalli, Ph.D.; Co-Investigators: Michael Naslund, MD; John Papadimitrou, MD; Elliott Siegel, MD.

CONTRACTING ORGANIZATION:

University of Maryland Baltimore
Baltimore, MD 21201

REPORT DATE:

S~{æ↑âæãÁGœ€íÁ

TYPE OF REPORT:

Final Report

PREPARED FOR: U.S. Army Medical Research and Materiel Command
Fort Detrick, Maryland 21702-5012

DISTRIBUTION STATEMENT:

× Approved for public release; distribution unlimited

The views, opinions and/or findings contained in this report are those of the author(s) and should not be construed as an official Department of the Army position, policy or decision unless so designated by other documentation.

REPORT DOCUMENTATION PAGE				<i>Form Approved</i> OMB No. 0704-0188	
<small>Public reporting burden for this collection of information is estimated to average 1 hour per response, including the time for reviewing instructions, searching existing data sources, gathering and maintaining the data needed, and completing and reviewing this collection of information. Send comments regarding this burden estimate or any other aspect of this collection of information, including suggestions for reducing this burden to Department of Defense, Washington Headquarters Services, Directorate for Information Operations and Reports (0704-0188), 1215 Jefferson Davis Highway, Suite 1204, Arlington, VA 22202-4302. Respondents should be aware that notwithstanding any other provision of law, no person shall be subject to any penalty for failing to comply with a collection of information if it does not display a currently valid OMB control number. PLEASE DO NOT RETURN YOUR FORM TO THE ABOVE ADDRESS.</small>					
1. REPORT DATE (DD-MM-YYYY) 01-11-2007		2. REPORT TYPE Final		3. DATES COVERED (From - To) 1 MAR 2004 - 1 OCT 2007	
4. TITLE AND SUBTITLE Improved Sensitivity and Specificity for Detection of Prostate Cancer				5a. CONTRACT NUMBER	
				5b. GRANT NUMBER W81XWH-04-1-0249	
				5c. PROGRAM ELEMENT NUMBER	
6. AUTHOR(S) Rao P. Gullapalli, Ph.D.				5d. PROJECT NUMBER	
				5e. TASK NUMBER	
				5f. WORK UNIT NUMBER	
7. PERFORMING ORGANIZATION NAME(S) AND ADDRESS(ES) University of Maryland Baltimore Baltimore, MD 21201				8. PERFORMING ORGANIZATION REPORT NUMBER	
9. SPONSORING / MONITORING AGENCY NAME(S) AND ADDRESS(ES) U.S. Army Medical Research and Materiel Command Fort Detrick, Maryland 21702-5012				10. SPONSOR/MONITOR'S ACRONYM(S)	
				11. SPONSOR/MONITOR'S REPORT NUMBER(S)	
12. DISTRIBUTION / AVAILABILITY STATEMENT Approved for Public Release; Distribution Unlimited					
13. SUPPLEMENTARY NOTES					
14. ABSTRACT Data collection for the project is complete with the recruitment of 25 patients into the study. Data on 14 patients have been completely analyzed and results from these patients have been presented at international conferences. Once the complete data analysis is finalized manuscripts will be submitted to international journal. One manuscript on image registration has been accepted for publication. Two other manuscripts are under preparation. One is on the radiology-pathology correlation using the advanced MR imaging techniques and the other is on the scientific outcome of the complete study.					
15. SUBJECT TERMS Prostate, spectroscopy, MRI					
16. SECURITY CLASSIFICATION OF:			17. LIMITATION OF ABSTRACT UU	18. NUMBER OF PAGES 203	19a. NAME OF RESPONSIBLE PERSON USAMRMC
a. REPORT U	b. ABSTRACT U	c. THIS PAGE U			19b. TELEPHONE NUMBER (include area code)

Table of Contents

Introduction.....	5
Body.....	5
Key Research Accomplishments.....	6
Reportable Outcomes.....	6
Conclusions.....	7
Appendices.....	8

Improved Sensitivity and Specificity for Detection of Prostate

PC031042

HSRRB Log No. A-12577

Introduction

The goal of this proposal is to diagnose prostate cancer more effectively using various magnetic resonance imaging techniques available with the ultimate goal of providing information with high specificity for either treatment planning purposes or patient management. To achieve this goal we would like to address the following two specific aims.

Specific Aim 1: To estimate the efficacy of image morphing and fusion techniques required providing appropriate distortion corrections on prostate images obtained from an endorectal coil for a more accurate assessment of the correlation between MRI/MRSI and histopathology.

Specific Aim 2: The development of a tumor index based on individual MRI/MRSI characteristics through correlation with step-section histology for a more accurate determination of the tumor extent and aggressiveness.

Body

Overall Status of the Project:

The goal of the study is to diagnose prostate cancer more effectively using various MRI techniques, with the ultimate goal of providing information with high specificity for either treatment planning purposes or patient management. The study was approved to enroll forty-six (40) participants. A total of twenty five participants were enrolled in this study from whom the complete MRI and histopathology information was obtained. The study is currently closed for recruiting new patients. The complete analysis of the data is near complete. However, several national and international presentations have been made with partial data with very encouraging results. In summary, results indicate that MR spectroscopy adds significantly to the data followed by diffusion-weighted imaging and kinetic parameters from perfusion-weighted imaging. In particular, perfusion-weighted imaging seems to be extremely sensitive with high Gleason scores compared to lower Gleason scores. T2-maps did not add additional information compared to T2-weighted imaging. Two manuscripts are under preparation. The first one is a review manuscript which presents radiology-pathology correlation using the data obtained from this study. The second manuscript is regarding the sensitivity and specificity improvements from the multi-parametric imaging study in the detection of prostate cancer. One manuscript regarding elastic registration of prostate images was recently accepted for publication in Journal of Digital Imaging. Future research studies from our group will use the information gained from this study to optimize radiation treatment protocols.

Brief Overview

Four imaging techniques, namely perfusion, diffusion, T2-mapping, and proton spectroscopy along with the normal T1 & T2 techniques were assessed on 25 patients that had opted for radical prostatectomy as part of their clinical work up. The subjects had an MRI scan using the above techniques prior to prostatectomy. The resected prostate was captured after surgery and MR imaging was performed at high-resolution prior to step-sectioning. Each of the ex vivo

prostates underwent 3 mm step sections using the prostate slicer which were then processed for H&E. The pathologist marked the regions of cancer on each of the slides including the Gleason score. Registration algorithms were employed to match the histology slides to the in vivo images. To overcome problems associated with tissue deformation, the ex vivo images were used to assist in accurate registration of the in vivo images to the histology slides. Each slice in the T2-weighted prostate image was divided into eight octants. These octants were transferred to the parametric images including T2-map, apparent diffusion coefficient map, K_{Trans} map, and the spectroscopic map of (choline+creatine)/citrate. From each of these octants, the specific parameteric values were extracted. While data analysis is ongoing on this project, we have results from 14 patients on whom the data is completely processed. Histology results were dichotomized at Gleason score of 5 & 6 and logistic regression was performed based on each of the individual techniques. Receiver operating characteristic (ROC) based analysis to compute the sensitivity, specificity, positive and negative predictive values and detection accuracy of each of the imaging techniques. Overall accuracy increased from 55% to 80% for the combined use of the information from all techniques compared to the radiologist reading from conventional MR alone (T1 and T2-weighted imaging). At high specificity spectroscopy and perfusion contributed to the overall accuracy. At moderate specificity spectroscopy and diffusion contributed to the overall accuracy. For the combined model we achieved a 60% sensitivity compared to histopathology at 80% specificity whereas the individual techniques had much lower sensitivities with spectroscopy providing the highest sensitivity. A high correlation ($r=0.39$; $p<0.0001$) of spectroscopic scores was observed with pathologist findings. Given the strength of these results we do not anticipate changes to the general trend in the data once all the data is processed. We are currently in the process of completing the data analysis and two manuscripts, one that provides the scientific information from this study and the second that provides a review of radiology pathology correlation are under preparation.

Key Research Accomplishments

To date we have been able to do the following:

1. Build a prostate phantom for validating all registration and deformation correction algorithm.
2. Explore and quantify the performance of novel methods of elastic registration including strain energy minimization and landmark based techniques. One manuscript accepted.
3. Develop a prostate slicer to obtain precise parallel axial cuts of the excised prostate prior to histopathological evaluation.
4. Implement all the tools necessary for the data analysis of the prostate imaging data.
5. Validate the tools on excised prostate samples available from the pathology department.
6. Presented several papers at scientific meetings (attached).
7. Two manuscripts under preparation: (1) Sensitivity & Specificity Improvements in Prostate Cancer through multi-parametric imaging; (2) Radiology – Pathology correlation using Advanced MR imaging of the Prostate..

Reportable Outcomes

Our research to date indicates that MR spectroscopy, diffusion-weighted imaging and perfusion weighted imaging add significantly to the overall sensitivity and specificity of prostate cancer

detection compared to conventional MRI alone. Our results also indicate that T2-maps do not add any additional value to the current practice of using T1 and T2-weighted imaging alone. Other outcome of our research is the development of a robust registration algorithm that is not just applicable to prostate MRI but is easily extendable to other imaging modalities that require such registration. In the future, we will be extending this technique for use in TRUS procedures in a manner that biopsies can be targeted through both ultrasound and MR image guidance.

Conclusions

Our study clearly indicates that advanced imaging techniques are extremely useful in increasing the sensitivity and specificity of detecting prostate cancer. Future prostate cancer patients, especially those who are watchful waiting should clearly benefit from these imaging techniques.

APPENDIX

List of presentations and publications attached:

1. Manuscript of invited talk on 'MRS of Prostate Diseases' at the International Society of Magnetic Resonance in Medicine' at Seattle, 2006
2. Presentation slides from the same meeting.
3. Elastic registration algorithm presented at the Annual Meeting of the International Society for Magnetic Resonance in Medicine, in Berlin, 2007.
4. Presentation of the scientific outcome of the study at the Radiological Society of North America, 2007.
5. Power point presentation of the scientific outcome of the study at the Annual Meeting of the International Society for Magnetic Resonance in Medicine, Toronto, CA 2008.
6. Presentation of the study at the World Congress of Endourology in Cancun, Mexico, 2007.
7. Letter of acceptance of manuscript regarding Elastic registration from the editor of Journal of Digital Imaging along with the manuscript.
8. Educational presentation of Radiology-Pathology correlation during RSNA 2007.
9. Presentation of the study on Landmark based registration using incompressible large deformation diffeomorphism at the Annual Meeting of the International Society for Magnetic Resonance in Medicine, Honolulu, HI, 2009.

MRS of Prostate Diseases

Rao P. Gullapalli, Ph.D.
Department of Radiology,
University of Maryland School of Medicine
Baltimore, MD. USA

According to the American Cancer Society, an estimated 234,460 new cases of prostate cancer (PCa) will occur and that there will be an estimated 27,350 deaths due to prostate cancer in the US during 2006 (1,2). The report also suggests that African American men are twice as vulnerable to prostate cancer compared to white men. Although the death rate has dropped over the last few years it still remains the second leading cause of cancer deaths among men after lung cancer in the United States. The ACS recommends that the PSA test and the digital rectal examination should be offered annually, beginning at age 50, to men who have a life expectancy of at least 10 years and those men that are at higher risk (African American men and those men with a strong family history of 1 or more first-degree relatives diagnosed with prostate cancer at an early age). The survival and successful treatment of PCa patients is dependent upon the early diagnosis of PCa. Further, the ability to monitor the progression and regression of malignancy is critical in the management of the disease. Currently the combination of digital rectal examination and prostate-specific antigen (PSA) testing is the primary diagnostic procedure. Typically, an elevated PSA or a nodule detected on physical examination prompts an evaluation and an eventual transrectal ultrasound-guided (TRUS) biopsy may reveal cancer. However in most cases, positive identification of PCa only becomes evident when malignancy has been established and the cancer has metastasized beyond the capsular region of the prostate. MRI in conjunction with endorectal coil provides superior visualization of zonal prostate anatomy compared to TRUS (3). MRI by itself can however be limited as various pathologies can mimic cancer thus compromising the diagnosis. In recent years, magnetic resonance spectroscopy of the prostate has shown to provide very useful metabolic information of the prostate. The combined use of MRI and MRSI has shown to increase the sensitivity and specificity in the detection of prostate cancer (4).

Citrate Metabolism

The metabolism of normal mammalian cells involves the complete oxidation of glucose and fat through the intermediary steps involving the synthesis and oxidation of citrate via the Krebs cycle (5). Coupled with phosphorylation, this intermediary synthesis and oxidation of citrate is essential for the cells to generate their major supply of cellular energy through the production of ATP. The citrate synthesized during this process in the Krebs cycle forms the source for acetyl-CoA required for lipogenesis. The Krebs cycle and the recycling of its intermediates are essential for the various reactions of amino acid metabolism. These established pathways are essential to normal mammalian aerobic cell metabolism, cellular function, survival, growth, and reproduction (6). The normal human prostate on the other hand does not go through the process of citrate oxidation thus accumulating large amounts of citrate which essentially is the end product of the intermediary metabolism. Cooper and Imfeld were the first to report that citrate levels were significantly decreased in prostate cancer tissue compared to the normal prostate or BPH (7). Shortly thereafter the same group suggested that the biochemical alterations seen through altered citrate metabolism may well occur before any malignant changes are histologically obvious (8). While these observations were made over four decades ago, it is only in the last decade that

scientists have been paying attention to the measurement of citrate levels within the prostate. The altered citrate metabolism has now been further studied by Costello, Franklin and their colleagues who have shed some light on the role of zinc in the production of citrate (9,10).

In addition to citrate, the normal and BPH prostate also accumulates high levels of zinc. The level of zinc in the normal prostate is about 150µg/g of tissue wet weight. However, the levels of zinc and citrate are not uniformly distributed throughout the prostate gland. For example in the normal peripheral zone there is high level of zinc concomitant with high levels of citrate. In the

Table 1	Citrate, nmole/g	Zinc µg/g
Normal (mixed tissue)	8,000	209
Normal (central zone)	4,000	-
Normal (peripheral zone)	13,000	-
BPH	8,000-15,000	589
PCa (mixed tissue)	1,000-2,000	55
PCa (malignant tissue)	500	-
Stromal tissue	150-300	-
Other soft tissue	150-450	30
Blood Plasma	90-110	1
Prostatic fluid	40,000-150,000	590

normal central gland, the levels of zinc and citrate are at a lower concentration (11). Table 1 lists the concentrations of citrate and zinc in different regions of the prostate in its different pathological condition. It is thought that in the presence of zinc, the mitochondrial aconitase activity that is responsible for citrate oxidation is severely limited in the normal prostate epithelial cells, which ultimately leads to the accumulation of citrate. The accumulation of citrate comes at the cost of ATP production which is reduced by about 65% in the normal prostate epithelial cells (14 moles of ATP) compared to other normal mammalian cells (38 moles of ATP) that completely oxidize glucose.

In prostate cancer however, the ability of intramitochondrial accumulation of zinc diminishes. It is thought that such a decrease in the zinc level restores the m-aconitase activity that leads to increased citrate oxidation. This is coupled with ATP production essential for progression towards malignancy (10,12,13). While many aspects of the zinc-citrate relationship are still under investigation, there is ample evidence suggesting that zinc-citrate interactions play an important role in the pathogenesis and progression of prostate malignancy.

Magnetic Resonance Imaging

Recent studies show that the combined use of an endorectal and phased-array coil and a high field strength MR imaging system provides the highest image resolution possible (3). MR imaging accurately depicts internal prostatic zonal anatomy and displays the physiologic complexity of the gland. Over the past several years, the superiority of MRI in the staging accuracy of cancer involving the peripheral zone has been consistently reported between 75% and 90 (4). Most prostate cancer involves the peripheral zone of the gland, where cancer is identified as low signal abnormality on T2-weighted imaging. Although MRI has allowed intra-prostatic evaluation of tumor location, results are often non-specific (14). Torricelli et al showed that cancer

could mimic post-biopsy hemorrhage, scar, prostatitis, or interglandular dysplasia on MR imaging of the prostate with specificity in the order of 50% (15).

Magnetic Resonance Spectroscopy

MRSI is a powerful tool that can provide useful biological information associated with many different metabolites (16). Proton (^1H) spectroscopy is attractive in terms of sensitivity, spatial resolution, signal to noise, and acquisition time. It has been widely used in the brain and its application and availability for imaging various anatomical regions of body has been increasing. MRS can provide a description of the chemical makeup of an imaged area in order to determine the presence of cancer (17). Molecules that can be studied with MRS include water, lipids, choline, citrate, lactate, creatine, and amino acids (16). Based on the initial work by Costello and Franklin at the University of Maryland, the prostate gland is unique in the body by the fact that it contains high levels of citrate (18). As the normal glandular epithelial cells are replaced by cancer, the concentration of citrate and choline change in the transformation to a malignant state. Choline levels increase and citrate levels decrease in the presence of active cancer (5). As mentioned above, the reason for the decline in the levels of citrate is the altered intermediate metabolism in the Krebs cycle (6). Although the mechanism for the elevation of the choline peaks is less understood, just as in the case of brain spectroscopy, its elevation is thought to be associated with changes in cell membrane synthesis and degradation that is normally associated with cancer. The choline resonance observed in-vivo at 3.22 ppm, sometimes referred to as total choline arises from the methyl hydrogens of trimethylamines and is comprised of choline, phosphocholine (PC), glycerophosphocholine (GPC), phosphoethanolamine (PE), glycerophosphoethanolamine (GPE), and ethanolamine (19-23). These compounds are essential in the synthesis and hydrolysis of phosphatidylcholine and phosphatidylethanolamines that are an integral part of the characteristic bilayer structure of cells and regulate membrane integrity and function. Polyamines such as spermine can be visualized in prostate MRSI (24). Polyamines are involved in many cellular processes such as maintenance of DNA structure, RNA processing, translation and protein activation (25,26). Disruption to the synthesis of polyamines is known to modulate the genetic effects of these genes. Polyamines can be visualized in proton MRSI as a broad peak between choline and creatine. Normal prostate epithelial cells will demonstrate large amounts of citrate and polyamines. The malignant cells on the other hand exhibit low levels of citrate and polyamines to the extent that the choline and creatine resonances are resolved to the baseline. One unfortunate consequence of prostate MRSI is the inability to monitor metabolites such as lactate and lipids in vivo due to the necessity for suppressing lipids to minimize contamination from the lipids surrounding the prostate gland. It has been shown in vitro that the citrate to lactate ratio can be used to discriminate prostate cancer from BPH and that the ratio can be used as an indicator of cancer aggressiveness (8). It is hoped that future MRSI improvements will allow for the interrogation of these metabolites.

MRSI Techniques

Although significant developments have been made with MRSI of the brain, the translation of this technology to other body parts including the prostate gland has proven to be far from trivial. In the case of the prostate gland, the deep location of the prostate, the possible movement of the prostate gland during the MRSI acquisition, and the dominating triglyceride signals from the

surrounding adipose tissues often pose a challenge in obtaining reliable quality spectra. Initial studies employing prostate spectroscopy used single voxel techniques such as STEAM (Stimulated Echo Acquisition Method) and PRESS (Point Resolved Spectroscopy) using the body coil (27-30). Usually the voxel size was large and encompassed both the peripheral zone and the central gland. Although these techniques showed the feasibility for performing proton spectroscopy, their use in the clinical setting was limited due to long scan times and the poor signal to noise of the spectra. However, with the arrival of 2D and 3D MRSI techniques the interest in prostate spectroscopy has increased (31-34). Several technical hurdles had to be overcome to reliably detect the resonances from the biologically relevant compounds in the prostate including accurate localization and the suppression of large signals from both water and lipids (35-38).

3D-MRSI technique appears to be the most suitable for the prostate gland as it is able to provide the prostate metabolite level information with high spatial resolution for the entire gland. Typically PRESS localization and band selective excitation with gradient dephasing (BASING) for water and lipid suppression is used (35). 3D-MRSI provides an array of spectra from contiguous voxels from the entire prostate gland. The contiguous array of spectra that map the entire prostate are in alignment with the anatomical T1- and T2-weighted images allowing for a comparative interpretation between the anatomical images and the metabolic information. Investigators at the University of California San Francisco (UCSF) showed that 3D-MRSI can be used to differentiate and localize the tumor foci to a volume as small as 0.24cc (39-43). Similar results have been reported by the group in the University of Nijmegen, Netherlands who further refined the 3D-MRSI technique by using elliptical encoding to further reduce the scan time (44-46).

Interpretation resulting from a combined evaluation of the MR images and by metabolic changes observed through MRSI leads to the most confident identification of cancer with a specificity of up to 98% (42). Decreased signal intensity on T2-weighted images in conjunction with decreasing levels of citrate and polyamines and a concomitant increase in the levels of choline increases the specificity in the diagnosis of prostate cancer. Hence an increased choline to citrate ratio is usually used as a method for depicting prostate cancer. Since the choline and creatine resonances are inseparable for quantification purposes, most investigators use [Choline+Creatine]/Citrate (CC/C) for spectral analysis. A standardized scoring method was developed by Jung et al which is based on the deviation of the CC/C ratio from its normal value of 0.22 ± 0.013 . A voxel CC/C value within one standard deviation of this normal value was given a score of 1, a value between 1 and 2 standard deviations was given a score of 2, a value between 2 and 3 standard deviations was given a score of 3, a value between 3 and 4 standard deviations was given a score of 4, and a value greater than 4 standard deviations was assigned a score of 5. Additional adjustments were made to the score to account for the elevation of choline over creatine, reduced polyamines, and poor signal to noise ratios. In this way each voxel obtained a score between 1 and 5 which was designated to an interpretative scale of likely benign, probably benign, equivocal, probably malignant and likely malignant corresponding to a voxel score from 1-5 respectively. Using this standardized five-point scale they were able to show good accuracy and excellent interobserver agreement. It should be noted that 3D-MRSI produces vast amounts of spectroscopic data and a standardized scale such as the one developed by Jung et al is likely to make the task of spectral interpretation less formidable (47). Such standardized scales will allow one to easily characterize the tumors aggressiveness and spatial extent.

The combination of MRI and MRSI in conjunction with the endorectal and phased-array body coil is emerging as the most sensitive tool for anatomic and metabolic evaluation of the prostate gland (4,48,49). Improvements in pulse sequences and MR technology have enabled the acquisition of the metabolic information from the entire prostate at high resolution within a reasonable time of ten minutes or less. Proton MRI/MRSI may be of great value for patients who are at increased risk for prostate cancer, for patients who have chosen watchful waiting, for longitudinal follow up from therapy, and in guiding various localized therapeutic treatments (50-52). MRI/MRSI of the prostate gland is likely to benefit from the recent trend towards ultra-high field magnet systems and emergence of multi-channel parallel imaging (53-55). Further newer techniques such as diffusion and perfusion are likely to increase the sensitivity and specificity of prostate cancer detection and characterization (56-64).

References:

1. American Cancer Society Web Site: cancer.org; Cancer Facts and Figures 2006, 2006.
2. Cancer Statistics. Cancer J, 000. 80: p.59.
3. Hricak H, White S, Vigneron D, et al. Carcinoma of the prostate gland: MR imaging with pelvic phased-array coils versus integrated endorectal-pelvic phased-array coils. *Radiology* 193:703-709, 1991.
4. Kurhanewicz J, Vigneron DB, Males RG, Swanson MG, Yu K, Hricak H. The prostate: MR imaging and spectroscopy. Present and Future. *Radiol Clin North Am* 38:115-138, viii-ix, 2000.
5. Costello LC, Franklin RB, and Narayan P. Citrate in the diagnosis of Prostate Cancer. *The Prostate* 38:237-245, 1999.
6. Costello LC, and Franklin RB. The intermediary metabolism of the prostate: A key to understanding the pathogenesis and progression of prostate malignancy. *Oncology* 59:269-282, 2000.
7. Cooper JF, and Imfeld H. The role of citric acid in the physiology of the prostate: A preliminary report. *J Urol* 81:157-163, 1959.
8. Cooper JF, and Farid I. The role of citric acid I the physiology of the prostate: Lactic/citrate ratios in benign and malignant prostatic homogenates as an index of prostatic malignancy. *J Urol* 92:533-536, 1964.
9. Costello LC, Liu Y, Franklin RB, Kennedy MC. Zinc inhibition of mitochondrial aconitase and its importance in citrate metabolism of prostate epithelial cells. *J Biol Chem* 46(14):28875-81, 1997.
10. Costello LC and Franklin RB. Novel role of zinc in the regulation of prostate citrate metabolism and its implications in prostate cancer. *The Prostate* 35:285-296, 1998.
11. Zaichick VY, Sviridova TV, Zaichick SV. Zinc concentration in human prostatic fluid: Normal, chronic prostatitis, adenoma and cancer. *Int Urol Nephrol* 28:687-694, 1996.
12. Zaichick VY, Sviridova TV, Zaichick SV. Zinc in the human prostate gland: Normal

hyperplasia, cancerous. *Int Urol Nephrol* 29:565-574, 1997.

13. Costello LC, Franklin RB, Liu Y, Kennedy MC. Zinc causes a shift toward citrate at equilibrium of the m-aconitase reaction of prostate mitochondria. *Inorg Biochem* 78:161-165, 2000.
14. Perrotti M, Han KR, Epstein RE, Kennedy EC, Rabbani F, Badani K, Pantuck AJ, Weiss RE, Cummings KB. Prospective evaluation of endorectal magnetic resonance imaging to detect tumor foci in men with prior negative prostatic biopsy: a pilot study. *J Urol* 162(4) 1314-7, 1999.
15. Torricelli P, Iadanza M, De Santis M, Pollastri CA, Cesinaro AM, Trentini G, Romagnoli R. Magnetic resonance with endorectal coil in the local staging of prostatic carcinoma. Comparison with histologic macrosectionis in 40 cases. *Radiol Med (Torino)* 97(6):491-498, 1999.
16. Negendank W. Studies of human tumors by MRS: a review. *NMR Biomed* 5(5):303-324, 1992.
17. Gillies RJ, Morse DL. In vivo magnetic resonance spectroscopy in cancer. *Annu Rev Biomed Eng*, 7:287-326, 2005.
18. Costello LC and Franklin RB. Bioenergetic theory of prostate malignancy. *Prostate* 25(3):162-166, 1994.
19. Cornel EB, Smuts GA, Oosterhof GO, et al. Characterization of human prostate cancer, benign prostatic hyperplasia and normal prostate by in vitro ¹H and ³¹P magnetic resonance spectroscopy. *J Urol* 150:2019-24, 1993.
20. Kurhanewicz J, Thomas A, Jajodia P. et al., ³¹P spectroscopy of the human prostate gland in vivo using a transrectal probe. *Magn Reson Med* 22:404-413, 1991.
21. Kurhanewicz J, Dahiya R, Macdonald JM et al. Phosphorus metabolite characterization of human prostatic adenocarcinoma in a nude mouse model by ³¹P magnetic resonance spectroscopy and high pressure liquid chromatography. *NMR Biomed* 5:185-192, 1992.
22. Schiebler M, Miyamoto KK, White M, Maygarden SJ, Mohler JL. In vitro high resolution ¹H-spectroscopy of the human prostate: benign prostatic hyperplasia, normal peripheral zone and adenocarcinoma. *Magn Reson Med* 29:285-291, 1993.
23. Kurhanewicz J, Dahiya R, Macdonald JM, Chang LH, James TL, Narayan P. Citrate alterations in primary and metastasis human prostatic Aden carcinomas: ¹H magnetic resonance spectroscopy and biochemical study. *Magn Reson Med* 29:149-157, 1993.
24. van der Graaf M, Schipper RG, Oosterhof GO, Schalken JA, Verhofstad AA, Heerschap A. Proton MR spectroscopy of prostatic tissue focused on the detection of spermine, a possible biomarker of malignant behavior in prostate cancer. *Magma* 10:153-159, 2000.
25. Childs AC, Mehta DJ, Gerner EW. Polyamine-dependent gene expression. *Cell Mol Life Sci* 60:1394-406, 2003.
26. Babban N and Gerner EW. Polyamines as modifiers of genetic risk factors in human intestinal cancers. *Biochem. Soc Trans.* 31:388-392, 2003.
27. Frahm J, Bruhn H, Gyngell ML, Merbolt KD, Hanicke W, Sauter R. Localized high-resolution proton NMR spectroscopy using echoes: initial applications to human brain in vivo. *Magn*

Reson Med 9:79-93, 1989.

28. Bottomley PA. Spatial localization in NMR spectroscopy in vivo. Ann N Y Acad Sci, 508:333-348, 1987.
29. Heerschap A, Jager G, de Koster A, Barentsz J, de la Rosette J, Debruyne F and Ruijs J. ¹H MRS of prostate pathology, in Proceedings of Soc of Magn Reson Med, 12th annual meeting, New York, 1993, p213.
30. Kurhanewicz J, Vigneron DB, Nelson SJ, Hricak HJ, McDonald JM, Konety B, Narayana P. Citrate as an in vivo marker to discriminate prostate cancer from benign hyperplasia and normal prostate peripheral zone: detection via localized proton spectroscopy. Urology 45:459-66, 1995.
31. Brown TR. Practical applications of chemical shift imaging. NMR Biomed. 5:238-243, 1992.
32. Brown TR, Kincaid BM, and Ugurbil K. NMR chemical shift in three dimensions. Proc Natl Acad Sci USA, 79:3523-26, 1982.
33. Maudsley AA, Hilal SK, Simon HE, Wittekoek S. In vivo MR spectroscopic imaging with P-31. Work in progress. Radiology 153:745-750m 1984.
34. Luyten PR, Marien AJ, den HJ. Acquisition and quantitation in proton spectroscopy. NMR Biomed 4:64-69, 1991.
35. Star-Lack J, Nelson SJ, Kurhanewicz J, Huang LR, Vigneron DB. Improved water and lipid suppression for 3D PRESS CSI using RF Band selective inversion with gradient dephasing (BASING). Magn Reson Med 38:311-321, 1997.
36. Tran T-KC, Vigneron DB, Sailasuta N, Tropp J, Le Roux P, Kurhanewicz J, Nelson S, Hurd R. Very selective suppression pulses for clinical MRSI studies of brain and prostate cancer. Magn Reson Med 43:23-33, 2000.
37. Star-Lack J, Vigneron DB, Pauly J, Kurhanewicz J, Nelson SJ. Improved solvent suppression and increased spatial excitation bandwidths for three-dimensional PRESS CSI using phase-compensating spectral/spatial spin-echo pulses. J Magn Reson Imaging 7:745-757, 1997.
38. Males RG, Vigneron DB, Star-Lack J, Falbo SC, Nelson SJ, Hricak H, Kurhanewicz J. Clinical application of BASING and Spectral/Spatial Water and Lipid Suppression Pulses for Prostate Cancer Staging and Localization by In Vivo 3D ¹H Magnetic Resonance Spectroscopic Imaging. Magn Reson Med 43:17-22, 2000.
39. Kurhanewicz J, Vigneron DB, Hricak H, Narayan P, Carroll P, Nelson SJ. Three-dimensional H-1 MR spectroscopic imaging of the in Situ human prostate with high (0.24-0.7 cm³) spatial resolution. Radiology 198:795-805, 1996.
40. Yu KK, Scheidler J, Hricak H, Vigneron DB, Zaloudek CJ, Males RG, Nelson SJ, Carroll PR, Kurhanewicz J. Prostate Cancer: Prediction of extracapsular extension with endorectal MR imaging and three-dimensional proton MR spectroscopic imaging. Radiology 213:481-88, 1999.
41. Coakley FV, Kurhanewicz J, Liu Y et al. Prostate cancer tumor volume: Measurement by endorectal MR imaging and MR spectroscopic imaging. Radiology 223:91-97, 2002.
42. Wefer AE, Hricak H, Vigneron DB, et al. Sextant localization of prostate cancer: comparison of sextant biopsy, magnetic resonance imaging and magnetic resonance spectroscopic imaging

with step section histology. *J Urol* 164:400-404, 2000.

43. Kurhanewicz J, Vigneron DB, Nelson SJ. Three-dimensional magnetic resonance spectroscopic imaging of brain and prostate cancer. *Neoplasia* 2:166-189, 2000.
44. Scheenen TWJ, Klomp DWJ, Roll SA, Futterer JJ, Barentsz JO, Heerschap A. Fast acquisition-weighted three-dimensional proton MR spectroscopic imaging of the human prostate. *Magn Reson Med* 52:80-88, 2004.
45. Scheenen TWJ, Gambarota G, Weiland E, Klomp DWJ, Futterer JJ, Barentsz, Heerschap A. Optimal timing for in vivo ¹H-MR Spectroscopic imaging of the human prostate at 3T. *Magn Reson Med* 53:1268-74, 2005.
46. Scheenen T, Weiland E, Futterer J, van Hecke P, Bachert P, Villeirs G, Lu J, Lichy M, Holshouser B, Roell S, Barentsz J, Heerschap A. Preliminary results of IMAPS: An International Multi-Centre Assessment of Prostate MR Spectroscopy. *Proceedings of the Thirteenth Int Soc Mag Reson Med.*, Miami Beach, 2005, p 260.
47. Jung JA, Coakley FV, Vigneron DB, Swanson MG, Qayyum A, Weinberg V, Jones KD, Carroll PR, Kurhanewicz J. Prostate depiction at endorectal MR spectroscopic imaging: Investigation of a standardized evaluation system. *Radiology* 233:701-708, 2004.
48. Swanson MG, Vigneron DB, Tran T-K C, Kurhanewicz J. Magnetic resonance imaging and spectroscopic imaging of prostate cancer. *Cancer Investigation* 19(5):510-523, 2001.
49. Hricak H. MR imaging and MR spectroscopic imaging in the pre-treatment evaluation of prostate cancer. *Br J Radiol* 78:S103-S111, 2005.
50. D'Amico AV, Whittington R, Malkowicz B, et al. Endorectal magnetic resonance imaging as a predictor of biochemical outcome after radical prostatectomy in men with clinically localized prostate cancer. *J Urol* 164:759-763, 2000.
51. DiBiase SJ, Hosseinzadeh K, Gullapalli RP, et al. Magnetic resonance spectroscopic imaging-guided brachytherapy for localized prostate cancer. *Int J Radiat Oncol Biol Phys* 52L429-8, 2002.
52. Mizowaki T, Cohen GN, Fung AY, Zaider M. Towards integrating functional imaging in the treatment of prostate cancer with radiation: the registration of the MR spectroscopy to ultrasound/CT images and its implementation in treatment planning. *Int J Radiat Oncol Biol Phys* 54:1558-64, 2002.
53. Sosna J, Rofsky NM, Gaston SM, DeWolf WC, Lenkinski RE. Determinations of prostate volume at 3-Tesla using an external phased array coil: Comparison to pathologic specimens. *Acad Radiol* 10:846-853, 2003.
54. Sosna J, Pedrosa I, Dewolf WC, Mahallati H, Lenkinski RE, Rofsky NM. MR imaging of the prostate at 3 Tesla: Comparison of an external phased-array coil to imaging with an endorectal coil at 1.5 Tesla. *Acad Radiol* 11:857-862, 2004.
55. Bloch BN, Rofsky NM, Baroni RH, Marquis RP, Pedrosa I, Lenkinski RE. 3 Tesla magnetic resonance imaging of the prostate with combined pelvic phased-array and endorectal coils: Initial experience. *Acad Radiol* 11:863-867, 2004.
56. Gibbs P, Pickles MD, Turnbull LW. Diffusion imaging of the prostate at 3.0 Tesla. *Invest Radiol* 41(2):185-188, 2006.

57. Pickles MD, Gibbs P, Sreenivas M, Turnbull LW. Diffusion-weighted imaging of normal and malignant prostate tissue at 3.0T. *J Magn Reson Imaging* 23(2):130-134, 2006.
58. Shimofusa R, Fujimoto H, Akamata H, Motoori K, Yamamoto S, Ueda T, Ito H. Diffusion-weighted imaging of prostate cancer. *J Comput Assist Tomogr* 29(2):149-153, 2005.
59. Padhani AR, Gapinski CJ, Macvicar DA, Parker GJ, Suckling J, Revell PB, Leach MO, Dearnaley DP, Husband JE. Dynamic contrast enhanced MRI of prostate cancer: Correlation with morphology and tumor stage, histological grade and PSA. *Clinical Radiology* 55:99-109, 2000.
60. Hara N, Okuizumi M, Koiki H, Kawaguchi M, and Bali V. Dynamic contrast-enhanced magnetic resonance imaging (DCE-MRI) is a useful modality for the precise detection and staging of early prostate cancer. *The Prostate* 62(2):140-147, 2004.
61. Huisman HJ, Engelbrecht MR, Barentsz JO. Accurate estimation of pharmacokinetic contrast enhanced dynamic MRI parameters of the prostate. *J Magn Reson Imaging* 13:607-14, 2001.
62. Engebrecht MR, Huisman HJ, Laheij RJF, Jager GJ, van Leenders GJLH, Hulsbergenvan de Kaa CA, de la Rosette JJMCH, Blickman JG. Discrimination of prostate cancer from normal peripheral zone and central gland tissue by using contrast-enhanced MR imaging. *Radiology* 229:248-254, 2003.
63. Buckley D, Roberts C, Parker GJM, Hutchinson CE. Prostate Cancer: Evaluation of vascular characteristics with dynamic contrast-enhanced T1-weighted MR imaging – Initial experience. *Radiology* 233:709-15, 2004.
64. van Dorsten FA, van der Graaf M, Engelbrecht MR, van Leenders GJLH, Verhofstad A, Rijkema M, de la Rosette JJMCH, Barentsz JO, Heerschap A. Combined quantitative dynamic contrast enhanced MR imaging and 1H MR spectroscopic imaging of human prostate cancer. *J Magn Reson Imaging* 20:279-287, 2004.

Magnetic Resonance Spectroscopy of Prostate Disease

Rao Gullapalli

**Magnetic Resonance Research Center
Department of Radiology
University of Maryland, Baltimore**



Prostate Cancer - Prevalance

- American Cancer Society estimates 234,460 new cases of prostate cancer (PCa) in 2006.
- With the aging of the baby boomers this number is estimated to increase to 450,000 by year 2015.
- Estimate of 27,350 deaths in 2006 due to PCa.
- African American men are twice as vulnerable compared to caucasian men.
- Second leading cause of cancer among men after lung cancer.

Prostate Cancer - Diagnosis

- **Combination of digital rectal examination and prostate-specific antigen(PSA) is the primary diagnostic procedure.**
- **Elevated PSA or a nodule detected during physical examination may eventually prompt an transrectal ultrasound-guided (TRUS) biopsy.**
- **Often negative biopsies occur due to sampling errors despite a rise in PSA levels.**
- **Thus better imaging of the cancer for guiding biopsies and staging cancer are needed.**

Prostate size

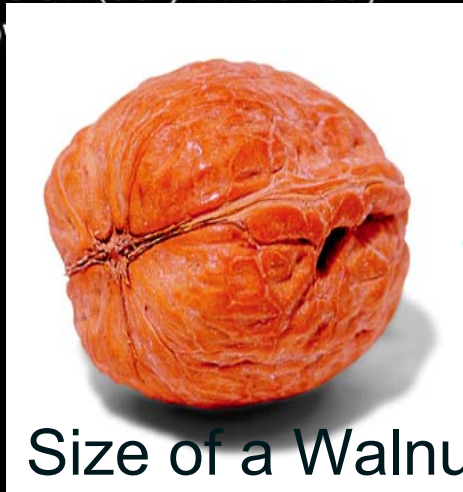
Tim

Local becomes total

205 cm (6'9") Whole Body

co

ty.



Size of a Walnut!

T2 TSE
512 Matrix, PAT 2,
Whole-body examination
acquired in 5 steps



- **Small Size and Deep location - requires specialized rf coils**
- **Complex Anatomy requires high spatial resolution and 3-D spectroscopy**
- **68 % of cancers in the periphery of the gland - requires accurate volume selection**

Exit

Combined Endorectal Pelvic Phased Array

Torso Array + Expandable Endorectal Coil

Torso array



MEDRAD
Expandable
Endorectal
coil

Torso
Connector

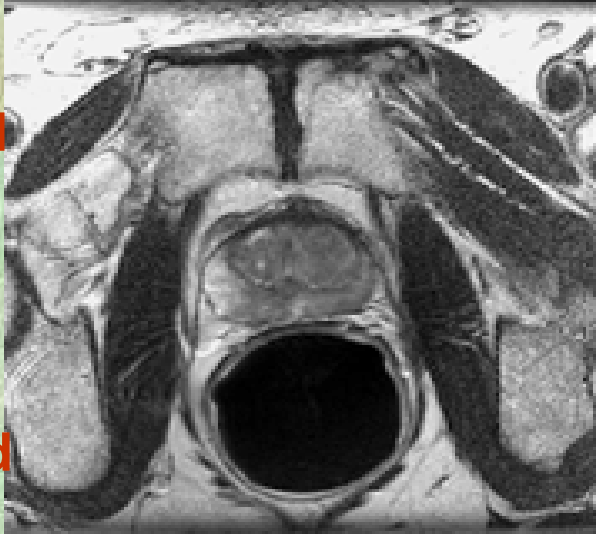
Courtesy: John Kurhanewicz, Ph.D. UCSF

Prostate Cancer - MRI

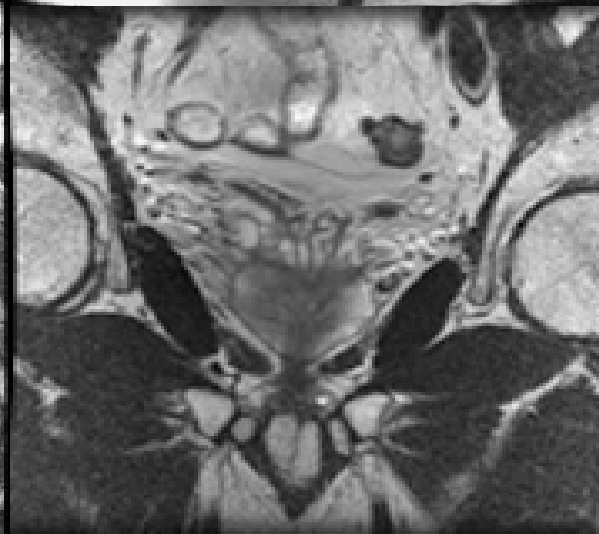
Sagittal Localizer
- check coil position, prescribe other images



T₂ Axial and Coronal Images - assess cancer location and stage



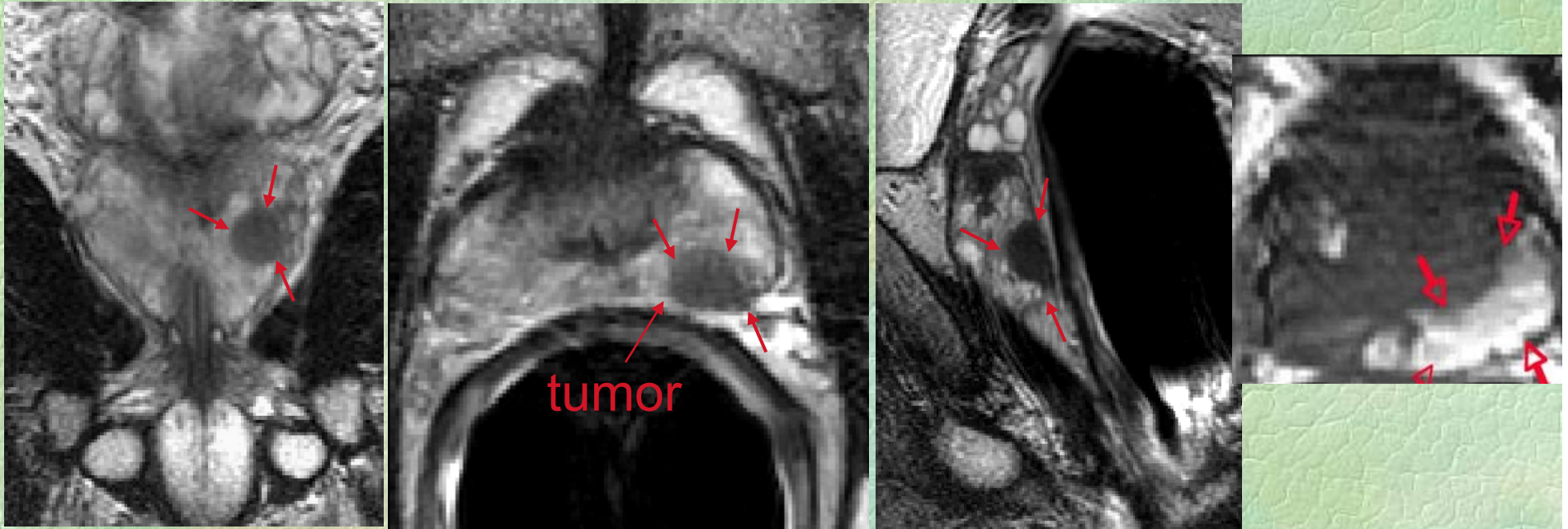
T₁ weighted Axial - assess biopsy artifact, lymph nodes and bone



T₂ weighted coronal images - assess cancer location and stage

MR Imaging \approx 20 min.

Prostate Cancer - MRI



- Multi-planar high-resolution T2 weighted images are acquired through the prostate and surrounding structures in order to assess the location, spatial extent and spread of prostate cancer. Cancer region is typically seen as a hypointense region within the gland.
- T1-weighted images are acquired through the prostate and pelvis in order to assess the presence of post-biopsy hemorrhage within the prostate and metastases to pelvic bone and lymph nodes.

Courtesy: **John Kurhanewicz, Ph.D. UCSF**

Post-Processing Correction for the Reception Profiles of the Endorectal and Phased Array Coils

Improves
Image
Interpretation

Prostate Analytical Coil Correction

Sagittal Coil Locate **Axial Coil Locate**

Pick Points: ☒ Set Points/Pan

Dis 1 Pt 1: R31 P10 I118
Dis 1 Pt 2: R31 P29 I193
Dis 2 Pt 1: R42 P12 I161
Dis 2 Pt 2: R10 P15 I161

Exam:
Series:
Image:

Correct Series

Choose One or More Series to Correct

Ser	Imgs	Description
1	20	Sag SE Lector
2	20	Sag SE Lector
3	35	Axial T1
4	22	Sag Hi-Res
5	29	Axial FSE T2
6	22	Coronal FSE T2
7	56	Dwssfse Tensor
8	22	PROSE 10/09
103	35	Corrected Axial T1
104	22	Corrected Sag Hi-Res
105	29	Corrected Axial FSE T2
106	22	Corrected Coronal FSE T2
304	22	PACC Sag Hi-Res
306	22	PACC Coronal FSE T2

Status: **Correction Successful**

Courtesy: John Kurhanewicz, Ph.D. UCSF

Technical Data (Sagittal):
 Sigma 1.5T S/S#tesla A 67
 EX: 20921 WEISBERG MEL
 SE: 2 M 61 43941313
 TR: 15 DCB: 23 Dec 1940
 Sag: R31.0 15 Nov 02
 10:00:04 AM
 Mag = 1.7
 F-
 ROT:
 ET:16
 FSE
 TR:1000
 TE:190/15
 EC:1/1 15.6kHz
 PELVIC
 FOV:28x28
 5.0cm/1.5cm
 20/01:39
 256X192/1.00 NEX
 I 232 k = 934 L = 552

Technical Data (Axial):
 Sigma 1.5T S/S#tesla A 41
 EX: 20921 WEISBERG MEL
 SE: 5 M 61 43941313
 TR: 15 DCB: 23 Dec 1940
 Ax: I160.6 15 Nov 02
 10:15:20 AM
 Mag = 2.1
 FL:
 ROT:
 ET:16
 FSE
 TR:1000
 TE:190/15
 EC:1/1 20.9kHz
 PELVIC
 FOV:14x14
 3.0cm/1.0cm
 20/03:42
 256X192/3 NEX
 NP/VR/1RF/SPF
 P 26 W = 1140 L = 1065

Corrected Image

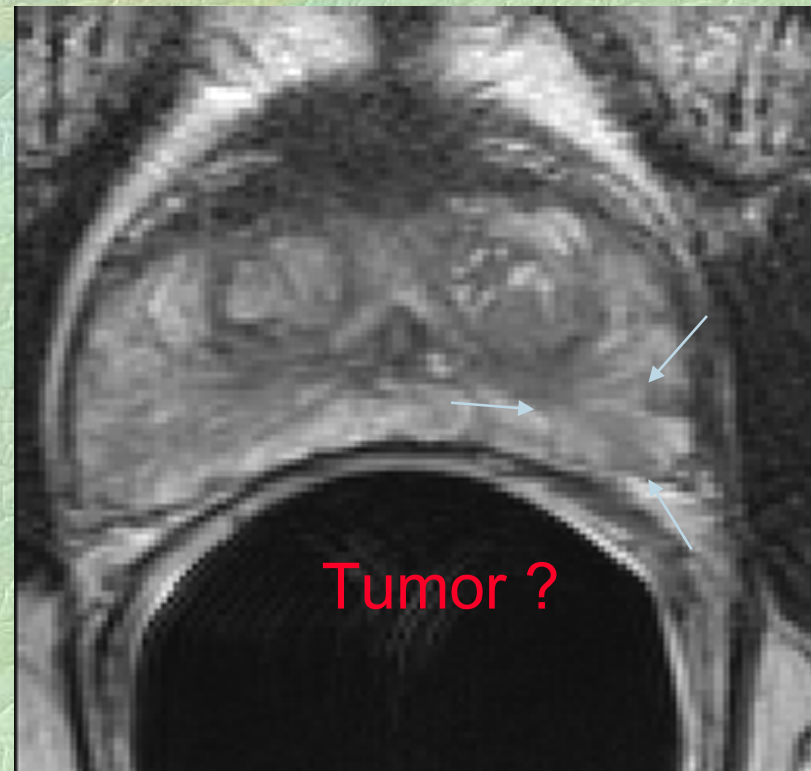
Technical Data (Corrected Axial):
 Sigma 1.5T S/S#tesla A 29
 EX: 20921 WEISBERG MEL
 SE: 5 M 61 43941313
 TR: 15 DCB: 23 Dec 1940
 Ax: I160.6 15 Nov 02
 10:15:20 AM
 Mag = 2.1
 FL:
 ROT:
 ET:16
 FSE
 TR:1000
 TE:190/15
 EC:1/1 20.9kHz
 PELVIC
 FOV:14x14
 3.0cm/1.0cm
 20/03:42
 256X192/3 NEX
 NP/VR/1RF/SPF
 P 26 W = 1140 L = 1065

Prostate Cancer - MRI

MRI alone has good accuracy in detecting seminal vesicle invasion (96%).

Assessment of spread through the capsule is more difficult (accuracy - 81%), and is getting harder with fewer men demonstrating gross ECE at diagnosis.

High Resolution MRI has demonstrated good sensitivity (79%) but low specificity (55%) in determining tumor location due to a large number of false positives.

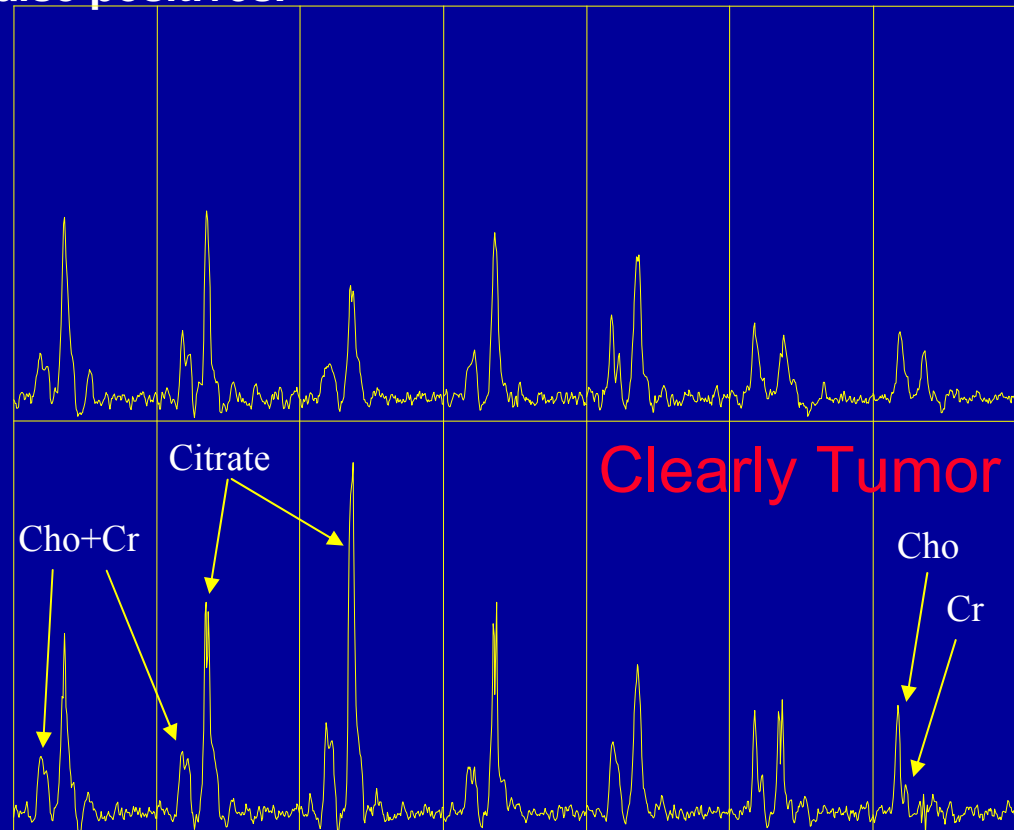
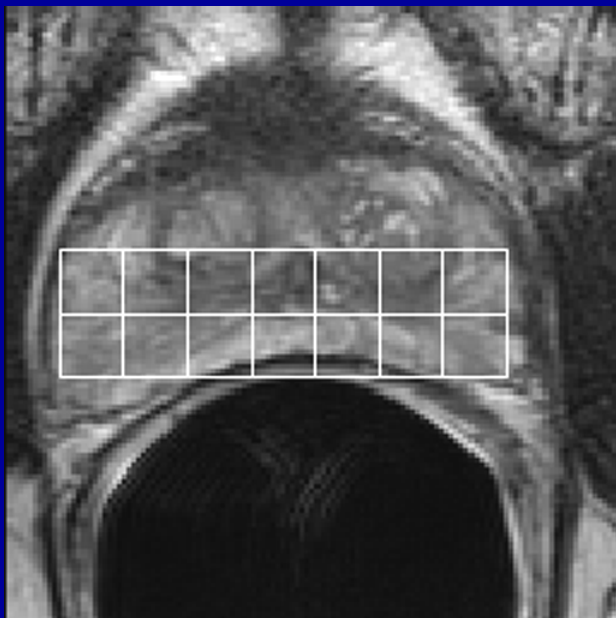
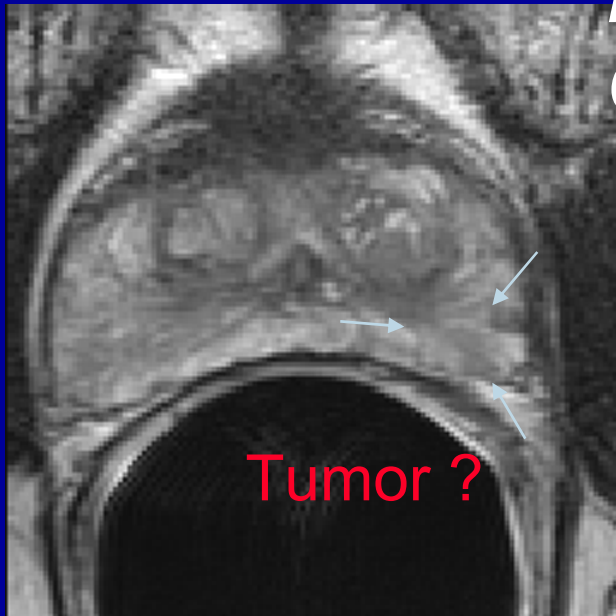


Courtesy: John Kurhanewicz, Ph.D. UCSF

MRI Lacks Specificity for Localizing Cancer within the Prostate

3D-MRSI Adds Specificity

High Resolution MRI has demonstrated good sensitivity (79%) but low specificity (55%) in determining tumor location due to a large number of false positives.



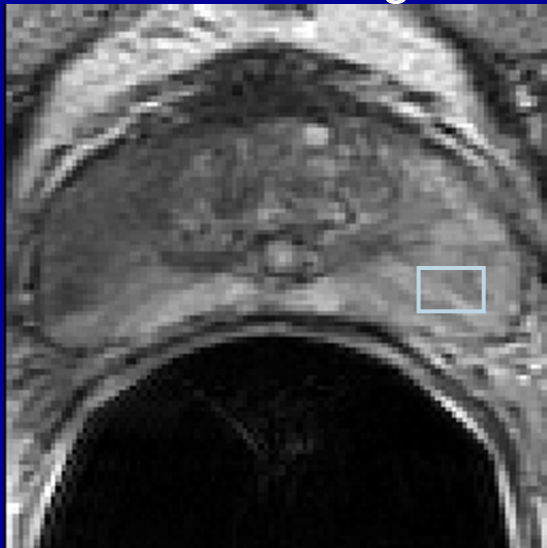
Radiology 1994;193:703-709

Prostate Magnetic Resonance Spectroscopy

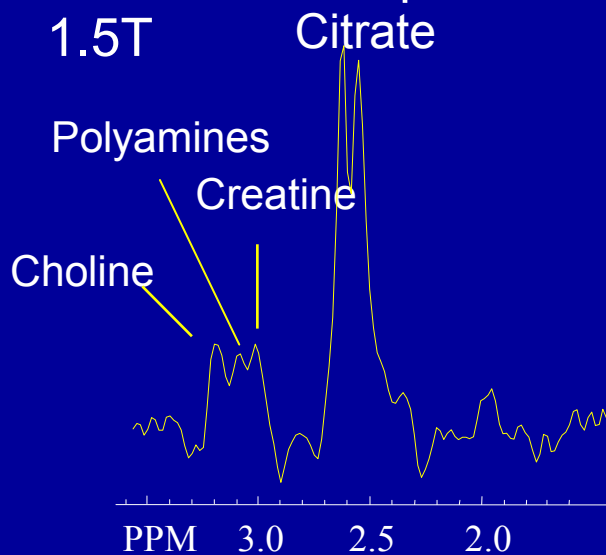
- Over a decade ago it was shown that proton NMR spectra of extracts contained signals from many metabolites including citrate, choline and creatine.
- Further it was shown that the signal from citrate may be reduced and that signals from choline compounds increase in PCa suggesting the possibility of differentiating between benign and cancerous tissues.
- Although spectra were obtained *in vivo* prior to the advent of endorectal coil, it is their arrival that made detection of prostate metabolites with good signal to noise over a reasonable scan time.

Healthy Prostate Metabolism

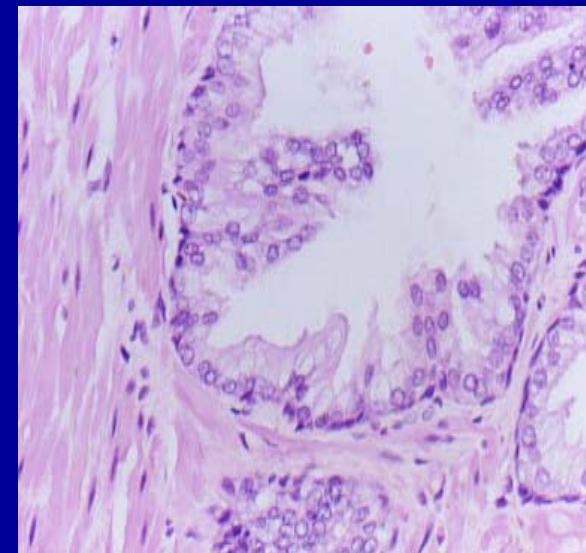
T2W MR Image



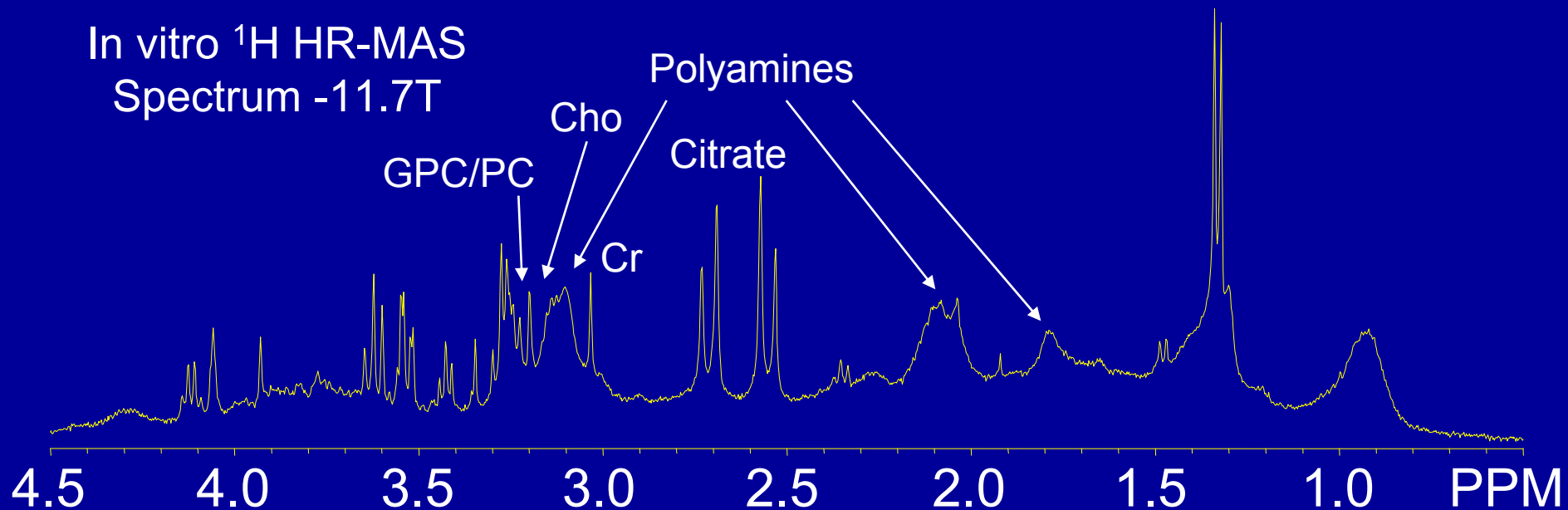
In vivo MRSI Spectrum - 1.5T



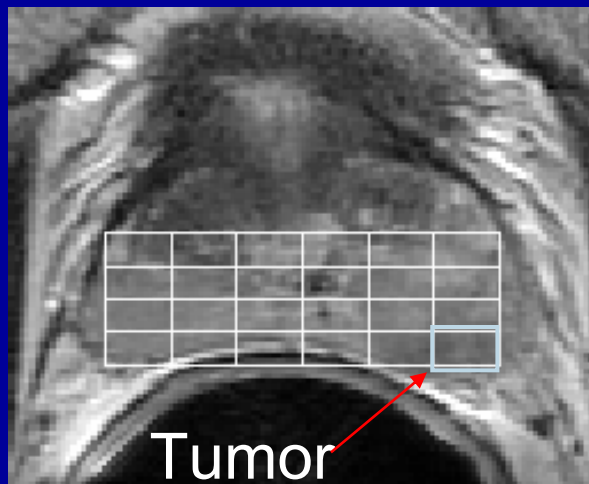
H&E Stain



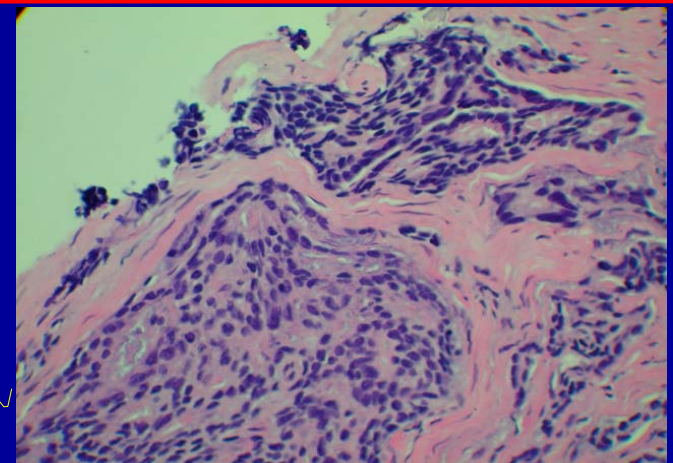
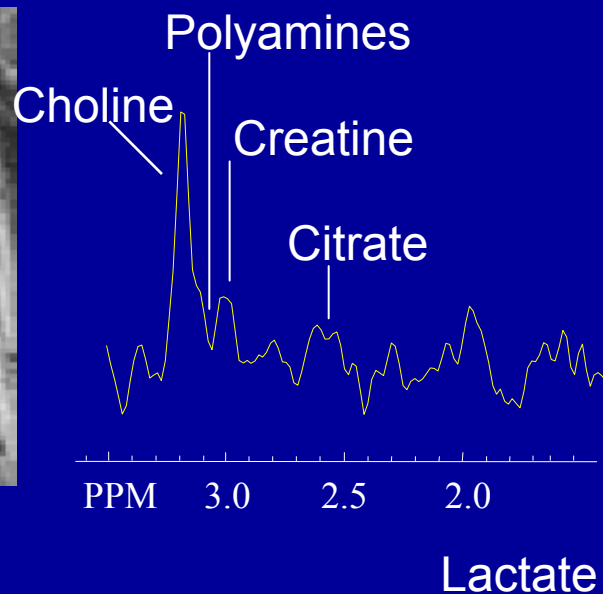
In vitro ^1H HR-MAS Spectrum - 11.7T



Malignant Prostate Metabolism



T2W MR image



50% G(4+4), 50% HS

1D HR-MAS Spectrum (500 MHz)

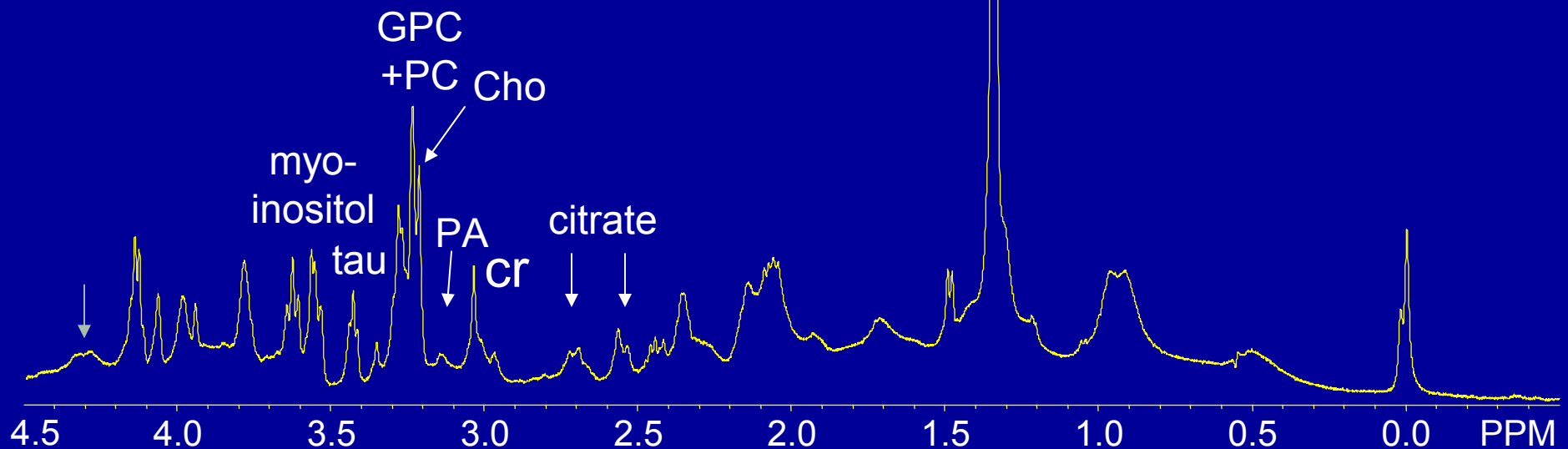
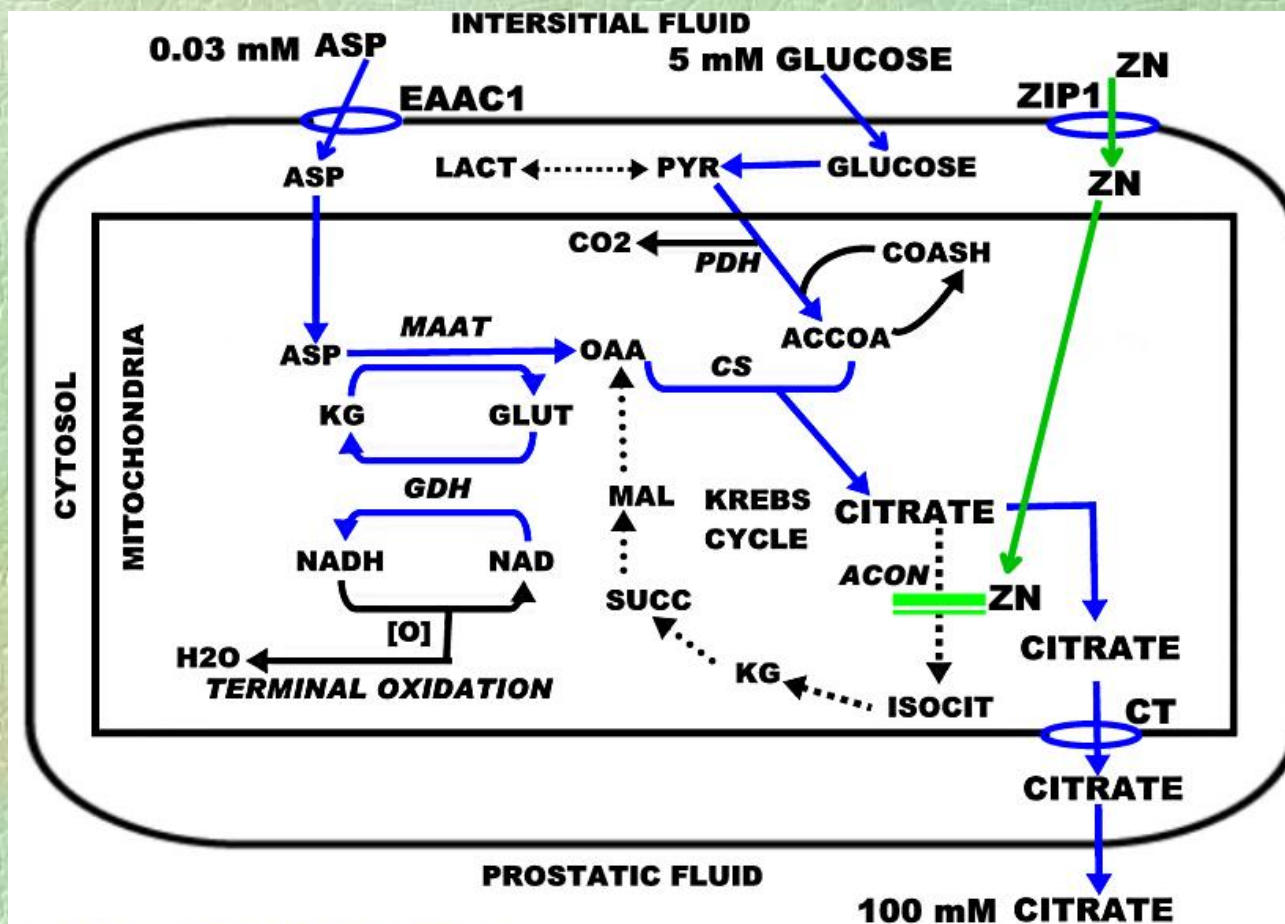


Table 1. Representative Citrate Levels in the Human Prostate
nmol/gm(from Costello et al)⁷

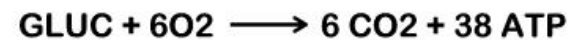
Normal Central Zone	5,000
Normal Peripheral Zone	13,000
BPH (mixed tissue)	10,000-15,000
BPH (glandular tissue)	20,000-50,000
PCa (mixed tissue)	1,000-3,000
Malignant tissue	<500
Stromal tissue	150-300
Other Soft tissues	150-450
Blood plasma	90-110
Prostatic fluid	40,000-150,000



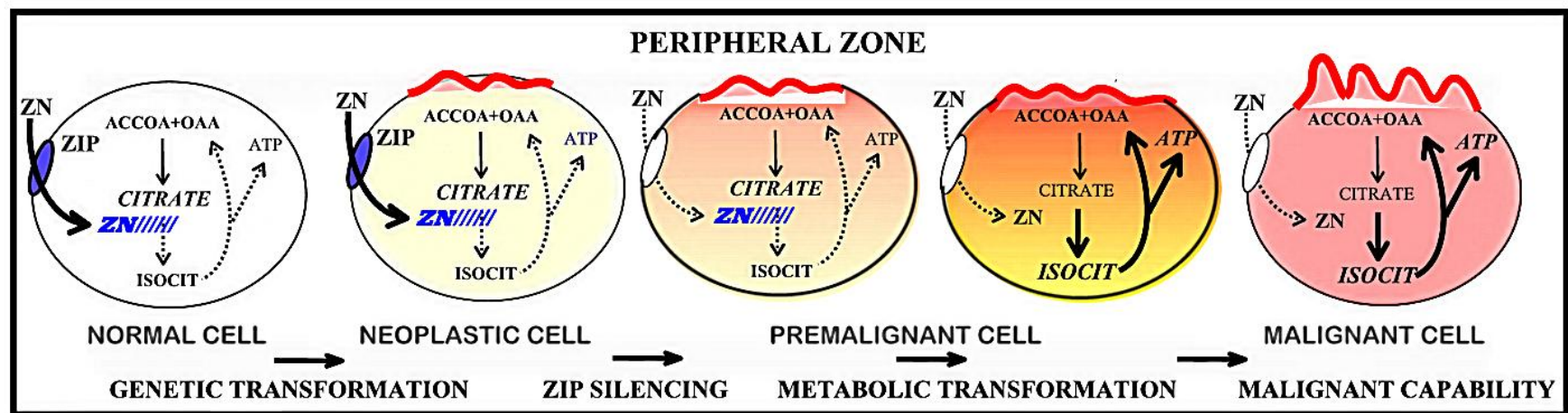
NORMAL PROSTATE CELLS



NORMAL MAMMALIAN CELLS & MALIGNANT PROSTATE CELLS



Courtesy: Costello & Franklin



Courtesy: Costello & Franklin

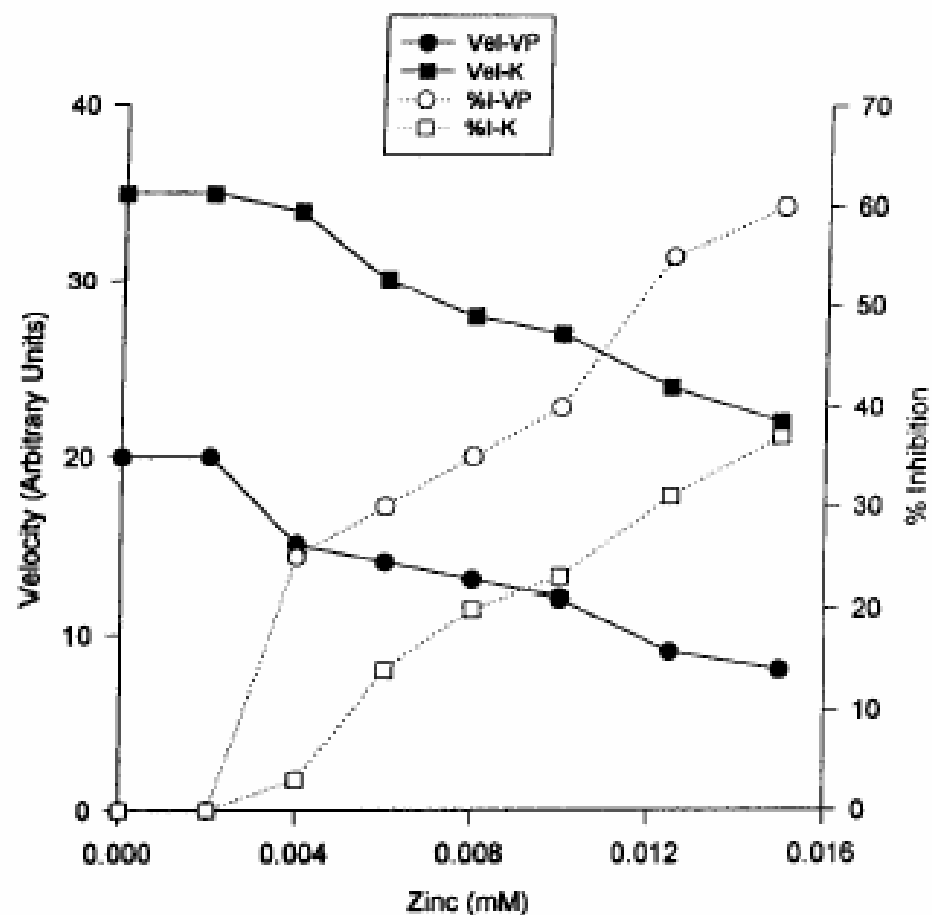
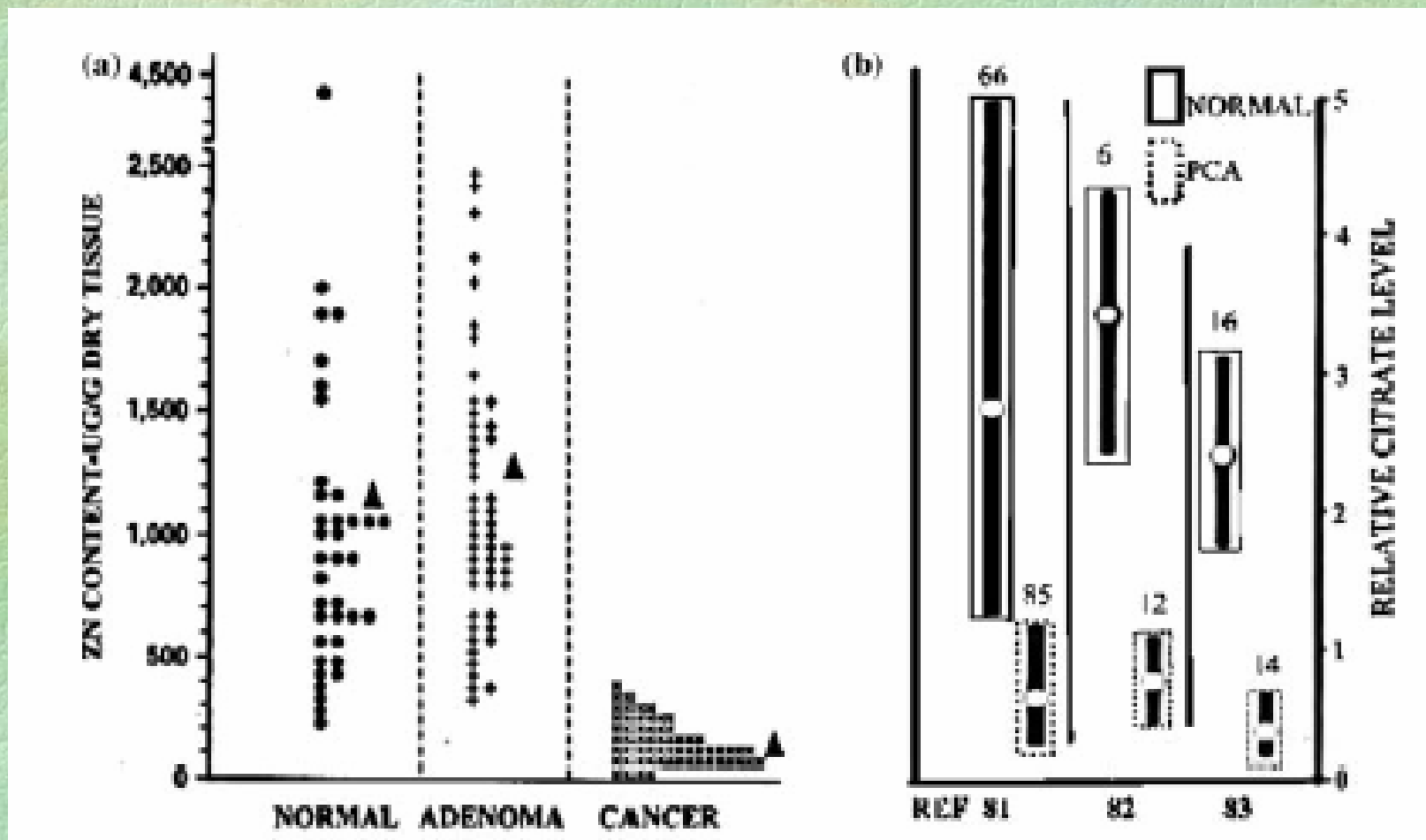


FIG. 1. The effect of zinc on the m-aconitase activity (*Vel*) of mitochondrial preparations from rat ventral prostate (*VP*) epithelial cells and kidney (*K*) cells. The activity was determined by fluoroenzymatic assay of the reaction citrate \rightarrow isocitrate. The reaction system contained 0.05 mM citrate and 80 μ g of mitochondrial protein. %*I*, % inhibition.



Zaichick et al Int Urol Nephrol 1997; Costello et al. Pros Cancer & Pros Dis 2004

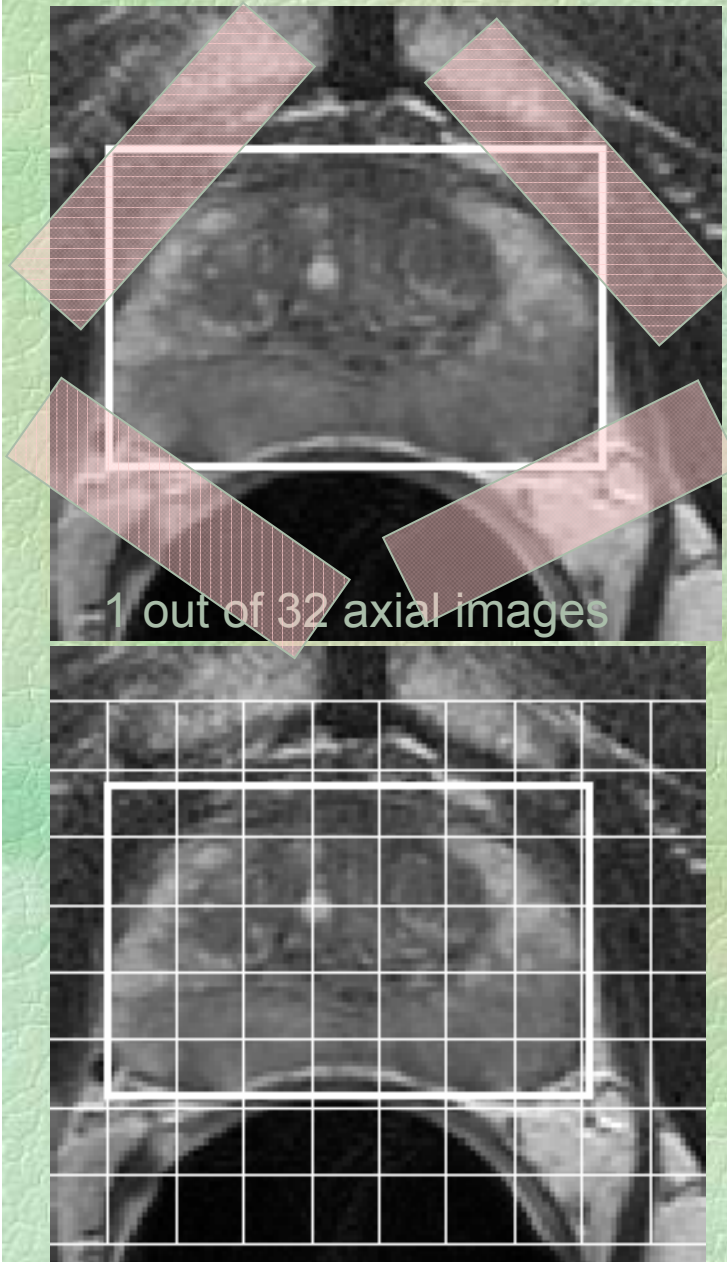
Zinc-Citrate Connection

- The zinc and citrate relationships are associated with the secretory epithelial cell component of the prostate gland
- In humans, high zinc and high citrate levels are associated with the lateral lobe of the peripheral zone, whereas low zinc and low citrate levels are associated with the central zone.
- High zinc levels inhibit citrate oxidation and increase citrate levels in prostate cells.

Zinc-Citrate Connection

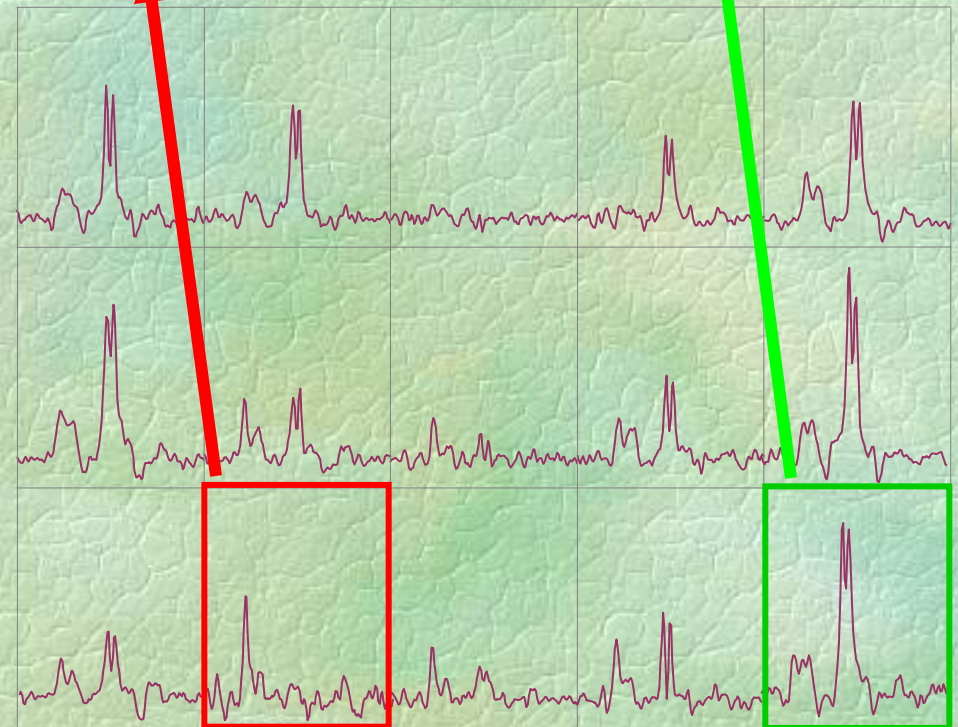
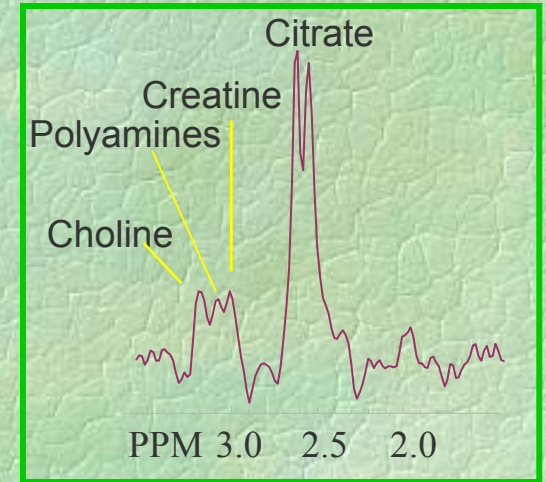
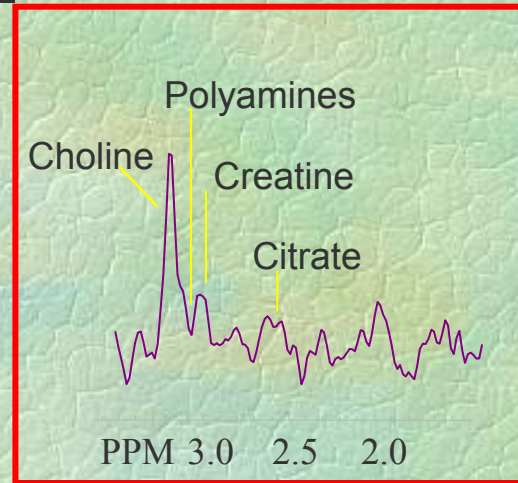
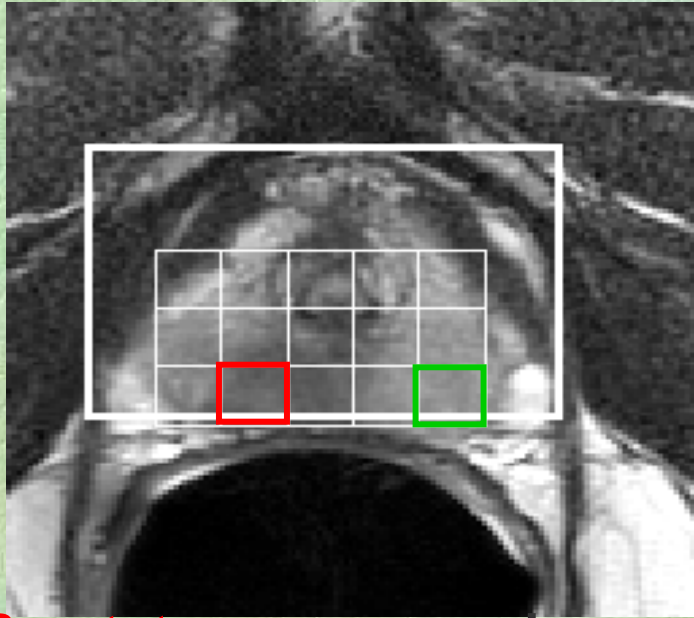
- Zinc and citrate levels are uniquely high in normal human prostate and in BPH
- Zinc and citrate levels are markedly decreased in PCa
- The decrease in zinc and citrate levels occurs early in malignancy
- High zinc levels inhibit citrate oxidation and increase citrate levels in prostate cells.

MRSI Methods



- ^1H PRESS selection of a volume encompassing the prostate (bold white box)
- Automatic “Phase Map” Shimming of selected volume.
- Water and Lipid Suppression - (BASING or Spectral Spatial)
- VSS outer volume suppression - (conformed selection, improved lipid suppression and reduced chemical shift artifact) –
- 3-D phase encoding -16x8x8 (1 NEX) phase-encoding TR- 750-900ms, weighted elliptical encoding – 9-12 min.

Methods - MRSI

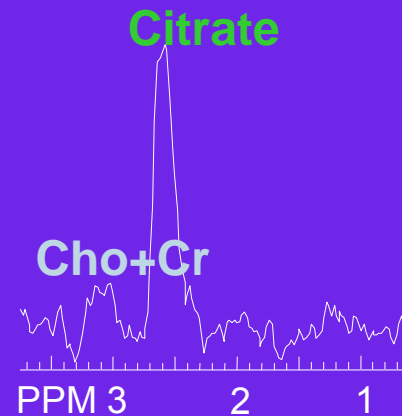
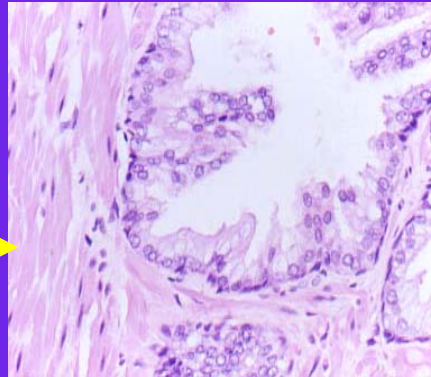
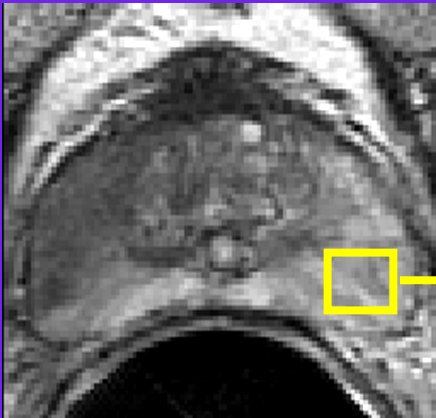


Portion of the 3-D MRSI spectral array

Prostate cancer can be discriminated from **healthy peripheral zone (PZ) tissue** based on low signal intensity on T2 weighted MRI and a significant reduction in the levels of citrate and polyamines and an elevation in choline on MRSI. The strength of the test is when MRI and MRSI results are concordant for cancer.

MRI and ^1H -MRSI - *Prostate: Metabolic Interrogation*

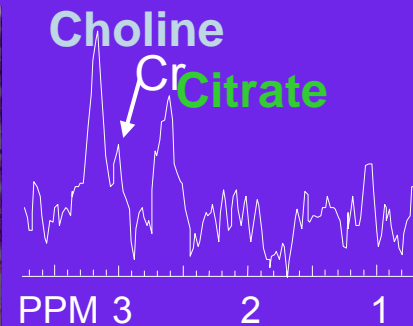
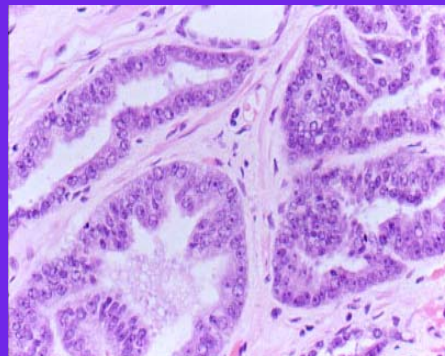
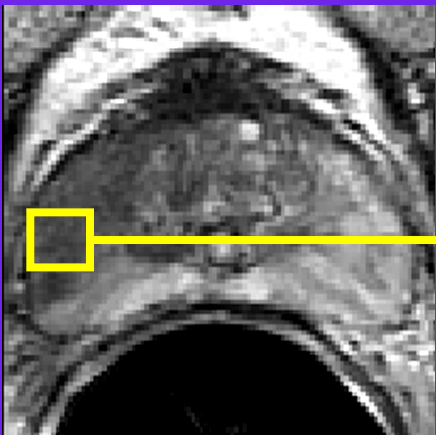
Benign Hypertrophy



Increased Choline - cellular proliferation, cell density, phospholipid composition and metabolism

Decreased Citrate - unique zinc and citrate metabolism and changes in ductal morphology

Prostate Cancer



Decreased Polyamines - least understood, possibly related to cellular proliferation and secretory function

Courtesy: Dr. Choyke, NCI

PRESS (Spectral/Spatial) + VSS

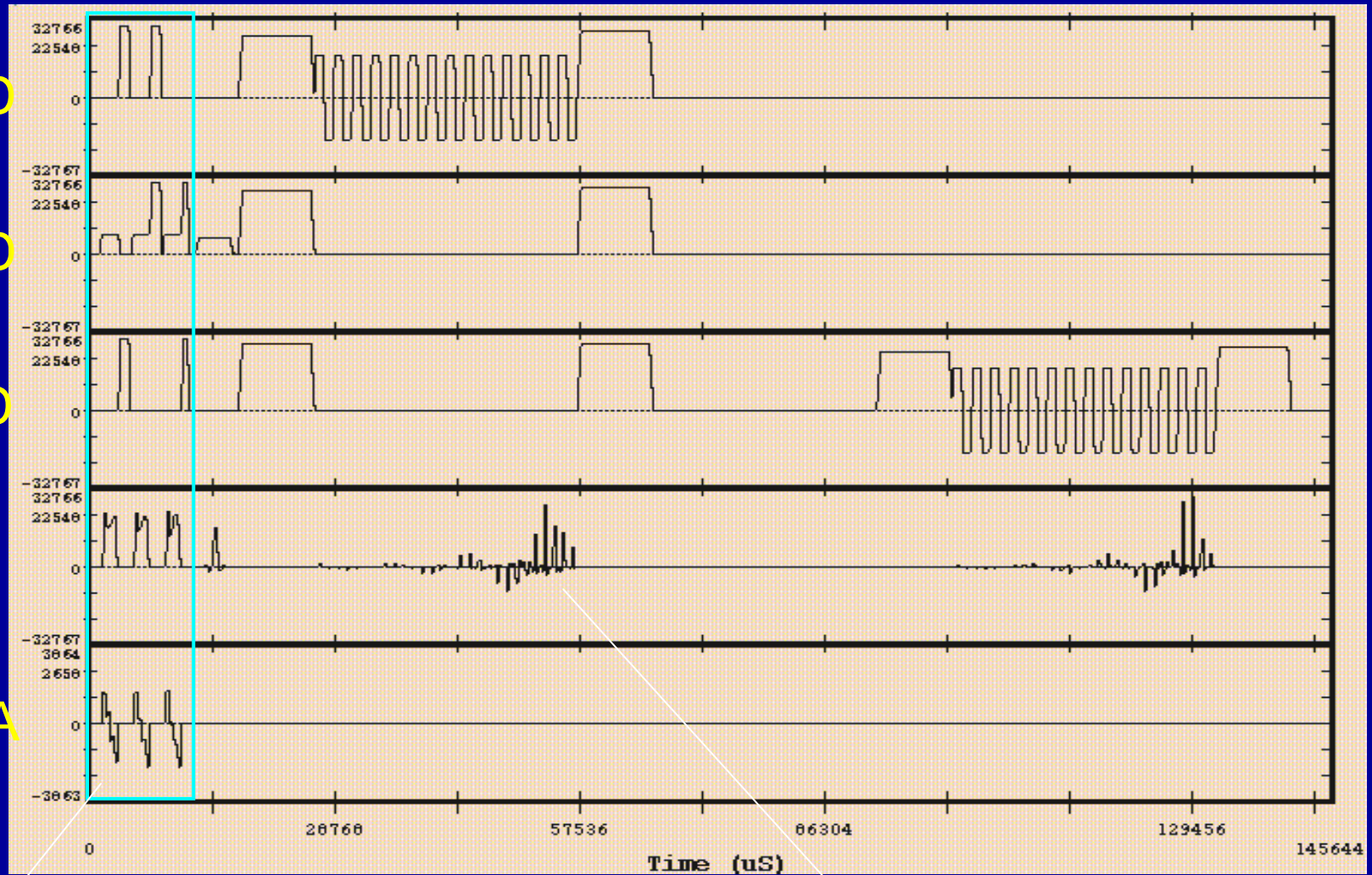
XGRAD

YGRAD

ZGRAD

RHO

OMEGA



VSS- Outer volume suppression

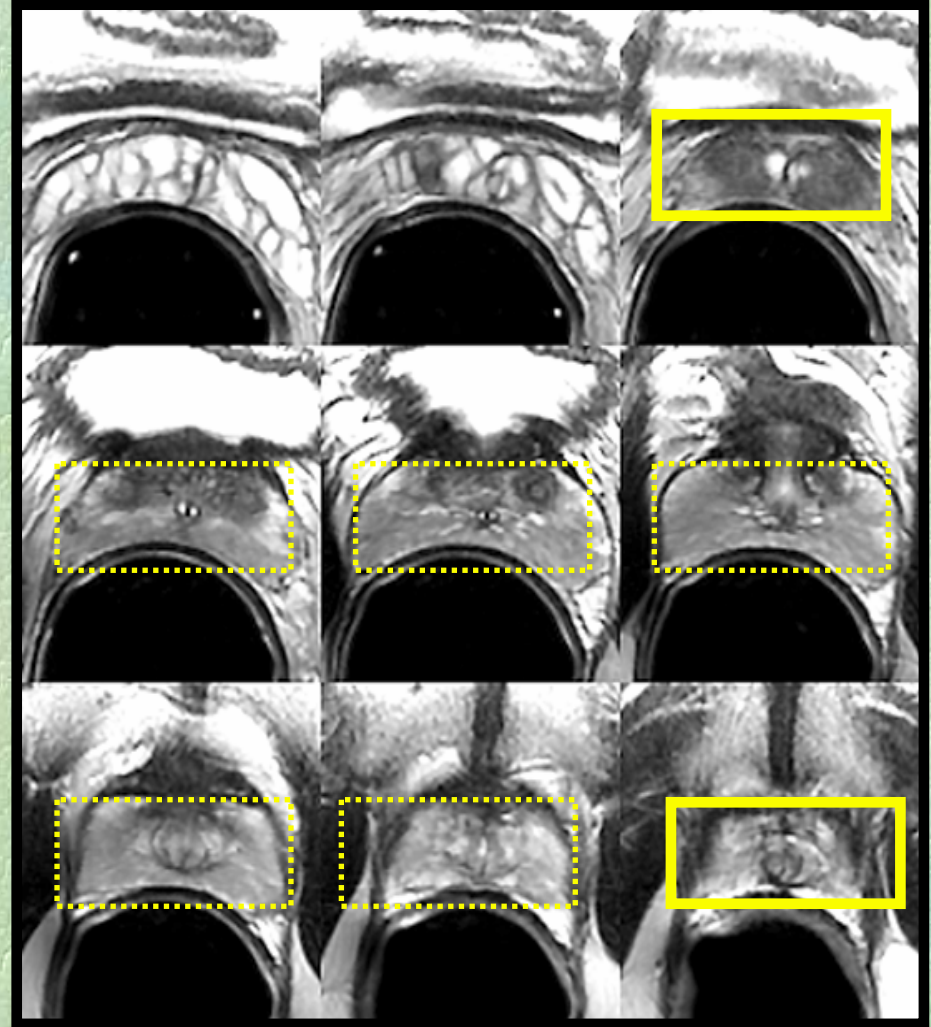
Time

Spectral Spatial Volume selection

Prostate MRSI: Prescribing the PRESS Volume

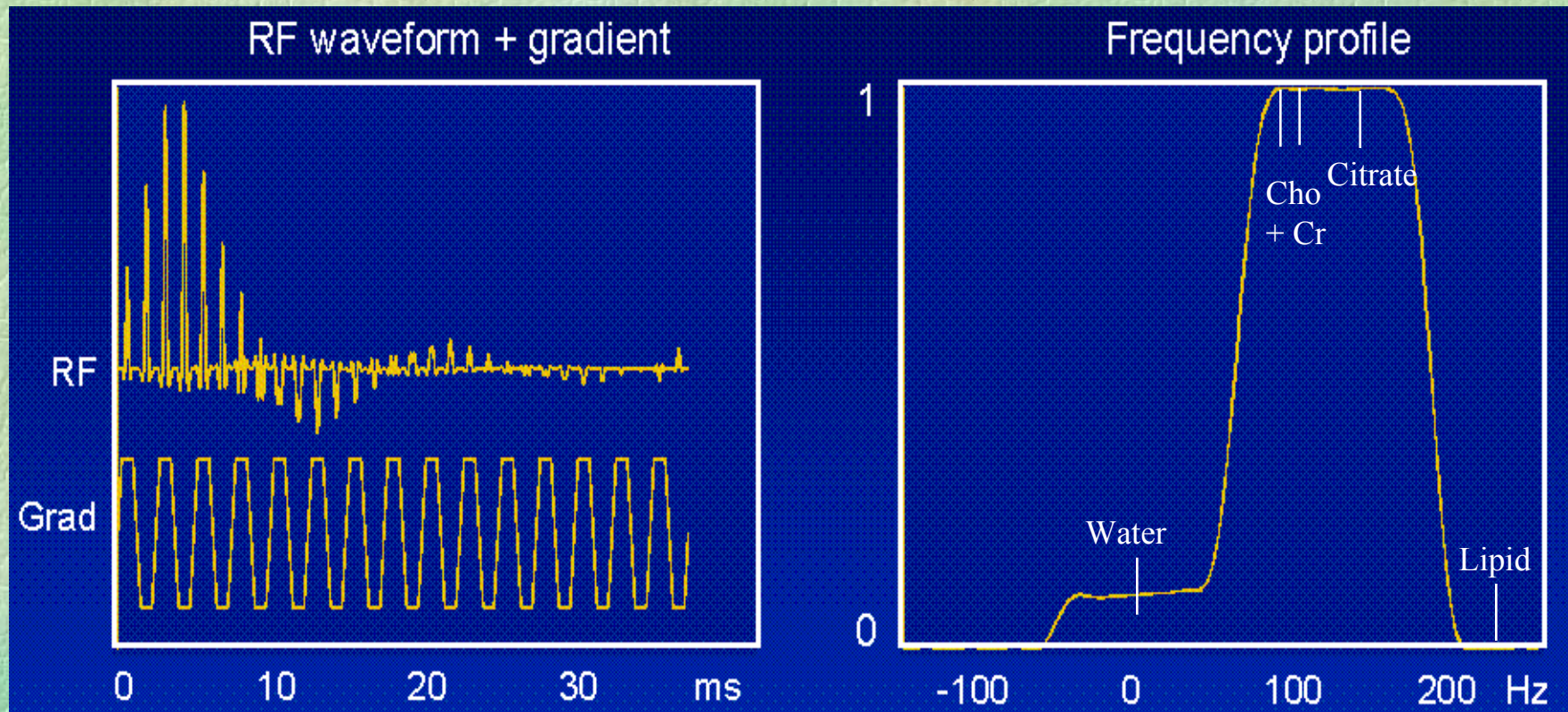
Goals:

- 1) Cover the gland especially the peripheral zone.
- 2) Minimize inclusion of air-interface.
- 3) Minimize lipid inclusion.



Courtesy: John Kurhanewicz, Ph.D. UCSF

Dual Band Spectral Spatial Acquisition

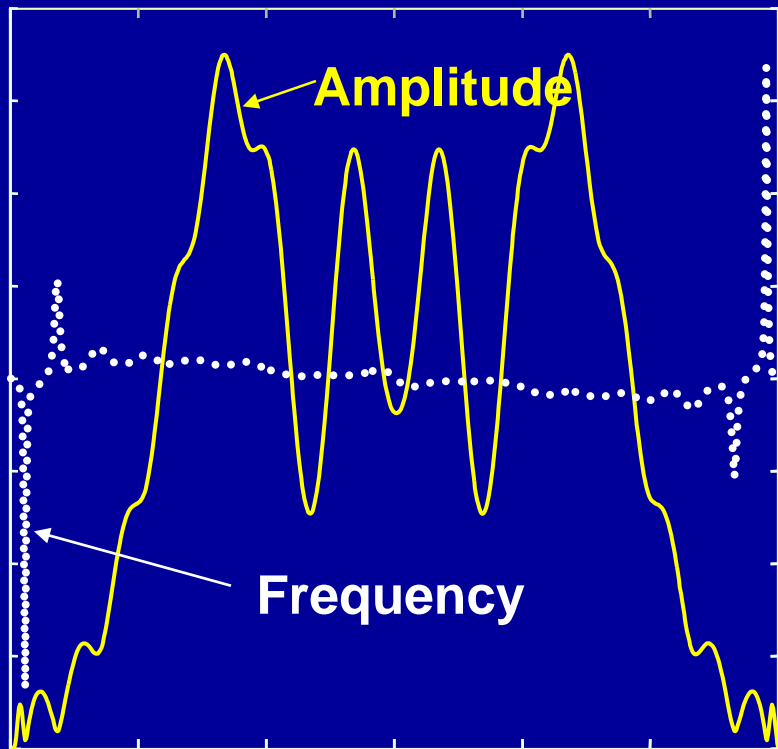


- Robust water and lipid suppression with ability to leave residual water for phase and frequency reference
- Reduced chemical shift artifacts
- Phase modulation reduces peak power requirements

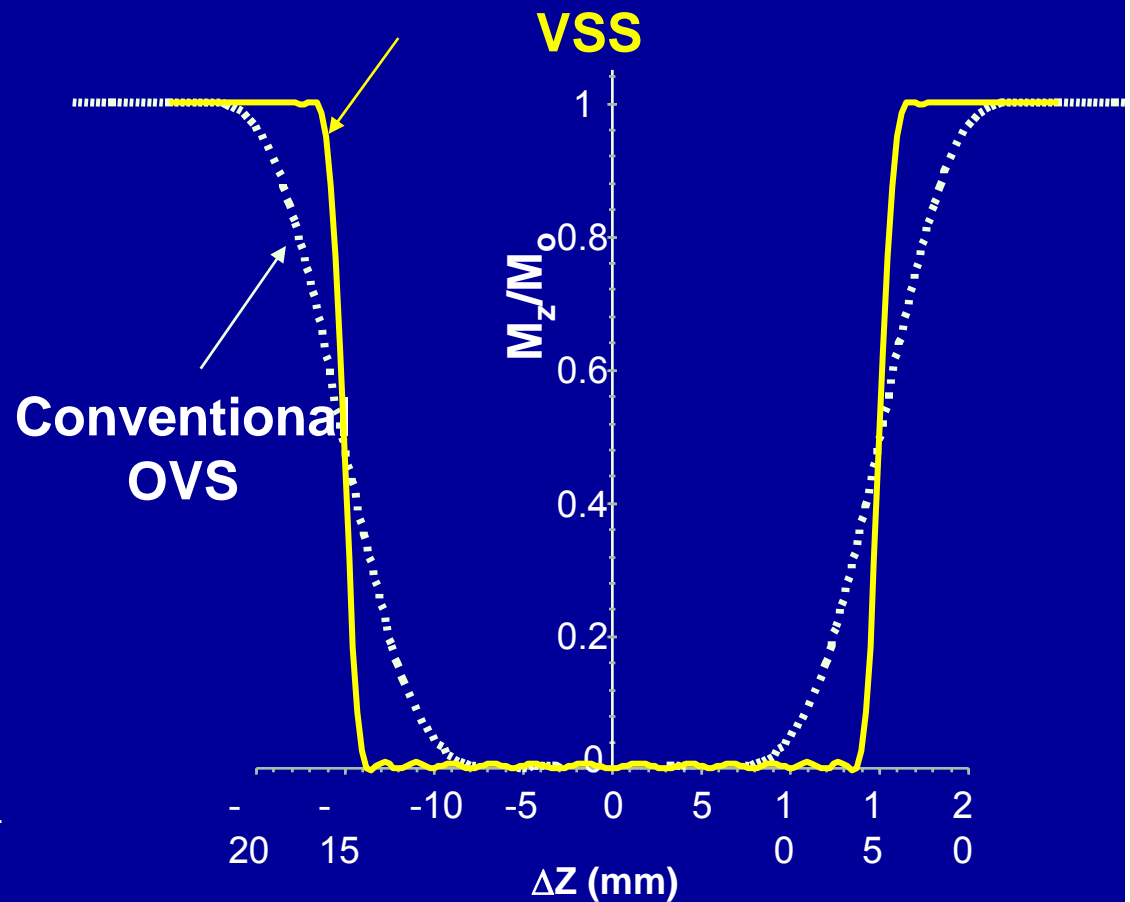
Courtesy: *John Kurhanewicz, Ph.D. UCSF*

Very Selective Saturation (VSS) Pulses

Amplitude and Frequency Profiles



Suppression Profiles



Courtesy: John Kurhanewicz, Ph.D. UCSF

Chemical Shift Misregistration

3 Overlaid Phantom PRESS Box Images acquired
with $\Delta\nu = -100, 0, +100$ Hz

Conventional PRESS

X: 180 SLR (1.1 kHz)

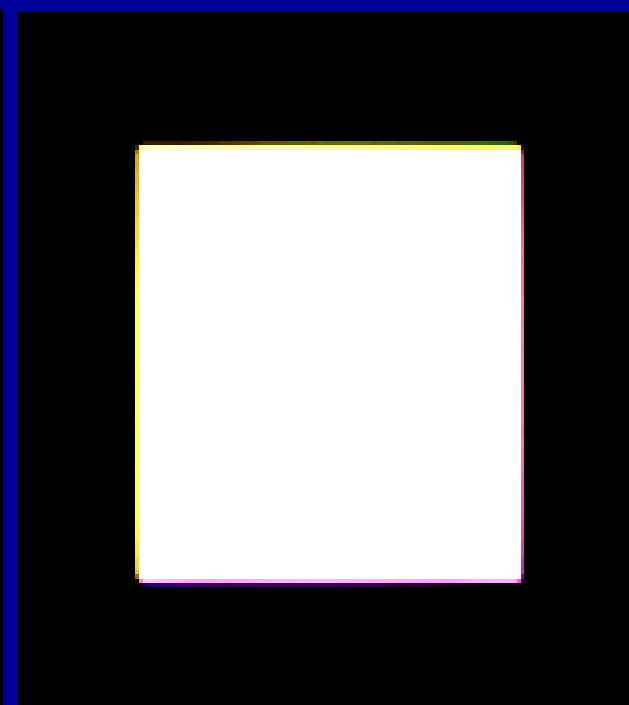
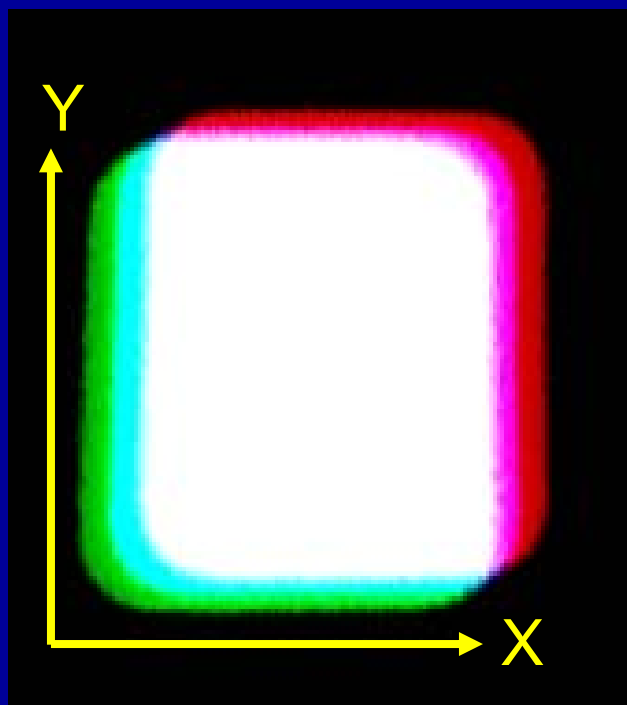
Y: 90 SLR (2.5 kHz)

Spectral/Spatial PRESS X:

180 Spec/Spat (5 kHz)

Y: 90 SLR (2.5 kHz)

Overprescribed
PRESS Box with VSS



Courtesy: John Kurhanewicz, Ph.D. UCSF

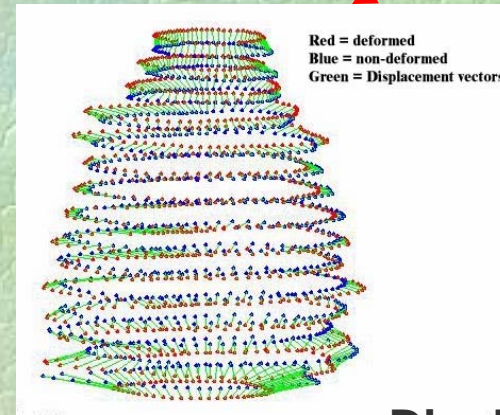
Prostate Deformation Correction



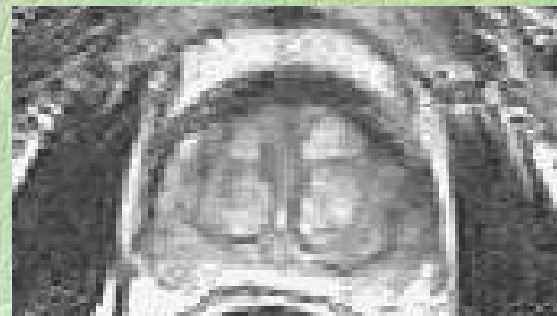
Reference Image



Deformed Image



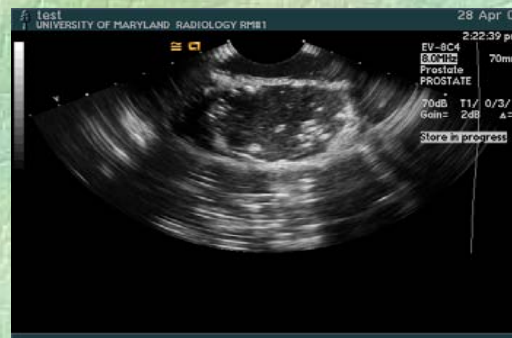
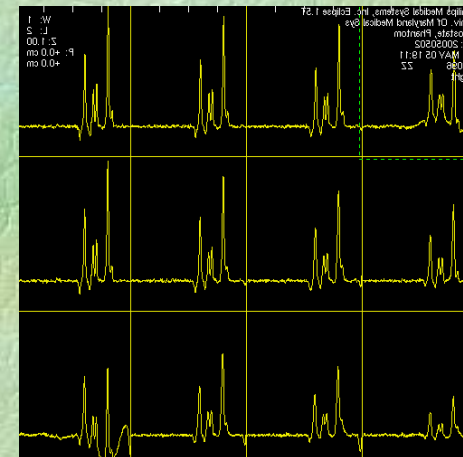
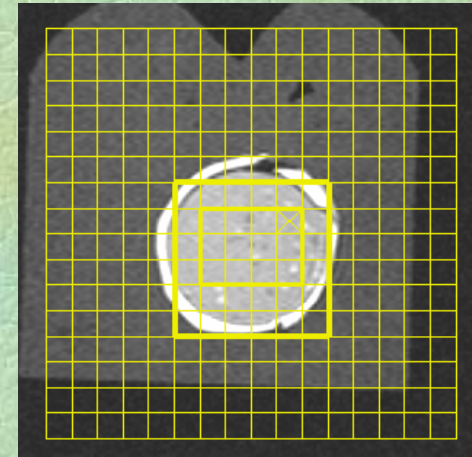
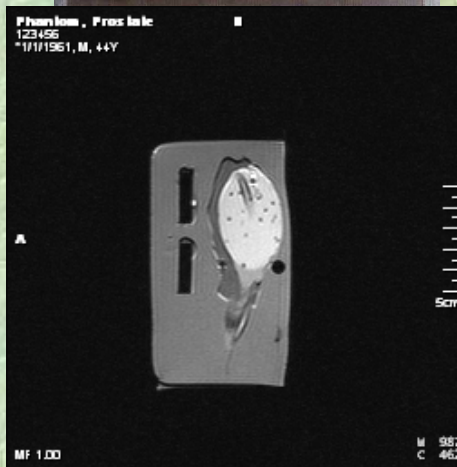
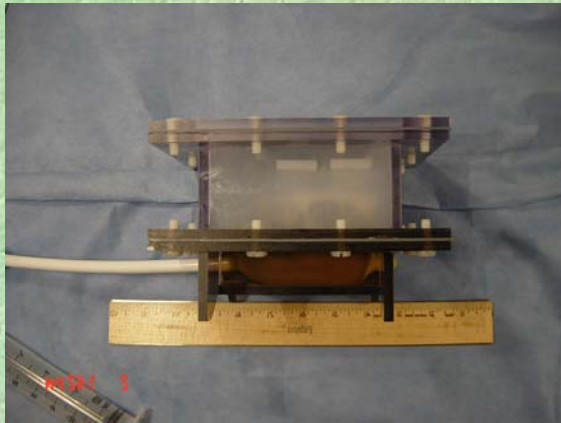
Displacement Vector Field



Corrected Image

Elastic Registration

Multipurpose Prostate Phantom



Spectral Interpretation: Distribution of Glandular Prostate Tissue and its Impact on Metabolism

Glandular tissue -most of the MRS signal

- **Peripheral zone**
- **Central zone**
- **Transition zone**

Vol %

70

25

5

PCa %

68

8

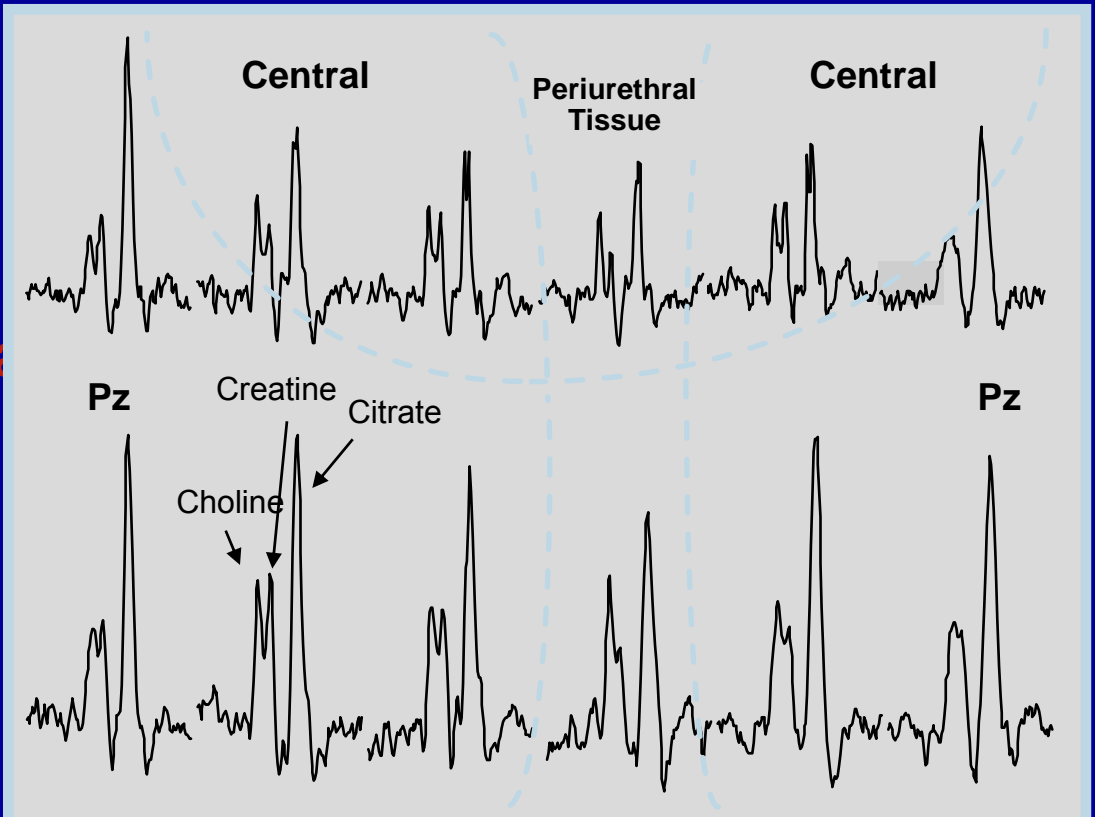
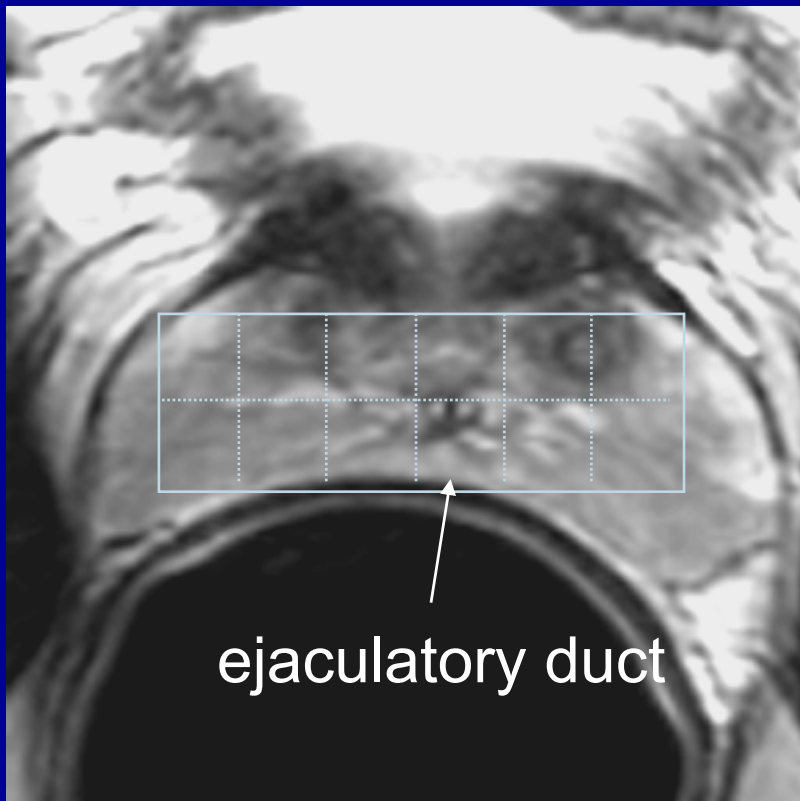
24

Non-glandular tissue - low MRS signal and no citrate.

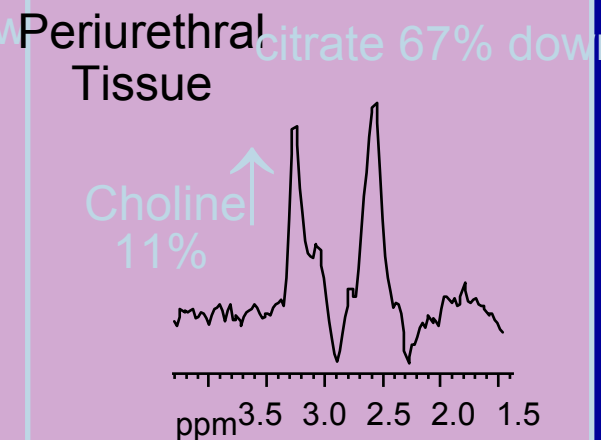
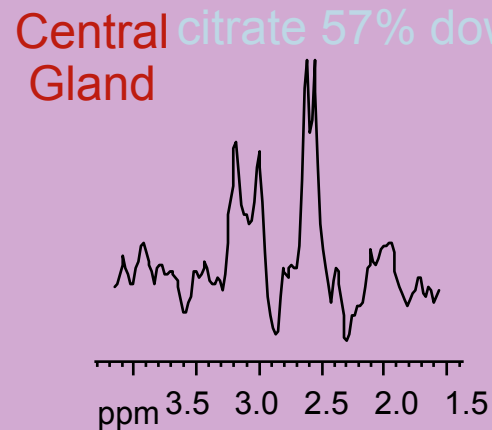
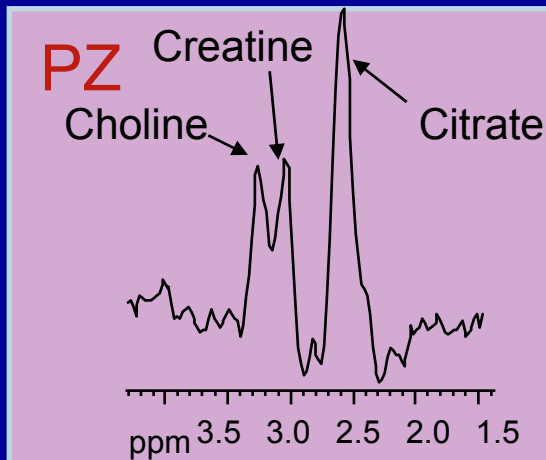
- **Urethra**
- **Anterior fibromuscular band**
- **Prostatic capsule**

Courtesy: John Kurhanewicz, Ph.D. UCSF

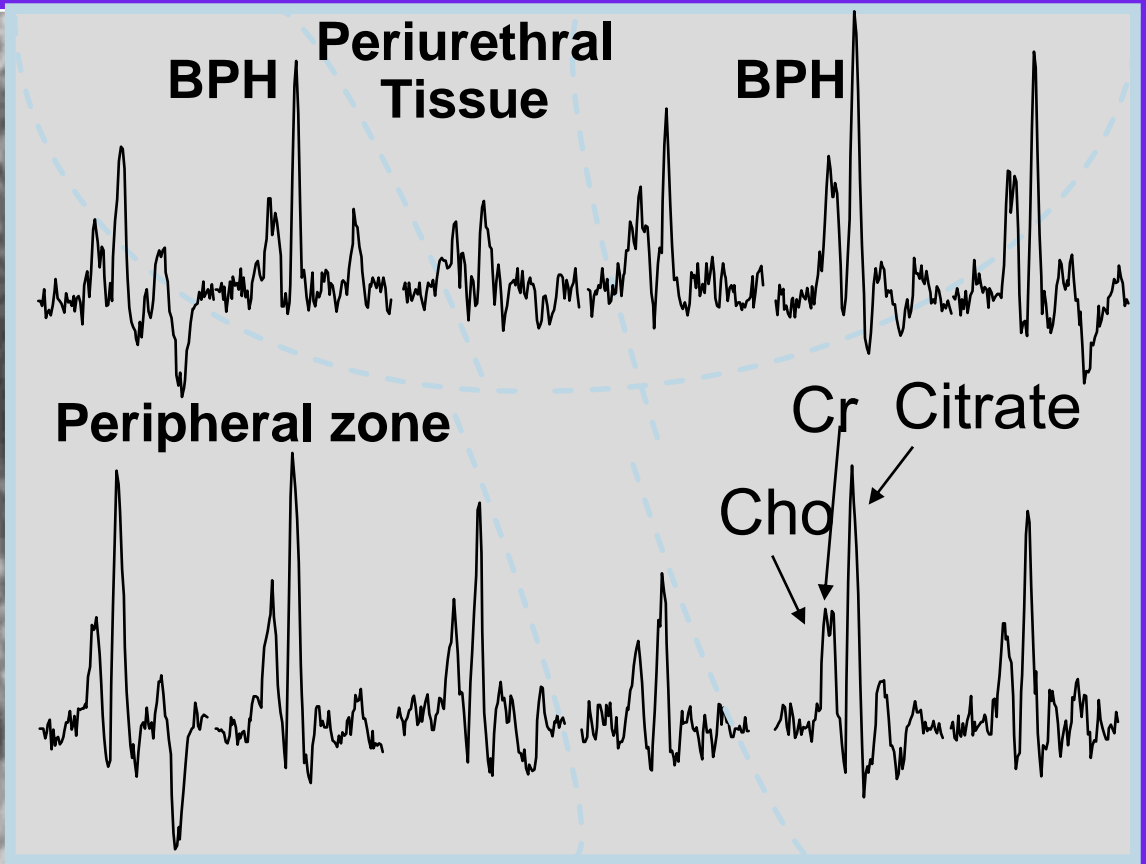
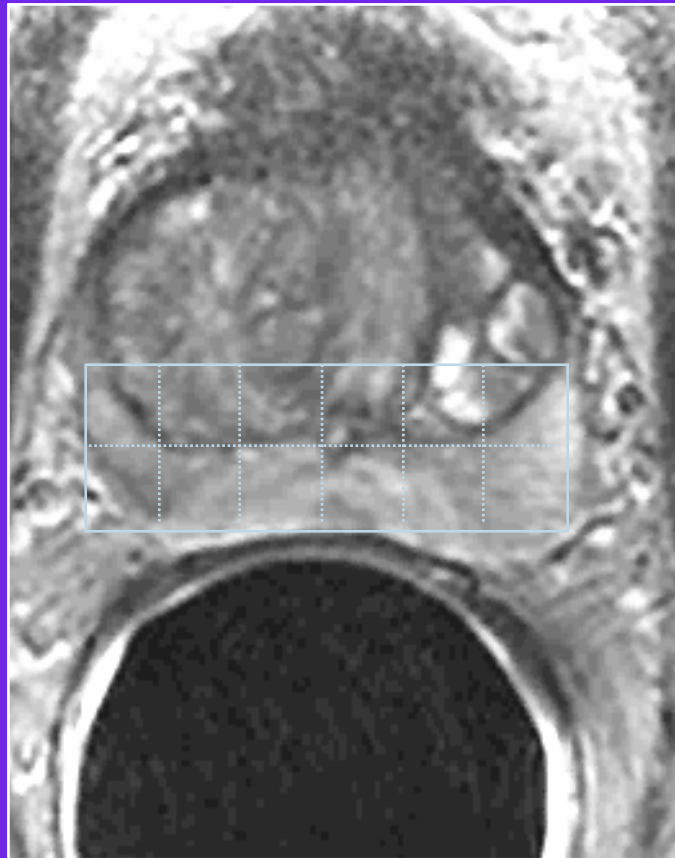
Spectral Interpretation: Healthy Young (age<40 years) Volunteer



Three Distinctive Metabolic Patterns

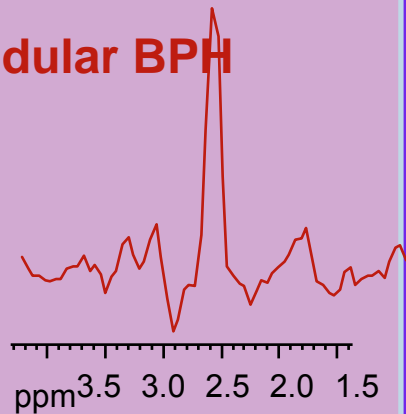


Spectral Interpretation: Development of BPH (age >40 years)

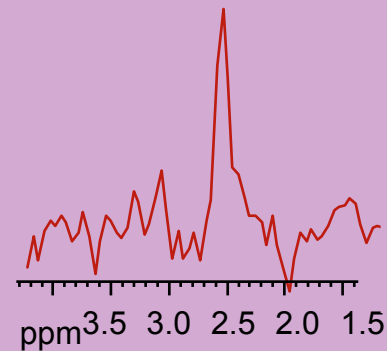


Variants of BPH

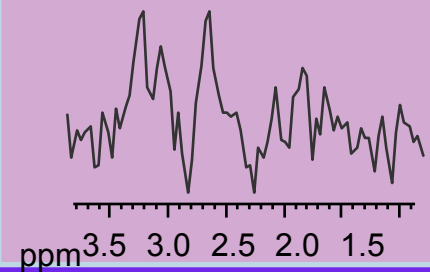
Glandular BPH



Mixed citrate 28% down



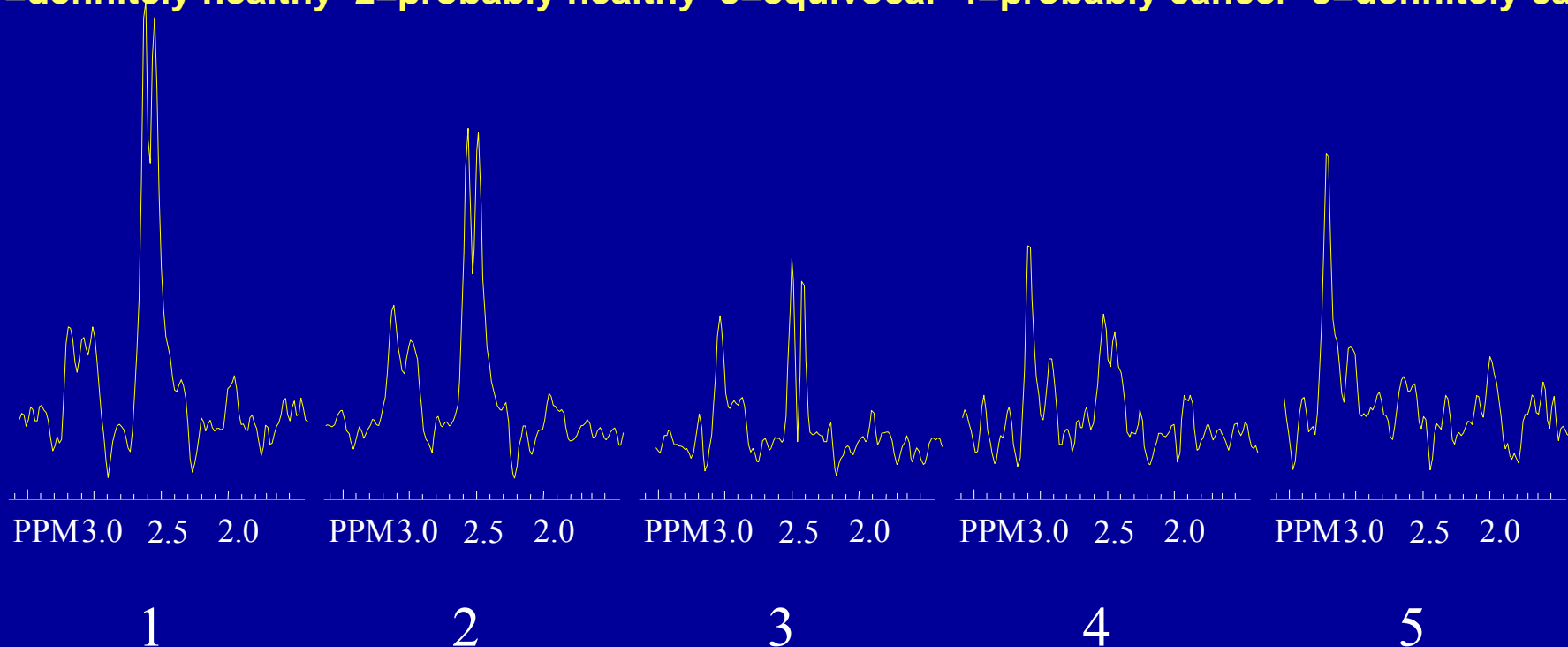
Stromal citrate 70% down



Systematic Scoring System for Peripheral Zone Abnormalities

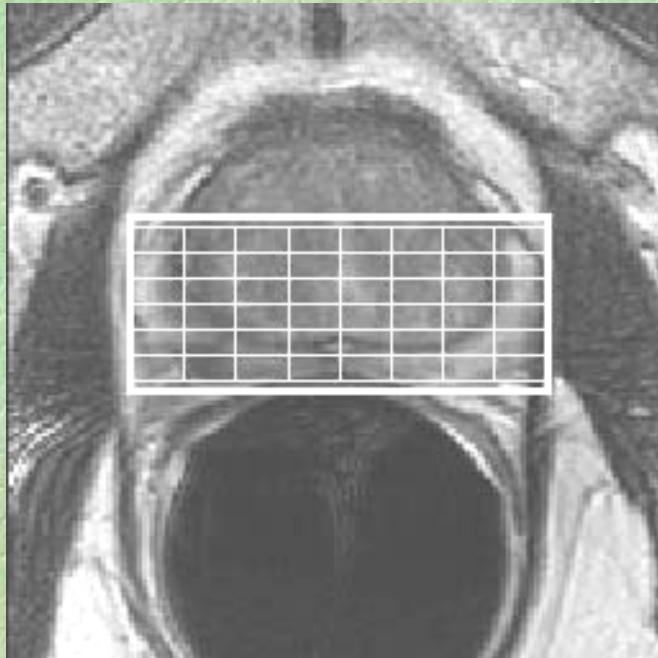
Step-section histopathological tumor maps were used to identify MRSI voxels of unequivocally benign (n = 306) or malignant (n = 81) peripheral zone tissue in 22 patients with MRI/MRSI studies prior to radical prostatectomy..

1=definitely healthy 2=probably healthy 3=equivocal 4=probably cancer 5=definitely cancer



- The score is based on primarily on the choline+creatine/citrate ratio
- Secondarily on choline/creatine ratio, levels of citrate, polyamines & spectral S/N

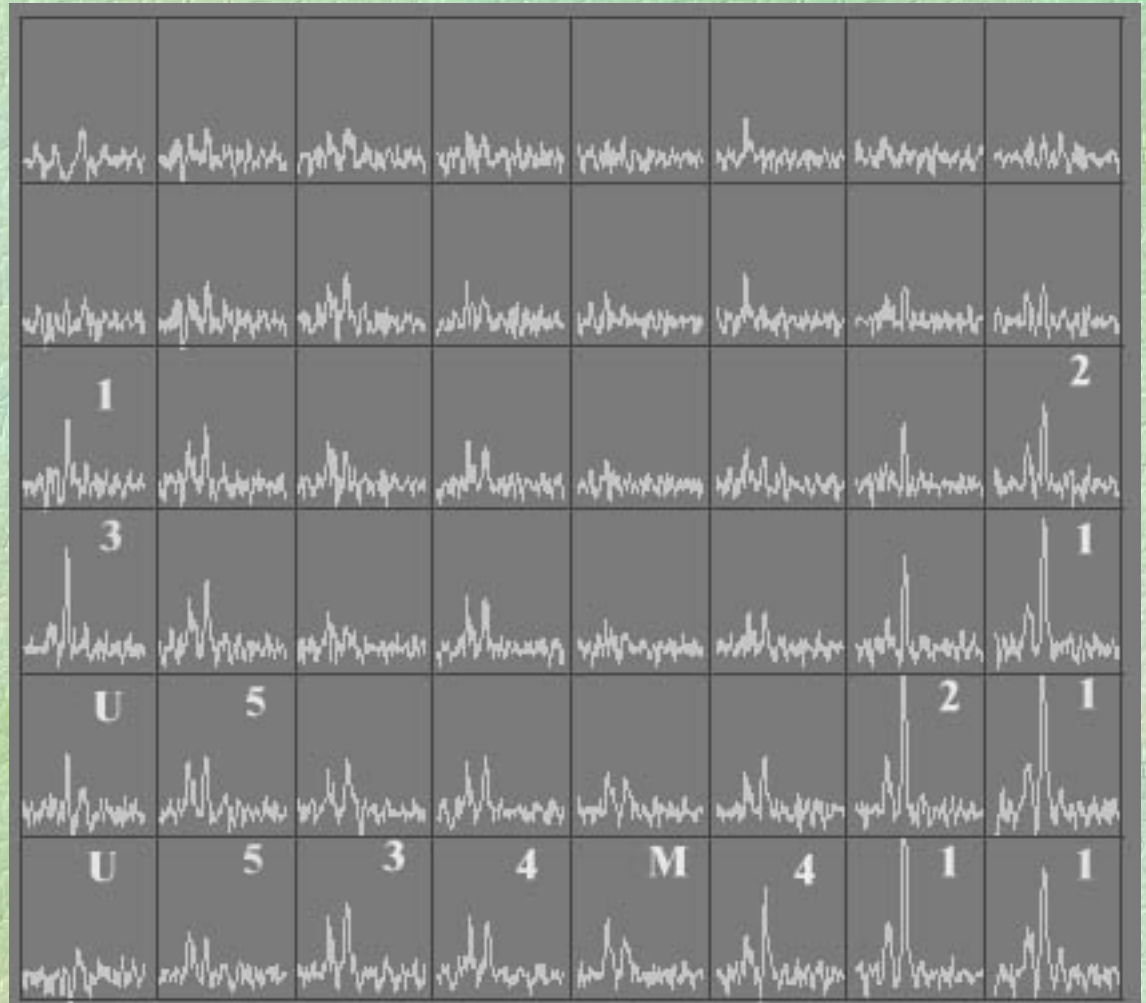
Courtesy: John Kurhanewicz, Ph.D. UCSF



5Point rating scale

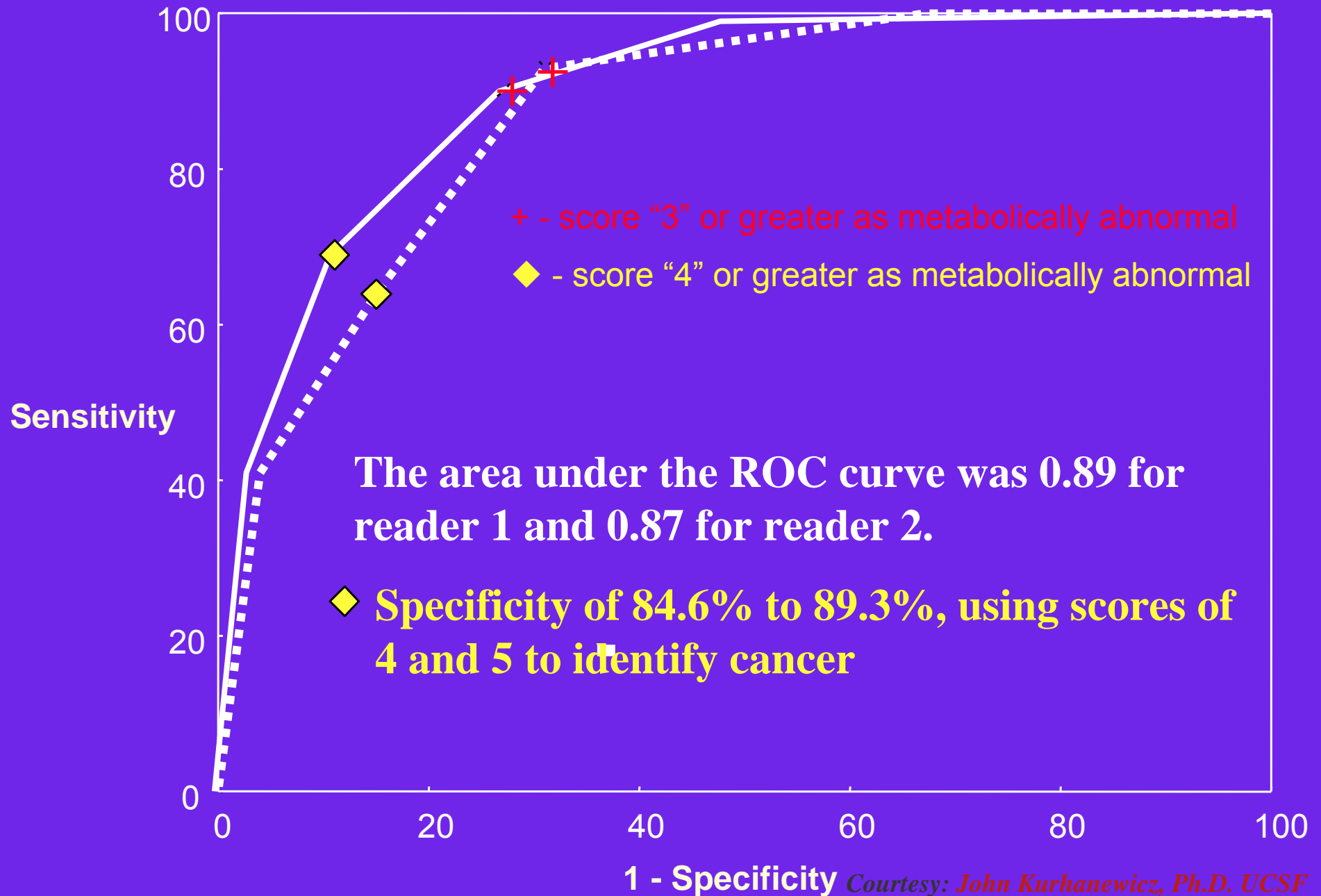
1=definitely healthy;
 2=probably healthy;
 3=equivocal;
 4=probably cancer;
 5=definitely cancer.

U=Unusable M=Mixed Tissue



The score is based on the
 choline+creatine/citrate ratio,
 choline/creatine ratio, levels of citrate
 and polyamines and the presence of
 low T2 signal intensity on MRI.

Systematic Scoring System for Metabolic Abnormalities



Multiparametric Prostate Imaging Exam

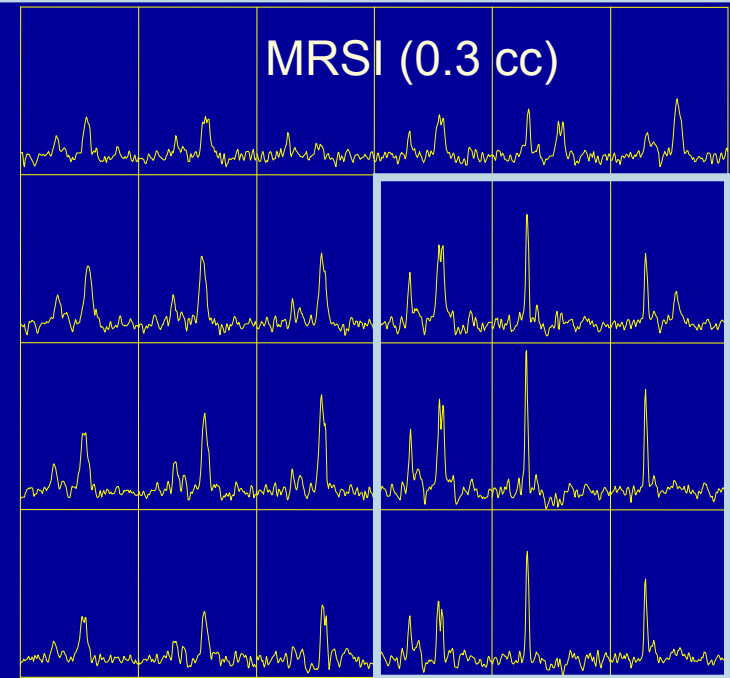
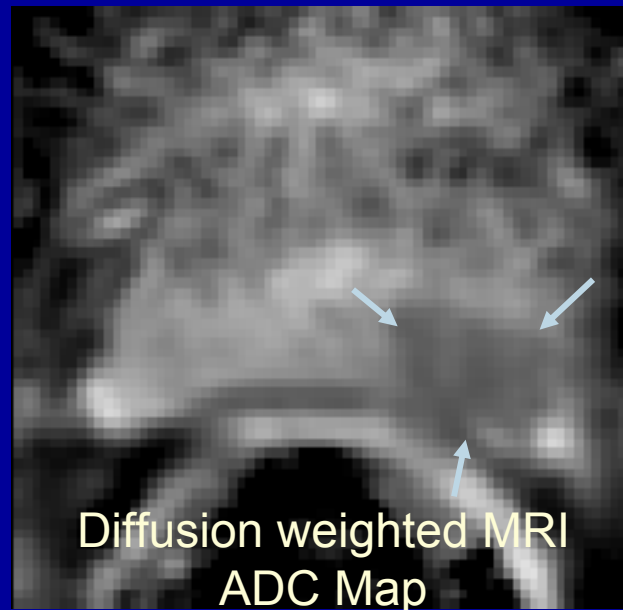
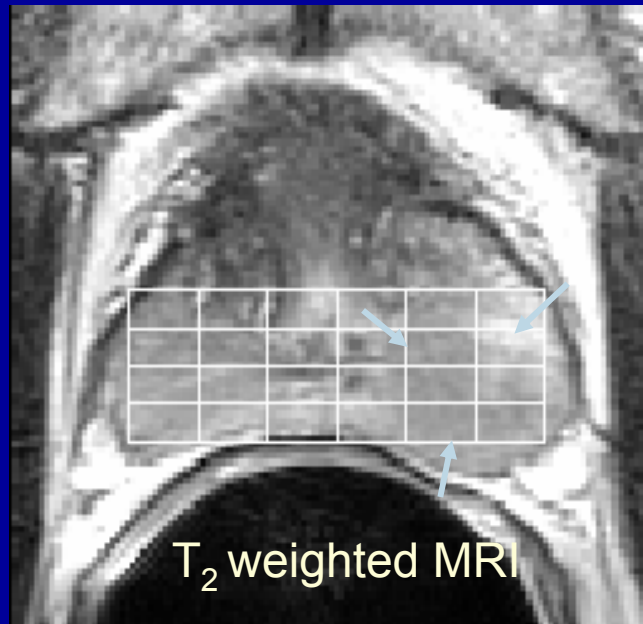
Decreased
Signal Intensity
on T2 weighted
Imaging

Reduced
water
diffusion

Elevated
choline

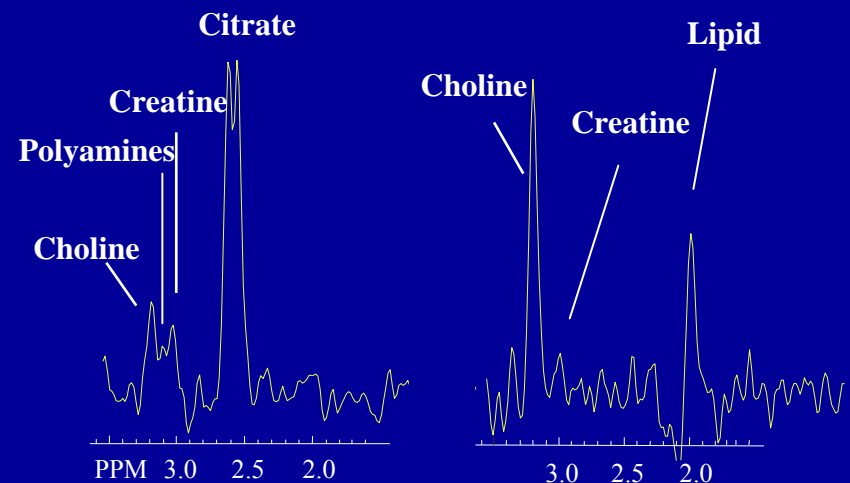
Reduced
citrate

Reduced
polyamines



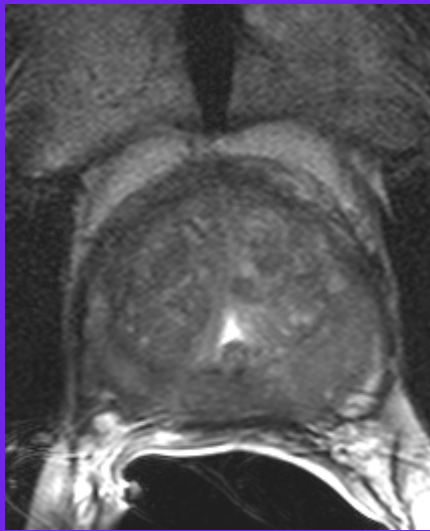
Healthy

Cancer

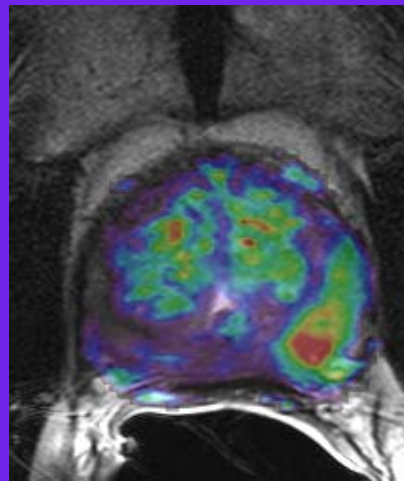


Multiparametric Prostate Imaging Exam – Dynamic Contrast Enhanced Imaging

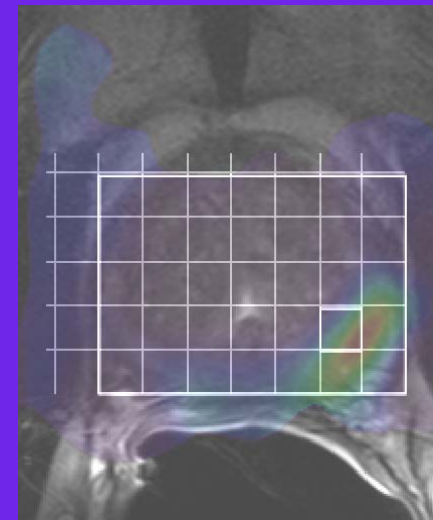
56 yo male PSA 4.8 Gleason 6 (3x)



T2w

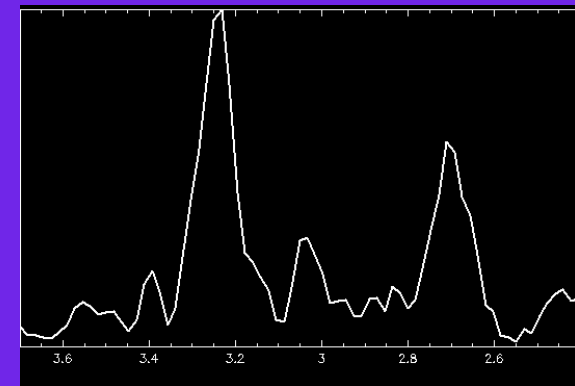


ktrans



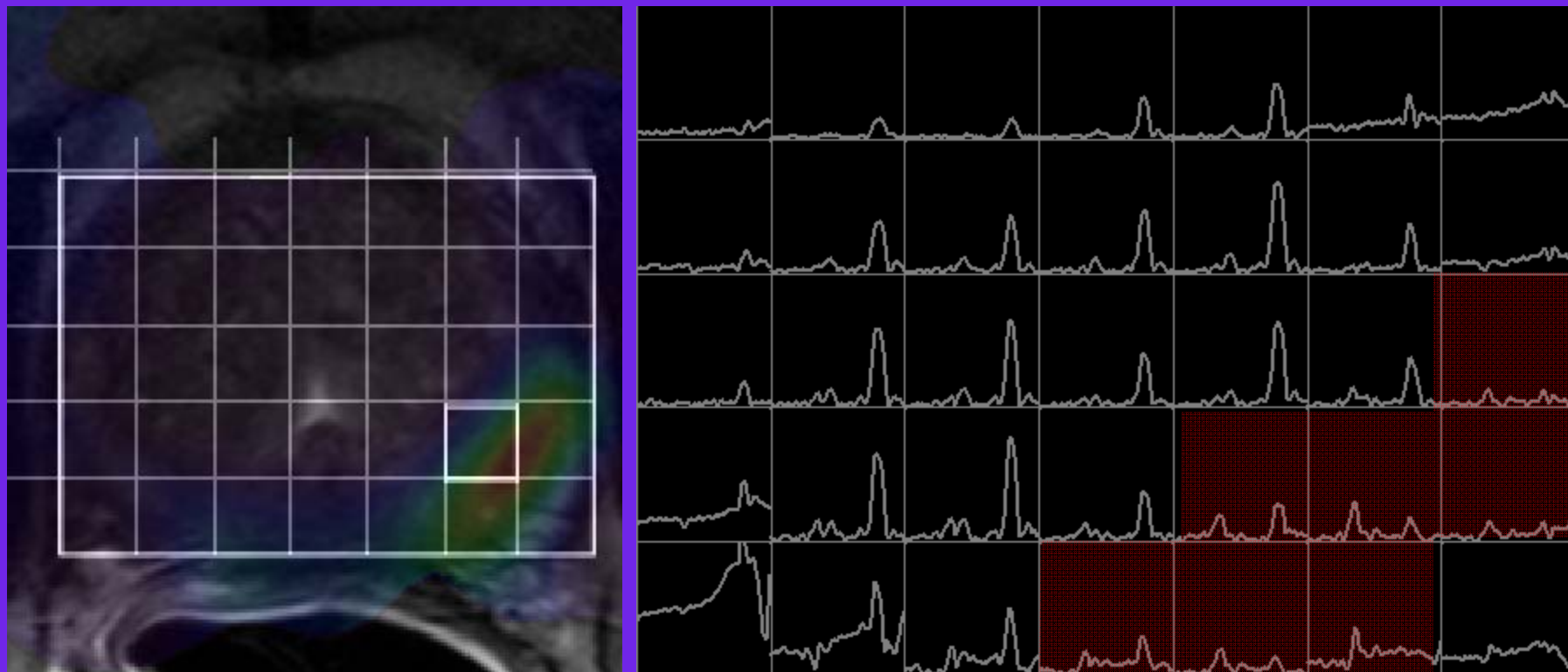
Cho/Cit

T2w: slice 10
DCE: Slice 4
3DSI: Slice 6 (0.5 z-shift)



Courtesy: Dr. Choyke, NCI

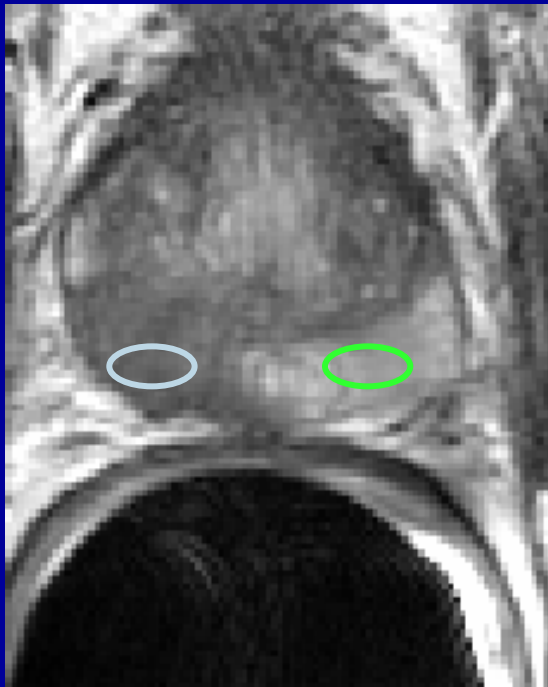
Multiparametric Prostate Imaging Exam – Dynamic Contrast Enhanced Imaging



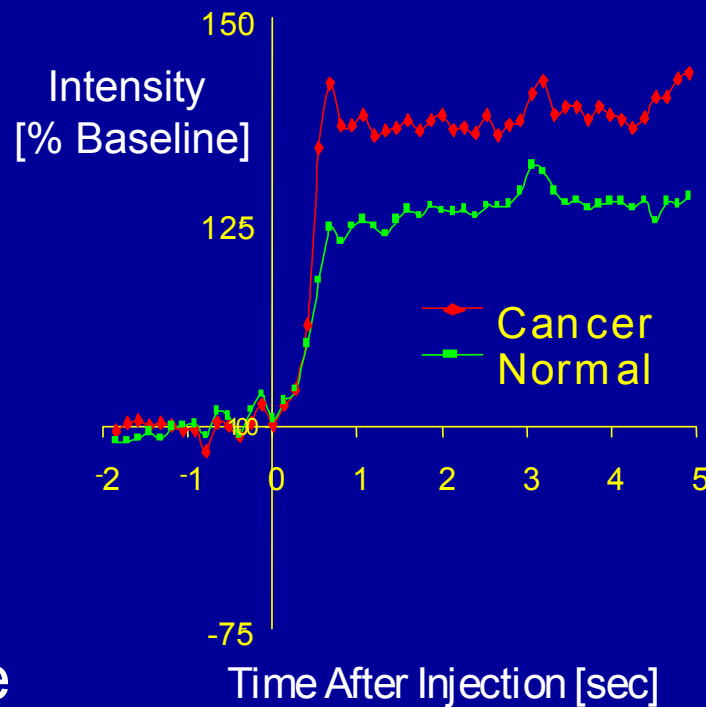
Courtesy: Dr. Choyke, NCI

Dynamic Contrast Imaging: Angiogenesis

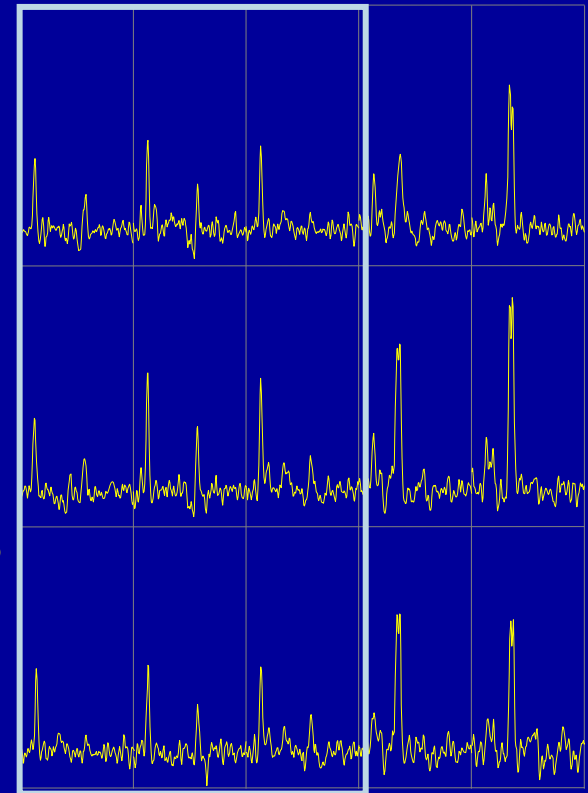
- Dynamic Contrast Imaging - Poorly differentiated tumors show earliest and greatest enhancement.



T2 weighted image
PSA - 4.2 ng/ml



Gd Contrast Uptake Curves



Spectroscopy

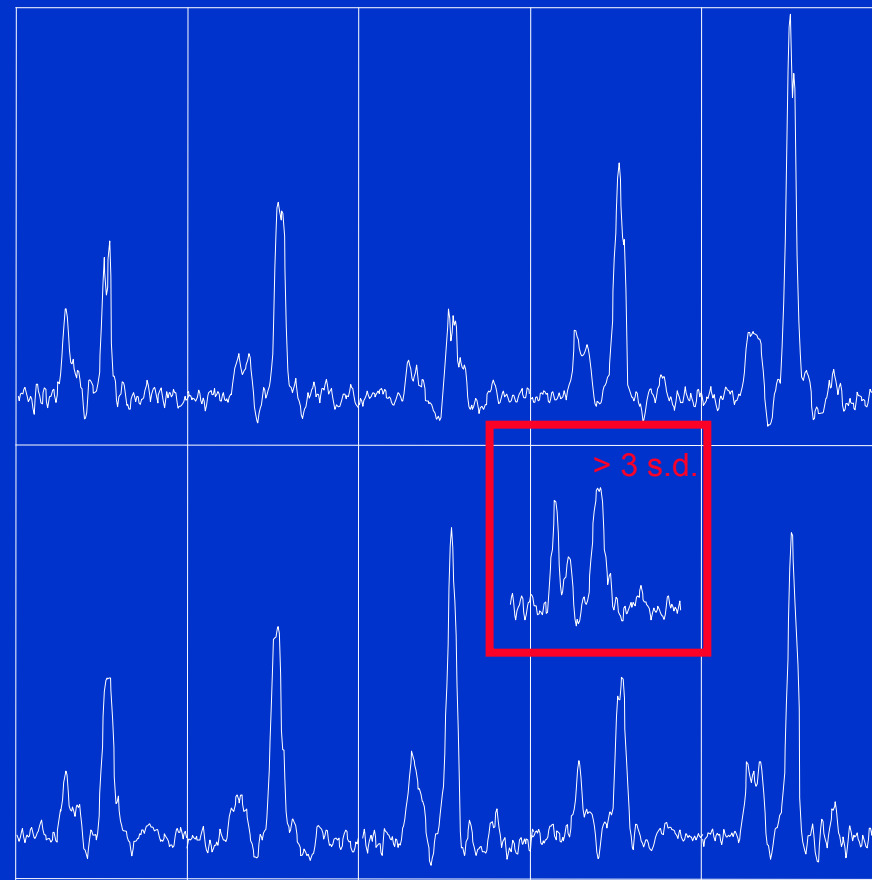
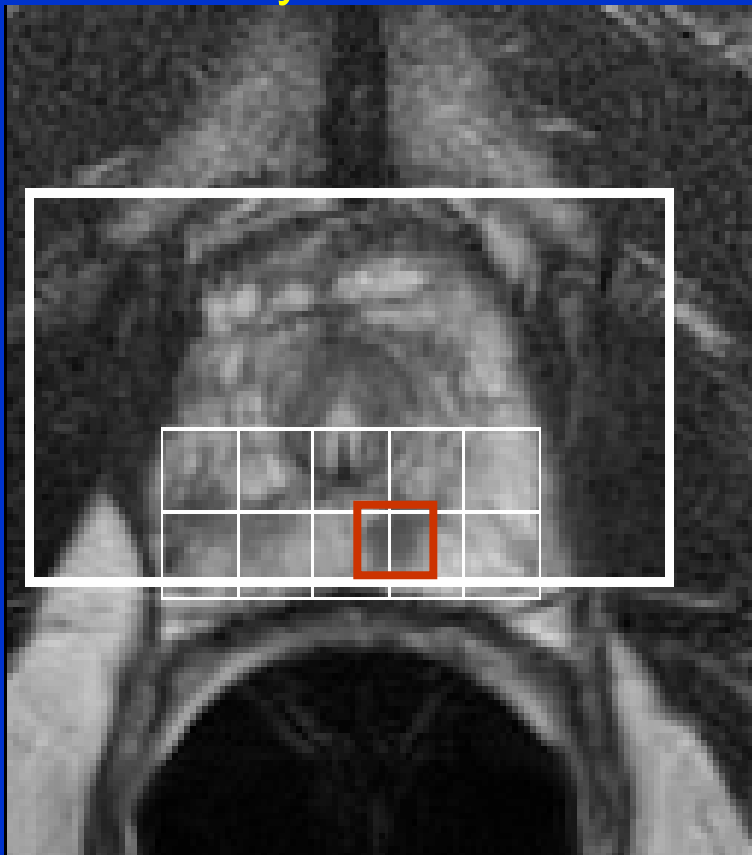
Barentsz JO. J Magn Reson Imaging 1999; 10:295-304. Brown. Clin Radiol 1995; 50:601-606. Heerschap A, Anticancer Res 1997; 17:1455-1460. Liney GP, NMR Biomed 1999; 12:39-44. Padhani. Clin Radiol 2000; 55:99-109.

Techniques for Localizing PCa

- **T2W MRI**
 - 95% sensitive but only 40% specific
- **DCE-MRI**
 - Increased specificity (80-85%)
- **MRSI**
 - Increased specificity (80-85%)
 - Tumor aggressiveness
- **Multi-parametric Imaging using MRSI/DTI/DCE-MRI may further increase specificity**

Confounding Factors: Partial Volume Effects

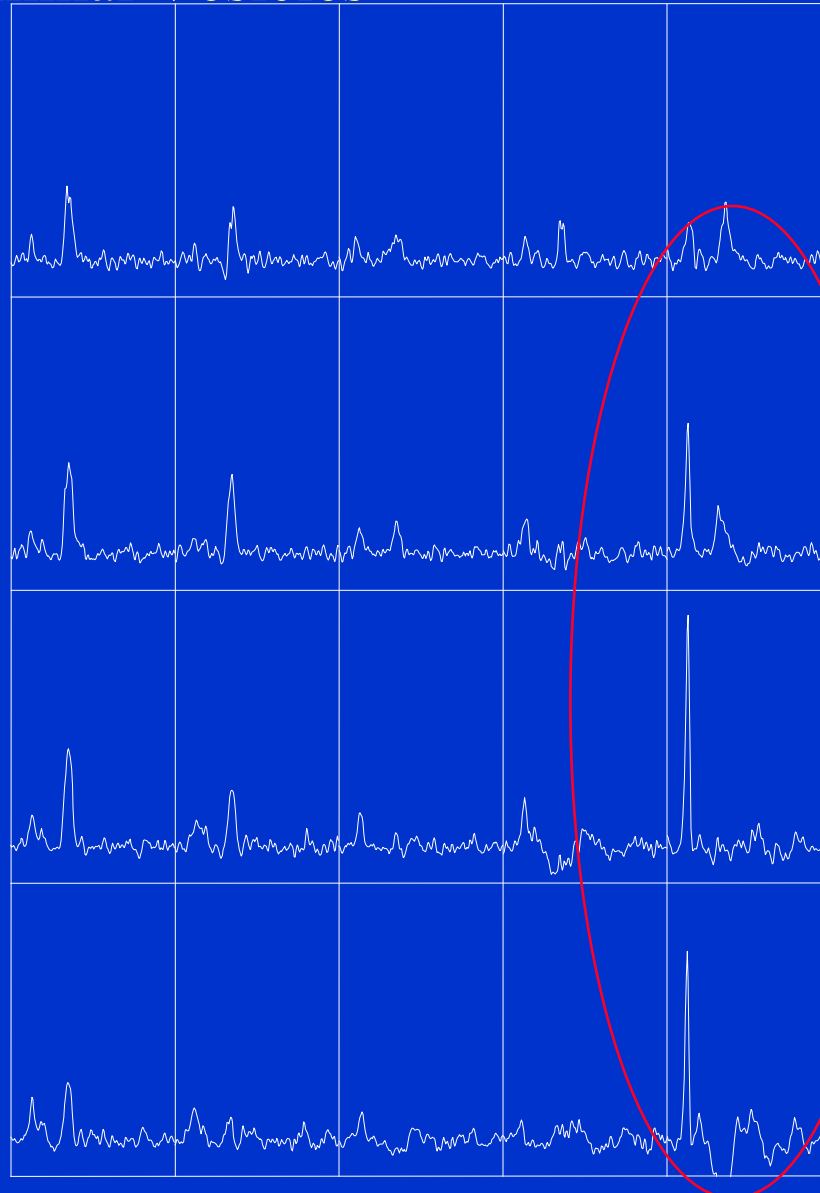
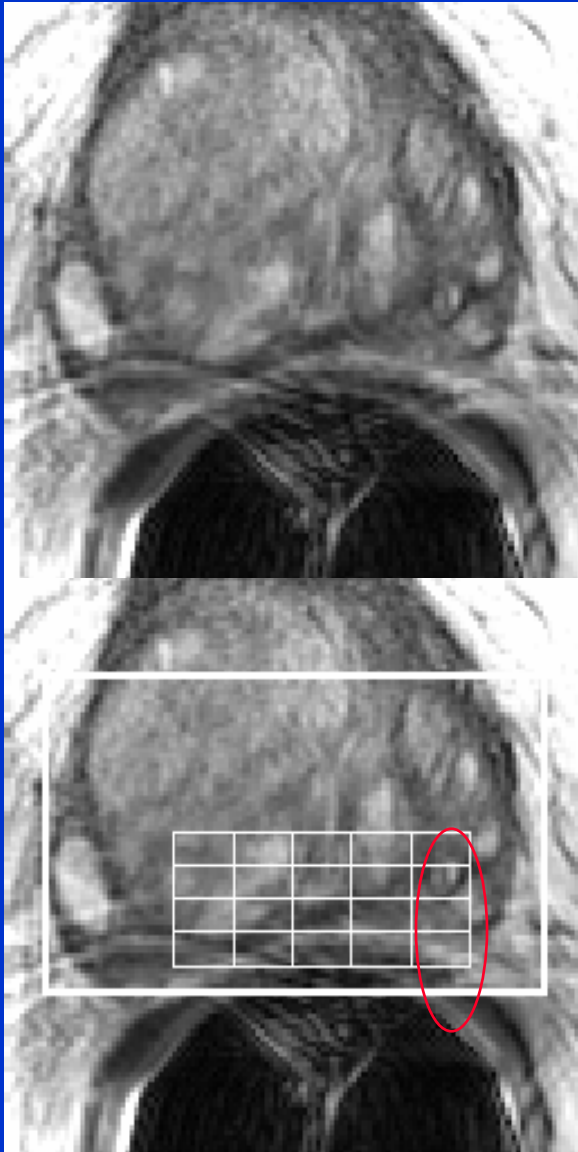
Many small, low grade tumors can be missed due to spectral signal averaging with surrounding healthy tissues. This problem can be reduced by acquiring higher spatial resolution spectral data and by shifting spectroscopic voxels in post-processing to optimally encompass the region of abnormality on MRI.



Courtesy: John Kurhanewicz, Ph.D. UCSF

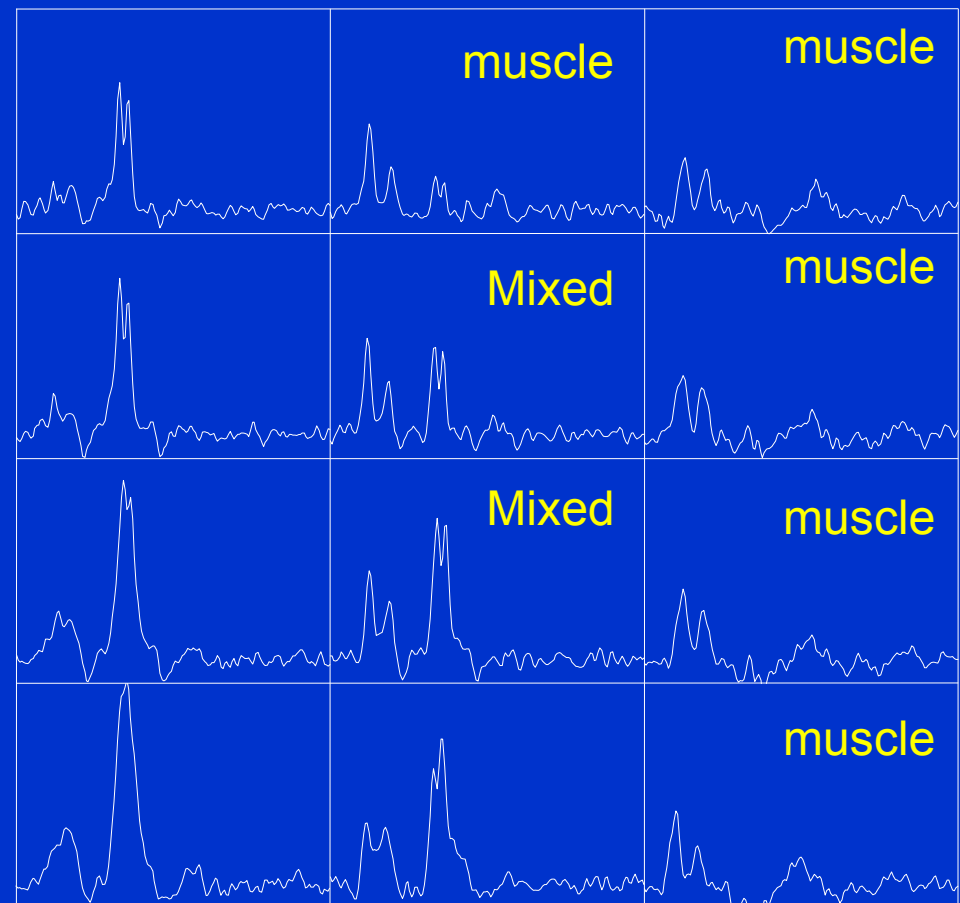
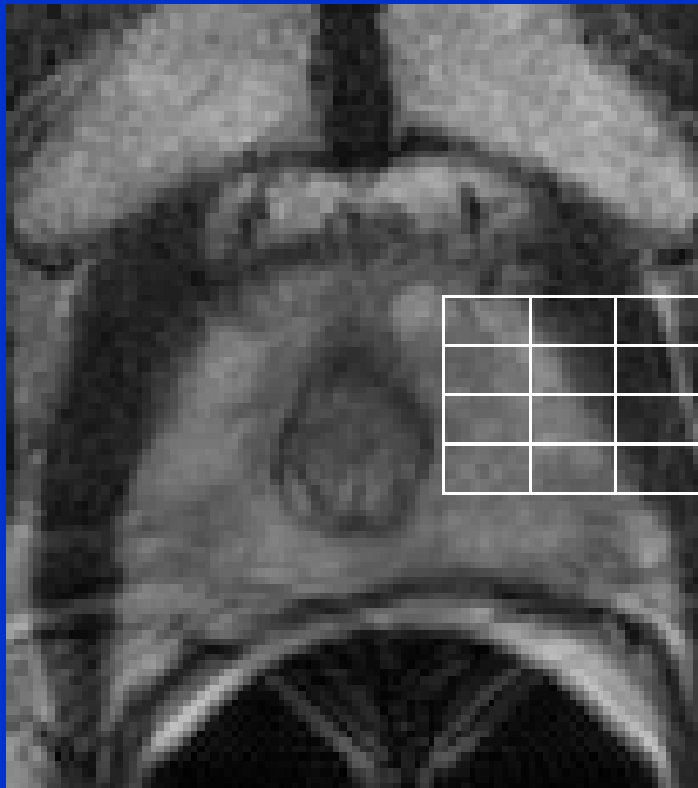
Confounding Factors: Interpretation of Spectra

Contamination from GPC in Seminal Vesicles

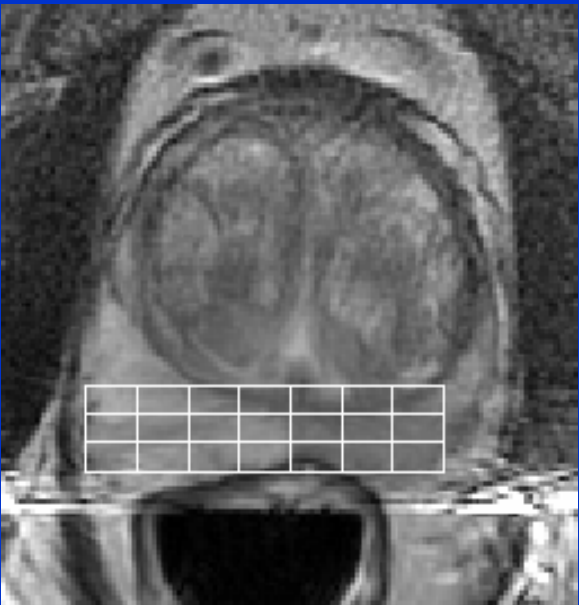
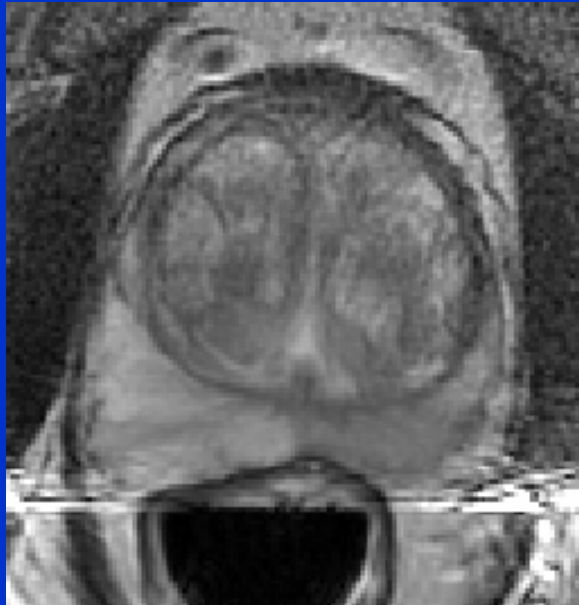


Confounding Factors: Interpretation of Spectra

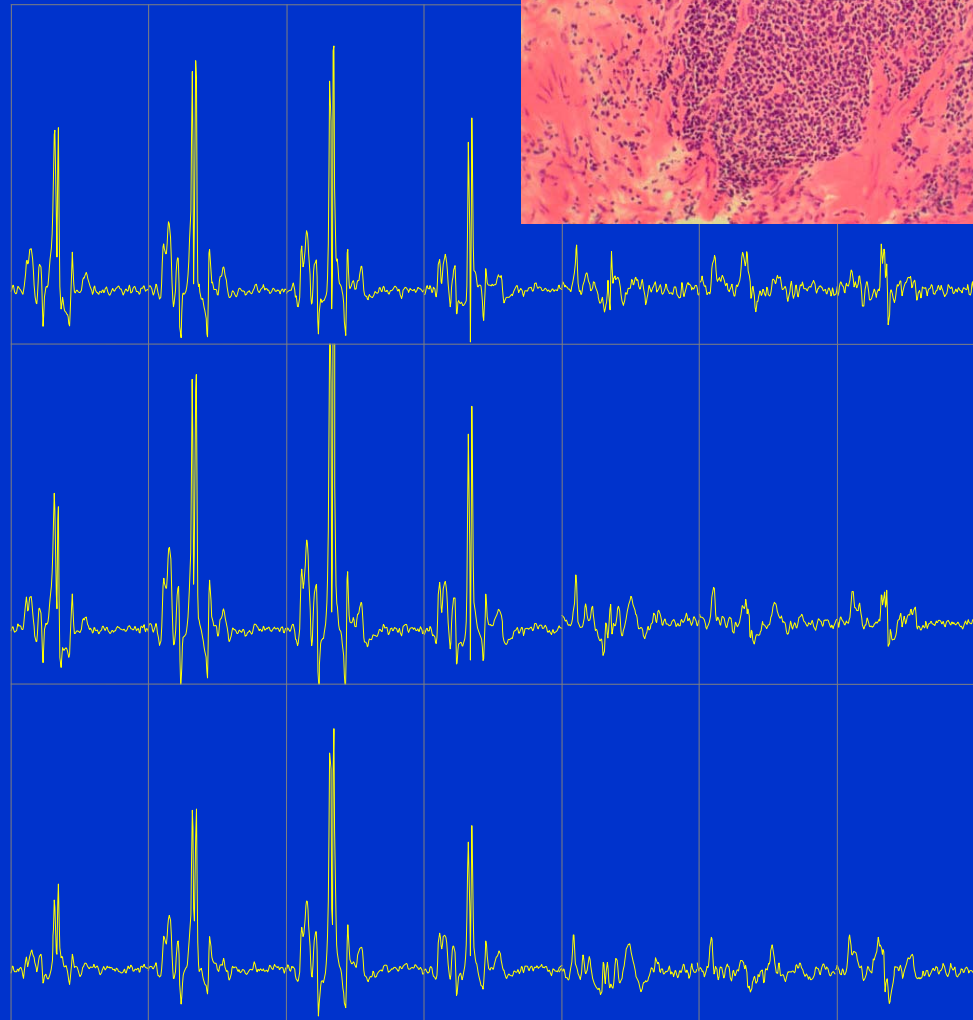
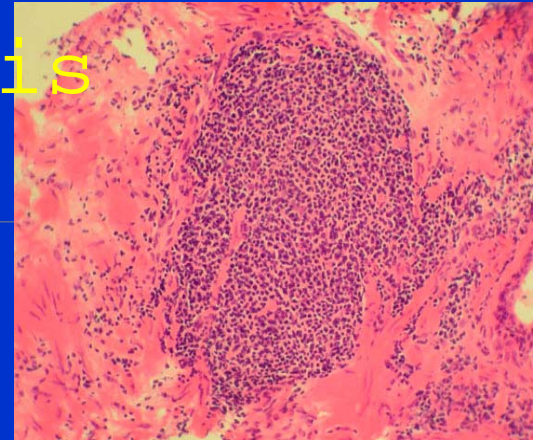
Contamination from surrounding muscle also needs to be considered when interpreting prostate spectra.



Confounding Factors: False Positives



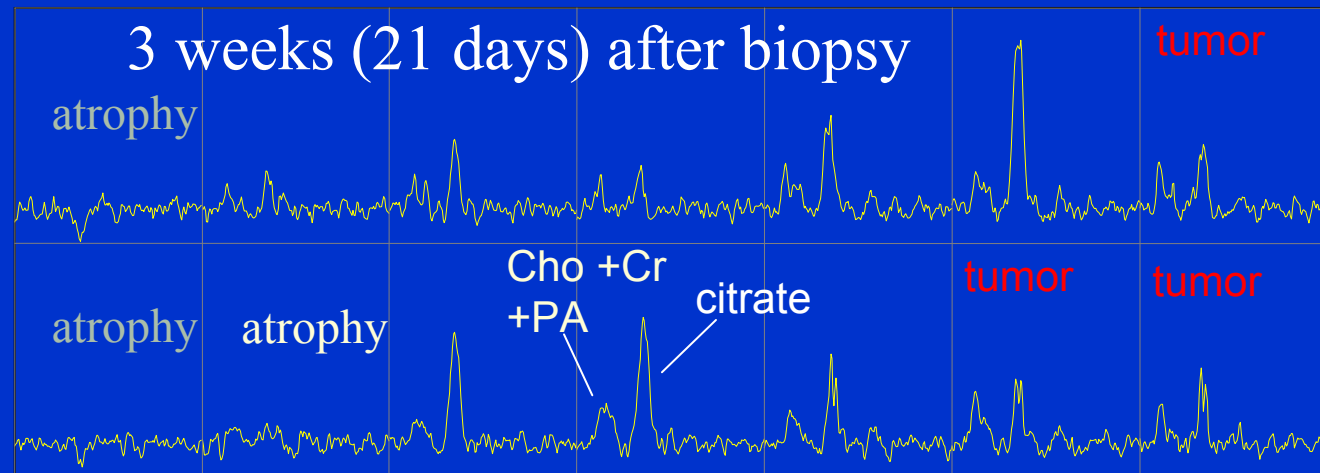
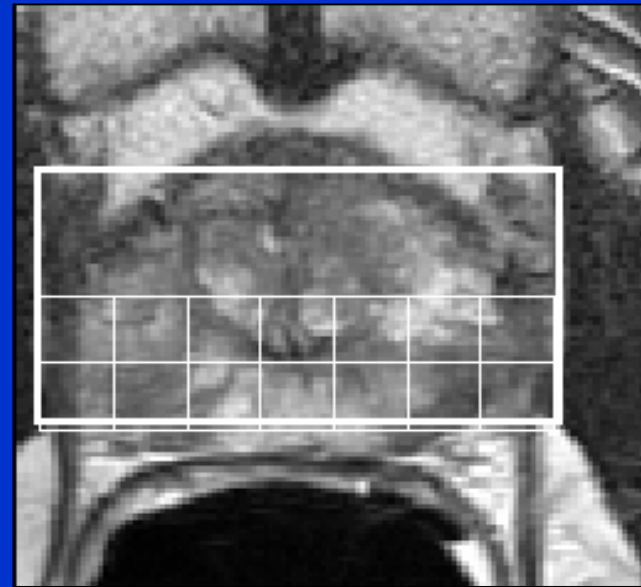
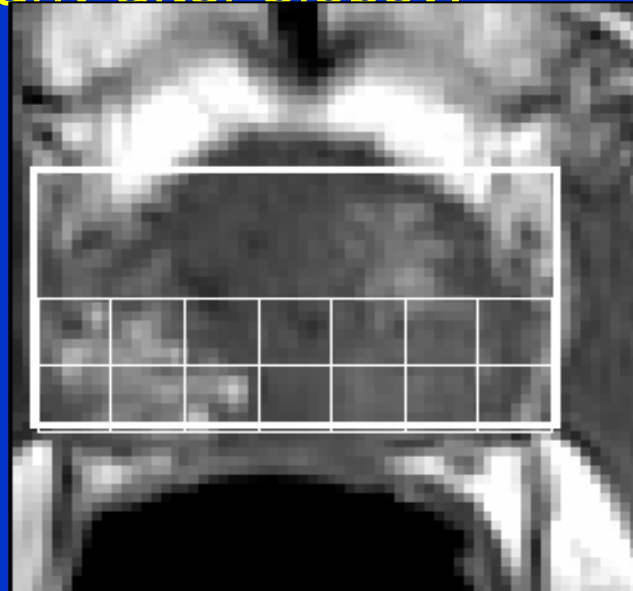
Prostatitis



Appearance of Spectra In Regions of Hemorrhage

Patients have demonstrated both metabolic atrophy and changes in their metabolite levels in regions of extensive hemorrhage, particularly early after biopsy.

18.5 % of spectral voxels were degraded within 8 weeks of biopsy as compared to 7% after 8 weeks.




AJR 2004;
183:1079-1083

Multi-Center Prostate MRSI Studies

- American College of Radiology Imaging Network - ACRIN 6659
- International Multi-Center Assessment of Prostate Spectroscopy - IMAPS

Aim of IMAPS (1.5T)



<http://get.to/imaps> 

[Home](#) | [Introduction](#) | [Participating sites](#) | [Acquisition protocol](#) | [Data submission](#) | [Links](#) |

IMAPS

**An International
Multi-Centre
Assessment of
Prostate MR
Spectroscopy**


[Introduction](#)
An introduction to the purpose of this trial




[Participating sites](#)
Listing of participating sites and partners

[Acquisition protocol](#)
Notes on the MR acquisition protocol

[Data submission](#)
How to submit data to IMAPS

[Links](#)
Links to partners and sites



Primary Objective

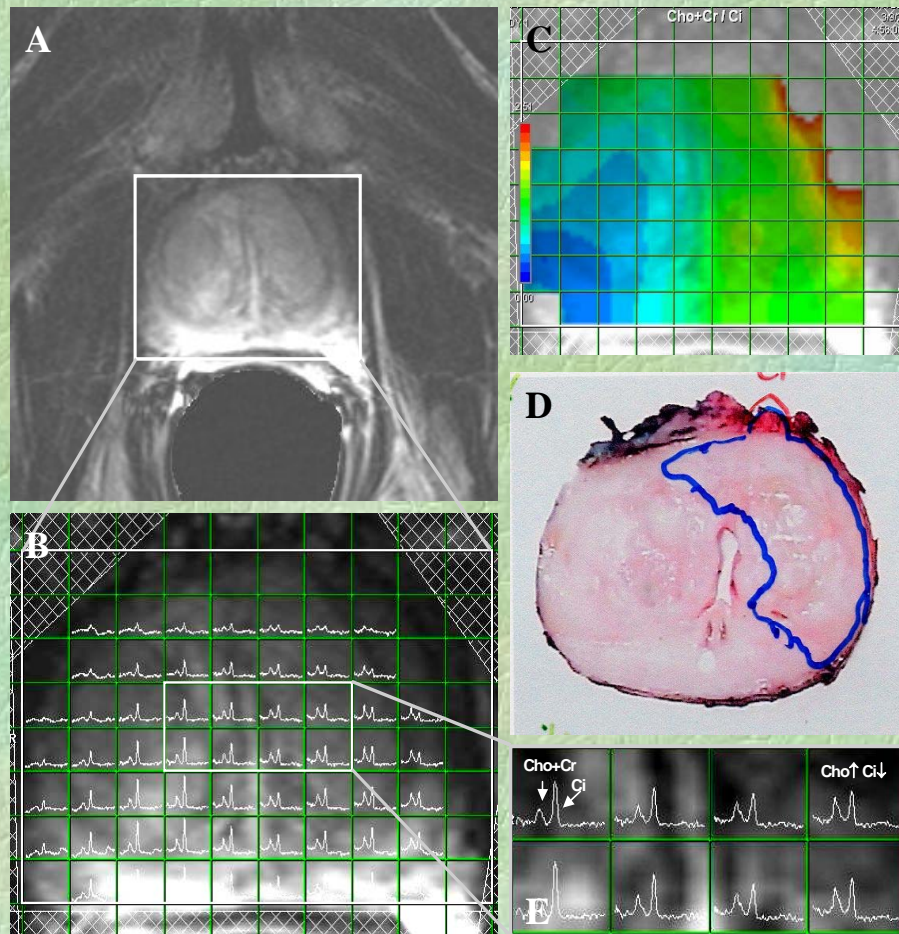
to prove in a multi center study that ^1H -MRSI can **detect AND localize** prostate carcinoma in the two major anatomical areas of the prostate.

*Courtesy of T. Scheenen and Prof. A. Heerschap, Radboud University Nijmegen Medical Center, Dept. of Radiology
The IMAPS community*

IMAPS (1.5T)



Data example

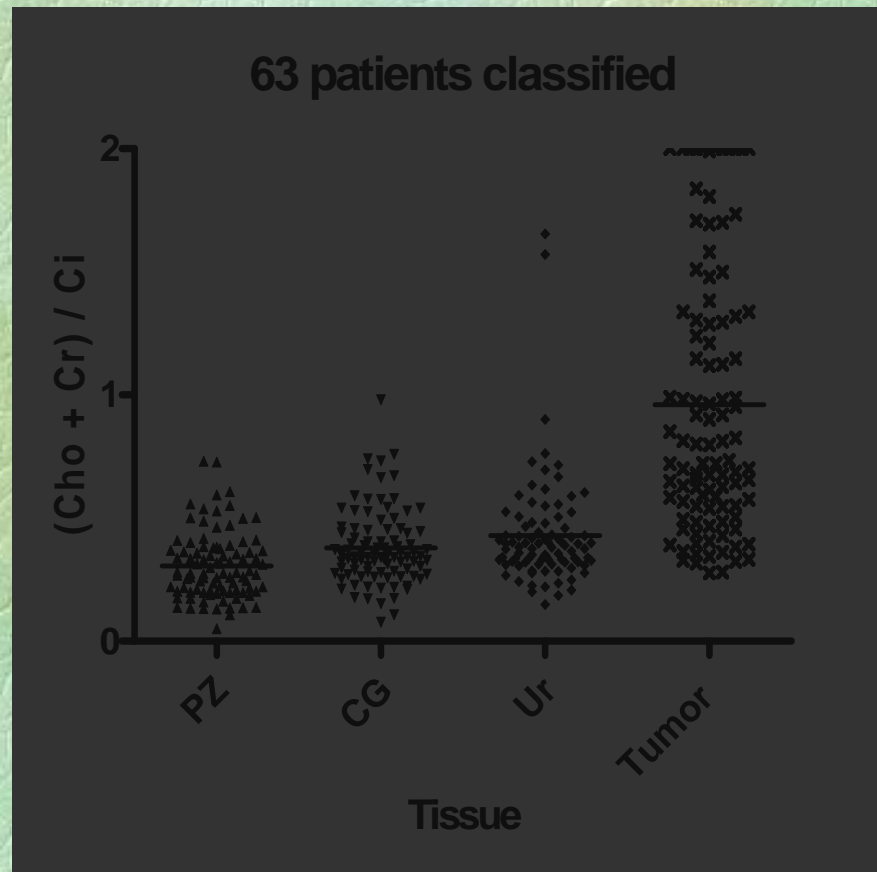


Prostate spectroscopy at 1.5T with endorectal coil

The axial T2-weighted image (A) is used for matching voxel locations to histopathological specimens (D). One of the spectral maps (B), partially expanded in (E), reflects the quality of the MRSI data throughout the slice. Deviations in the (Cho + Cr)/Ci metabolite ratio map in (C) largely correspond to the tumor location indicated with the blue line in (D).

Courtesy of T. Scheenen and Prof. A. Heerschap, Radboud University Nijmegen Medical Center, Dept. of Radiology
The IMAPS community

63 patients included (1.5T)



PZ peripheral zone
CG central gland
Ur (peri-)urethral area

Tumor is represented by the
highest CC/C ratio within 5 mm
of the classified voxel.

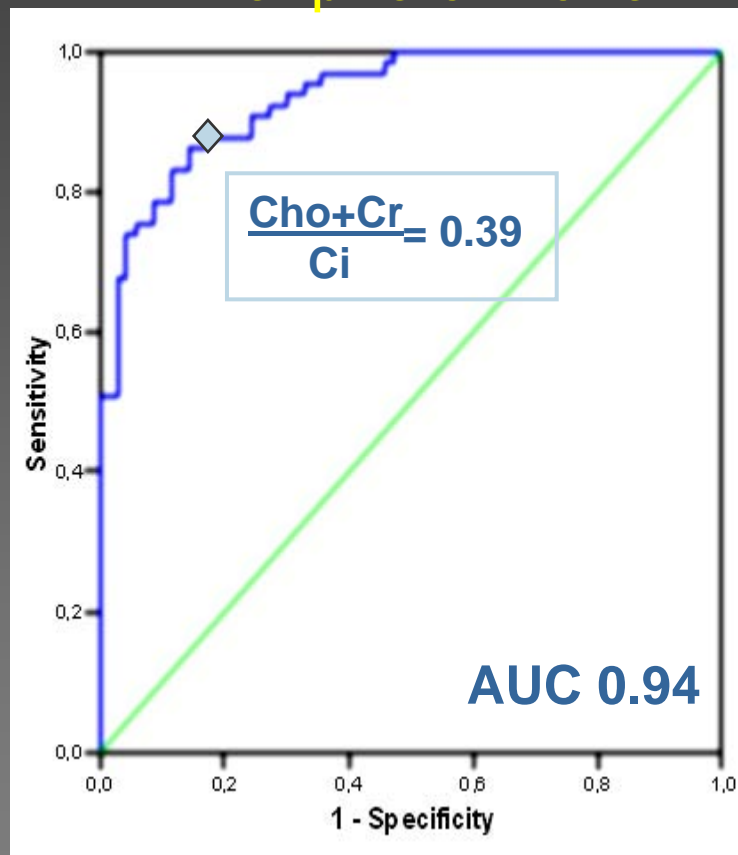
Mean	0.31	0.38	0.43	0.96
SD	0.14	0.15	0.23	0.54

*Courtesy of T. Scheenen and Prof. A. Heerschap, Radboud University Nijmegen Medical Center, Dept. of Radiology
The IMAPS community*

ROC-analysis 47 patients (1.5T)



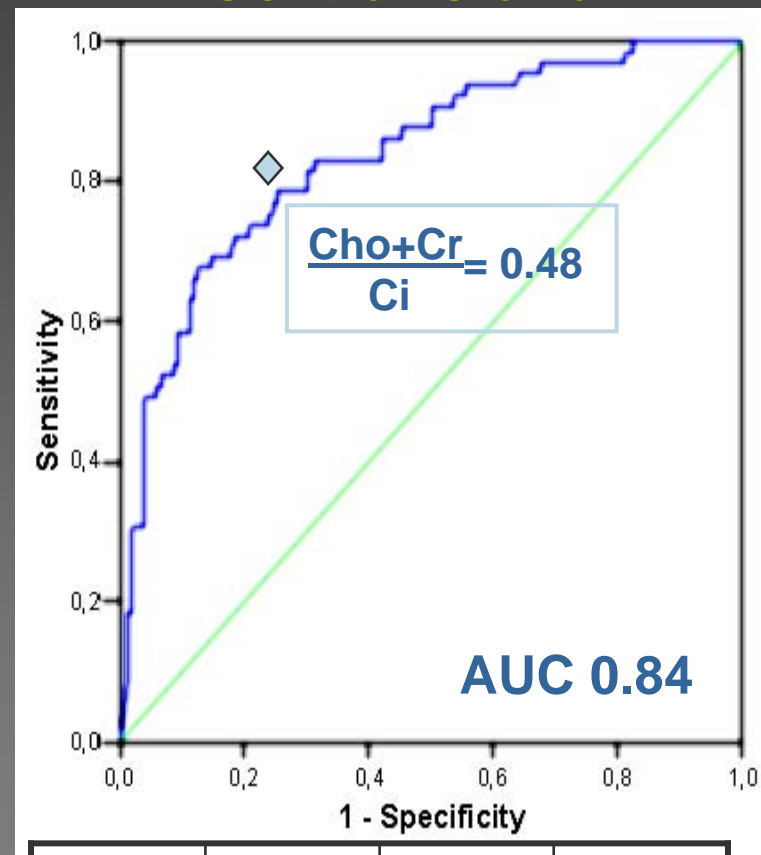
Peripheral Zone



Sens	86%	PPV	0.85
Spec	86%	NPV	0.87

Tumor is represented by the highest CC/C ratio within 5 mm of the classified voxel.

Central Gland

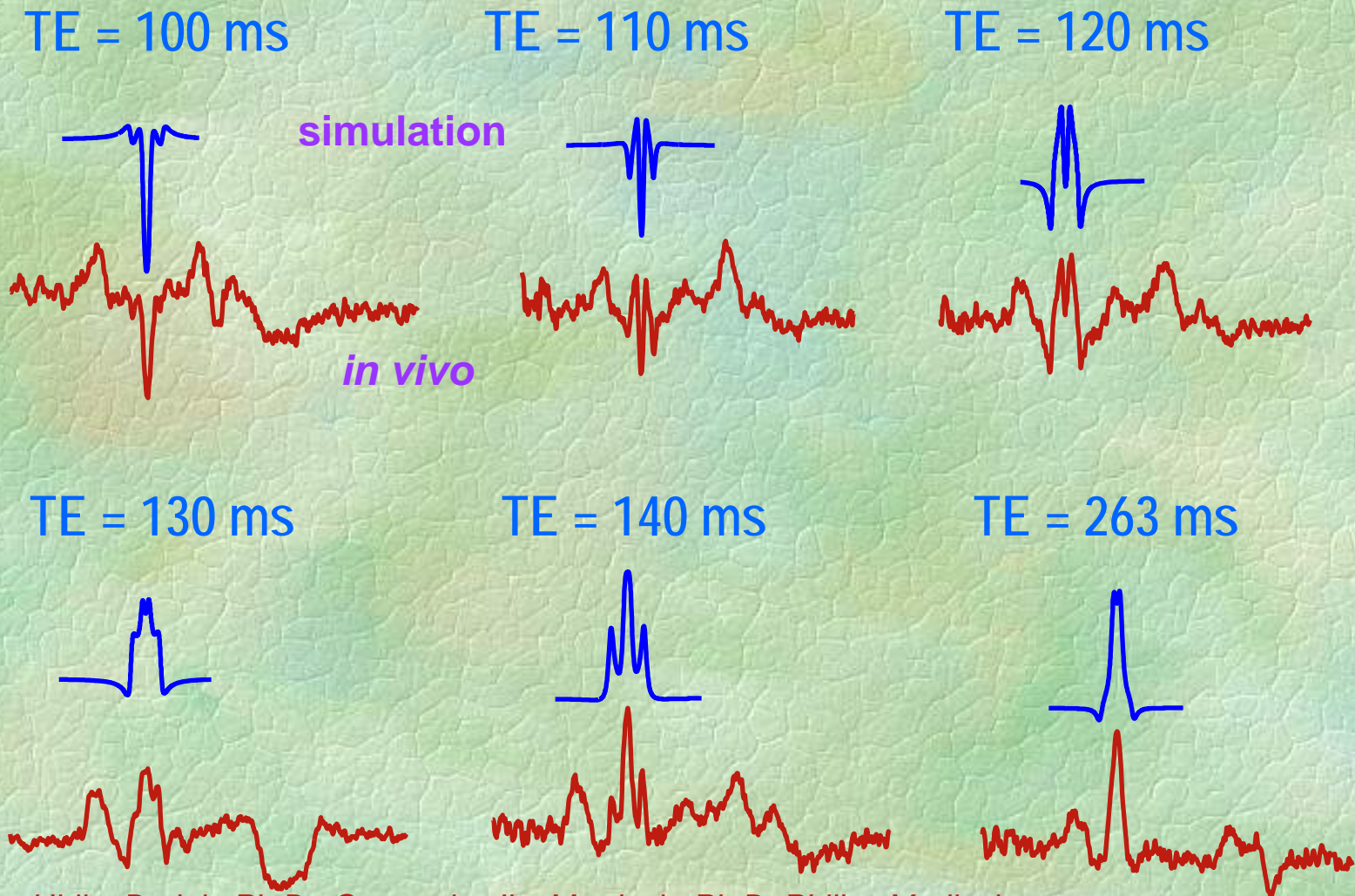


Sens	79%	PPV	0.57
Spec	74%	NPV	0.89

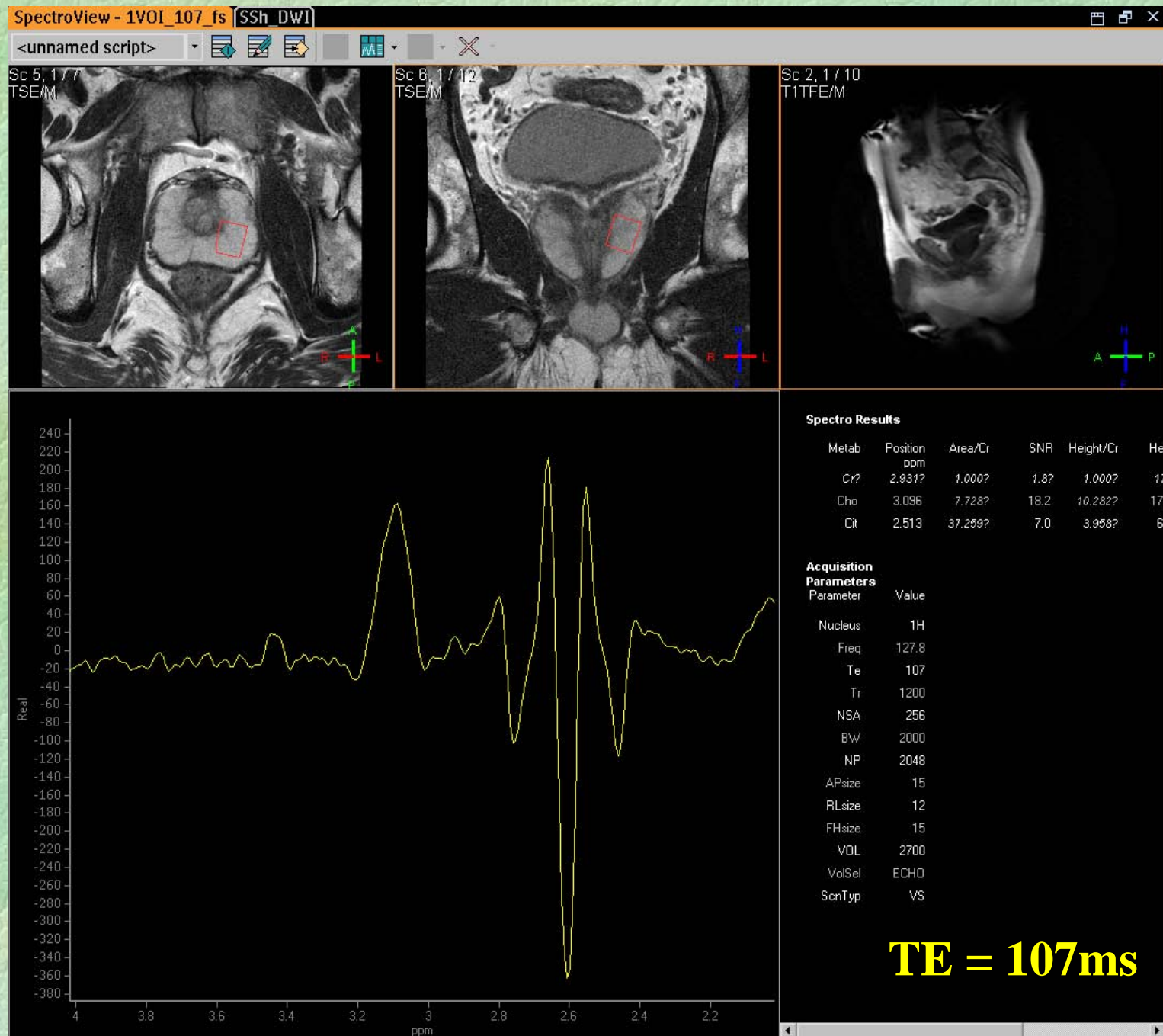
Courtesy of T. Scheenen Prof. A. Heerschap, Radboud University Nijmegen Medical Center, and the IMAPS community



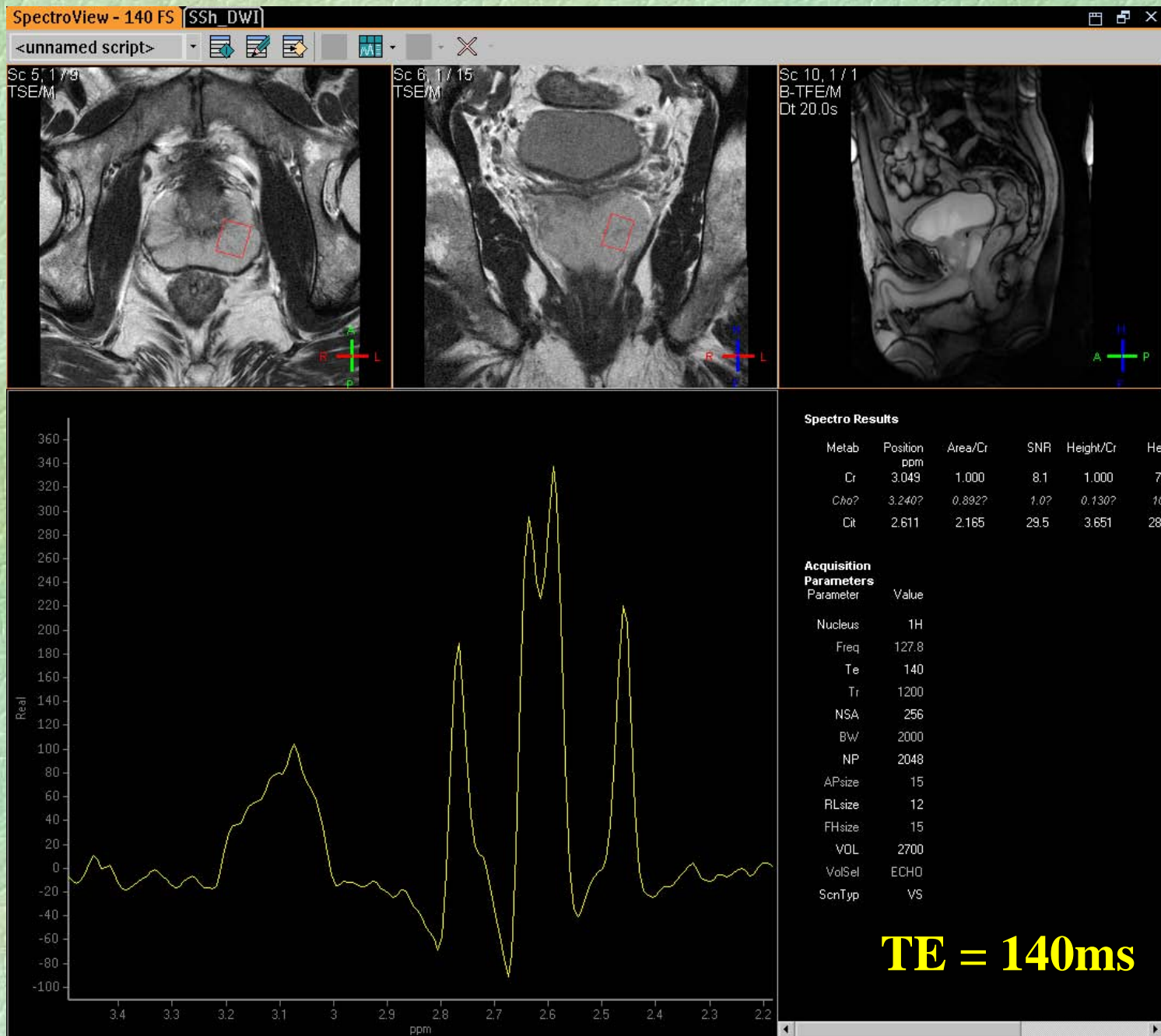
Coupling evolution of citrate at 3T



Courtesy: Ulrike Dydak, Ph.D., Gyrotools; Jim Murdoch, Ph.D. Philips Medical

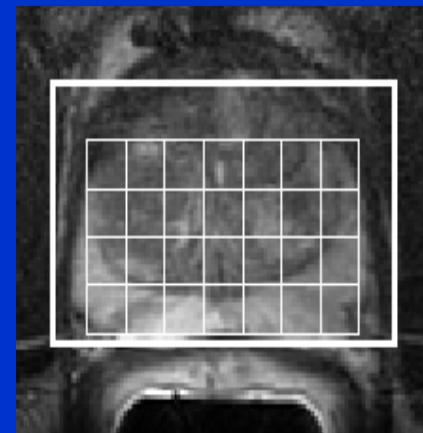
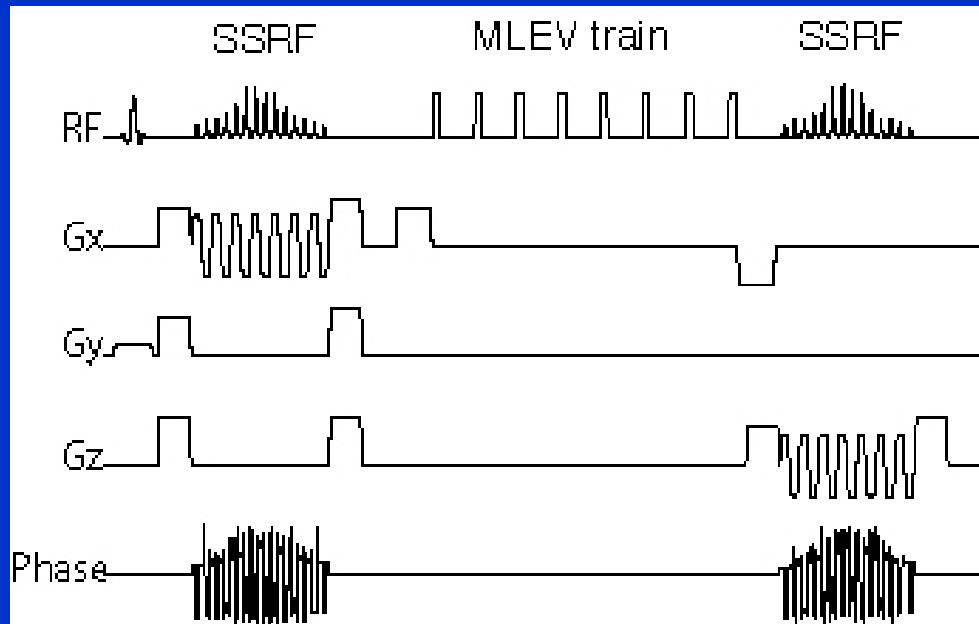


Courtesy: Ulrike Dydak, Ph.D., Gyrotools; Jim Murdoch, Ph.D. Philips Medical

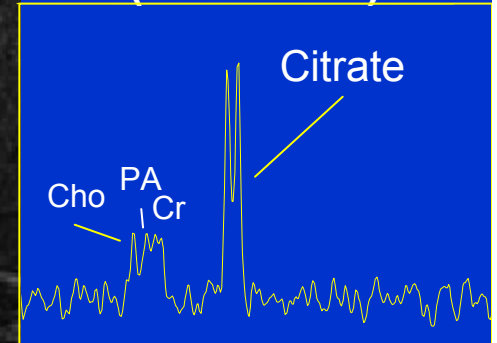


Courtesy: Ulrike Dydak, Ph.D., Gyrotools; Jim Murdoch, Ph.D. Philips Medical

3 Tesla High Resolution 3D MR Spectroscopic Imaging of the Prostate with a MLEV-PRESS Sequence

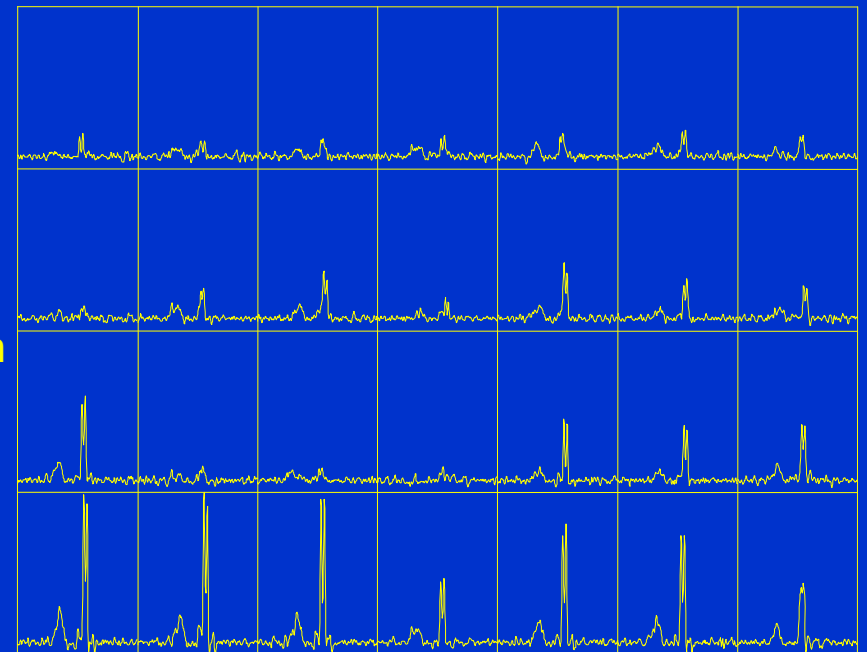


CPMG-PRESS
(TE = 85 ms)



The modified PRESS sequence for prostate MRSI at 3T. Conventional refocusing pulses are replaced with phase-modulated spectral-spatial pulses (SSRF). Between the dual-band refocusing pulses, a non-selective inversion pulse train utilizing a MLEV phase cycling scheme was used to refocus the J-modulation of citrate.

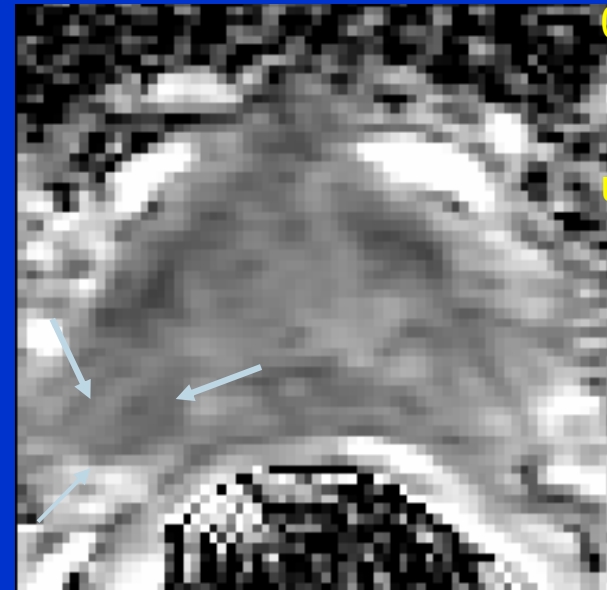
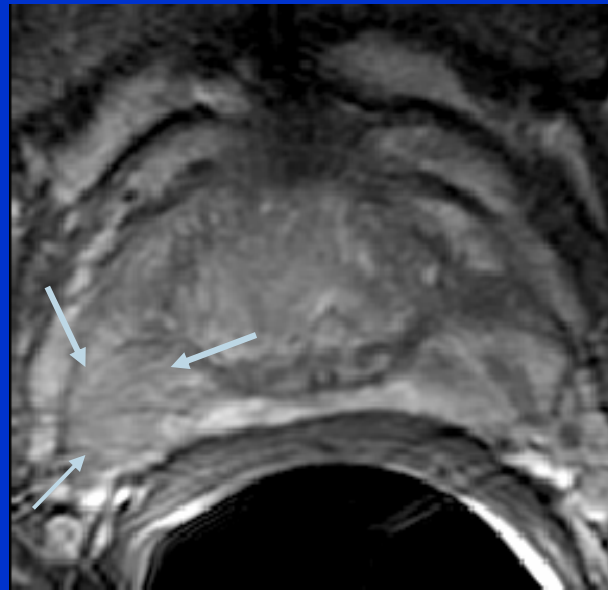
Courtesy: John Kurhanewicz, Ph.D. UCSF



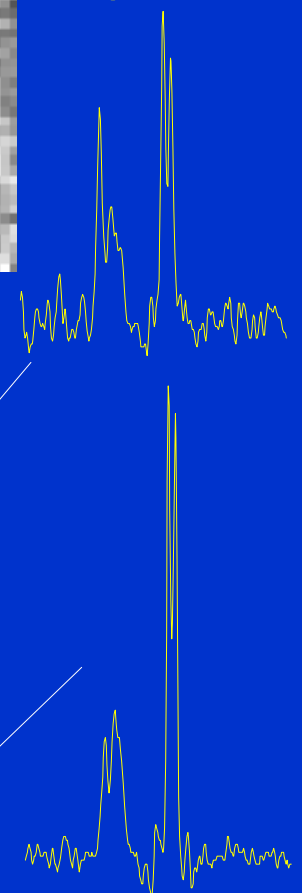
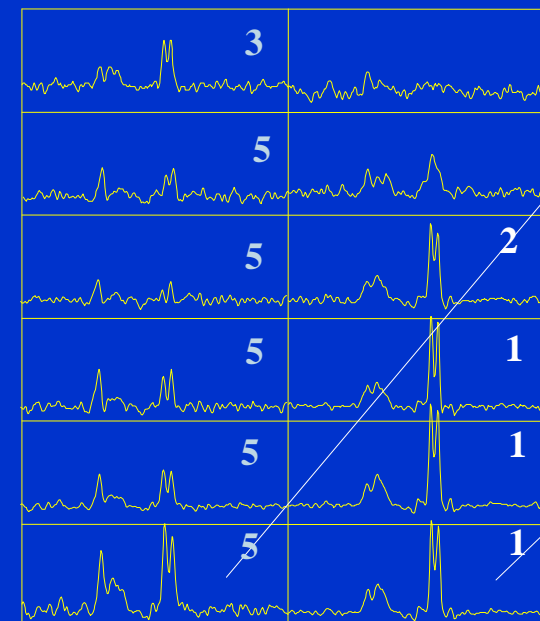
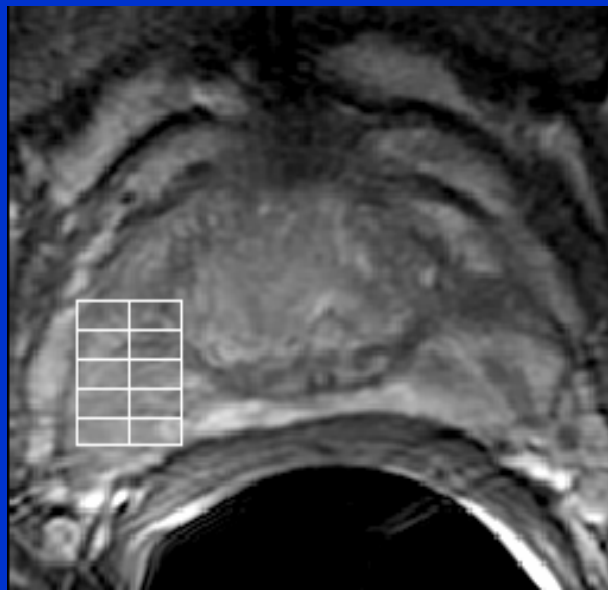
3T MRSI: Increased Spatial and Spectral Resolution

A patient with a PSA of 2.0 and biopsy proven cancer (1/9 cores of G3+3, 1% of total volume in the R lobe). The patient has been on Proscar since 2003.

We observe a large volume of clear-cut metabolic abnormality (5 s and 4 s) within the right midgland towards the base.



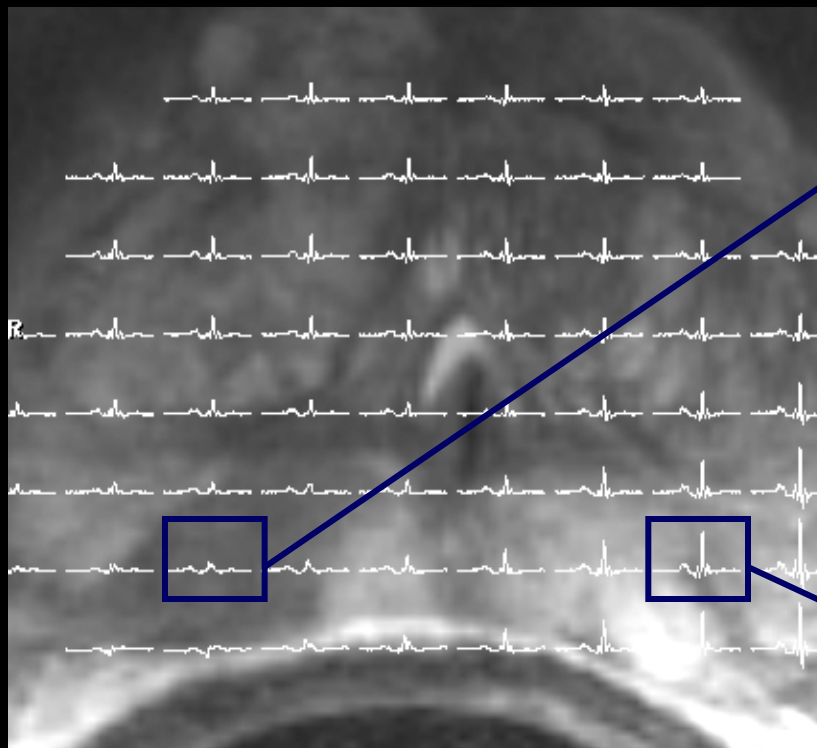
0.15 cc Spatial Resolution Spectral Data using a MLEV-PRESS sequence



Courtesy: *John Kurhanewicz, Ph.D. UCSF*

Spectroscopy: 3T, ERC

Endorectal coil only, axial slice
Weighted, elliptical k-space sampling



TE 145[#] ms, TR 750 ms, TA 9:36 min
6 ave (Hamming), 14 x 10 x 12 matrix
5 x 5 x 5 mm

Histopathology
Whole mount section

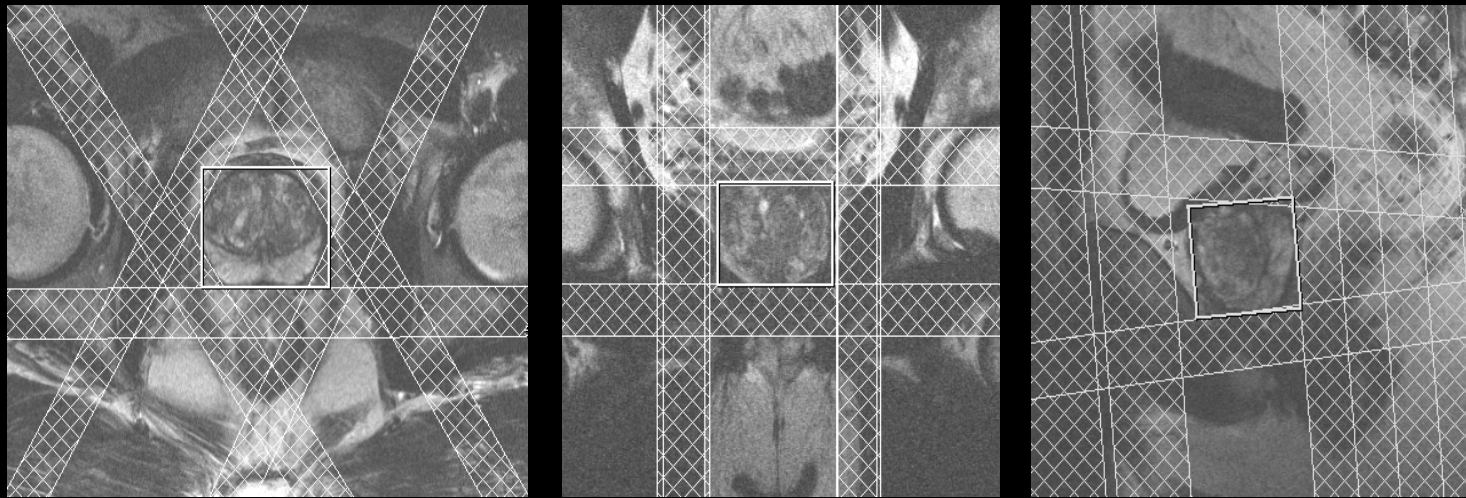


Gleason 8

Gleason 5

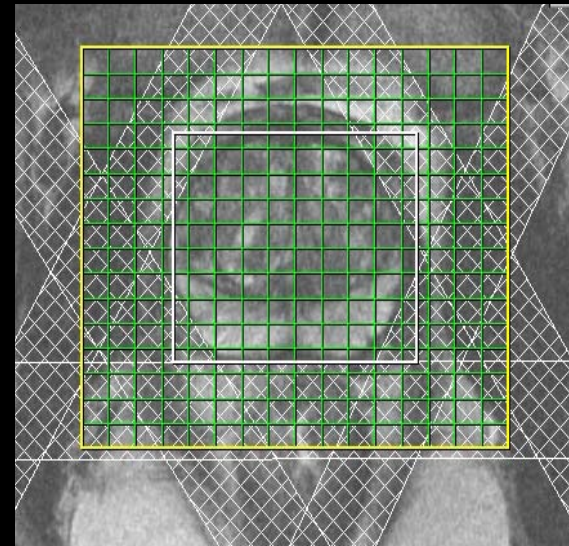
4.0 3.5 3.0 2.5 2.0 1.5

Spectroscopy: 3T, Body array coil

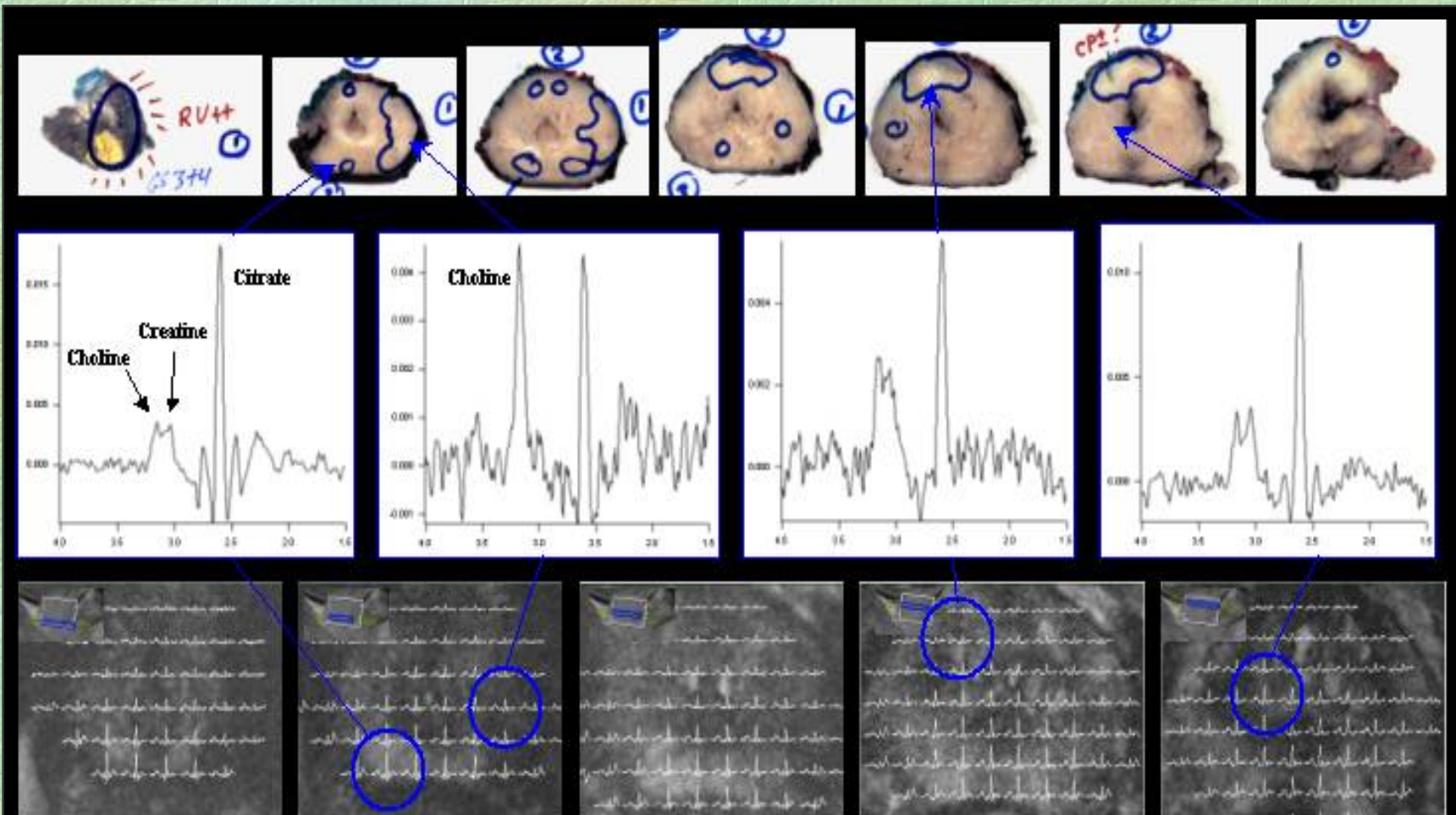


Matrix spectroscopy **without ERC**

TE 145 ms, TR 750 ms, TA 9 min
11 ave (Hamming), 12 x 10 x 10 matrix
7 x 7x 7 mm



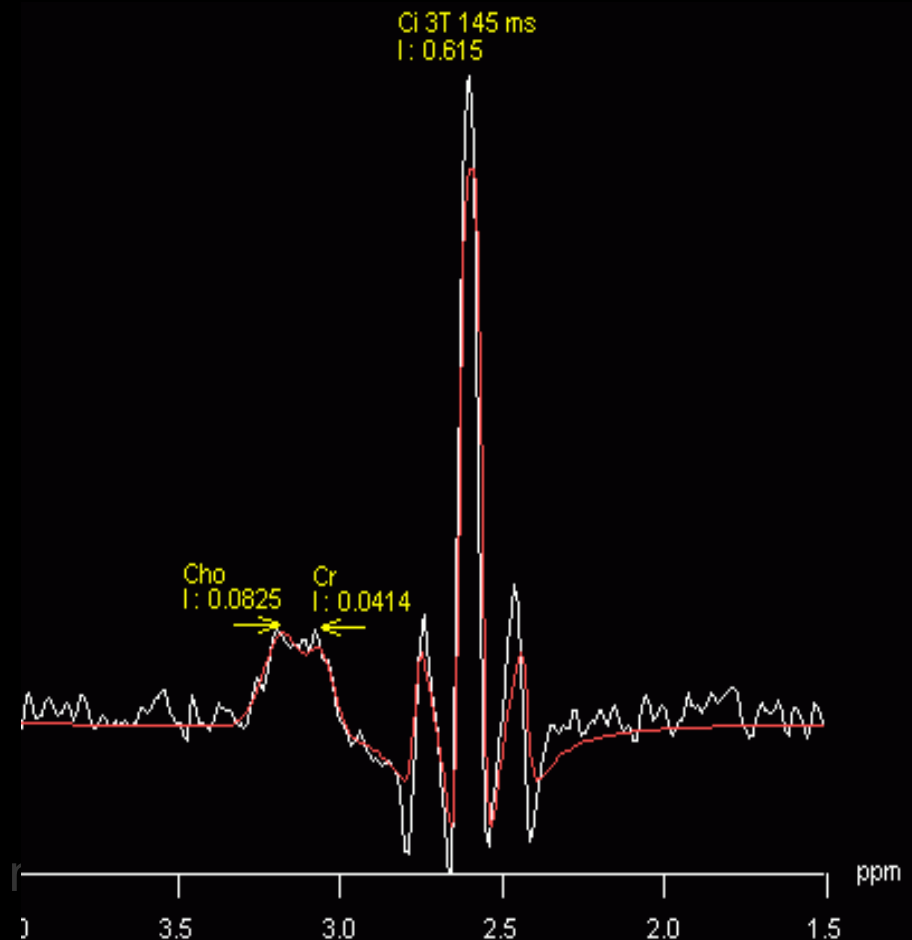
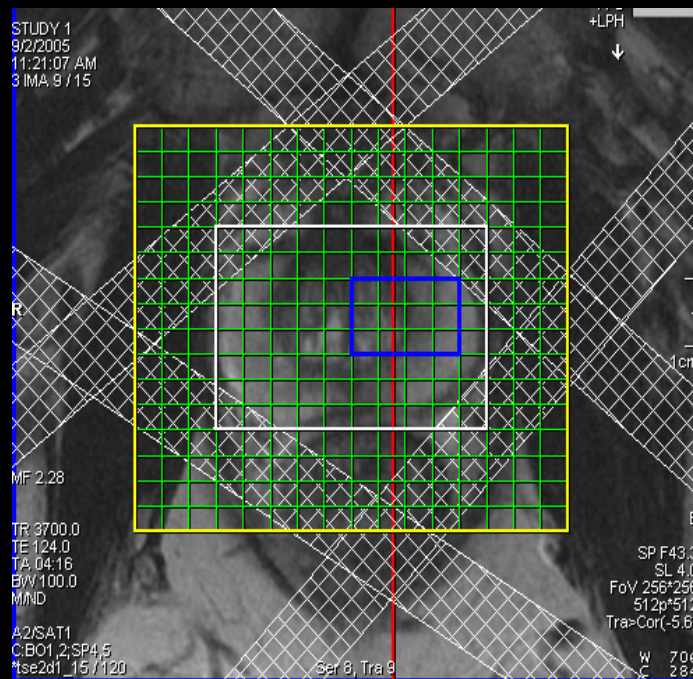
Spectroscopy: 3T, Body array coil



TE 145 ms, TR 750 ms, TA 9 min, 11 ave (Hamming), 12 x 10 x 10 matrix 7x7x7 mm

Spectroscopy: 3T, TIM

Tim Matrix spectroscopy



Resolution and measurement time equal to 1.5T with EF

Summary

- The metabolic transformation of citrate-producing nonmalignant cells to citrate-oxidizing malignant cells occurs early (probably as a premalignant stage), which permits the identification of PCa prior to histopathological identification.
- Commercial packages to perform prostate MRI/MRSI are available with all the major MRI vendors
- However with all new technologies training is extremely important.
- Care in positioning the PRESS box and the outer volume suppression pulses is extremely important.
- Similarly a good shim of the order of 20 Hz or better is required over the PRESS box for a reliable MRSI exam.

Summary

- Prostate cancer can be identified based on decrease in citrate and polyamines and an increase in choline signal.
- Diffusion weighted imaging can complement MRSI exams where PCa is characterized by a reduction in ADC.
- Similarly dynamic contrast enhanced imaging can also complement MRSI through the visualization of angiogenesis.
- A multi-parametric MRI approach to prostate cancer is likely to significantly increase the sensitivity and specificity in the detection of prostate cancer.
- MRSI of the prostate at the higher field strength seems very promising.

Acknowledgements

- **Dr. John Kurhanewicz**, UCSF
- **Dr. Arend Heerschap**, Radboud University Nijmegen Medical Center
- **Dr. Scheenan**, Radboud University Nijmegen Medical Center
- **Dr. Ulrike Didak**, Gyrotools, University and ETH Zürich
- **Dr. James Murdoch**, Philips Medical Systems
- **Dr. Peter Choyke**, National Cancer Institute, Uniformed Services University of The Health Sciences
- **Dr. Nouha Salibi**, Siemens Medical Center
- Partly supported by a grant from DOD IDEA grant W81XWH-04-1-0249 (PC031042)

Thank You!

An Elastic Registration Algorithm based on Strain Energy Minimization and its Application to Prostate MR images

B. Zhang¹, R. P. Gullapalli¹

¹Magnetic Resonance Research Center, Dept of Radiology, University of Maryland School of Medicine, Baltimore, MD, United States

Background

Magnetic resonance imaging using the endorectal coil (erMRI) has become the clinical standard in the diagnosis of prostate cancer as it provides excellent quality high resolution images. However the images and spectra obtained using the endorectal coil experience certain amount of displacement from their original position and the prostate is imaged in this displaced, distorted position. Such displacement and distortion during diagnosis leads to uncertainties in the localization of prostate cancer during therapeutic intervention as in the case of radiation therapy. Image registration is a necessary exercise to transform the diagnostic images to their undistorted state. Rigid body registration is inadequate since the prostate encounters non-rigid elastic deformation. Elastic registration is of particular interest in erMRI since it takes into account the physical process that prostate has experienced during the medical imaging procedure. Traditional elastic image registration schemes derive forces from image data using some similarity measure and then deform the source image into target. [1,2] Instead of computing the forces and solving the Navier-Lame equation for deformation, the proposed registration algorithm in this work models the image as a dynamic system in equilibrium and derives the deformation using the principle of strain energy minimization.

Method

Strain Energy Minimization According to the principles of dynamics, the potential energy function has a stationary value if the system is conservative and is in equilibrium. Especially, if the system is stable, then the potential energy function is minimized. [3] In prostate erMRI, the prostate is in equilibrium before and after the insertion of endorectal coil, hence the above theorem can be applied to derive the underlying deformation within the prostate.

Treating the prostate as an incompressible elastic body, the potential energy function is purely the strain energy U . It is defined as

$$U = G \iiint \left[\left(\frac{\partial u}{\partial x} \right)^2 + \left(\frac{\partial v}{\partial y} \right)^2 + \left(\frac{\partial w}{\partial z} \right)^2 \right] dx dy dz + \frac{1}{2} G \iiint \left[\left(\frac{\partial u}{\partial y} + \frac{\partial v}{\partial x} \right)^2 + \left(\frac{\partial v}{\partial z} + \frac{\partial w}{\partial y} \right)^2 + \left(\frac{\partial u}{\partial z} + \frac{\partial w}{\partial x} \right)^2 \right] dx dy dz$$

where G is the shear modulus characterizing the prostate constitutive property, u , v , and w are displacements in x , y , and z directions, respectively. The strain energy minimization requires $\delta U = 0$. The boundary conditions of this problem are of the Dirichlet boundary form:

$$\vec{u}|_{\partial\Omega_1} = \vec{u}(u, v, w)|_{\partial\Omega_1} = 0 \text{ and } \vec{u}|_{\partial\Omega_2} = \vec{u}(u, v, w)|_{\partial\Omega_2} = (u(x, y, z), v(x, y, z), w(x, y, z))|_{\partial\Omega_2}$$

where $\partial\Omega_1$ denotes the outer boundary of the data volume and $\partial\Omega_2$ denotes the surface of the prostate.

Discretization Using the forward difference formula for first derivative of displacement, the strain energy minimization equation can be expressed in discrete form as a function of pixel positions $(X_{ijk}, Y_{ijk}, Z_{ijk})$:

$$X_{ijk} = \frac{2X_{i+1jk} + 2X_{i-1jk} + X_{ij+1k} + X_{ij-1k} + X_{ijk+1} + X_{ijk-1} + (Y_{i+1jk} - Y_{ijk}) - (Y_{i+1j-1k} - Y_{ij-1k}) + (Z_{i+1jk} - Z_{ijk}) - (Z_{i+1jk-1} - Z_{ijk-1})}{8}$$

$$Y_{ijk} = \frac{Y_{i+1jk} + Y_{i-1jk} + 2Y_{ij+1k} + 2Y_{ij-1k} + Y_{ijk+1} + Y_{ijk-1} + (Z_{ij+1k} - Z_{ijk}) - (Z_{ij+1k-1} - Z_{ijk-1}) + (X_{ij+1k} - X_{ijk}) - (X_{i-1j+1k} - X_{i-1jk})}{8}$$

$$Z_{ijk} = \frac{Z_{i+1jk} + Z_{i-1jk} + Z_{ij+1k} + Z_{ij-1k} + 2Z_{ijk+1} + 2Z_{ijk-1} + (X_{ijk+1} - X_{ijk}) - (X_{i-1jk+1} - X_{i-1jk}) + (Y_{ijk+1} - Y_{ijk}) - (Y_{ij-1k+1} - Y_{ij-1k})}{8}$$

Combining the discretized boundary conditions, the final position can be determined.

Numerical Implementation

Note, that in the above solutions, the new position $(X_{ijk}, Y_{ijk}, Z_{ijk})$ is always explicitly expressed by its closest neighbors. This particular form of solution suggests that Gauss-Seidel method can be directly used for the computation of $(X_{ijk}, Y_{ijk}, Z_{ijk})$.

Data Acquisition The prostate phantom and patient data were acquired on Philips Eclipse 1.5T system. The prostate phantom was built in-house and incorporates all the necessary elements of a prostate gland including the tissue consistency, and the biochemicals contained within a normal prostate tissue.[4] The prostate phantom also has incorporated within it seeds that serve as landmarks and are helpful in assessing the accuracy of registration. The image size of the prostate phantom was $256 \times 256 \times 29$, and the resolution was $0.625 \times 0.625 \times 2.5$ mm. T2-weighted images ($256 \times 256 \times 25$) of the prostate were obtained from patients with the endorectal coil in its fully inflated position and completely deflated position at a TE of 110ms and a TR of 3500ms at a voxel resolution of $0.625 \times 0.625 \times 3.5$ mm.

Results

Figure 1 displays the representative resulting images from the registration along with the displacement vectors. The registration error was found to be 1.0 ± 0.6 pixels (or 0.6 ± 0.4 mm) for displacements ranging from 4-6mm due to the insertion of the coil. These results quantitatively demonstrated the excellent performance of the registration algorithm. Representative images from a patient's prostate are shown in figure 2. The similarity measure shows that normalized correlation coefficient improved from 0.62 ± 0.12 to 0.98 ± 0.08 by the registration.

Conclusion

In conclusion, a novel registration algorithm based on a strain energy transformation was implemented. This algorithm was tested on phantom and actual clinical data respectively. The results from phantom data showed that the accuracy of our registration is within 1 pixel. The clinical prostate data showed the feasibility of the registration algorithm to prostate imaging.

References

1. Davatzikos C. et al., *IEEE Trans on Medical Imaging* 15 (1996) 112-115.
2. Peckar W. et al., *J. of mathematical imaging and vision* 10 (1999) 143-162.
3. Greenwood DT, *Classical Dynamics*, Dover, 1997.
4. Zhang B, Gullapalli RP, *Proc of ISMRM* (2005) pp2115.

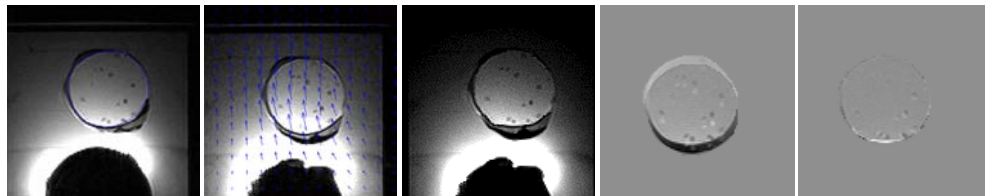


Fig. 1: Representative registration results for prostate phantom images. (a) reference image (b) source image overlapped with the displacement obtained. (c) registered image. (d) difference between the segmented reference and source. (e) difference between the segmented reference and the registered image.

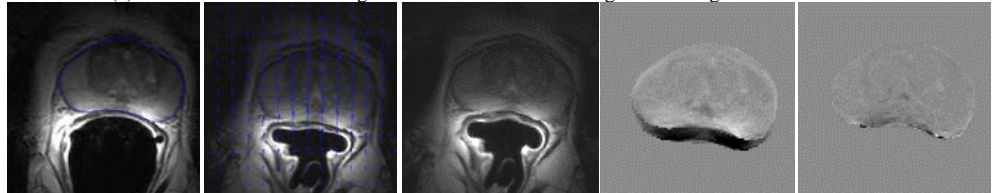


Fig. 2: Representative registration results for actual prostate images. (a) reference image (b) source image overlapped with the displacement obtained. (c) registered image. (d) difference between the segmented reference and source. (e) difference between the segmented reference and the registered image.

Multi-parametric MR Imaging of the Prostate with Step-section Histopathology Correlation

Rao Gullapalli¹, PhD;

Khan Siddiqui^{1,2}, MD; Bao Zhang¹ MS;

Danielle Holanda³, MD; Steve Roys¹, MS;

John Papadimitriou³, MD, PhD;

James Borin⁴, MD; Harris Yfantis³, MD;

Michael Naslund⁴, MD; Eliot Siegel^{1,2} MD



¹Department of Radiology, University of Maryland Medical Center

²Department of Radiology, VA Maryland Health Care System

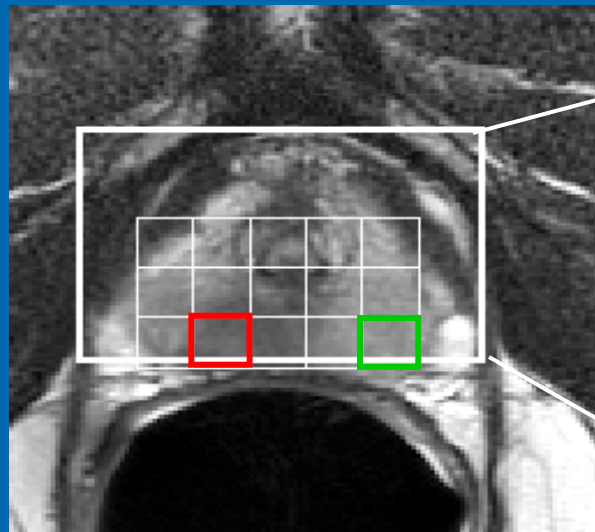
³Department of Pathology, University of Maryland Medical Center

⁴Department of Surgery, University of Maryland Medical Center

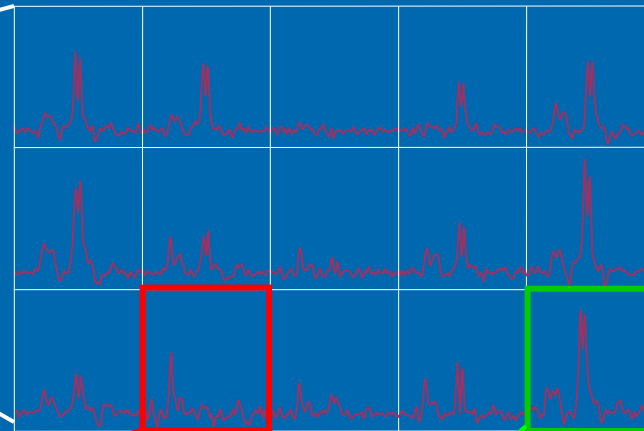
Objectives

- To verify the effectiveness of multi-parametric prostate MRI in diagnostic accuracy in comparison with whole mount histopathology using the following techniques
 - MR spectroscopic imaging
 - Dynamic contrast enhanced MRI
 - Diffusion weighted imaging
 - T2 relaxometry

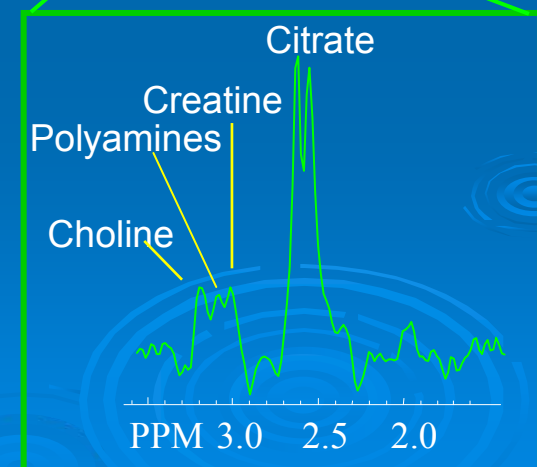
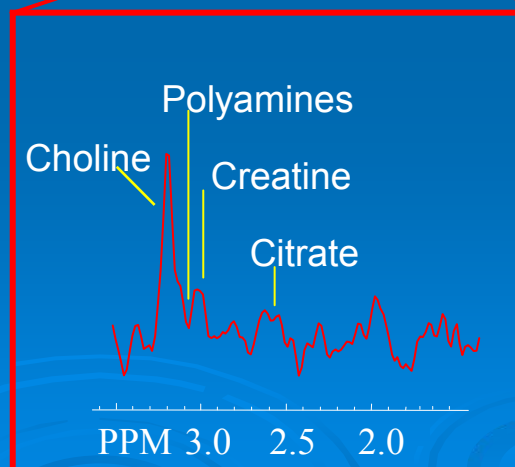
MR spectroscopic imaging



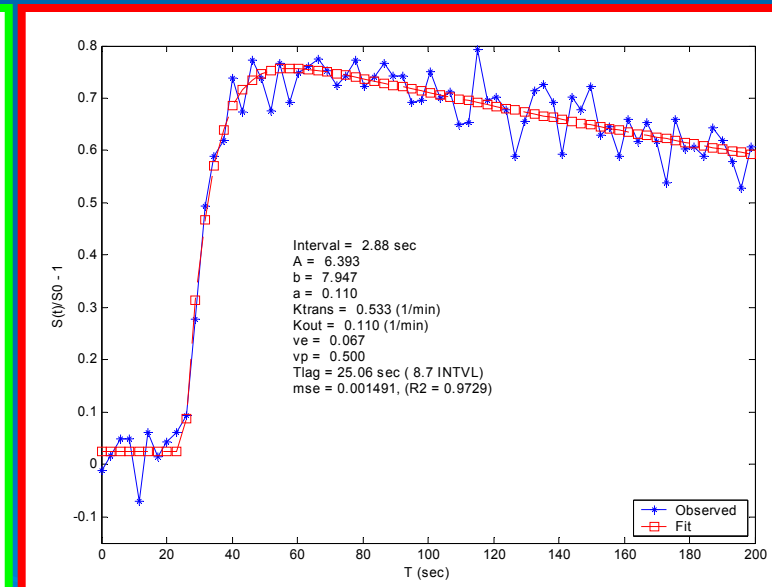
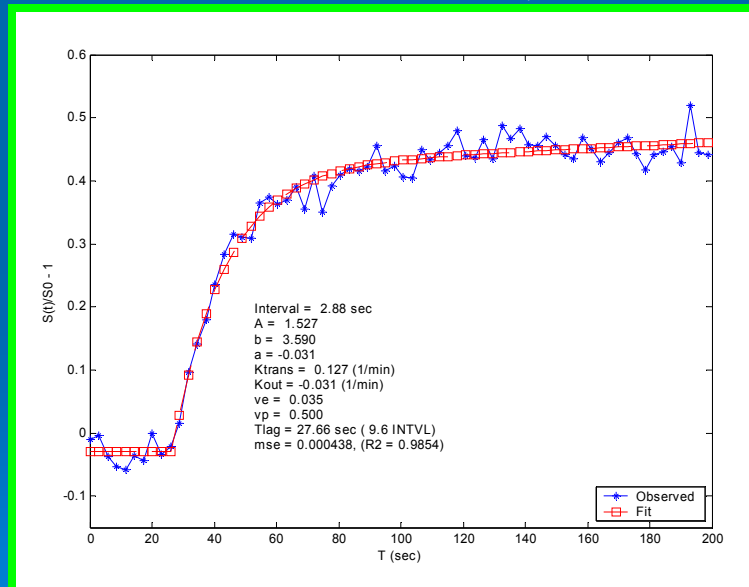
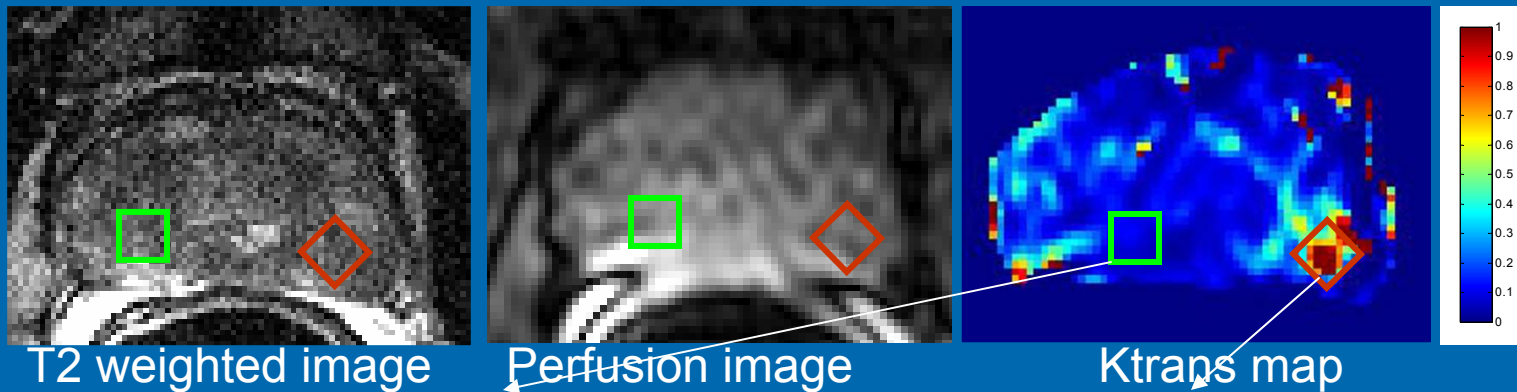
Portion of the 3-D MRSI spectral array



Prostate cancer can be discriminated from **healthy peripheral zone (PZ) tissue** based on a significant reduction in the levels of citrate and polyamines and an elevation in choline on MRSI.



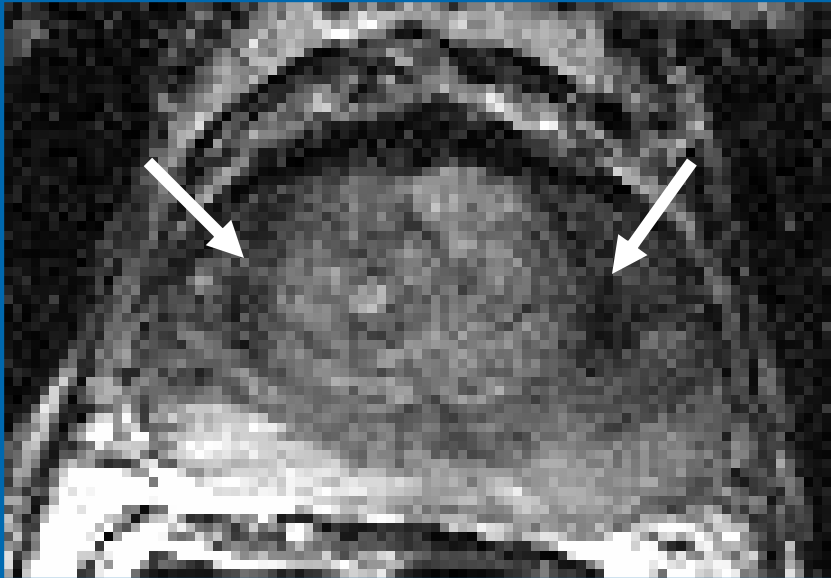
Dynamic contrast enhanced MRI



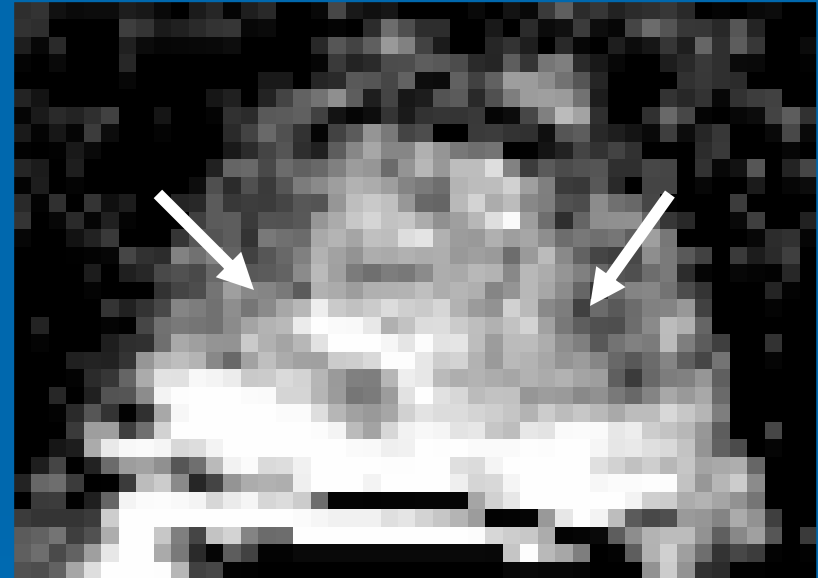
Tofts model was adopted for kinetic analysis to determine K_{trans}

Tofts PS, et al, J Magn Reson Imaging 1999;10(3):223-232.

Diffusion-weighted imaging



T2 weighted image

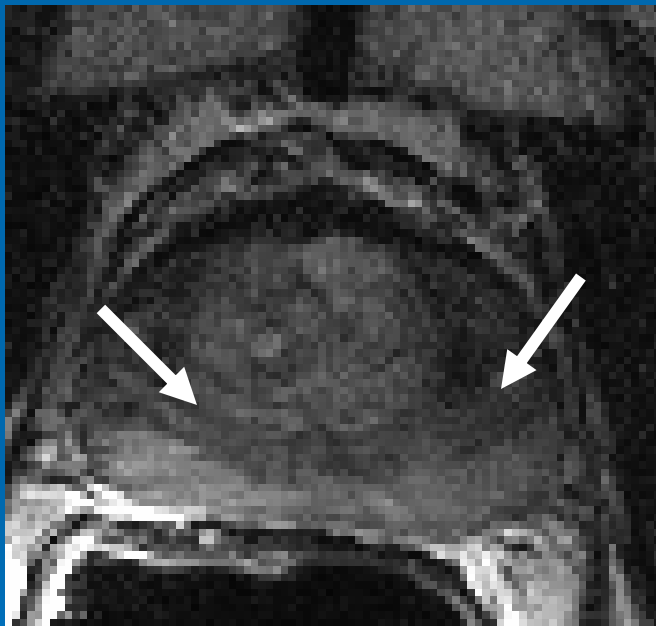


ADC map

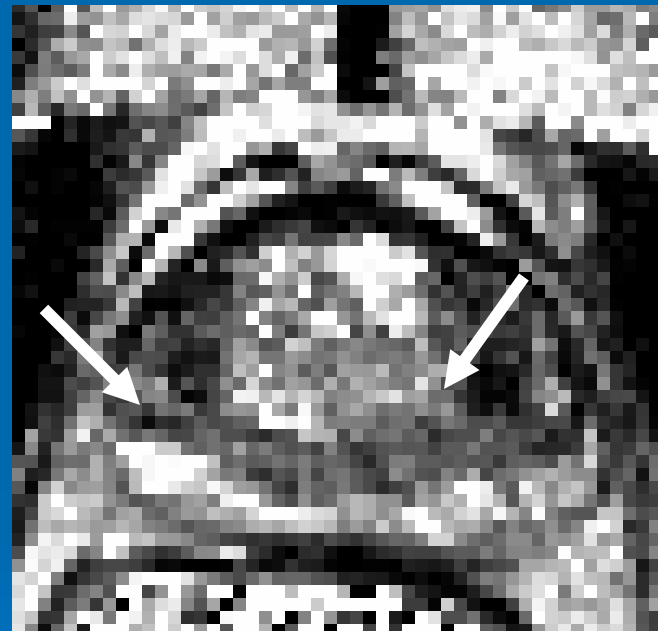
ADC map from DWI demonstrates tumor foci as area of decreased water diffusion in the peripheral zone.

T2 Maps

➤ CPMG sequence



T2 weighted image



Calculated T2 map

T2 map showing cancerous regions with lower T2 values

Subjects

- 26 patients with biopsy proven prostate cancer
 - Age: 42-73, mean 58 ± 8 yrs
 - PSA: 0.5-29 ng/ml mean 9.4
 - Gleason Score: 4-8, mean 6 (62%) or 7 (38%)
 - All patients had MRI at least 4 weeks after biopsy.
 - One subject was recruited post radiation.
 - Patients went to surgery within three weeks following their MRI procedure
 - Informed consent approved our Internal Review Board was obtained from all patients

In vivo MRI data acquisition

➤ Protocol

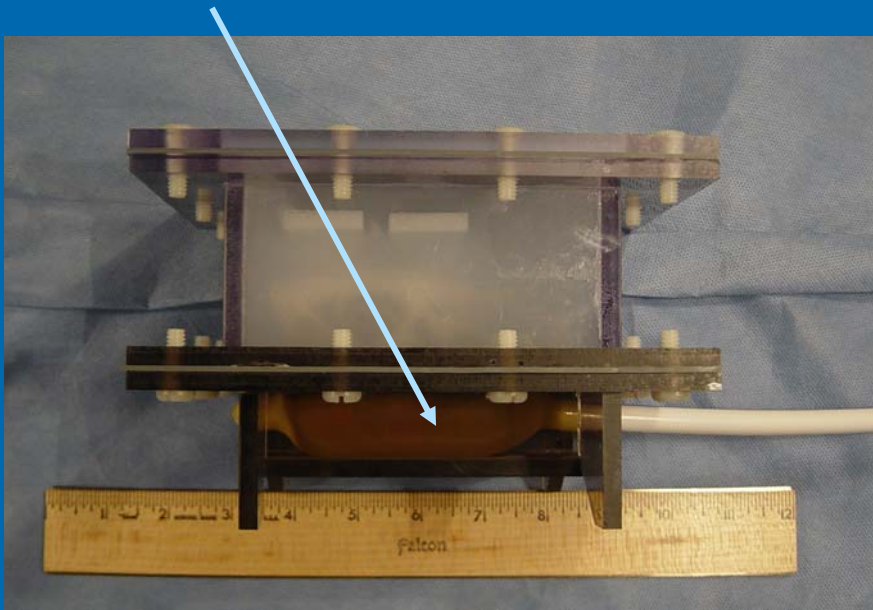
- T1-weighted
- T2 weighted
- T2 relaxometry imaging
- Diffusion weighted imaging
- Perfusion weighted imaging
- MR spectroscopy imaging

➤ Sequence Validation for 3D-MRSI

- Home built prostate phantom
- Healthy volunteer

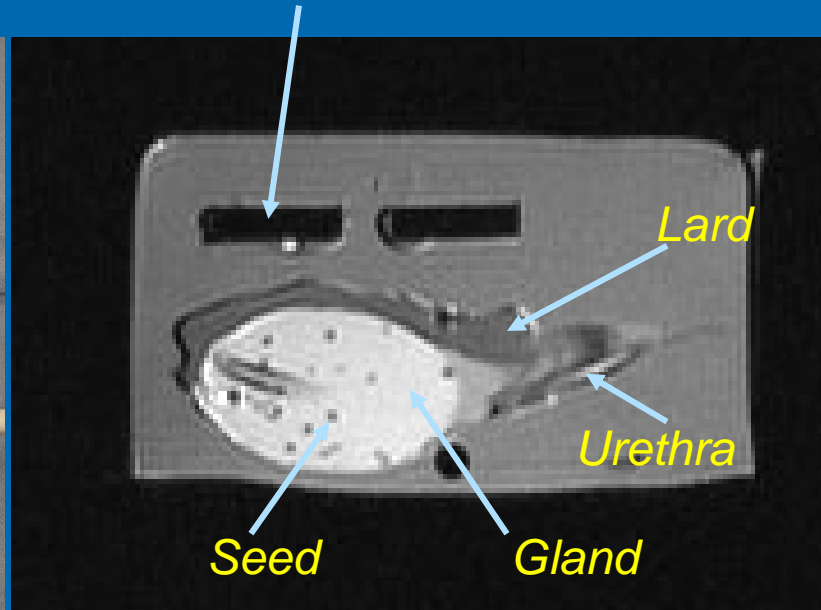
Prostate phantom

Endorectal coil



Prostate phantom

Pubic bone



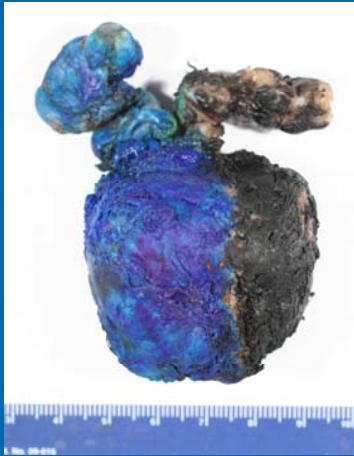
Sagittal MR image of the Phantom.

Prostate phantom was constructed to mimic the actual situation when imaging the prostate. The gland itself was made of agar gel mixed with the relevant proportions of choline, creatine, and citrate observed in the normal prostate. Sesame seeds were included in the phantom which allowed clinicians to practice for biopsy and also for placement of seeds.

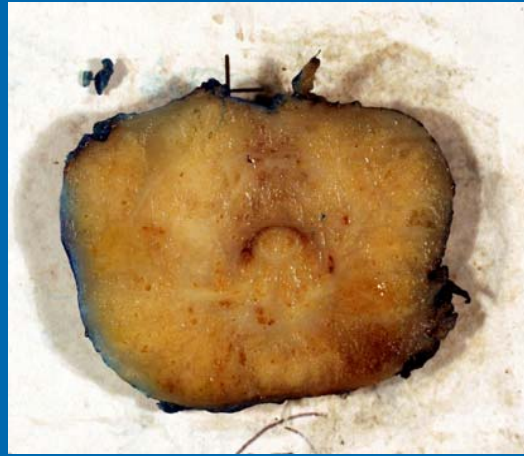
MR imaging parameters

	TR (ms)	TE (ms)	Matrix	FOV (mm)	No. of Slices	Thickne ss (mm)	Gap (mm)
Axial T1-weighted	710	15	230X256	160X160	26	3	0
Axial T2-weighted	4030	97	256x256	180X180	26	3	0
CPMG	2000	10:10:80	192X256	225X300	10	3	3
DTI	11500	93	128X128	230X230	50	2	0
DWI	5900	81	192X192	230X230	16	3	0
3D MRSI (PRESS box adjusted to prostate volume)	780	120	16x16	96x96	16	6	0
Perfusion FLASH	61	2.4	192X256	200X200	10	6	0

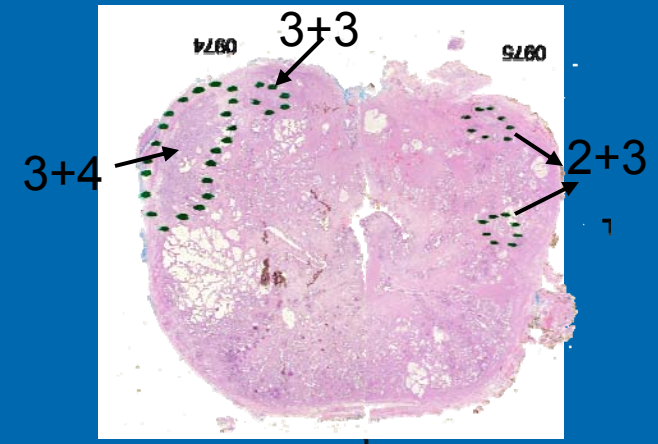
Histopathology



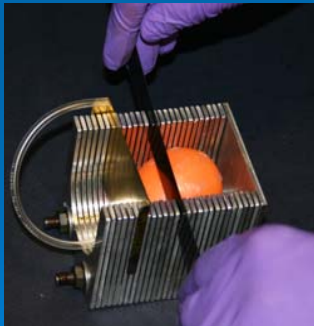
Prostate Specimen



Individual 3mm section



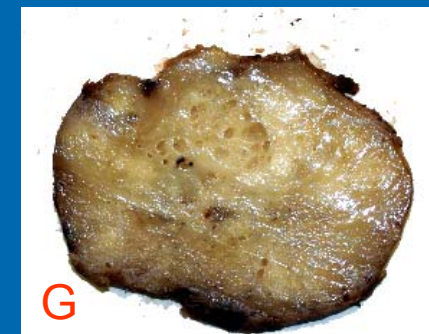
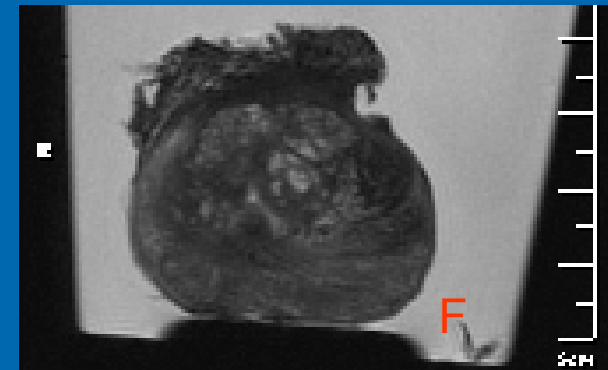
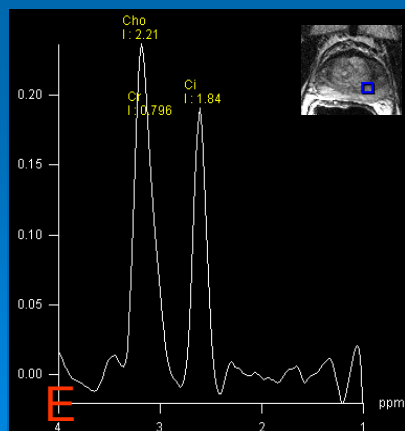
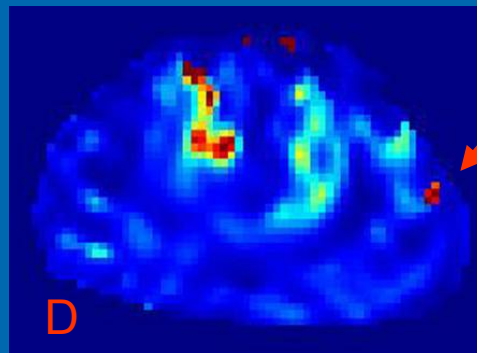
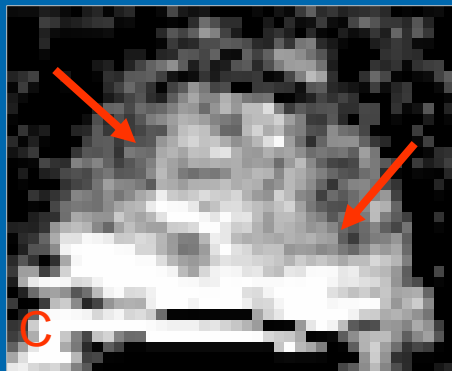
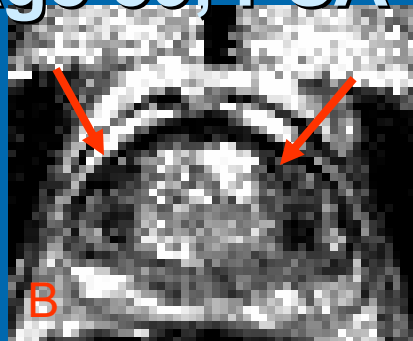
Histology slide



Prostate Slicer

A prostate slicer was designed to facilitate whole mount prostate. The excised prostate was color coded to differentiate its orientation. Uniform 3 mm parallel slices were then cut followed by 50 micron sections from each of the slices for H&E staining. On each of the slides the pathologist marked regions of cancer along with their Gleason Score.

Example 1: Patient with multifocal cancer and prostatitis. Age 59, PSA 5.9 ng/l, Gleason 6

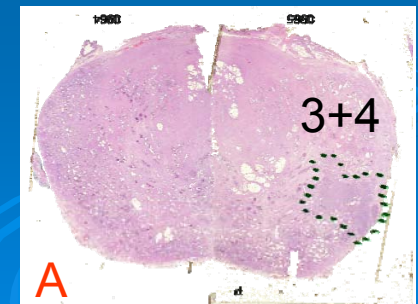
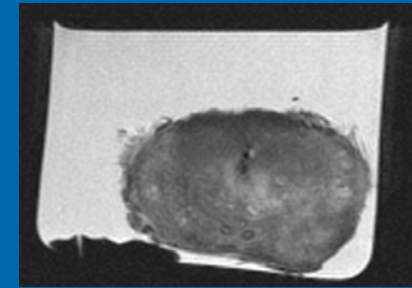
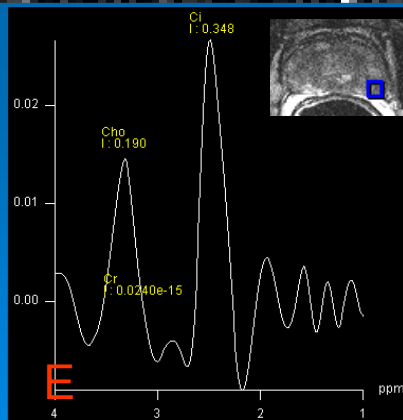
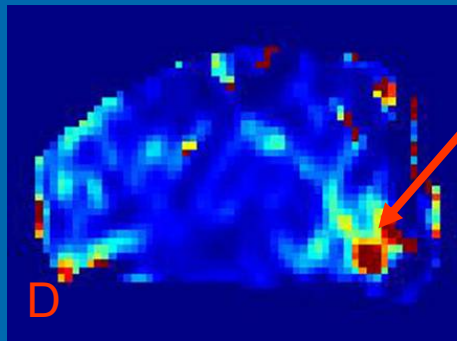
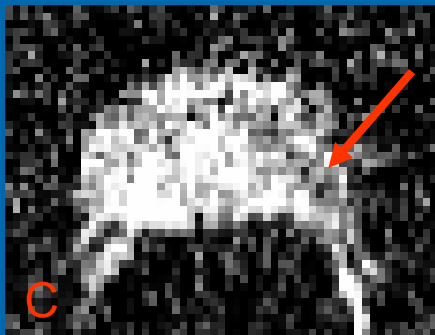
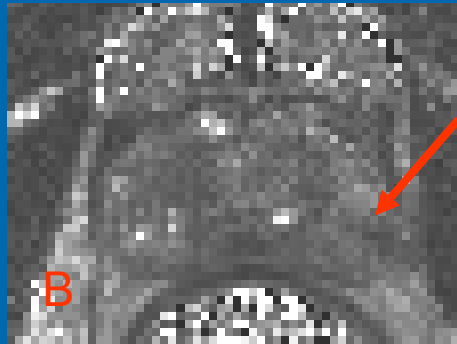
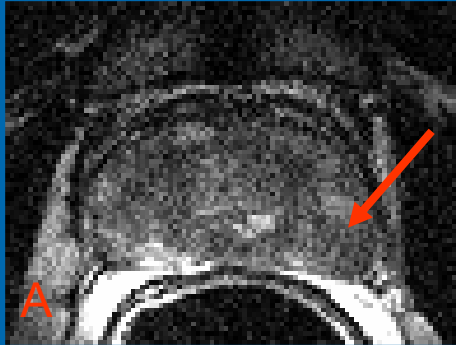


In vivo, ex vivo MR images: (A) T2-weighted image, (B) T2-map, (C) ADC map, (D) Ktrans map, (E) spectra from the tumor area, (F) ex-vivo prostate, (G) section of the prostate, and (H) corresponding histology slide with pathologists findings of multifocal cancer and prostatitis.

3+2

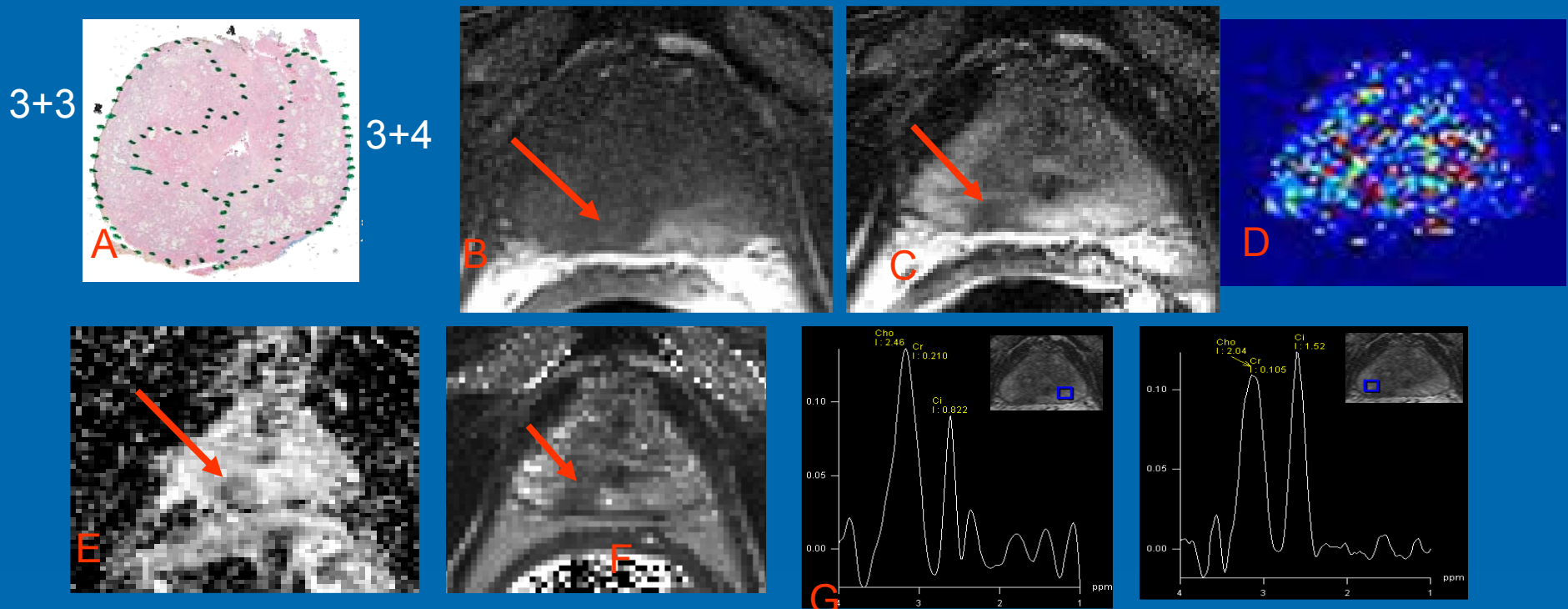
Multifoci
lesion 3+4

Example 2: Focal Tumor with Extracapsular extension, Age 44, PSA 6.7 ng/L, Gleason 6



(A) T2-weighted image, (B) T2-map, (C) ADC map, (D) Ktrans map, (E) spectra from the tumor area, (F) ex-vivo prostate, (G) section of the prostate, and (H) corresponding histology slide with pathologists findings of cancer and extracapsular extension.

Example 3: Case of Diffuse prostate cancer, Age 61, PSA 5.4, Gleason 6



(A) histology slide with pathologist score, (B) T1-weighted image (C) T2-weighted image, (D) Ktrans map, (E) ADC map, (F) T2 map, (G) spectra from the normal appearing (from T2-weighted images) area of the left PZ, and (H) spectra from the abnormal appearing area from the right PZ.

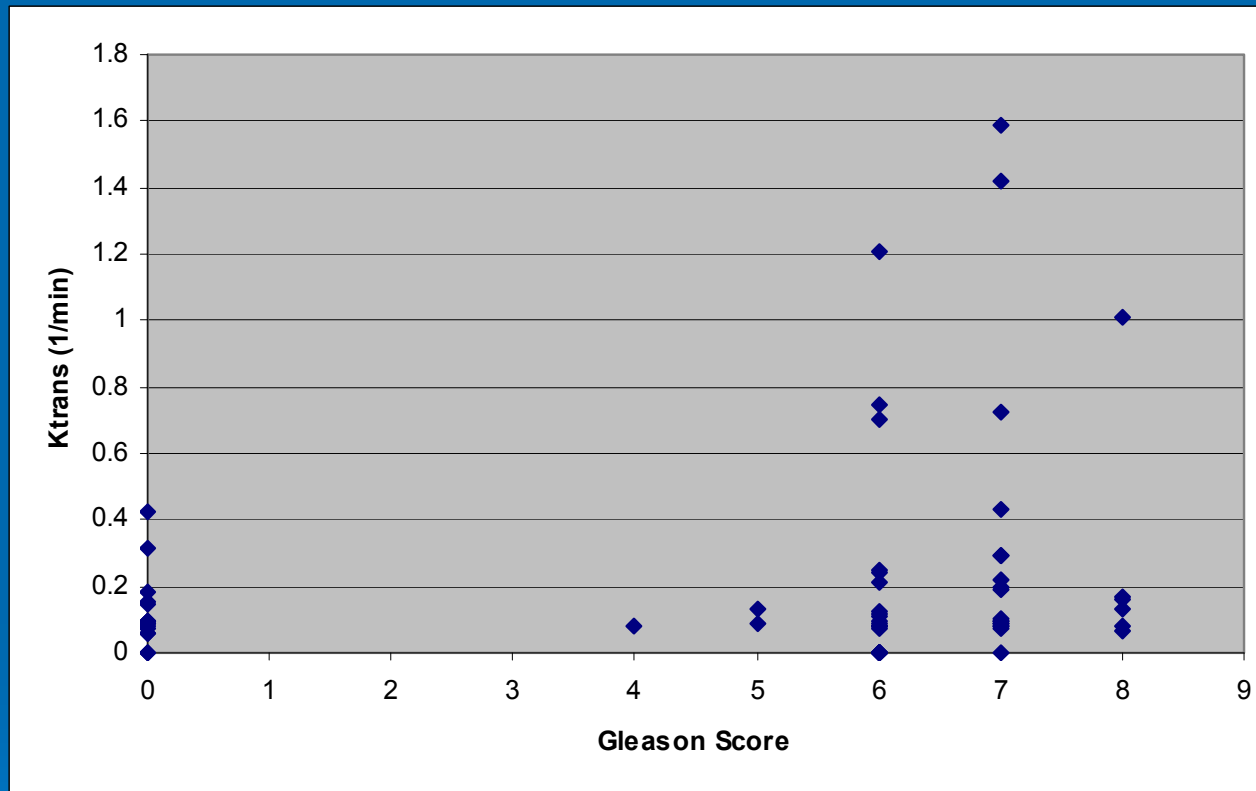
Although, diffusion, and T2-map seem to indicate abnormal area only in the right PZ, spectroscopy indicates bilateral abnormality and perfusion map is unable to differentiate kinetic differences.

Multi-parametric Measures

	Normal tissue	Tumor Gleason 4	Tumor Gleason 5	Tumor Gleason 6	Tumor Gleason 7	Tumor Gleason 8
Cho+Cr/Cit	0.6 ± 0.25	0.43	0.56 ± 0.13	1.61 ± 0.88	1.47 ± 1.12	2.20 ± 2.22
K^{trans} (1/min)	0.14 ± 0.11	0.08	0.11 ± 0.03	0.28 ± 0.34	0.36 ± 0.46	0.27 ± 0.37
T2 (ms)	111.3 ± 22.7	113.6	94.7 ± 25.4	105.3 ± 28.1	131.2 ± 28.2	115.2 ± 55.7
ADC ($10^{-3}\text{mm}^2/\text{s}$)	1.15 ± 0.44			1.10 ± 0.47	1.34 ± 0.39	1.13 ± 0.16

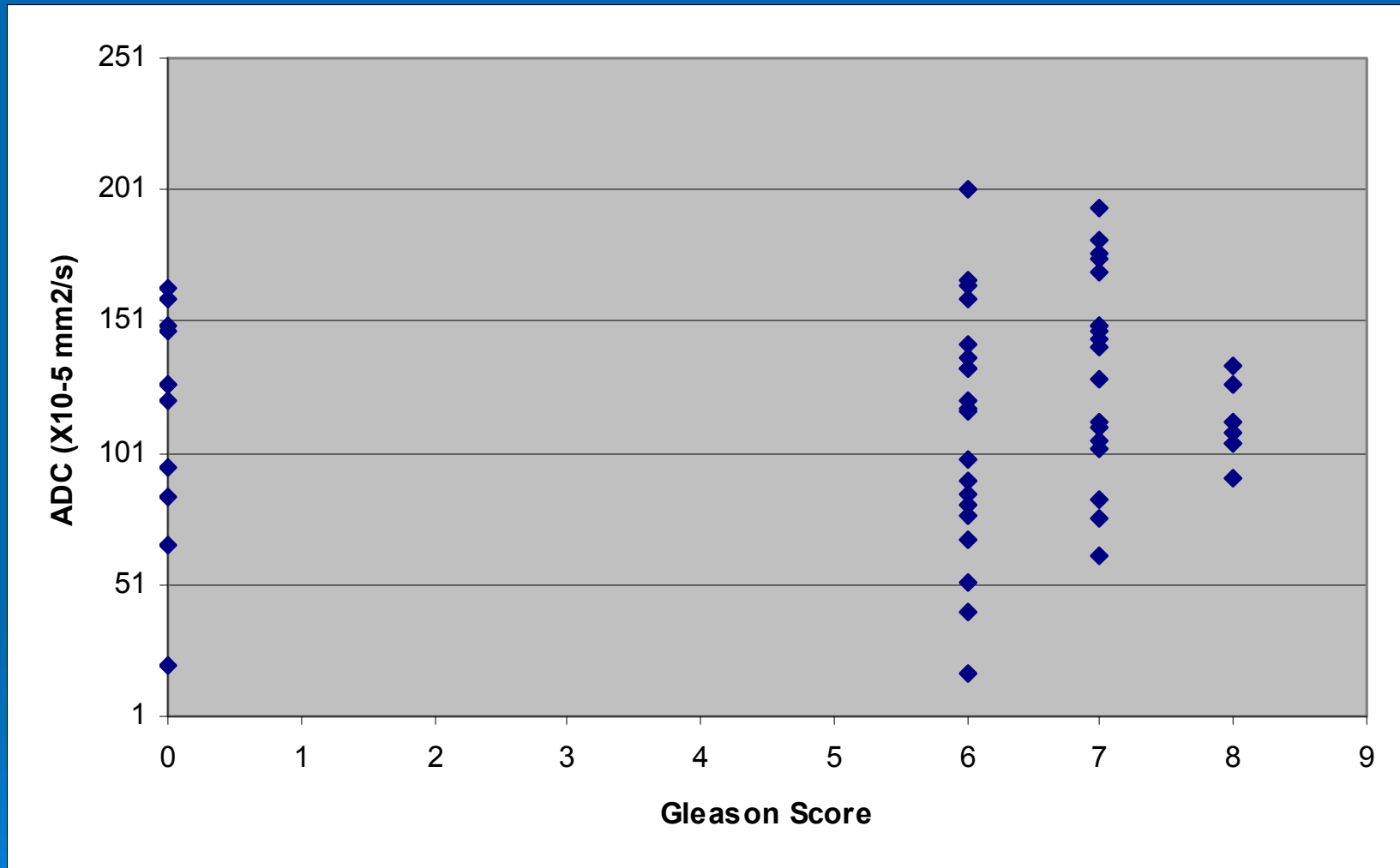
Individual parameter values from the 14 patients with lesions interrogated from 68 locations and 16 normal locations in the peripheral zone.

Results: Ktrans



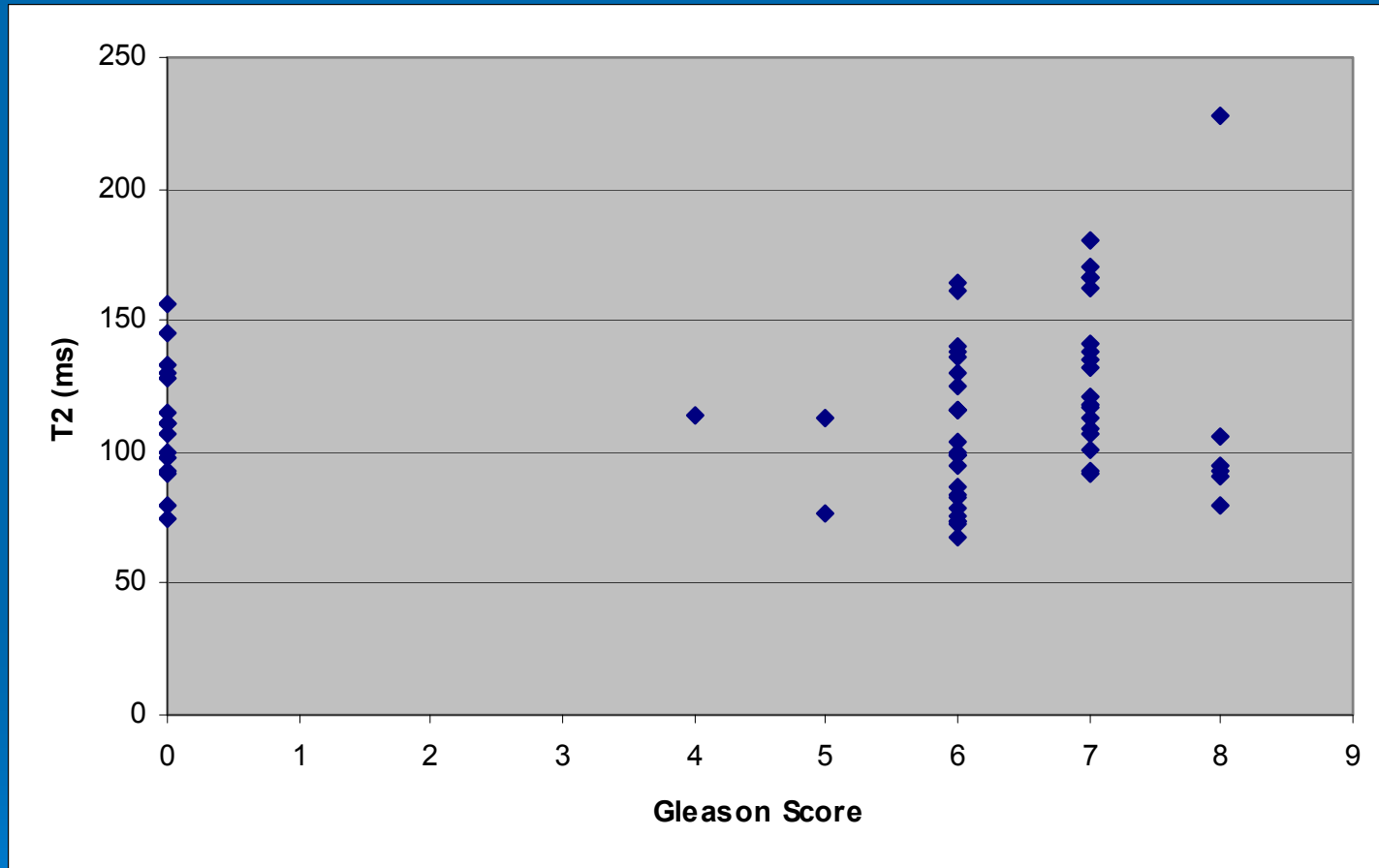
Ktrans is able to distinguish normal tissue from abnormal tissue. However, it is unable to distinguish the different grades of tumor within the peripheral zone. Normal regions are shown along Gleason Score of zero.

Results : ADC



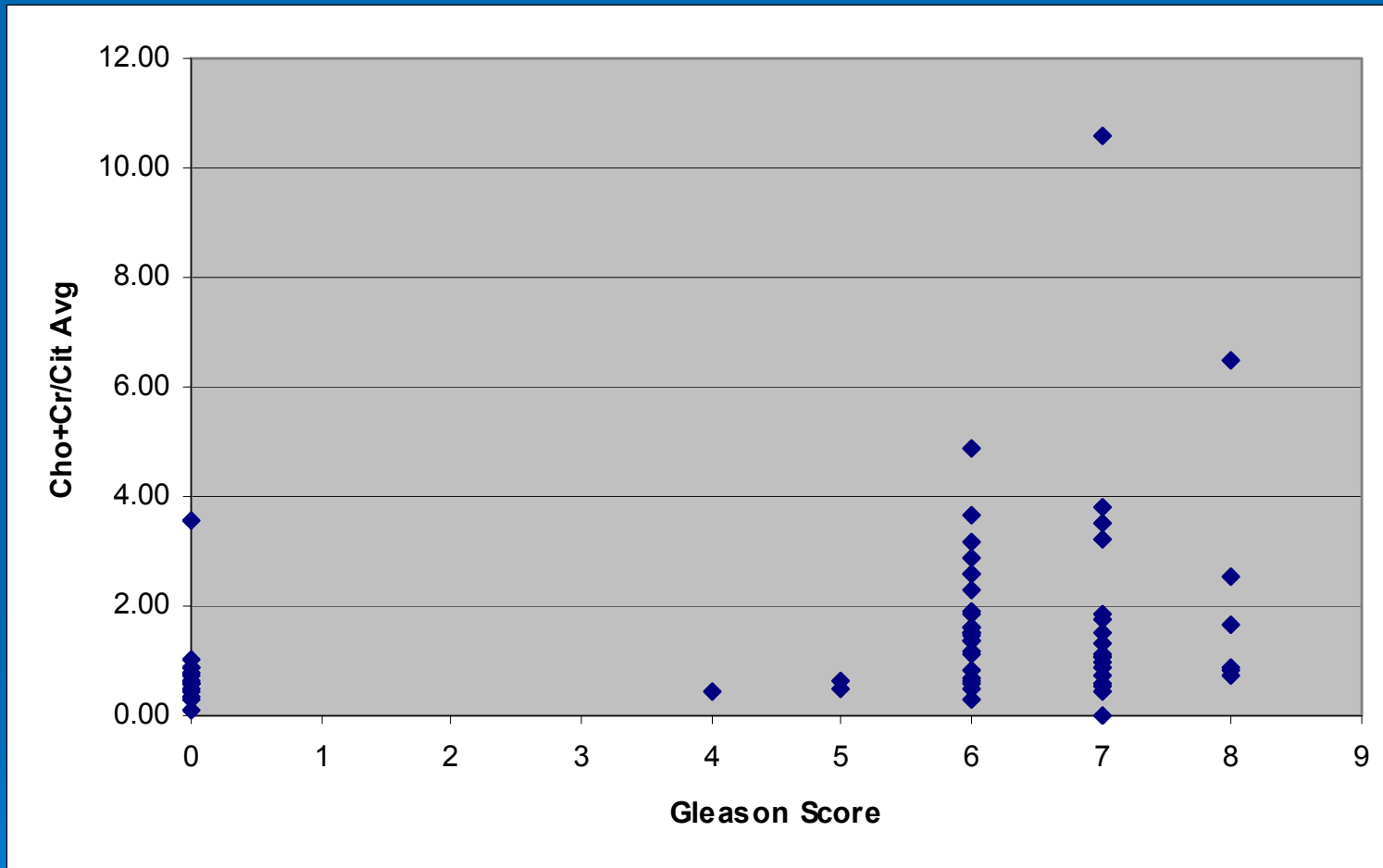
In our sample we could not find a significant difference in ADC between normal and abnormal tissue as determined by the pathologist. ADC values although we had a trend towards a lower ADC value in tumors.

Results : T2 Maps



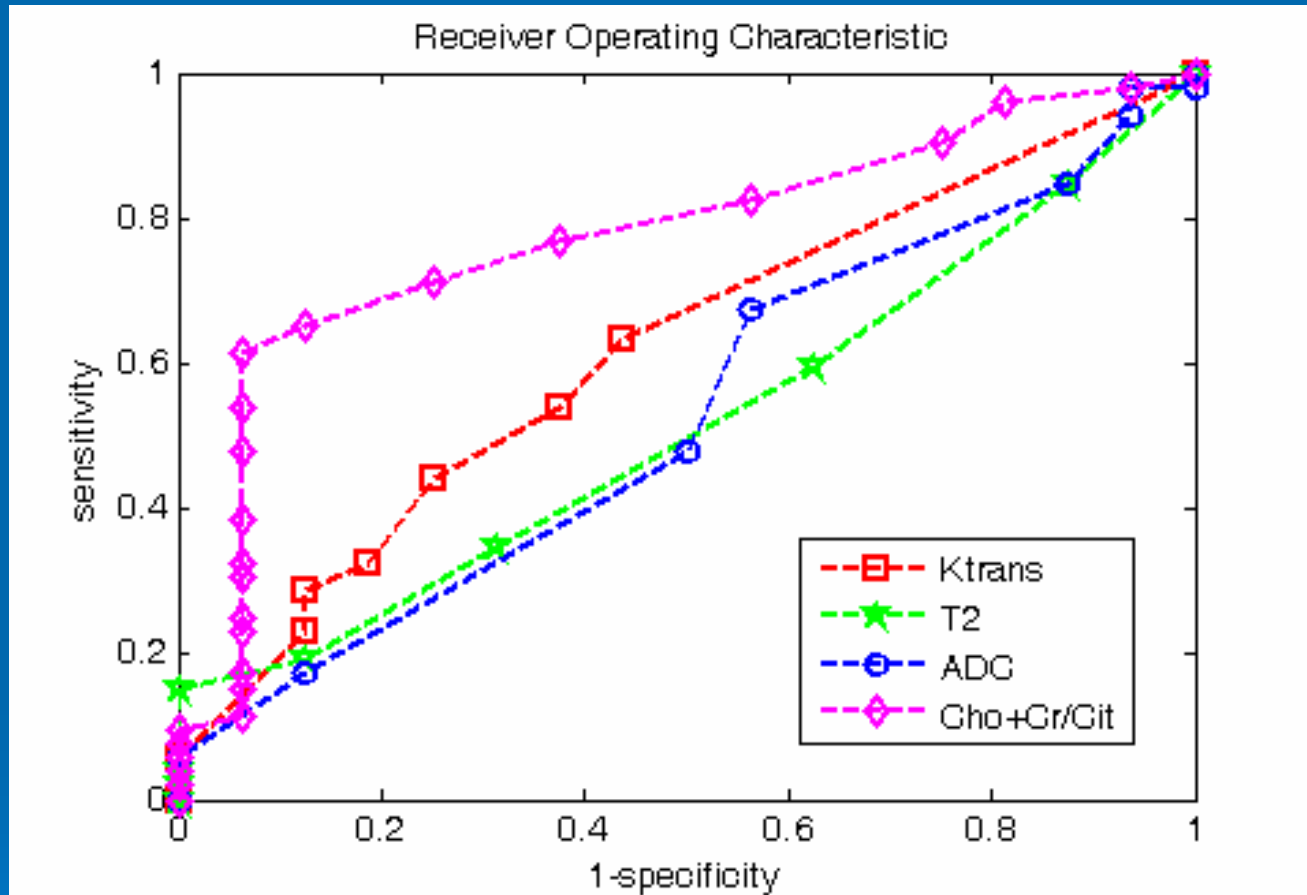
In our sample we could not find a significant difference in T2- values between normal and abnormal tissue as determined by the pathologist. A very feeble trend was seen towards a lowered T2 value in the tumor areas.

Results: Choline+Creatine/Citrate



Cho+Cr/Cit ratio is able to distinguish normal tissue from abnormal tissue. However, a trend towards higher Cho+Cr/Cit was seen with increasing tumor burden, like Ktrans it was unable to distinguish different grades of tumor within the peripheral zone. Normal regions are shown along Gleason Score of zero.

Receiver Operating Characteristic



ROC curve shows that spectroscopy has the highest sensitivity and specificity for detecting cancer in comparison to pathologists findings followed by perfusion scans. Both diffusion-weighted imaging and T2-maps had the least sensitivity and specificity. The area under the curve for Ktrans, T2, ADC and Cho+Cr/Cit are 0.65, 0.51, 0.54, and 0.79 respectively.

Summary

Based on our analysis, it appears that using appropriate thresholds for Cho+Cr/Cit and Ktrans one can differentiate tumor from normal tissue. The thresholds, corresponding sensitivity, specificity, positive and negative predictive values, and accuracy are listed in the table

	Threshold	Sensitivity	Specificity	PPV	NP V	ACC
MRSI (Cho+Cr/Cit)	0.9	0.68	0.85	0.95	0.45	0.72
DCE-MRI (K^{trans} , 1/min)	0.2	0.65	0.6	0.94	0.36	0.65

Conclusions

The preliminary results demonstrate that the multi-parametric MR imaging approach can improve the accuracy of prostate cancer detection.

Spectroscopic imaging had the highest sensitivity and specificity of The combination of each of the techniques increased the sensitivity and specificity of 0.68 and 0.85 respectively.

Sensitivity and specificity of perfusion scan was 0.65 and 0.6.

Results from diffusion weighted imaging and T2 map showed weak correlation with pathologists findings.

Analysis from a larger group of patients is underway to assess if the above conclusions hold true.

Magnetic Resonance Spectroscopic Imaging and Dynamic Contrast Enhanced Prostate MRI: Correlation with Histopathology

Bao Zhang¹, Steve Roys¹, Khan Siddiqui^{1,2},
Danielle Holanda³, John Papadimitriou³,
James Borin⁴; Harris Yfantis³
Michael Naslund⁴, Eliot Siegel^{1,2}
Anindya Roy⁵, Rao Gullapalli¹

¹Department of Radiology, University of Maryland Medical Center

²Department of Radiology, VA Maryland Health Care System


³Department of Pathology, University of Maryland Medical Center

⁴Department of Surgery, University of Maryland Medical Center

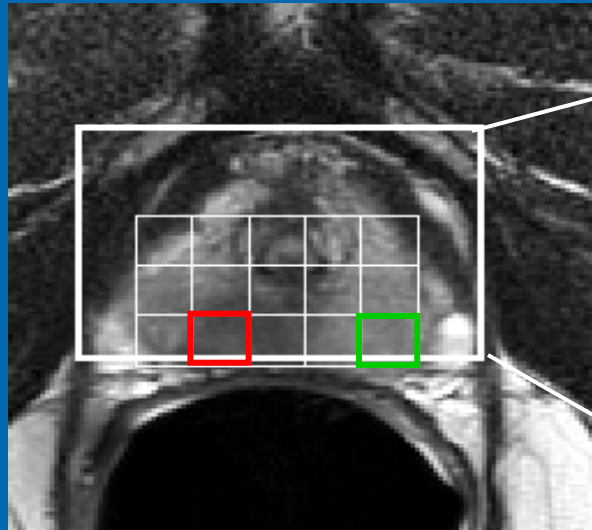
⁵Dept of Mathematics & Statistics, Univ of Maryland Baltimore County



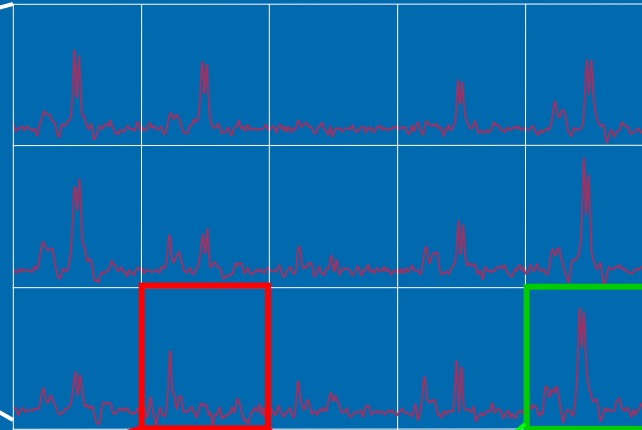
Objectives

- To verify the diagnostic accuracy of multi-parametric prostate MRI in comparison with whole mount histopathology using the following techniques
 - MR spectroscopic imaging
 - Dynamic contrast enhanced MRI
 - Diffusion weighted imaging
 - T2 relaxometry
- 
- The bottom right corner of the slide features a decorative graphic consisting of several concentric circles, resembling ripples in water, rendered in a lighter blue shade against the main blue background.

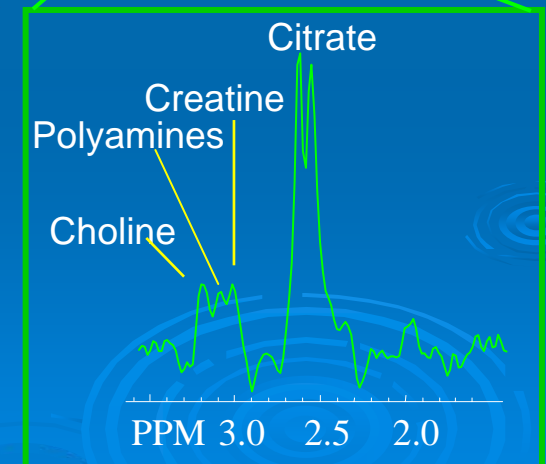
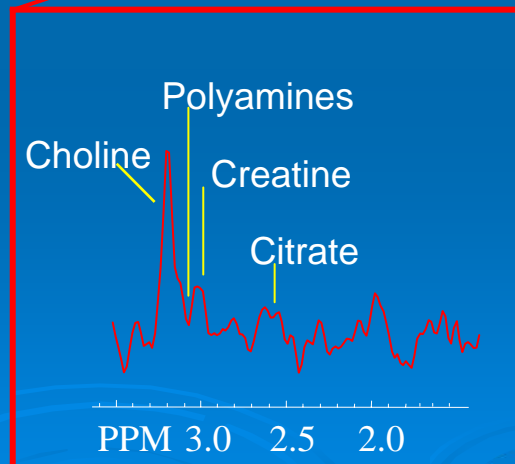
MR spectroscopic imaging



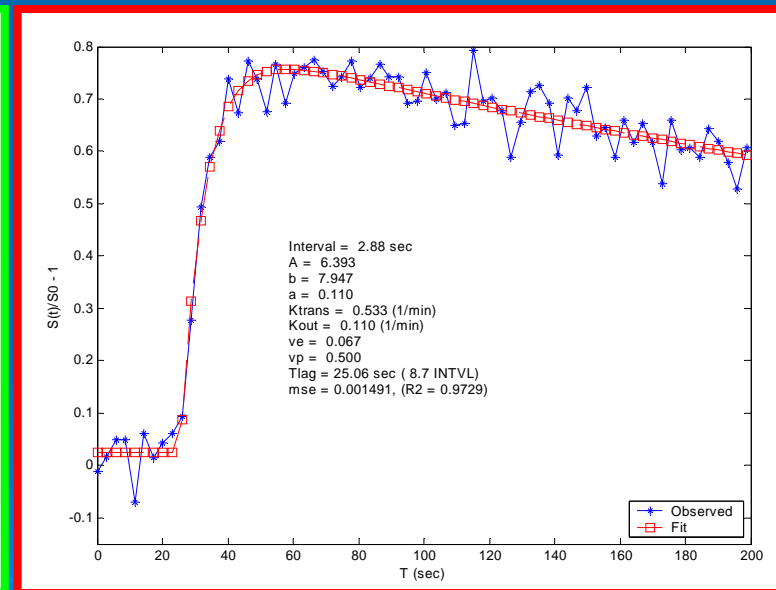
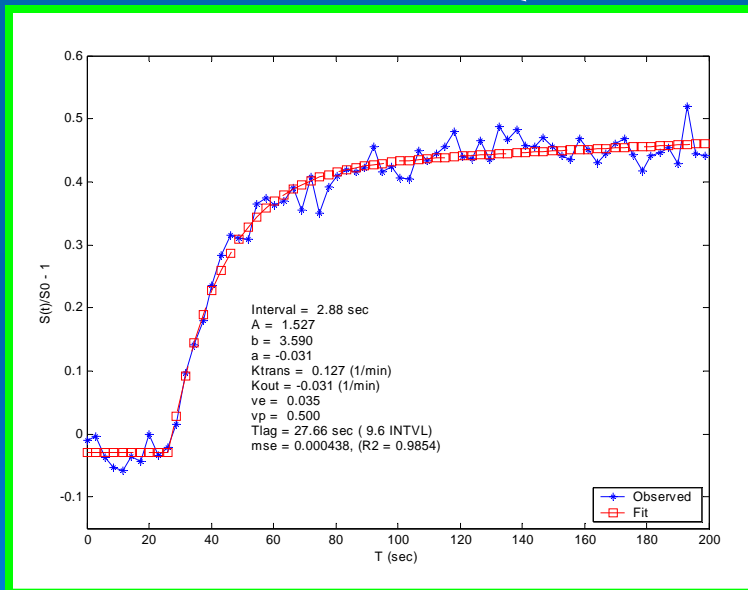
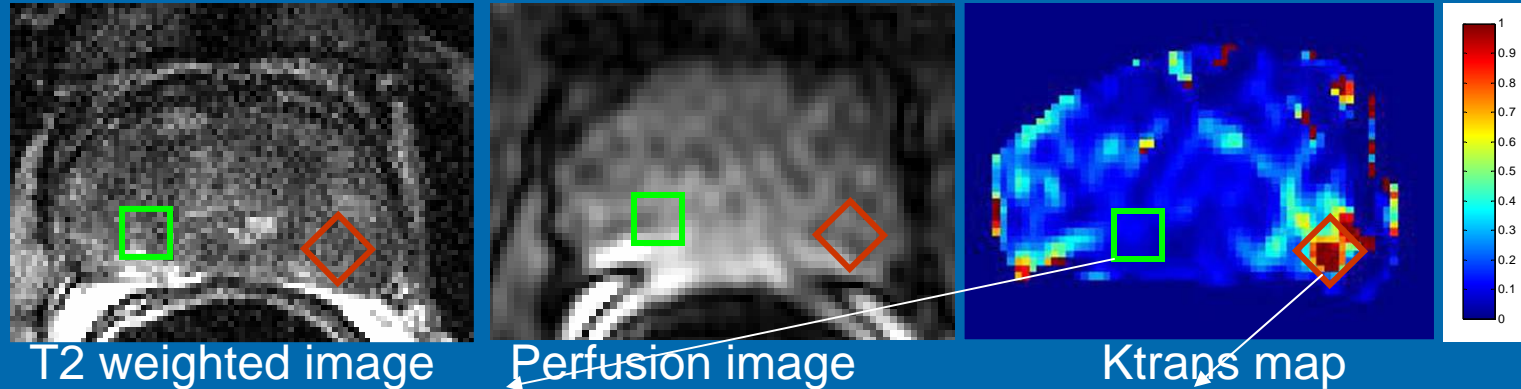
Portion of the 3-D MRSI spectral array



Prostate cancer can be discriminated from **healthy peripheral zone (PZ) tissue** based on a significant reduction in the levels of citrate and polyamines and an elevation in choline on MRSI.

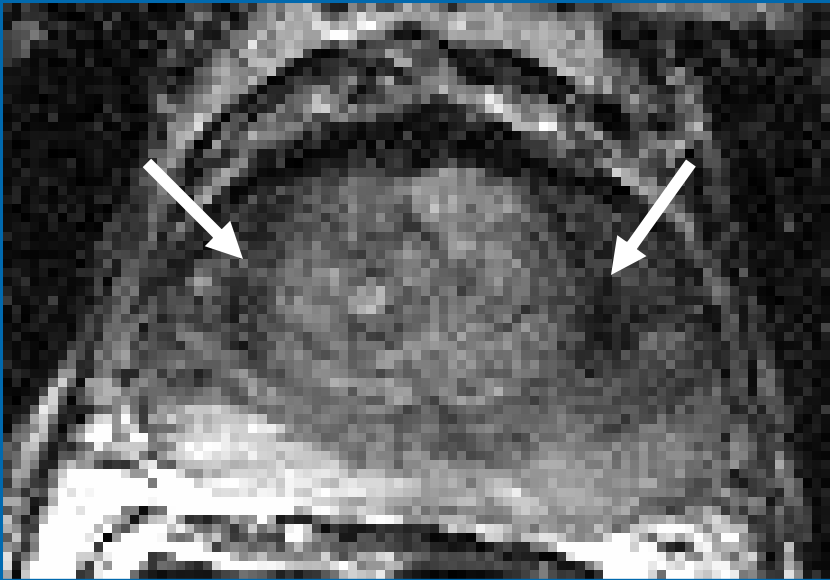


Dynamic contrast enhanced MRI

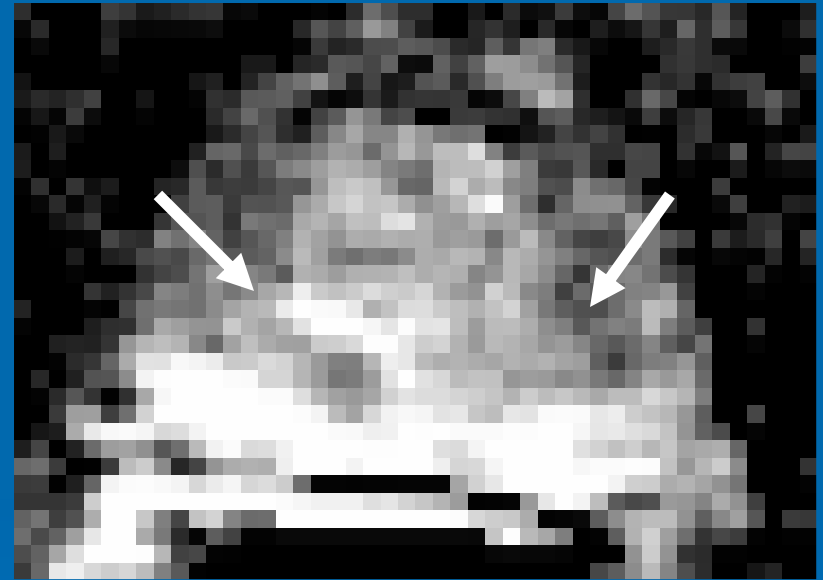


Tofts model was adopted for kinetic analysis to determine K_{trans}

Diffusion-weighted imaging



T2 weighted image

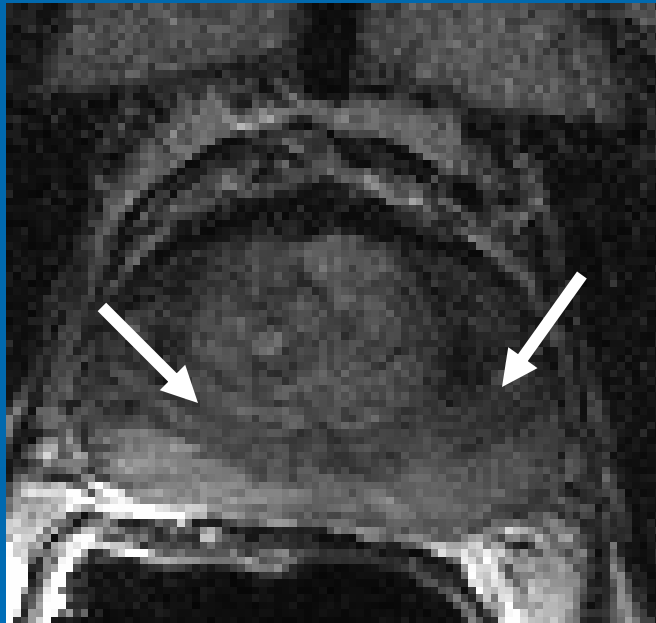


ADC map

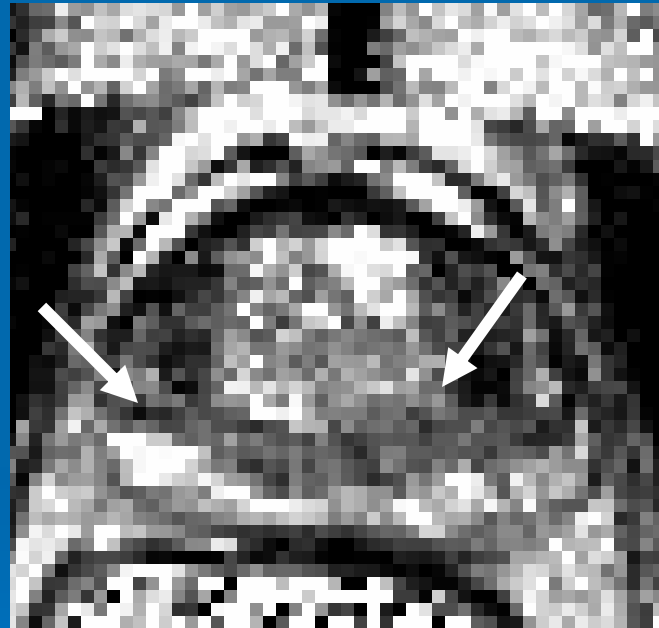
ADC map from DWI demonstrates tumor foci as area of decreased water diffusion in the peripheral zone.

T2 Maps

➤ CPMG sequence



T2 weighted image



Calculated T2 map

T2 map showing cancerous regions with lower T2 values

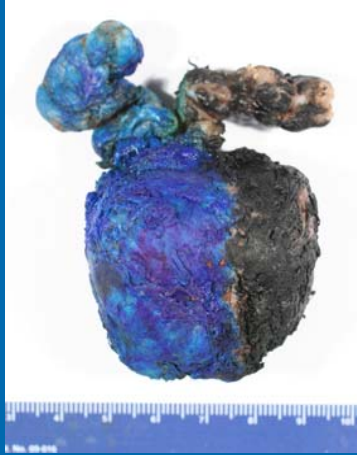
Subjects

- 14 patients with biopsy proven prostate cancer
 - Age: 42-73, mean 58 ± 8 yrs
 - PSA: 0.5-29 ng/ml mean 9.4
 - Gleason Score: 4-8,
 - All patients had MRI at least 4 weeks after biopsy.
 - One subject was recruited post radiation.
 - Patients went to surgery within three weeks following their MRI procedure
 - Informed consent approved by Internal Review Board was obtained from all patients

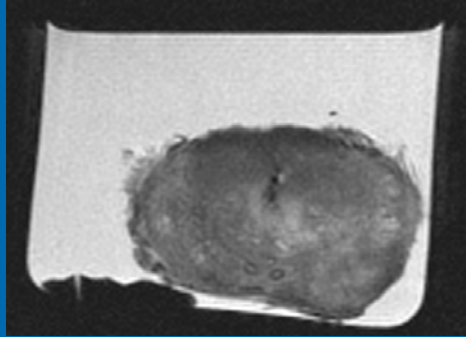
In vivo MRI data acquisition

- Siemens 1.5T Avanto with 18 channels
- Endorectal coil from Medrad
- Protocol
 - T1-weighted (3mm slices no gap)
 - T2 weighted (3mm slices no gap)
 - T2 relaxometry imaging
 - TE 10-80ms every 10ms; 3mm slices
 - Diffusion weighted imaging
 - $b=1000\text{s/mm}^2$; 3mm slices
 - Perfusion weighted imaging
 - 0.1 mmol/kg Gad; 6mm slice; temp res 3 s; 70 frames
 - MR spectroscopy imaging
 - 3D PRESS 16x16x12 ($6\times6\times6\text{ mm}^3$); TE 120ms; weighted av; OVS

Histopathology



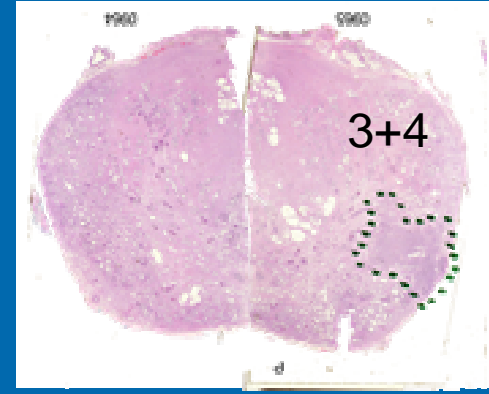
Prostate Specimen



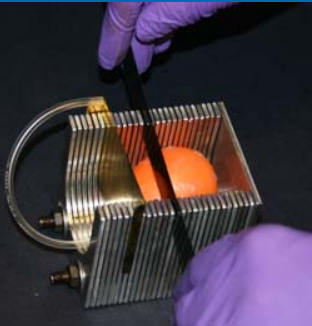
ex vivo image



Individual 3mm section



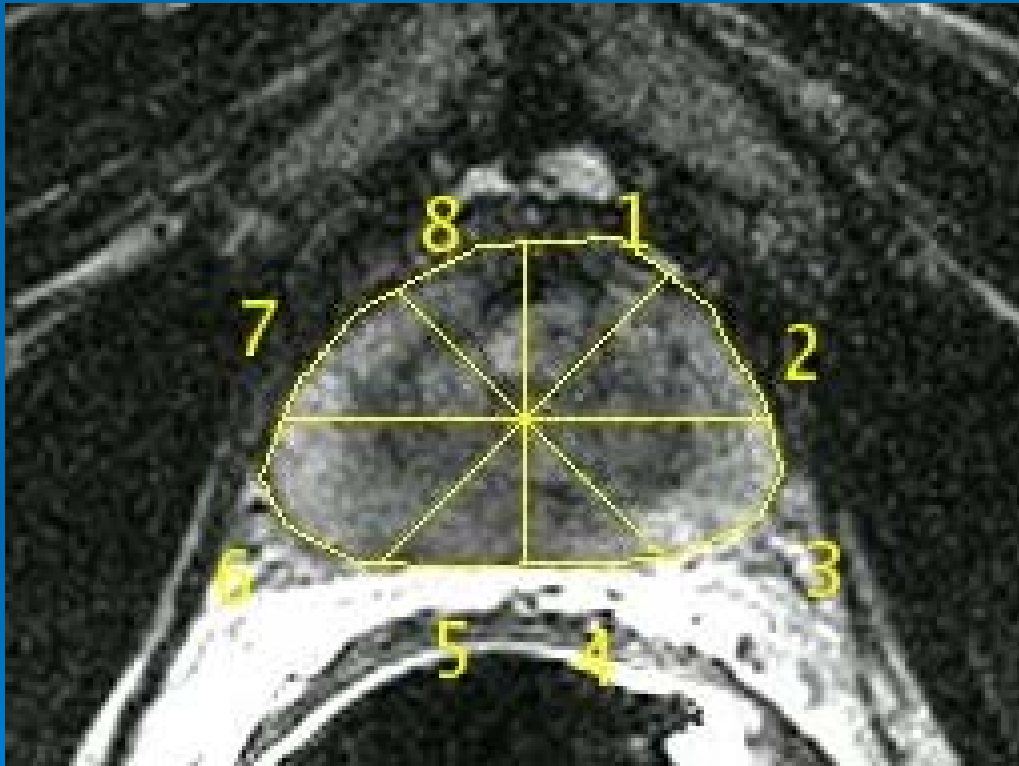
Histology slide



Prostate Slicer

- A prostate slicer was designed to facilitate prostate sectioning.
- The excised prostate was color coded to differentiate its orientation.
- Uniform 3 mm parallel slices were then cut followed by 50 micron sections from each of the slices for H&E staining.
- On each of the slides the pathologist marked regions of cancer along with their Gleason Score.

Data Analysis



-Octants were hand drawn on each of the slice.

-From each octant mean values were derived along with their histogram values

-A total of 748 octants were examined.

-After careful examination for image quality the number of octants reduced to 418 octants which were used in the final analysis.

Scoring Methodology

➤ Radiology score

- Consensus Yes/No for cancer by 2 radiologists
- Indicate confidence level for each score
- Neurovascular involvement
- Seminal vesicle invasion
- Extracapsular invasion

➤ Mean ADC scores

➤ Mean T2 value

➤ Mean K_{trans}

Scoring Methodology

➤ Spectroscopy

The likelihood of tumor presence was encoded using a 5 point rating scale based on Cho+Cr/Cit ratio

1=definitely healthy

2=probably healthy

3=equivocal

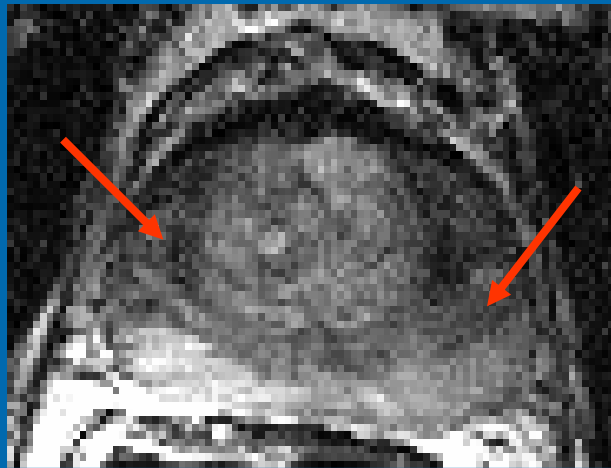
4=probably cancer

5=definitely cancer

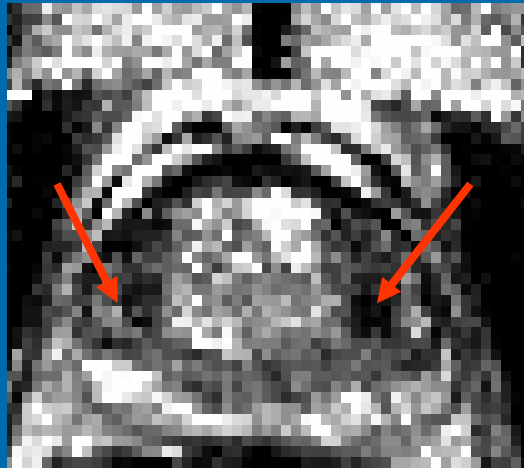
Statistical Analysis

- Dichotomized histology at Gleason Score of 5 & 6
- Logistic regression of binary histology scores based on individual technique scores
- ROC curves based on thresholded predictive probabilities obtained from logistic regression
- All analysis was performed using PROC Logistic under SAS v9.1

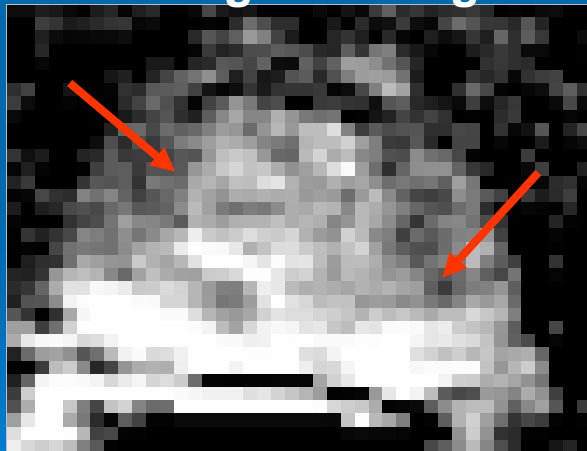
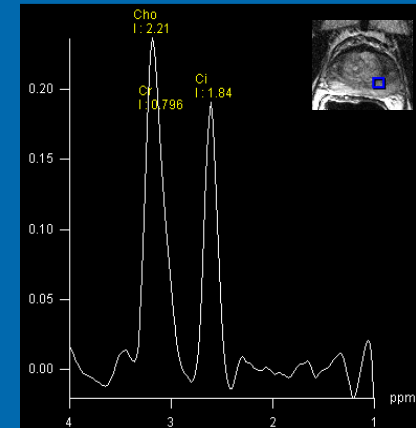
Example 1: Patient with multifocal cancer and prostatitis. Age 59, PSA 5.9 ng/l, Gleason 6



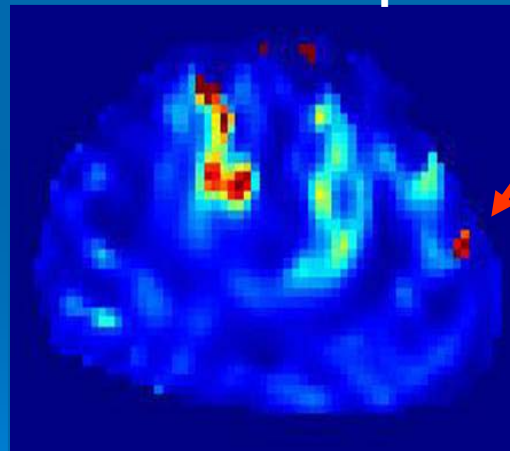
T2-weighted image



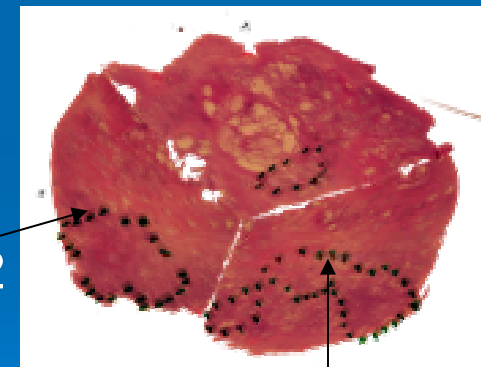
T2-map



ADC Image



k_{trans} -map

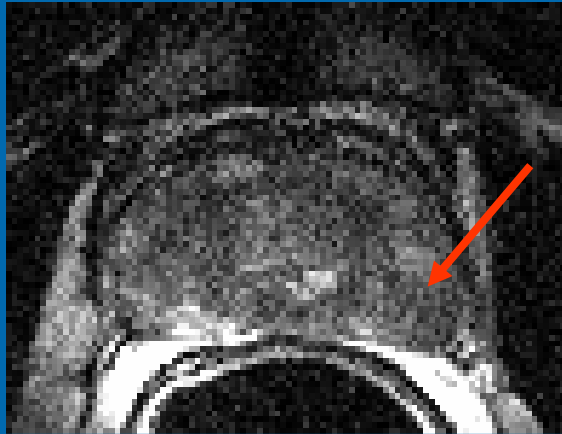


3+2

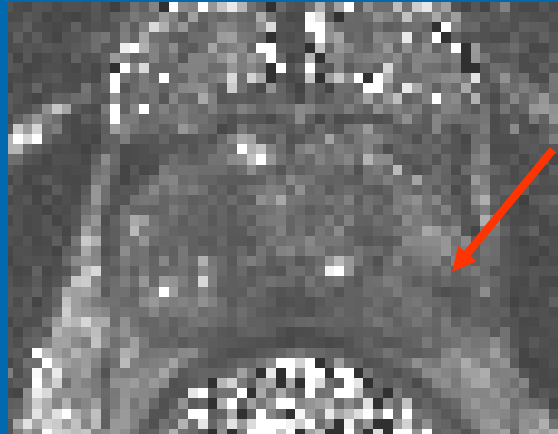
3+4

E

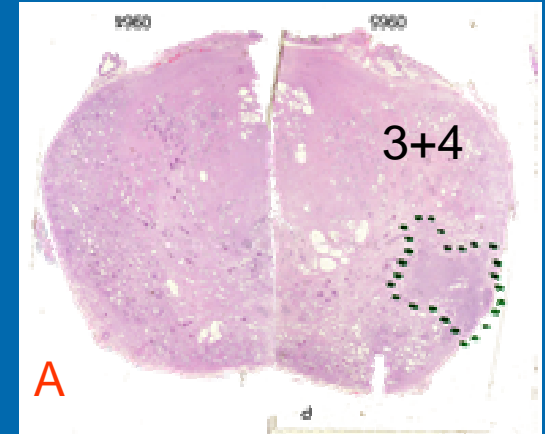
Example 2: Focal Tumor with Extracapsular extension, Age 44, PSA 6.7 ng/L, Gleason 6



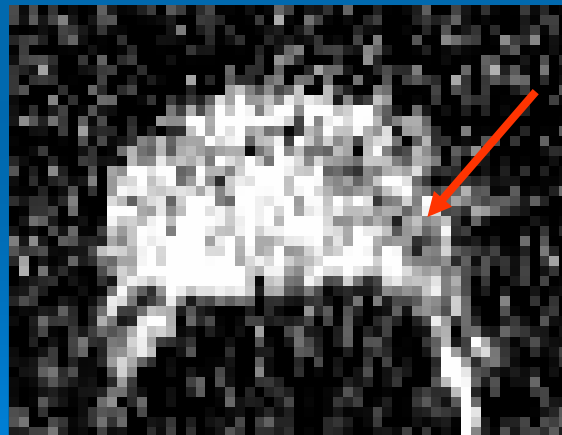
T2-weighted image



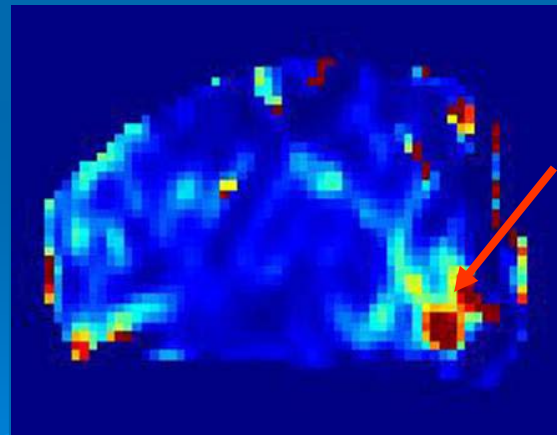
T2-map



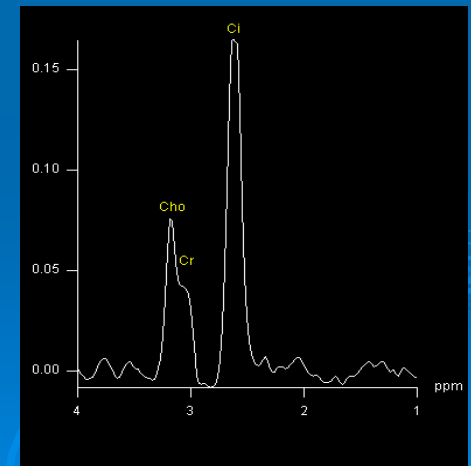
A



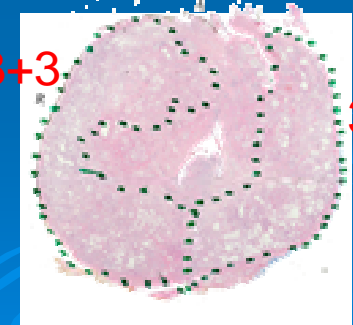
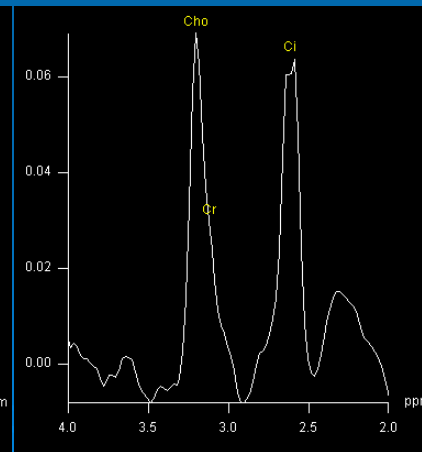
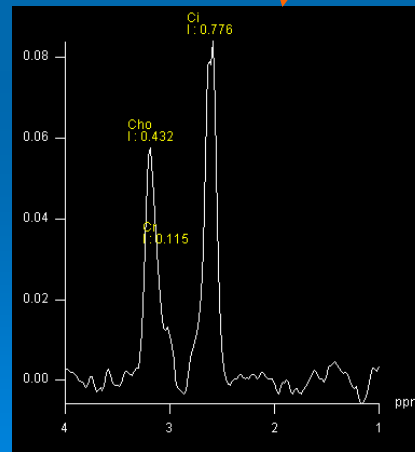
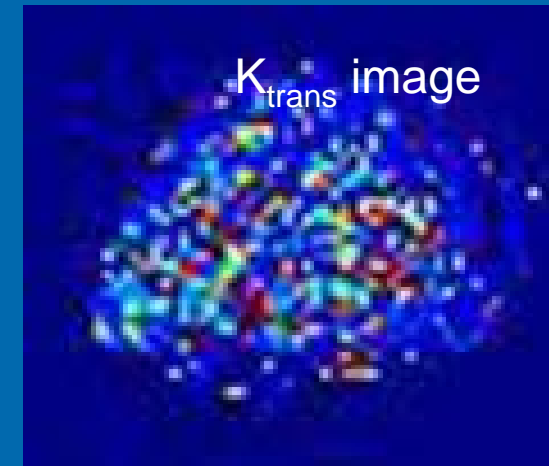
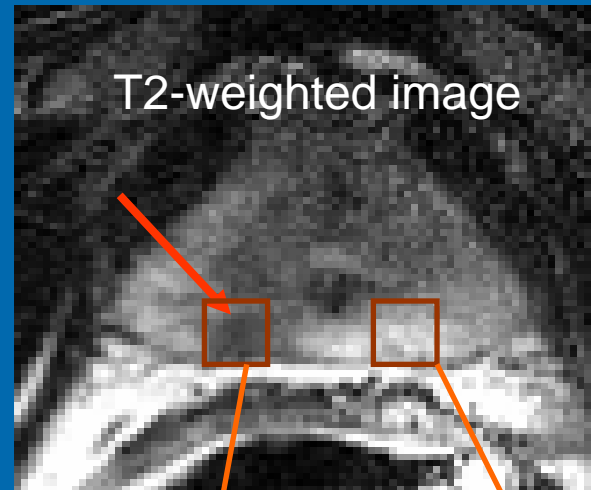
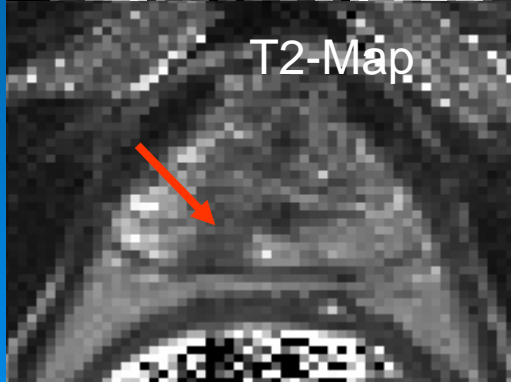
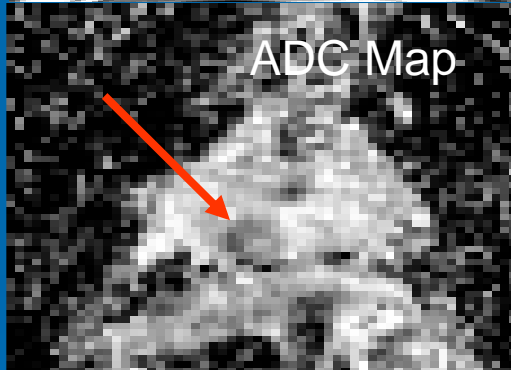
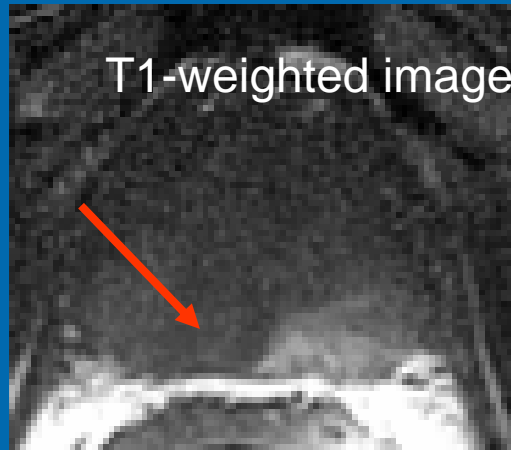
ADC Image



k_{trans} -map



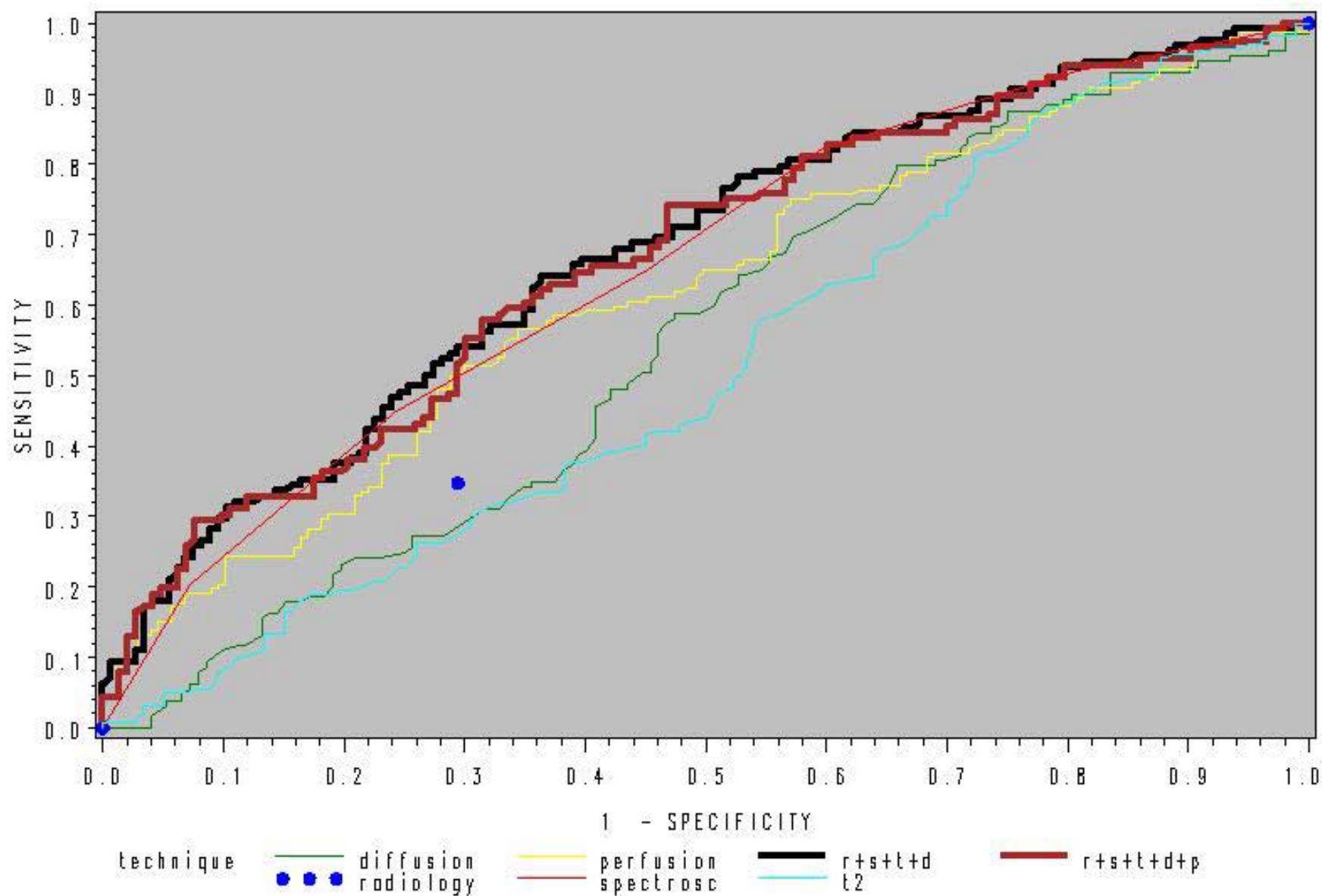
Example 3: Case of Diffuse prostate cancer, Age 61, PSA 5.4, Gleason 6



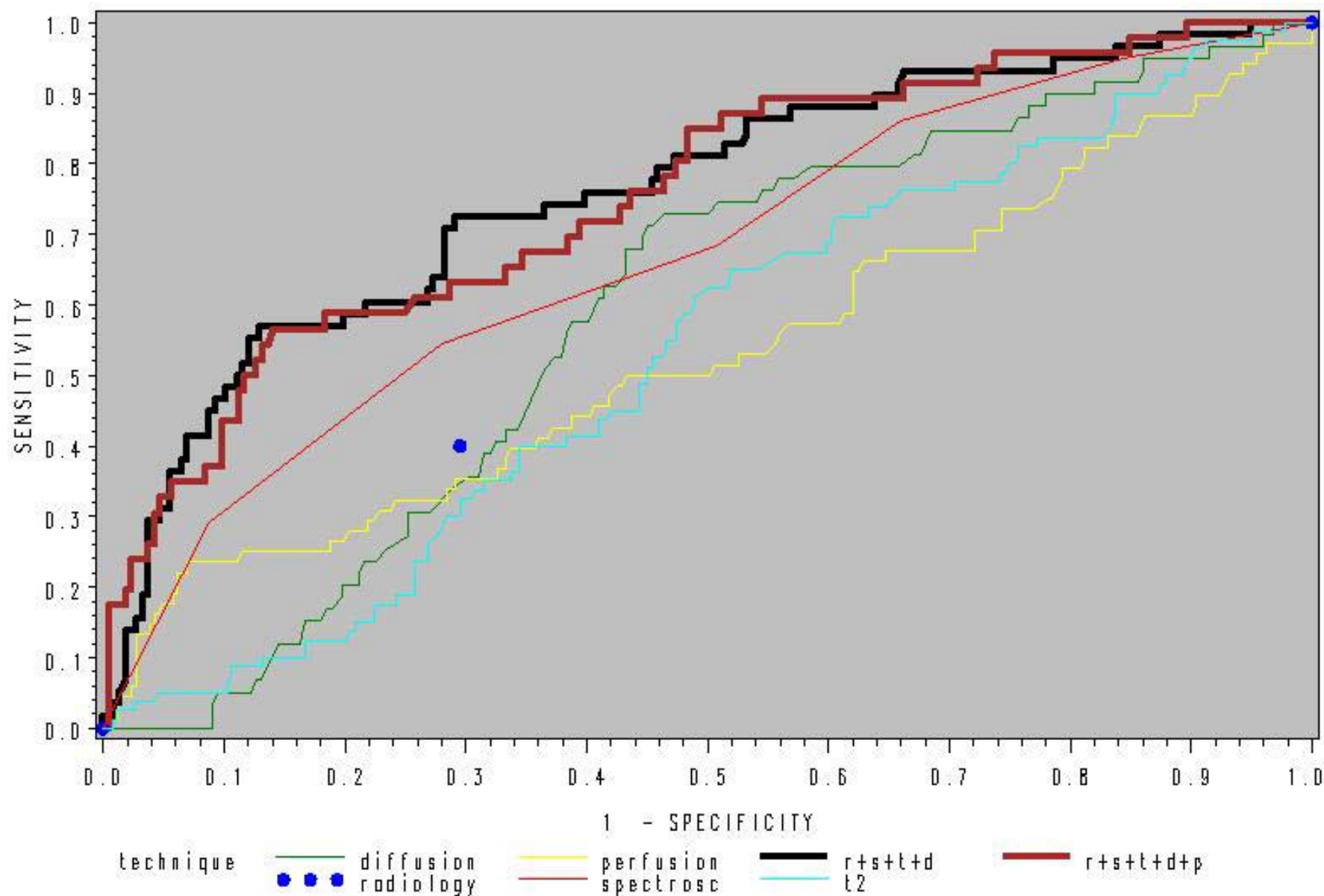
3+3

3+4

ROC Curves (Hist > 5): Individual vs Combined Techniques



ROC Curves (Hist > 6): Individual vs Combined Techinques



Summary

- Overall accuracy increased from 55% to 80% for the combined use of information from the different techniques compared to radiologist read alone.
- At high specificity spectroscopy and perfusion contributed to the overall accuracy.
- At moderate specificity spectroscopy and diffusion contribute to the overall accuracy.
- For combined model we obtain 60% sensitivity at 80% specificity where as the individual techniques have 40% (spectroscopy), 28% (perfusion) 22%(diffusion) and 20%(t2) sensitivity
- Spectroscopic score had a significant correlation (0.34; $p < 0.0001$) with pathologists findings

Conclusions

The preliminary results demonstrated that the multi-parametric MR imaging approach can improve the accuracy of prostate cancer detection.

Combined use of techniques was significantly more sensitive to presence of tumor than any individual technique at all specificity levels.

Spectroscopic imaging had the highest sensitivity and specificity among all techniques.

Ktrans maps showed high specificity at high Gleason scores.

Results from diffusion weighted imaging and T2 map showed weak correlation with pathologists findings.

Analysis from a larger group of patients is underway to assess if the above conclusions hold true.

Thank You!





IMPROVED DETECTION OF PROSTATE CANCER USING MULTI-PARAMETRIC MAGNETIC RESONANCE IMAGING (MRI): CORRELATION OF *IN VIVO* AND *EX VIVO* SCANS WITH WHOLE MOUNT HISTOLOGICAL SECTIONS

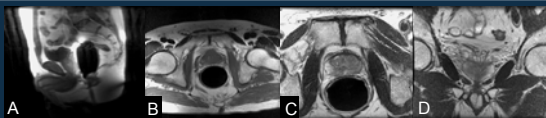
James F. Borin¹, Bao Zhang², Khan Siddiqui², John Papadimitriou³, Harris Yfantis³, Danniele Holanda³, Steven Roys², Michael Naslund¹, Michael Phelan¹, Andrew Kramer¹, Rao Gullapalli²

University of Maryland, Baltimore, MD, USA; ¹Division of Urology, ²Department of Radiology, ³Department of Pathology

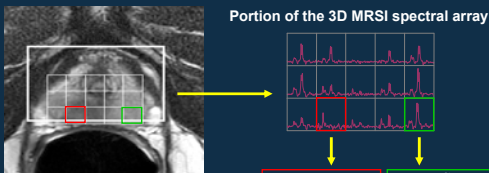
(Supported by a grant from the Department of Defense, Proposal No. PC031042, Award No. W81XWH-04-1-0249)

INTRODUCTION: We performed magnetic resonance spectroscopy imaging (MRSI), perfusion weighted imaging, and T2 mapping along with traditional T2-weighted MR image acquisition on patients prior to radical prostatectomy and compared the results with *ex vivo* scans and whole mount histopathology.

METHODS: 13 men with prostate cancer (T1c=69%, cT2=31%) who elected radical prostatectomy were enrolled. *In vivo* data acquisition was conducted on a 1.5 Tesla scanner using an endorectal coil prior to and after a 20 ml bolus of gadolinium. The *ex vivo* prostate was imaged again following surgery, then fixed in formalin and sectioned in 3 mm axial slices. *In vivo* and *ex vivo* MR images were aligned and compared with the individual hematoxylin and eosin stained slices of the prostate.



A. Sagittal localizer to assess coil position. B. T₂ weighted Axial - assess biopsy artifact, lymph nodes and bone. T₂ Axial (C) and Coronal (D) Images - assess cancer location and stage.



Prostate cancer can be discriminated from healthy peripheral zone tissue based on low signal intensity on T2 weighted MRI and a significant reduction in the levels of citrate and polyamines combined with an elevation in choline on MRSI. The strength of the test is when MRI and MRSI results are concordant for cancer.

RESULTS: Mean age = 55 y (44-67), PSA = 9.4 ng/ml (0.5-29). Gleason scores were 6 (62%) or 7 (38%). Cancer loci > 10 mm³ were well delineated by the T2 map. Kinetic perfusion maps (figure 1) revealed a significant difference between normal and abnormal tissue (p<0.001). Neither map was sensitive to changes in tumor grade between cancer loci. MR spectroscopy had high sensitivity and correlated well with the histological sections for lesions > 0.2 mm³. The combination of imaging techniques significantly improved sensitivity and specificity for detection of prostate cancer compared to standard MRI findings (90% and 89% vs. 72% & 80%).

RESULTS:

Patient #1: age 57, PSA 5.9, Gleason 3+3=6, clinical T1c, pT2c

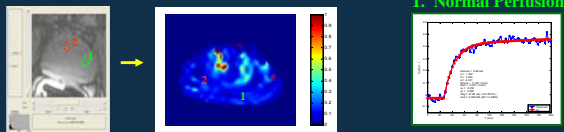
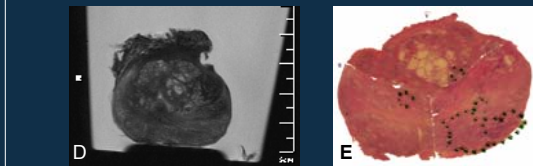
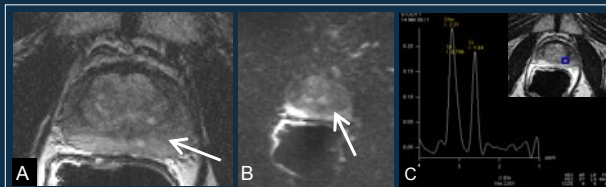
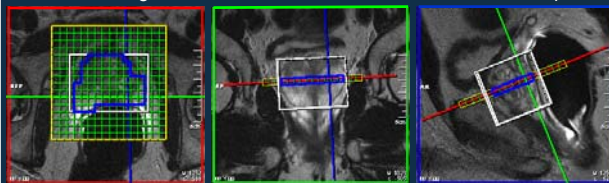


Figure 1. Kinetic Perfusion (K_{Trans}) Map demonstrating normal and cancerous loci. Concentration-time curves 1 & 2 demonstrate normal and abnormal perfusion, respectively, following a bolus of gadolinium.

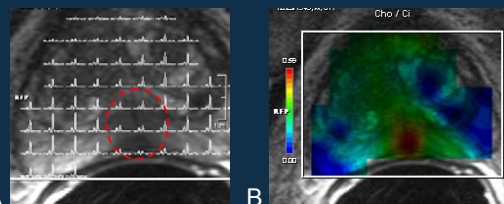


Patient #1, different slice. An area of hypointensity (arrow) on T2 weighted (A) and diffusion weighted (B) images corresponded to an abnormal choline+creatine: citrate ratio (C). *Ex vivo* images (D) were used to help correlate *in vivo* images with histopathology (E), which, in this case, demonstrated several foci of Gleason 3 prostate cancer.

Patient #8: age 61, PSA 13.15, Gleason 3+4=7, clinical T1c, pT3b



Axial, coronal, and sagittal T2 images with spectroscopic grid overlays. Each 3D voxel is .216 cm³ (0.6 x 0.6 x 0.6 cm).

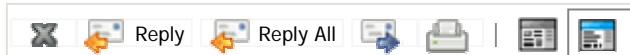


A. MR spectra from each voxel superimposed on an axial image. B. A color map of the ratio of choline+creatine: citrate demonstrates an abnormality (solid red) which corresponds to the area of low signal intensity seen on the T2-weighted image (red dashed line). These two imaging techniques combine to provide a highly concordant localization of prostate cancer.

CONCLUSION: These preliminary results demonstrate that a multi-parametric MRI approach can improve the accuracy of prostate cancer detection and may aid in preoperative planning.

Mail Message

N



Mail

From: <jhoneyman@siimweb.org> Saturday - February 13, 2010 4:57 PM
To: <sroys@umm.edu>
CC: <jdi@siimweb.org>
Subject: Journal of Digital Imaging - JDI-09-12-0161
Attachments: Mime.822 (8 KB) [\[View\]](#) [\[Save As\]](#)

Dear Mr. Steven Roys,

I am pleased to inform you that your manuscript, "THREE-DIMENSIONAL ELASTIC IMAGE REGISTRATION BASED ON STRAIN ENERGY MINIMIZATION: APPLICATION TO PROSTATE MAGNETIC RESONANCE IMAGING" will be accepted for publication in the Journal of Digital Imaging with a few minor revisions described below.

After your revisions are made, please submit your revision online at Manuscript Central; detailed instructions and additional required information are described below:

INSTRUCTIONS FOR AUTHORS:

Authors have 30 days to submit revisions online.

To submit a revision:

- Log into JDI Manuscript Central (<https://mc.manuscriptcentral.com/jdi>)
- Click on "Submitting Author Center"
- Select the "Manuscript With Decisions" link
- Locate the manuscript



**THREE-DIMENSIONAL ELASTIC IMAGE REGISTRATION
BASED ON STRAIN ENERGY MINIMIZATION: APPLICATION
TO PROSTATE MAGNETIC RESONANCE IMAGING**

Journal:	<i>Journal of Digital Imaging</i>
Manuscript ID:	JDI-09-12-0161.R1
Manuscript Type:	Hypothesis-Driven Research
Keywords:	3D Imaging (Imaging, Three-Dimensional), Algorithms, Image Registration
Additional Keywords:	



THREE-DIMENSIONAL ELASTIC IMAGE REGISTRATION BASED ON STRAIN ENERGY
MINIMIZATION: APPLICATION TO PROSTATE MAGNETIC RESONANCE IMAGING

Bao Zhang^{1,2}, Dwayne D Arola², Steven Roys,¹ Rao P. Gullapalli¹ *

¹Magnetic Resonance Research Center, Department of Diagnostic Radiology, University of
Maryland School of Medicine,., Baltimore Maryland, USA 21201

²Department of Mechanical Engineering, University of Maryland Baltimore County, Catonsville,
MD, USA 21250

* Corresponding author

Rao P. Gullapalli, PhD

Magnetic Resonance Research Center

Department of Diagnostic Radiology

University of Maryland School of Medicine

22 South Greene St.

Baltimore Maryland, USA 21201

Phone: (01)410-328-2099

Fax: (01)410-328-5937

E-mail: rgullapalli@umm.edu

1
2
3 **1. INTRODUCTION**
4
5
6

7 The use of magnetic resonance imaging (MRI) in the staging and follow-up of patients
8 with prostate cancer (PCa) has been steadily increasing, and MRI has been used for preoperative
9 evaluation, cancer staging, and image guidance for prostate interventions (Sanchez-Chapado et
10 al., 1997; Futterer et al., 2007; Susil et al., 2004; Nguyen et al., 2007). Magnetic resonance
11 imaging in conjunction with endorectal coil and MR spectroscopy (MRS) has been shown to
12 further improve the sensitivity and specificity of cancer detection, providing high-quality images
13 with nearly a 10-fold signal-to-noise improvement over body phased-array coils (Schnall et al.,
14 1991; Husband et al., 1998; D’Amico et al., 1998). Although rigid endorectal probes are available,
15 the most popular endorectal probe uses a balloon. This device involves the insertion of the
16 endorectal coil in the rectum followed by inflation of the balloon that covers the coil to about 40 ~
17 60 cc of air while ensuring that the coil face is against the posterior portion of the prostate gland.
18 This procedure secures the prostate gland between the coil and pubic bone and ensures that the
19 gland itself does not move during the imaging procedure. However, this technique results in
20 images with significant distortion. For image-guided interventions such as external-beam therapy
21 or brachytherapy, such distortions must be taken into account before an effective treatment plan
22 can be generated.
23
24

25 Several investigators have proposed both rigid and nonrigid registration to correct for
26 prostate image distortion introduced by the endorectal coil. Rigid body registration deals with the
27 translation and rotation of images (Dubois et al., 2001; Fei et al., 2002). The underlying global
28 transformation is expressed in terms of a finite number of parameters (i.e., 3 parameters each for
29 translation, rotation, scaling, and shear). Under certain circumstances, however, these global
30 transformations are inadequate to describe the transformation, especially in the case of highly
31 localized deformation. This has led to the development of nonrigid registration techniques. The 2
32 general transformation functions employed in nonrigid registration that delineate the local
33 distortion are polynomials (Wu et al., 2004) and thin-plate splines (TPS) (Venugopal et al., 2005;
34 Lian et al., 2004; Fei et al., 2003). The coefficients of the polynomial and the TPS functions are
35
36
37
38
39
40
41
42
43
44
45
46
47
48
49
50
51
52
53
54
55
56
57
58
59
60

obtained by maximizing the cost functions using normalized cross correlation (NCC) or mutual information (Fei et al., 2003).

Other nonrigid registration methods provide transformations that are solutions to the governing equations based on the physical model used. These methods include elastic registration (Broit, 1981; Davatzikos et al., 1996; Gee et al., 1997; Peckar et al., 1999), fluid registration (Christensen et al., 1996), diffusion-based registration (Thirion, 1998), and optical flow-based registration (Beuchemin and Barron, 1995). Among these registration methods, elastic registration is of particular interest in prostate imaging because it appropriately models the prostate as a 3D, incompressible elastic object.

Here we present a novel elastic registration algorithm that is based on strain energy minimization. Rather than computing the forces and solving the force-balance equations for deformation as demonstrated by many investigators, the proposed registration algorithm derives the deformation using the strain energy minimization technique. Results from this algorithm are presented on simulated digital images, prostate phantom images, and images obtained from patients who underwent prostate MR imaging using the endorectal coil.

2. MATERIALS AND METHODS

2.1 Theory of Strain Energy Minimization

According to the principles of dynamics, the potential energy function has a stationary value if the system is conservative and is in equilibrium. This implies that when the system is stable, the potential energy function is at a minimum (Greenwood 1997). This theorem has broad applications in engineering in determining the deformation, stress, and strain distributions of a static system. This theorem forms the basis in deriving the transformation matrix to align endorectal coil based images before and after distortion.

FIGURE1

Treating the prostate as an elastic body, the potential energy of the system at static equilibrium is purely the strain energy U , as defined in the following expression (Ugural and Fenster, 1995):

$$U = \iiint_{\Omega} \frac{1}{2} \left[\lambda e^2 + 2\mu(\varepsilon_x^2 + \varepsilon_y^2 + \varepsilon_z^2) + \mu(\gamma_{xy}^2 + \gamma_{yz}^2 + \gamma_{xz}^2) \right] d\Omega \quad (1)$$

where, λ and μ are two Lamé constants characterizing material constitutive properties, μ is the shear modulus of the material characterizing the rigidity, λ is an engineering constant that describes the effects of dilatation based on tensile stress, ε_p ($p = x, y$ or z) is the normal strain in p direction, γ_{pq} ($pq = xy, yz$, or xz) is the shear strain in the p plane pointing toward q , e is the unit volume change, and Ω is the prostate volume (Fig. 1).

Krouskop et al. (1998) determined the Poisson's ratio of prostate tissue to be 0.495, this was also confirmed by Read's study (Read et al., 2001). Given this the first term λe^2 in Eq. (1) can be ignored since it is two orders of magnitude lower than the other two terms (see appendix 1). Thus the above equation is simplified to:

$$U = \mu \iiint_{\Omega} \left[(\varepsilon_x^2 + \varepsilon_y^2 + \varepsilon_z^2) + \frac{1}{2}(\gamma_{xy}^2 + \gamma_{yz}^2 + \gamma_{xz}^2) \right] d\Omega \quad (2)$$

Based on the strain–displacement relationship (Ugural and Fenster, 1995), this equation can be rewritten in terms of displacement (position change of a point) in the Cartesian coordinate system as:

$$U = \mu \iiint \left[\left(\frac{\partial u}{\partial x} \right)^2 + \left(\frac{\partial v}{\partial y} \right)^2 + \left(\frac{\partial w}{\partial z} \right)^2 \right] dx dy dz + \frac{1}{2} \mu \iiint \left[\left(\frac{\partial u}{\partial y} + \frac{\partial v}{\partial x} \right)^2 + \left(\frac{\partial v}{\partial z} + \frac{\partial w}{\partial y} \right)^2 + \left(\frac{\partial u}{\partial z} + \frac{\partial w}{\partial x} \right)^2 \right] dx dy dz \quad (3)$$

where, u , v , and w are the displacements in x , y , and z directions, respectively.

The strain energy minimization requires that

$$\delta U = 0 \quad (4)$$

and when this is subjected to the Dirichlet boundary conditions:

$$u|_{\partial\Omega} = v|_{\partial\Omega} = w|_{\partial\Omega} = 0 \quad (5)$$

where $\partial\Omega$ denotes the boundary of volume Ω (see Fig. 1).

Eq. (4) is also constrained by the correspondences of image features (such as contours in 2D or surfaces in 3D) between the source and target images. Please note that the source image is the non-deformed image, the target image, or the reference image is the one obtained in the deformed state, and the registered image is the source image that has been transformed to the reference image. Suppose that we have a point $p(x, y, z)$ in the source image, and as a result of distortion correction it moves to point $P(X, Y, Z)$ (P is to be determined through registration). If point $p(x, y, z)$ belongs to Σ (the set of voxels of those features in the source image that have corresponding features in the target (Fig. 1), it will move to its corresponding point $P'(X', Y', Z')$ in the target image for which a position is measured manually or automatically. Then the constraint can be expressed in the form of the energy function:

$$\int_{\Sigma} (P - P')^2 d\Sigma = 0 \quad (6)$$

The transformation between the source and target images can be obtained by solving Eqs. (4–6). The obtained transformation, that is, the strain energy minimization transformation (SEMT), forms the basis of the novel elastic registration on prostate endorectal coil MR imaging (erMRI).

2.2. Discretization

Suppose we have 2 images I_s and I_t , where I_s is the source image and I_t is the target image. The voxel $p_{ijk}(x_{ijk}, y_{ijk}, z_{ijk})$ in I_s evolves into the voxel $P_{ijk}(X_{ijk}, Y_{ijk}, Z_{ijk})$ in I_t . Here i, j , and k are in the range of $[1, L]$, $[1, M]$, and $[1, N]$, respectively, and (L, M, N) are the dimensions of the image volume. The displacement vector (u, v, w) of voxel p_{ijk} is:

$$(u, v, w) = P_{ijk} - p_{ijk} = (X_{ijk} - x_{ijk}, Y_{ijk} - y_{ijk}, Z_{ijk} - z_{ijk}) \quad (7)$$

Plugging in Eqs. (3) and (7) to Eq. (4) and using forward difference formula, Eq. (4) can be discretized to a set of linear equations. The new positions $P_{ijk}(X_{ijk}, Y_{ijk}, Z_{ijk})$ are the solutions of the linear equation system:

$$\begin{aligned}
X_{ijk} &= \frac{\left[2X_{i+1jk} + 2X_{i-1jk} + X_{ij+1k} + X_{ij-1k} + X_{ijk+1} + X_{ijk-1} + (Y_{i+1jk} - Y_{ijk}) \right]}{8} \\
&\quad - (Y_{i+1j-1k} - Y_{ij-1k}) + (Z_{i+1jk} - Z_{ijk}) - (Z_{i+1jk-1} - Z_{ijk-1}) \\
Y_{ijk} &= \frac{\left[Y_{i+1jk} + Y_{i-1jk} + 2Y_{ij+1k} + 2Y_{ij-1k} + Y_{ijk+1} + Y_{ijk-1} + (Z_{ij+1k} - Z_{ijk}) \right]}{8} \\
&\quad - (Z_{ij+1k-1} - Z_{ijk-1}) + (X_{ij+1k} - X_{ijk}) - (X_{i-1j+1k} - X_{i-1jk}) \\
Z_{ijk} &= \frac{\left[Z_{i+1jk} + Z_{i-1jk} + Z_{ij+1k} + Z_{ij-1k} + 2Z_{ijk+1} + 2Z_{ijk-1} + (X_{ijk+1} - X_{ijk}) \right]}{8} \\
&\quad - (X_{i-1jk+1} - X_{i-1jk}) + (Y_{ijk+1} - Y_{ijk}) - (Y_{ij-1k+1} - Y_{ij-1k})
\end{aligned} \tag{8}$$

for $2 \leq i \leq L-1$, $2 \leq j \leq M-1$, $2 \leq k \leq N-1$, and $(i, j, k) \notin \Sigma$.

The boundary conditions as described by Eq. 5 and the constraints as expressed in Eq. 6, leads us to the following:

$$X_{ijk} = x_{ijk}, \quad Y_{ijk} = y_{ijk}, \quad Z_{ijk} = z_{ijk} \quad \text{for } i = 1 \text{ or } L, j = 1 \text{ or } M, k = 1 \text{ or } N \tag{9}$$

$$X_{ijk} = X'_{ijk}, \quad Y_{ijk} = Y'_{ijk}, \quad Z_{ijk} = Z'_{ijk} \quad \text{for } (i, j, k) \in \Sigma \tag{10}$$

The final registered image volume can be computed from Eqs. (8–10).

Note that there are no constitutive parameters such as λ and μ in Eqs. (8–10), which makes this algorithm essentially parameter free. The new voxel position $P_{ijk}(X_{ijk}, Y_{ijk}, Z_{ijk})$ is expressed as an explicit function of the positions of its closest neighbors.

FIGURE2

2.3. Numerical Implementation

The Gauss–Seidel method was used to iteratively compute the solutions of the linear equation system (Eqs. 8–10). Convergence for the numerical implementation was set such that the position difference (or displacement) of any voxel between 2 consecutive iterations was less than ϵ (0.01 pixels in our case) or when the number of iteration reached s_0 . Figure 2 illustrates the procedure of this novel registration algorithm and the numerical implementation of SEMT. This algorithm was implemented in the MATLAB environment (Mathworks, Inc., Natick, MA).

To estimate the number of iterations required for convergence, the above algorithm was applied to a pair of digital images consisting of a rectangular grid of correspondence points with a deformation similar to the one depicted in Fig. 1. After each iteration, the maximum difference

between the source and target correspondence points (in voxels) was found. Figure 3 shows a typical relationship between the difference of two consecutive iterations and the iteration number. As can be seen, a difference of 0.01 is approached when the number of iterations reaches 300. For the purpose of our study we set the maximum number of iterations, s_0 , to 300. The computation time needed for 300 iterations is about 20 seconds for a 2D registration and 15–30 minutes for 3D registration on a 3.4GHz personal computer.

FIGURE3

2.4. Validation

Validation of the algorithm was accomplished on digital phantoms, a prostate phantom designed in house, and actual prostate MR images acquired using an endorectal coil. To assess the accuracy of the SEMT algorithm, the intensity difference, normalized cross correlation coefficient (NCC), and displacement of known landmarks were computed.

2.4.1. Digital Phantom

A digital phantom was generated that consisted of a sphere (radius 10, arbitrary units) centered in a $30 \times 30 \times 30$ (arbitrary units) volume. A 3D character 'F' was embedded in the sphere as shown in Figure 4. For simplicity, the sphere was assumed to be elastic, isotropic, and homogeneous. A known deformation was applied to this digital phantom to test the efficacy of the algorithm in registering the sphere to the ellipsoid. In our study the sphere was elastically deformed to an ellipsoid (3 semiaxes: $a = 9$, $b = 12$, and $c = 10$ in x , y , and z directions, respectively) along with the embedded 3D character 'F'. In this case the sphere is the source image, which is deformed to the ellipsoid, the target or reference image. A total of 186 predefined matching landmarks on the surfaces of the sphere and the ellipsoid were used to derive the transformation matrix using the SEMT algorithm.

FIGURE4

2.4.2. Prostate Phantom

The prostate phantom as shown in Fig. 5 was built in house and incorporates all the necessary elements of a prostate gland, including tissue consistency and the biochemicals contained within a normal prostate tissue (Zhang and Gullapalli, 2005). The gland was constructed from 0.5% agarose (Type I Low EEO 9012-36-6, Sigma Chemical Co., St. Louis, MO) and was made in the shape of an ellipsoid with dimensions of $50 \times 40 \times 30 \text{ mm}^3$ in the x, y, and z directions. The gland was doped with 0.1 mM gadolinium diethyltriaminepentaacetic acid, producing visible contrast between the gland and the background gel. The biochemicals choline (10 mM), creatine (30 mM), citrate (100 mM), and lactate (35 mM), which are predominantly seen in prostate MRS imaging, were also added. A thin layer of lard was added surrounding the gland to mimic periprostatic fat. A piece of polycarbonate bar was placed above the gland to constrain deformation, much as the pubic bone would do in the actual prostate. At the bottom of the phantom a tunnel allowed insertion of the endorectal coil. Sesame seeds were randomly embedded within the prostate phantom, and their displacement was used in assessing the accuracy of the registration. Images of this prostate phantom were first obtained with the endorectal inserted but with no balloon inflation (source images). As in normal prostate erMRI, the balloon was then inflated with 100 cc of air, which allowed the prostate phantom to distort in a manner similar to that of a real prostate gland during an in vivo erMRI procedure. MR images were obtained in this distorted position (target images).

FIGURE5

Forty matching landmark points along each of the semi-automatically drawn contours were used to correct for deformation. In total there were 400 landmark points for the entire prostate that were used in determining the transformation matrix.

2.4.3. In Vivo Data

The registration algorithm was also applied on ten sets of human prostate data, each with 2 typical deformation states (one with 0 cc of air and the other with 40–60 cc of air inflated in the endorectal coil balloon). Once again the source images are obtained with deflated coil and the target images are obtained with the balloon inflated. The matching landmarks along the prostate

surface were selected in the same fashion as stated in the section above. There were a total of 200 ~ 400 landmarks used to derive the transformation depending on the size of each prostate. Approval from the University of Maryland Institutional Review Board was obtained for this study.

2.4.4. Registration Evaluation

The performance of the registration algorithm was assessed using normalized correlation coefficient (NCC) between the target and the registered images using the following relationship:

$$NCC = \frac{\sum_i \sum_j \sum_k (I_{1ijk} - \bar{I}_1)(I_{2ijk} - \bar{I}_2)}{\sqrt{\left(\sum_i \sum_j \sum_k (I_{1ijk} - \bar{I}_1)^2 \right) \left(\sum_i \sum_j \sum_k (I_{2ijk} - \bar{I}_2)^2 \right)}}$$

where I_{1ijk} and I_{2ijk} are the image intensities at point (i,j,k) in image I_1 and I_2 , respectively, and \bar{I}_1 and \bar{I}_2 are the average intensities of I_1 and I_2 , respectively. If $NCC = 1$, then I_1 and I_2 are identical, which means a perfect registration.

Registration error was assessed by averaging the displacement of a fiducial landmark in the target image to its corresponding point in the registered image. These fiducial landmarks were either geometric or anatomic, both of which were identified in the target image and have correspondences in the registered image. A typical dataset usually used 2 to 6 fiducial landmarks per slice depending on the visible features inside the prostate. In the case of the prostate phantom, the embedded sesame seeds allowed us to measure the displacement of a point resulting from the inflation of the coil balloon and then to assess the accuracy of the registration algorithm.

2.5 Comparison to other registration techniques

We compared the results of our SEMT registration with established affine and B-spline registration techniques. Both these techniques are available on MIPAV (Ver 3.1.1, 2007, Center for Information Technology, National Institute of Health, Rockville, MD). We performed 12-parameter affine registration, which includes 3 translation, 3 rotation, 3 scaling and 3 shearing. For the B-spline registration, the degree of the basis functions was set to three, which guarantees

1
2
3
4
5
6
7
8
9
10
11
12
13
14
15
16
17
18
19
20
21
22
23
24
25
26
27
28
29
30
31
32
33
34
35
36
37
38
39
40
41
42
43
44
45
46
47
48
49
50
51
52
53
54
55
56
57
58
59
60

a smooth displacement field. Tri-linear interpolation for performing registration operations and correlation ratio as the cost function was used for both methods.

2.6 MRI Data Acquisitions

The prostate phantom and patient data were acquired on a Philips Eclipse 1.5-T system (Philips Medical System, Cleveland, OH). An endorectal coil (Medrad, Inc., Indianola, PA) was used to acquire the T2-weighted axial images using a fast spin echo sequence.

The T2-weighted images of the prostate phantom were acquired while the inserted endorectal coil was fully deflated or was inflated with about 100 cc of air. The acquisition parameters were: TR/TE = 3412/91 ms, matrix = 256 × 192, field of view (FOV) = 16.0 cm, slice thickness = 3.0 mm, and number of slices = 29.

Ten patients (ages, 61 ± 9 y) with biopsy-confirmed prostate malignancy underwent erMRI. T2-weighted axial images of the prostate gland were obtained from patients with the inserted endorectal coil in its inflated state (40–60 cc air inflation) and completely deflated state (TE = 91 ms, TR varied from 3500 to 4500 ms depending on the patients, matrix = 256 × 192, FOV = 16 cm, and slice thickness = 3.0 mm). The slice number varied from 25 to 38, depending on the size of the prostate.

3. RESULTS

3.1. Simulated Phantom Data

FIGURE6

Figure 6 displays the registration results in 3 orthogonal central planes of the object shown in Fig 4. The first row shows results in the *xy* plane; the second row, the *yz* plane; and the third row, the *xz* plane respectively. Each column in Fig. 6 shows the target, source, registered images, the intensity difference images between the source and target images, and the intensity difference images between the target and registered images in all 3 orthogonal planes. Also shown in Fig. 6 is the displacement distribution along the 3 planes, which is superimposed on the source images in the second column. The blue arrows represent the displacement vectors with the length of the arrows representing their magnitude. To facilitate visual comparison of the intensity difference between the pre- and post-registration images (Fig. 6, column 4 and column 5), the same grayscale was adopted between the 2 sets of images. As shown in Fig. 6, the registration reduced the intensity difference in the subtracted images between the target and the registered images. The NCC improved from 0.91 to 1.0 after SEMT registration.

TABLE1

To assess the registration error, ten corners of the character “F” (Fig. 6, *xy* plane and column 1) on the central slice were selected to serve as fiducial landmarks. Table 1 summarizes the displacement of these landmarks between the source and target images and the registration error. The average displacement of the landmarks between the source and target images was 1.0 ± 0.5 pixels. The algorithm attained an average registration error of 0.2 ± 0.1 pixels.

3.2. Prostate Phantom Data

Figure 7 shows the registration results from one of the axial MR images taken through the center of the prostate phantom shown in Fig. 5. A comparison of the intensity difference between the target and source (Fig. 7d) and the target and registered images (Fig. 7e) qualitatively demonstrates the registration accuracy obtained using the SEMT algorithm. The

NCC improved from 0.84 to 0.99 after registration. Twelve sesame seeds were used as features that were matched between the target and registered information to assess the registration error. Table 2 provides a list of measurements made using these twelve seeds. The average displacement of the sesame seeds was 4.8 ± 0.4 pixels (3.0 ± 0.3 mm). The registration error was found to be 1.0 ± 0.6 pixels (0.6 ± 0.4 mm).

FIGURE7

TABLE2

3.3. *In Vivo Prostate Data*

Figure 8 shows an example registration from in vivo prostate images. The blue arrows shown in Fig. 8b show the direction and magnitude of displacement. The comparison of intensity difference images in Fig. 8d and 8e before and after registration, qualitatively demonstrates the registration accuracy as determined by the SEMT algorithm. Five feature landmarks (see Fig. 8a) depicting benign prostatic hyperplasia nodules of the prostate were chosen to evaluate the registration error for the slice shown. The average displacement of these 5 landmarks was 6.7 ± 1.5 pixels (4.2 ± 0.9 mm). The registration error was 1.7 ± 1.3 pixels (1.1 ± 0.8 mm).

FIGURE8

The NCC was computed over the segmented volume of the prostate and was found to improve from 0.69 to 0.97 for this particular case.

The results on all 10 sets of patient images were summarized in Table 3. The NCC was improved on average from 0.72 ± 0.10 to 0.96 ± 0.03 for the whole group after SEMT registration ($P < 0.0001$). The average displacement of fiducial landmarks inside the prostate gland from all the subjects was found to be 6.1 ± 1.9 pixels (3.8 ± 1.2 mm) before registration, which was reduced to 1.8 ± 0.7 pixels (1.1 ± 0.4 mm) after registration. Also shown in Table 3 are the registration errors made by the 12-parameter affine registration and B-spline registration programs. The registration errors were 5.2 ± 1.6 pixels (3.2 ± 1.0 mm) when using the affine registration method and 2.9 ± 1.4 pixels (1.8 ± 0.9 mm) when using the B-spline method.

TABLE3

4. DISCUSSION

MR images of the prostate are typically obtained when the prostate is in its distorted position. Advanced imaging techniques, such as diffusion-weighted imaging, perfusion-weighted imaging, and MRS, have been shown to increase specificity in the detection of cancer. However, all the information provided from these techniques is obtained with the prostate in its deformed state. For techniques such as external-beam therapy and brachytherapy to be effective, prostate images obtained in the distorted state must be registered back to their original state. For example in the case of external beam brachytherapy, the images and the spectroscopic information obtained from the prostate with the endorectal coil (deformed images) can be registered to the MR images obtained without the use of endorectal coil (non-deformed images). These images and spectra can then be co-registered with the CT images for treatment planning. This will ensure accurate localization of the tumor in its undistorted state and will allow for accurate treatment planning.

We have developed a novel SEMT algorithm to perform prostate image registration that registers images to single-pixel accuracy. The algorithm requires that the object undergoing deformation be elastic, incompressible, and in equilibrium while scanning. Incompressible tissue, such as the breast and prostate, are suitable candidates for such elastic registration (Dubois et al. 2001; Fei et al. 2003). In a physically conservative system, the potential energy has a stationary value if the system is in equilibrium. In the case of our registration problem, in which image volumes are treated as elastic bodies, the potential energy is purely the strain energy. The minimization of this strain energy allows for the transformation of the deformed elastic, incompressible objects to be registered.

In most in vivo situations it is difficult to quantitatively evaluate the performance of a registration algorithm because of the lack of 'ground truth'. Our initial results on the simulated digital phantom and the development of a prostate phantom were essential in evaluating the robustness of the SEMT algorithm (Zhang and Gullapalli, 2005). This multipurpose phantom

mimicked the tissue property of the prostate and provided us a scenario that was as close as possible to that routinely experienced in the clinical setting. Because it has all the necessary tissue properties and biochemicals normally seen in a prostate gland, the phantom can be used to test the robustness of new imaging and spectroscopic techniques. The periprostatic fat also allows us to mimic the difficulty associated with saturating outer-volume chemical species that may alias into the volume of interest, especially when performing MRS. The sesame seeds also may be used for practicing image-guided biopsies. However, here we used the seeds to determine the registration error of the SEMT algorithm.

The transformation matrix obtained by SEMT relies on feature correspondences between the source and target images. Any mismatch of the correspondences may result in registration errors. We have chosen well populated, uniformly distributed points along the whole surface of the prostate to derive the transformation between the source and target images. We have shown that our algorithm is accurate up to 1.1 mm based on the measurements made at corresponding feature points of the prostate. Other methods, such as active contour (Kass et al., 1988) and/or active surface models (Cohen L and Cohen I, 1993), may be adopted to generate the correspondences automatically to further reduce the resolution to a subpixel level.

We compared our SEMT algorithm to two other well-established methods of registration namely the 12-parameter affine registration and B-spline registration. Figure 9 shows the performance of these two techniques in comparison to our SEMT algorithm. Given the range of displacements seen in ten prostate images as shown by the first metric in Fig 9, the SEMT algorithm out performed the other two techniques by demonstrating nearly 38% reduction in registration errors over B-spline, and over 60% reduction in errors in comparison to the affine registration technique respectively.

FIGURE9

In the last decade, many applications of image registration for prostate images have been reported. Dubois et al. (2001) implemented a rigid registration on a prostate phantom and obtained a registration error of 1.6 ± 0.7 mm. Because of anatomical variability in the prostate and because of the fairly nonrigid characteristics of transformation, rigid registration may not yield

accurate results for registration of prostate images. Wu et al. (2004) adopted a polynomial transformation to register prostate MRSI with an error of 2 mm or less. Fei et al. (2003) applied TPS to prostate image registration, reducing the prostate centroid displacement from 3.4 to 0.6 mm. Wang et al. (2005) implemented a 'demons' algorithm (a grayscale-based deformable image registration algorithm) on a phantom prostate and achieved a tracking accuracy of better than 1.5 mm. The results from our method are either comparable or better than these reported methods. A notable difference between our study and those mentioned here is that our approach is based on the use of correspondence points coupled with physical constraints, whereas the cited studies used voxel-intensity based approaches for registration.

The proposed SEMT approach is similar to those reported in the literature in that they all identify the feature correspondences (points, contours, or surfaces) in the source and target images and then use these correspondences as input to derive the underlying deformation transformation. The principal difference between our method and these others is that our transformation is derived from strain energy minimization using elastic theory. Broit (1981) was the first to use a model derived from elasticity theory to match 2D and 3D images. He defined a cross-correlation coefficient between local regions in 2 images to derive forces that deform the source image to the target. The transformation is obtained by solving the Navier–Lame equations. Instead of using the local similarity as the measure of external driving forces, Davatzikos et al. (1996) proposed a spring model in which the external force is obtained from mapping the contours of structures in the source and target images. They obtained their transformation by empirically choosing the two Lamé constants ($\lambda = \mu = 1.5 \times 10^{-9}$) in the equilibrium equations. Pecker et al. (1999) incorporated the known displacements of some boundary structures in the source and target images as hard constraints to the registration to compute the transformation. In that study, λ was intentionally set to zero and the other constant μ was eliminated. This makes the registration model completely parameter free. Unlike traditional elastic registration methods, which solve the equilibrium equations for the transformation, the SEMT method obtains the transformation by minimizing the strain energy of the registered image volume. Making a reasonable assumption of incompressibility (Krouskop, 1998), the registration model is parameter

1
2
3
4
5
6
7
8
9
10
11
12
13
14
15
16
17
18
19
20
21
22
23
24
25
26
27
28
29
30
31
32
33
34
35
36
37
38
39
40
41
42
43
44
45
46
47
48
49
50
51
52
53
54
55
56
57
58
59
60

free. The advantages of the proposed approach include the need for only a scalar energy function instead of a set of equilibrium equations; the reasonable assumption of incompressibility, which makes the algorithm parameter free; and the ability to handle both rigid and nonrigid deformation equally well.

It should be noted that we performed the registration on the entire prostate image with a subtle assumption that the image volume has the same mechanical property throughout. As we know, many different structures and tissues are inside and outside the prostate gland. So this assumption may lead to some systematic registration error. For more accurate registration it would be necessary to take these structures into consideration. Some differences in the mechanical property of the tissue are expected, but when dealing with tissues that have significantly different mechanical properties, it should be noted that the SEMT algorithm no longer remains parameter free. Hence a modification to Eq. (8) is required that takes into consideration the surrounding tissue characteristics. Our future studies will characterize tissues from different regions of and surrounding the prostate for an accurate assessment of displacement and strain during compression of the prostate.

5. CONCLUSION

We have implemented a novel registration algorithm based on strain energy minimization and demonstrated its effectiveness on phantom and prostate images. Results from our study show registration error of approximately 1 mm over the entire volume of the prostate. Accurate registration of prostate images obtained in the deformed state can be useful in treatment planning and also for longitudinal evaluation of progression/regression in patients with prostate cancer. In addition, although we have demonstrated the utility of our algorithm on MR images, we believe that this method can also be applied to images from any two different imaging modalities provided that corresponding features are available in both.

ACKNOWLEDGMENT

The work was supported by the U.S. Department of Defense IDEA grant W81XWH-04-1-0249 (PC031042).

REFERENCES

- [1] Sanchez-Chapado M, Angulo JC, Ibarburen C, Aguado F, Ruiz A, Viano J, Garcia-Segura JM, Gonzalez-Esteban J, Rodriquez-Vallejo JM: Comparison of digital rectal examination, transrectal ultrasonography, and multicoil magnetic resonance imaging for preoperative evaluation of prostate cancer. *Eur Urol* 21:140-149, 1997.
- [2] Futterer JJ: MR imaging in local staging of prostate cancer. *Eur J Radiol* 63(3):328-334, 2007.
- [3] Susil RC, Camphausen K, Choyke P, McVeigh ER, Gustafson GS, Ning H, Miller RW, Atalar E, Coleman CN, Menard C: System for prostate brachytherapy and biopsy in a standard 1.5T MRI scanner. *Magn Reson Med* 52(3):683-687, 2004.
- [4] Nguyen PL, Chen MH, D'Amico AV, Tempany CM, Steele GS, Albert M, Cormack RA, Carr-Locke DL, Bleday R, Suh WW: Magnetic resonance image-guided salvage brachytherapy after radiation in select men who initially presented with favorable-risk prostate cancer: a prospective phase 2 study. *Cancer* 110(7):1485-1492, 2007.
- [5] Schnall MD, Imai Y, Tomaszewski J, Pollack HM, Lenkinski RE, Kressel HY: Prostate cancer: local staging with endorectal surface coil MR imaging. *Radiology* 178:797-802, 1991.
- [6] Husband JE, Padhani AR, Mac Vicar AD, Revell P: Magnetic resonance imaging of prostate cancer: comparison of image quality using endorectal and pelvic phased array coils. *Clin Radiol* 53:673-681, 1998.
- [7] D'Amico AV, Schnall M, Whittington R, Malkowicz SB, Schultz D, Tomaszewski JE, Wein A: Endorectal coil magnetic resonance imaging identifies locally advanced prostate cancer in select patients with clinically localized disease. *Urology* 51:449-454, 1998.
- [8] Dubois DF, Bice Jr WS, Prestige BR: CT and MRI derived source localization error in a custom prostate phantom using automated image coregistration. *Med Phys* 28:2280-2284, 2001.

[9] Fei B, Wheaton A, Lee Z, Duerk JL, Wilson DL: Automatic MR volume registration and its evaluation for the pelvis and prostate. *Phys Med Biol* 47:823-838, 2002.

[10] Wu X, Dibiase SJ, Gullapalli R, Yu CX: Deformable image registration for the use of magnetic resonance spectroscopy in prostate treatment planning. *Int J Radiat Oncol Biol Phys* 58:577-583, 2004.

[11] Venugopal N, McCurdy B, Hnatov A, Dubey A: A feasibility study to investigate the use of thin-plate splines to account for prostate deformation. *Phys Med Biol* 50:2871-2885, 2005.

[12] Lian J, Xing L, Hunjan S, Dumoulin C, Levin J, Lo A, Watkins R, Rohling K, Giaquinto R, Kim D, Spielman D, Daniel B: Mapping of the prostate in endorectal coil-based MRI/MRSI and CT: a deformable registration and validation study. *Med Phys* 31:3087-3094, 2004.

[13] Fei B, Kemper C, Wilson DL: A comparative study of warping and rigid body registration for the prostate and pelvic MR volumes. *Comput Med Imaging Graph* 27:267-281, 2003.

[14] Broit C: Optimal Registration of Deformed Images, PhD thesis. University of Pennsylvania, Philadelphia, 1981.

[15] Davatzikos C, Prince JL, Bryan RN: Image registration based on boundary mapping. *IEEE Trans Med Imaging* 15:112-115, 1996.

[16] Gee J, Haynor D, Briquer L, Bajcsy R: Advances in elastic matching theory and its implementation, in J. Troccas, W.E.L. Grimsom, R. Mosges (Eds.), *Proceedings of the First Joint Conference on Computer Vision, Virtual Reality and Robotics in Medicine and Medical Robotics and Computer-Assisted Surgery*. London: Springer-Verlag, 1997, 63-72.

[17] Peckar W, Schnorr C, Rohr K, Stiehl HS: Two step parameter-free elastic image registration with prescribed point displacements. *J Math Imaging Vision* 10:143-162, 1999.

[18] Christensen GE, Rabbit RD, Miller MI: Deformable templates using large deformation kinematics. *IEEE Trans. Image Process* 5:1435-1447, 1996.

[19] Thirion JP: Image matching as a diffusion process: an analogy with Maxwell's demons. *Med Image Anal* 2:243-260, 1998.

[20] Beuchemin SS, Barron JL: The computation of optical flow. *ACM Comput Surveys* 27:433-467, 1995.

- [21] Greenwood, DT: Classical Dynamics, Dover, Mineola, NY: Dover Publications, 1997.
- [22] Ugural AC, Fenster SK: Advanced Strength and Applied Elasticity, 3rd ed., Upper Saddle River, NJ: Prentice-Hall, Inc., 1995.
- [23] Krouskop TA, Wheeler TM, Kallel F, Garra BS, Hall T: Elastic moduli of breast and prostate tissues under compression. Ultrasonic Imaging 20:260-274, 1998.
- [24] Read K, Hosseinzadeh K, Dibiase S, Gullapalli R: Characterization of prostate deformation during MR examination using endorectal coil for accurate localization of tumor during brachytherapy. Proc Intl Soc Mag Reson Med 2340, 2001.
- [25] Zhang B, Gullapalli RP: Multipurpose prostate phantom. Proc Intl Soc Mag Reson Med 2115, 2005.
- [26] Kass M, Witkin A, Terzopoulos D: Snakes: active contour models. Int J Comput Vision 1:321-331, 1988.
- [27] Cohen L, Cohen I: Finite-element methods for active contour models and balloons for 2D and 3D images. IEEE Trans Pattern Anal Mach Intell 15:1131-1147, 1993.
- [28] Wang H, Dong L, O'Daniel J, Mohan R, Garden AS, Ang KK, Kuban DS, Bonnen M, Chang JY, Cheung R: Validation of an accelerated 'demons' algorithm for deformable image registration in radiation therapy. Phys Med Biol 50:887-905, 2005.

1
2
3
4
5
6
7
8
9
10
11
12
13
14
15
16
17
18
19
20
21
22
23
24
25
26
27
28
29
30
31
32
33
34
35
36
37
38
39
40
41
42
43
44
45
46
47
48
49
50
51
52
53
54
55
56
57
58
59
60

Appendix 1:

The relationship between the two constants λ and μ is:

$$\lambda = \frac{2\nu\mu}{1-2\nu} \tag{A. 1}$$

And the relationship between the unit volume change e and normal strain ε_x is:

$$e = (1-2\nu)\varepsilon_x \tag{A. 2}$$

So the first term λe^2 of Eq. (1) can be rewritten as:

$$\lambda e^2 = \frac{2\nu\mu}{1-2\nu} ((1-2\nu)\varepsilon_x)^2 = 2\nu\mu(1-2\nu)\varepsilon_x^2 \tag{A. 3}$$

Given Poisson's ratio $\nu = 0.495$ (Krouskop et al. 1998), the above expression is approximately

$$\lambda e^2 = 0.01\mu\varepsilon_x^2 \tag{A. 4}$$

which makes it negligible as compared to the other two terms in Eq. (1).

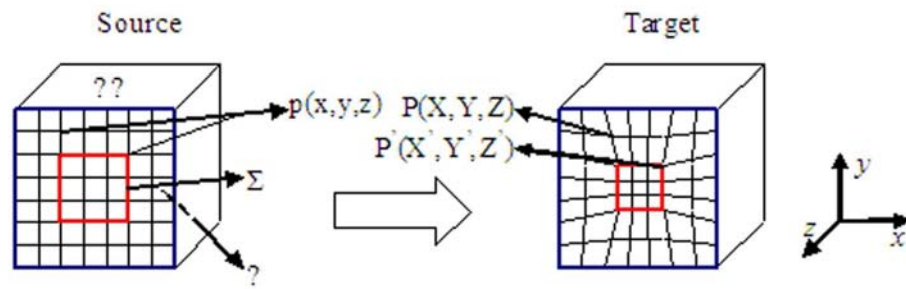


Figure 1: Schematic of the registration model. Voxels in the source image are denoted $p(x,y,z)$. Under deformation they evolve into $P(X,Y,Z)$ or $P'(X',Y',Z')$ if the source voxel belongs to the set Σ . In this figure, Σ is a voxel set of interest as denoted by the red square. Also, Ω denotes the image volume, and $\partial\Omega$ denotes the surfaces of volume Ω .

140x44mm (600 x 600 DPI)

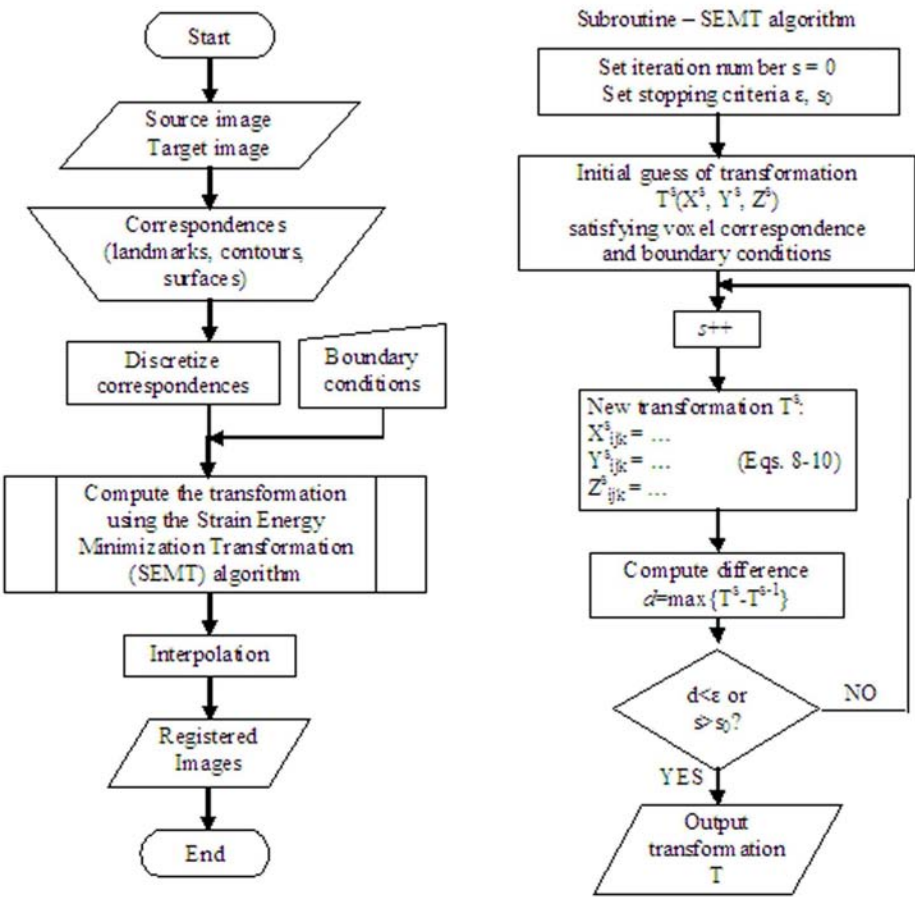


Figure 2: Flowchart of the registration procedure and the SEMT algorithm using Gauss–Seidel method.
152x139mm (600 x 600 DPI)

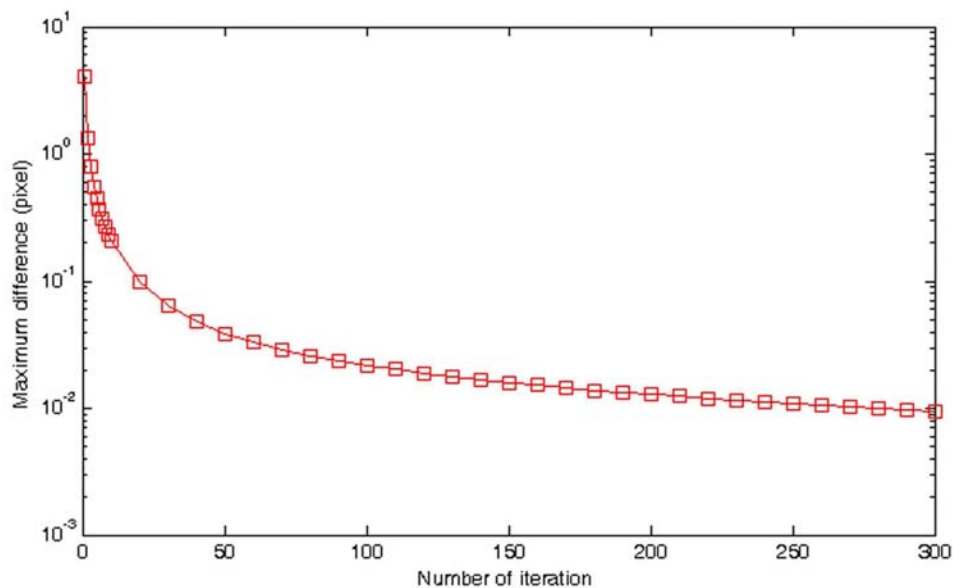


Figure 3: Semi-log plot depicting the number of iterations required for a given maximum difference.
152x92mm (600 x 600 DPI)

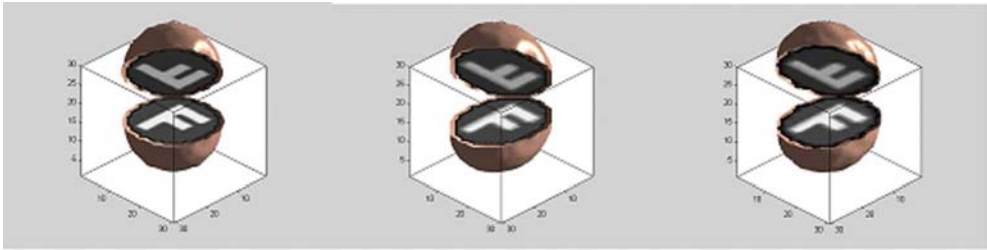


Figure 4: The 3D open look of (a) the source sphere, (b) the target ellipsoid, and (c) the registered volume with a character 'F' inside. The Cartesian coordinate system is shown for later reference in Fig. 6.

134x37mm (600 x 600 DPI)

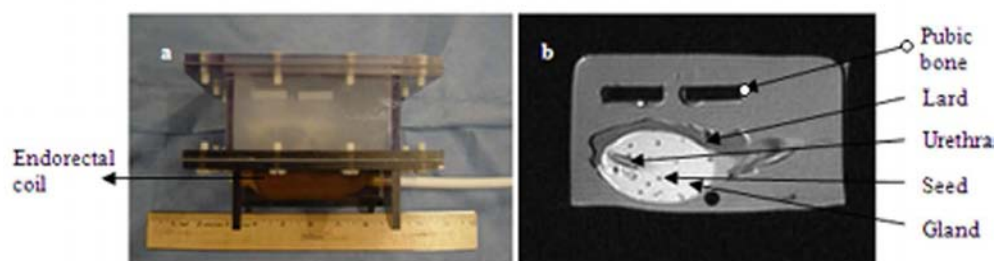


Figure 5: Prostate phantom: (a) picture of the prostate phantom, and (b) representative MR image. Sesame seeds are shown as dark dots in the gland.
133x38mm (600 x 600 DPI)

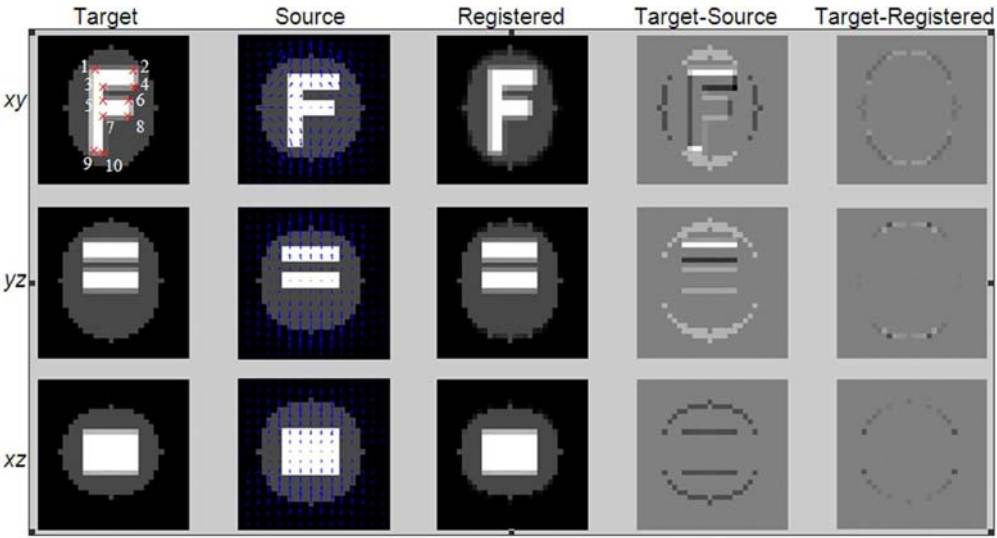


Figure 6: Registration results on the synthesized digital phantom. Each row shows images in each of the orthogonal planes. Columns represent image type. The source image column is overlaid by the displacement vectors in 3 orthogonal planes. Also shown in target image (xy plane) are the landmarks (marked by red crosses) used to measure the accuracy of registration. NCC improved from 0.91 to 1.0.
147x80mm (600 x 600 DPI)

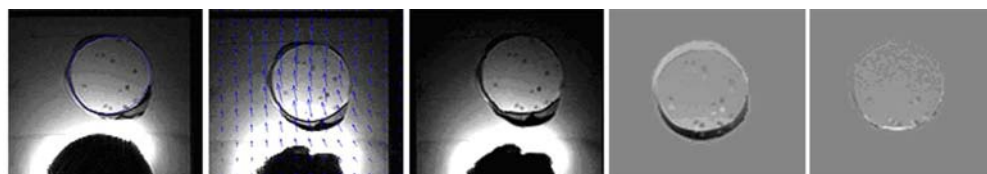


Figure 7: Registration results of the prostate phantom in the xy plane: (a) target image; (b) source image overlaid with the displacement; (c) registered image; (d) intensity difference image (a)-(b); and (e) intensity difference image (a)-(c). NCC improved from 0.84 to 0.99.
152x25mm (600 x 600 DPI)

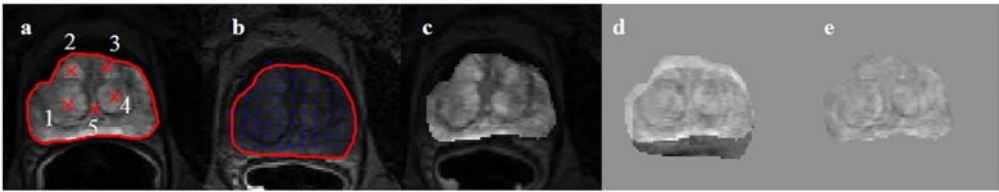


Figure 8: Representative registration results for a prostate patient: (a) target image with 5 feature landmarks marked by red crosses; (b) source image overlaid with the displacement; (c) registered image; (d) intensity difference image (a)-(b); and (e) intensity difference image (a)-(c). NCC improved from 0.69 to 0.97.
156x29mm (600 x 600 DPI)

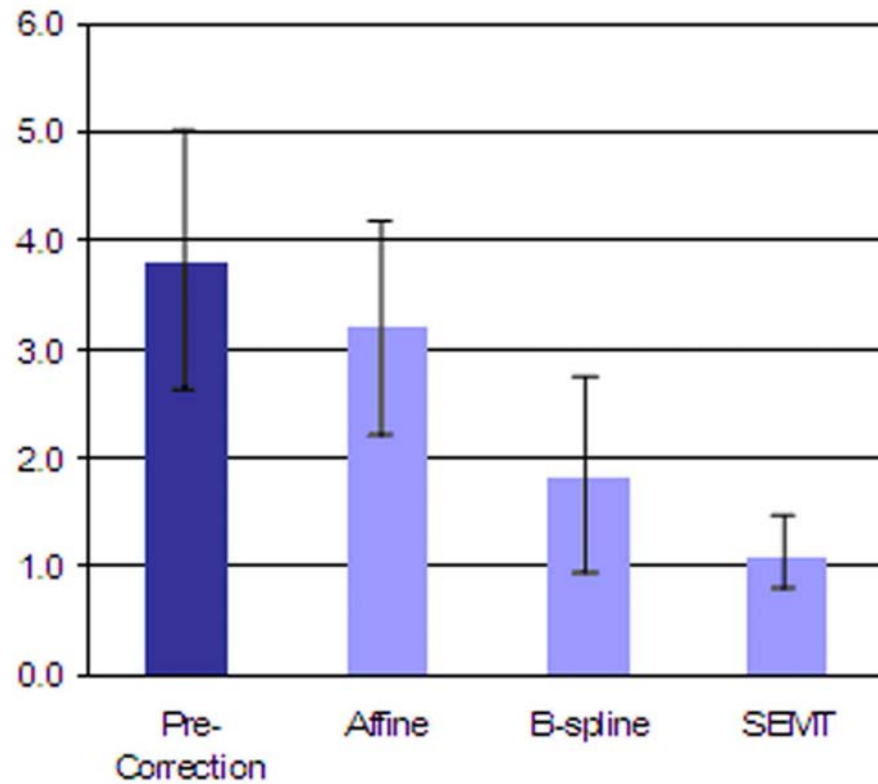


Figure 9: Graph depicting the performance of SEMT, B-spline, and affine registration algorithms on prostate images. Minimum registration errors are realized with the SEMT algorithm.
85x75mm (600 x 600 DPI)

Corner	Position (x,y) (pixel)			Displacement	Error
	Source	Target	Registered	(pixel)	(pixel)
C1	(9.0,7.0)	(10.0,6.4)	(10.0,6.1)	1.3	0.3
C2	(18.3,7.0)	(17.2,6.4)	(17.4,6.2)	1.4	0.3
C3	(11.7,9.9)	(11.8,9.1)	(11.7,9.1)	0.9	0.1
C4	(18.3,9.9)	(17.2,9.1)	(17.3,9.0)	1.5	0.2
C5	(11.7,12.0)	(11.8,11.9)	(11.7,11.9)	0.2	0.1
C6	(17.4,12.0)	(16.2,11.9)	(16.5,12.0)	1.3	0.3
C7	(11.7,14.7)	(11.8,14.7)	(11.7,14.7)	0.1	0.1
C8	(17.4,14.7)	(16.2,14.7)	(16.5,14.8)	1.3	0.3
C9	(9.0,20.4)	(10.0,21.1)	(10.0,21.3)	1.3	0.2
C10	(11.7,20.4)	(11.8,21.1)	(11.7,21.1)	0.8	0.1

Sesame seed	Position (pixel)			Displacement (pixel)	Error (pixel)
	Source	Target	Registered		
S1	(130,170)	(130,174)	(130,175)	4.0	1.0
S2	(126,157)	(126,162)	(125,161)	5.0	1.4
S3	(119,160)	(119,165)	(120,165)	5.0	1.0
S4	(117,161)	(115,165)	(116,165)	4.5	1.0
S5	(140,150)	(140,155)	(140,154)	5.0	1.0
S6	(135,139)	(135,144)	(135,144)	5.0	0.0
S7	(130,138)	(130,143)	(130,142)	5.0	1.0
S8	(107,141)	(107,146)	(106,146)	5.0	1.0
S9	(141,131)	(141,136)	(139,135)	5.0	2.2
S10	(134,127)	(133,132)	(133,132)	5.1	0.0
S11	(125,126)	(124,131)	(123,131)	5.1	1.0
S12	(121,128)	(120,132)	(120,133)	4.1	1.0

Patient	NCC*		Original Displacement (Pixel)	Registration Error (Pixel)		
	Before	After		SEMT	Affine	B-spline
P1	0.71	0.98	6.0	1.3	2.2	2.1
P2	0.50	0.92	6.1	1.1	(fail)	4.8
P3	0.75	0.99	6.7	1.6	6.5	2.7
P4	0.73	0.90	6.4	3.1	5.0	1.9
P5	0.72	0.98	8.5	1.5	7.4	4.6
P6	0.74	0.98	3.0	1.4	4.6	3.6
P7	0.74	0.98	5.6	2.9	5.3	1.8
P8	0.69	0.97	6.7	2.0	6.3	1.9
P9	0.75	0.96	3.0	1.7	3.9	0.9
P10	0.62	0.98	8.8	1.2	5.6	4.8
mean±std	0.72±0.10	0.96±0.03	6.1±1.9	1.8±0.7	5.2±1.6	2.9±1.4

Log Number: PC031042

Title: Correlation of In vivo MR Imaging findings with whole mount histological sections from radical prostatectomy patients

Author(s):

Bao Zhang, Khan A Siddiqui, John Papadimitriou, Harry Yfantis, Danielle Hollanda, Steven Roys James Borin, Michael Naslund, Rao Gullapalli

Presenter: Rao P. Gullapalli

Abstract:

Introduction: Magnetic resonance imaging (MRI) and spectroscopy (MRS) along with the use of an endorectal coil has shown to increase the sensitivity and specificity in detecting prostate cancer (PCa). In recent years several new MRI techniques such as dynamic contrast enhanced (DCE) MRI and diffusion tensor imaging (DTI) have shown to be useful in detecting and providing the status of the prostate tumors. These techniques combined with high resolution imaging have the potential to improve the accuracy in detecting prostate cancer non-invasively as well, while still in its early stages. In this project we have performed MRSI, DTI, perfusion weighted imaging (PWI), T2 map along with traditional MRI T2-weighted MRI image acquisition on patients who have opted for radical prostatectomy and compared the results with whole mount histopathology.

Methods: 14 patients with diagnosed prostate cancer who elected for radical prostatectomy were enrolled in this study. The patients' age ranged from 44-68 and the PSA varied from 0.5-14. Data acquisition was conducted on a 1.5T Magnetom Avanto MRI scanner. The sequences used to acquire the images included (a) T2 weighted MR images (b) 3D-CSI covering the entire prostate using PRESS localization with 0.56cc resolution; (c) DCE-MRI following a 20ml GD-DTPA injection at 4ml/s at a temporal resolution of 2.88s; (d) DTI with diffusion weighting in six colinear directions; (e) T2 mapping using a CPMG acquisition with eight echo times from 10-90ms. The ex-vivo prostate was also imaged following the prostatectomy procedure and enabled us to accurately localize the pathology findings with the in vivo findings. After radical prostatectomy, the prostate specimen was fixed overnight in a 10% formalin bath. Three millimeter axial sections from the specimen were made using a home built prostate slicer. H&E staining was performed on 50 micron sections from each of the slides. Digital images of both the slices and the pathologic slides were obtained.

Tofts model that included the duration of contrast injection was used for the kinetic analysis of perfusion data to obtain Ktrans maps. Cho+Cr/Cit map was computed from MRSI data. Apparent diffusion coefficient and fractional anisotropy maps were made from the DTI data. In vivo images were aligned with the ex vivo MR images which were in turn aligned to the individual slices of the prostate cuts submitted to pathology. Cancerous regions noted by the pathologist were located on the in vivo images and comparisons were made between the in vivo findings and pathology.

Results: Cancerous regions with a focus larger than 10mm³ were well delineated by the T2-map and Ktrans maps. Ktrans maps revealed a significant difference between normal

and abnormal tissue ($p < 0.001$). However these maps were not sensitive to changes in the grade of the tumors. DWI was able to reveal lesions larger than 40mm³ probably due to poor image resolution. MR spectroscopy had high sensitivity but was unable to respond to lesions of size less than 0.2cc. However the response of spectroscopy correlated well with the histological scoring.

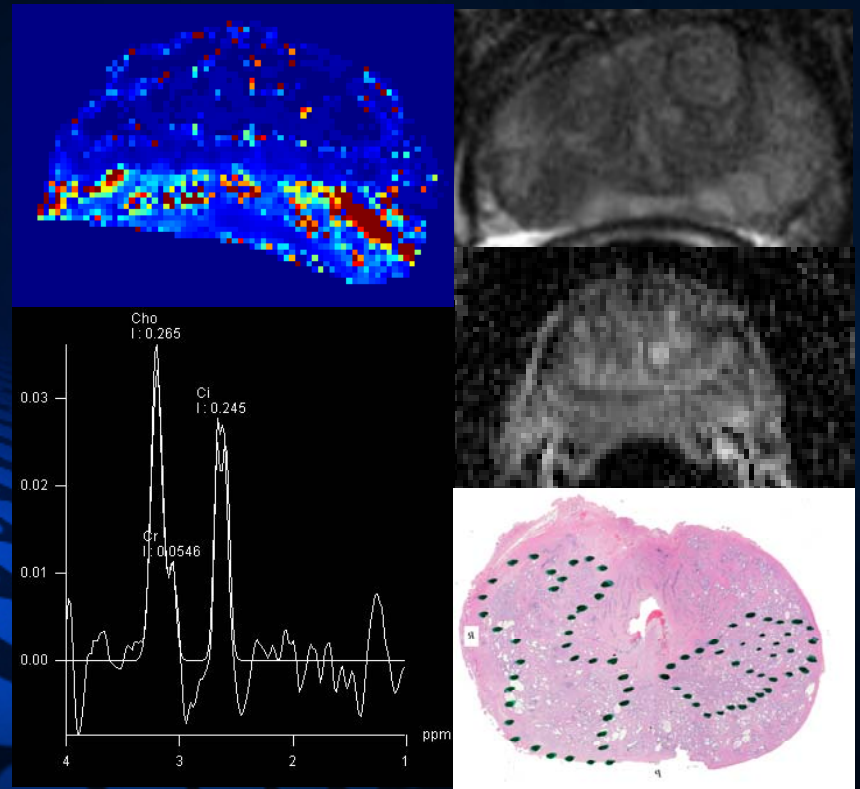
Conclusions: The preliminary results demonstrate that the multi-parametric MR imaging approach can improve the accuracy of prostate cancer detection. The combination of each of the techniques increased the sensitivity and specificity from 72% & 80% respectively to 90% & 89% respectively when compared with normal MRI findings alone.

Created: 03/15/2007 at 3:56 PM CDT

Last Updated: 03/15/2007 at 4:51 PM CDT

Advanced MR Imaging of Prostate Cancer: Radiology Pathology Correlation

Andrew Rosenkrantz¹, MD;
Rao Gullapalli¹, PhD;
Khan Siddiqui², MD; Bao Zhang¹ MS;
John Papadimitriou³, MD, PhD;
Danielle Holanda³, MD; Steve Roys¹, MS;
Harris Yfantis³, MD; James Borin⁴, MD;
Michael Naslund⁴, MD; Eliot Siegel^{1,2} MD



¹Department of Radiology, University of Maryland Medical Center

²Department of Radiology, VA Maryland Health Care System

³Department of Pathology, University of Maryland Medical Center

⁴Department of Surgery, University of Maryland Medical Center

Supported by a grant from the Department of Defense,
Proposal No. PC031042, Award No. W81XWH-04-1-0249

Aim/Purpose

To review the findings of advanced MRI (MR spectroscopy, dynamic contrast-enhanced MR, and diffusion-weighted MR) in a spectrum of prostate cancer patients, with pathologic correlation



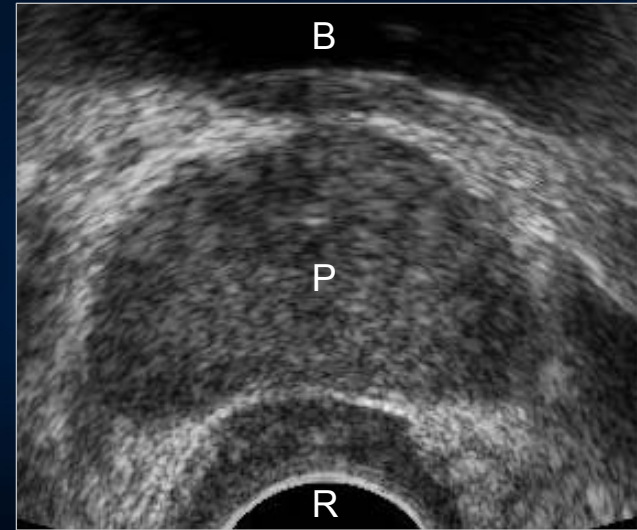
Why Perform Prostate MRI

BENEFITS OF PROSTATE MRI

- Detection of tumor
- Localization within prostate
- Evaluate extra-prostatic spread
- Distant staging
- Assess total prostate size
- Help select treatment method
- Guide targeted therapies
- Surgical planning
- Predict risk of recurrence
- Treatment follow-up

TARGETED THERAPIES NEEDING ACCURATE LOCALIZATION

- Intensity-modulated radiation therapy
- High-intensity focused ultrasound
- Radiofrequency ablation
- Cryoablation



TRANS-RECTAL ULTRASOUND:

B: Bladder base. P: Normal prostate.
R: Rectum with trans-rectal probe in place.

TRANS-RECTAL ULTRASOUND-GUIDED BIOPSY TO DETECT PROSTATE CANCER:

- Random process requiring many samples
- May need repeat biopsy sessions
- Limited sensitivity (reports of below 50%)
- Poor visualization of transitional zone tumors
- Poor localization of tumor within prostate
- Unreliable assessment of extra-prostatic tissues



How to Perform Prostate MRI

PATIENT PREPARATION

- Delay MRI about 6 weeks after biopsy
- Bowel prep (i.e., fleets enema)
- 1mg glucagon IV prior to study
- Rectal exam performed prior to endorectal coil placement

TECHNICAL ISSUES

- High field-strength magnet
- Integrated endorectal and pelvic phased array coils
- High-resolution (i.e., 3-mm) T2W images of prostate in all 3 planes
- Unenhanced T1W axial images of prostate and of entire pelvis
- Routine acquisition of contrast-enhanced images not universally accepted



ENDORECTAL COIL:

- Increased SNR
- Higher spatial resolution
- Widely available disposable **expandable coil**
- Entails inflating balloon with air, leading to susceptibility artifact
- Agents other than air now being used to reduce susceptibility:
 - ❖ Liquid perfluorocarbon
 - ❖ Barium sulfate
- Alternative solid **rigid coil** also used:
 - ❖ Reusable
 - ❖ Does not require inflation with air
 - ❖ Smaller size associated with less rectal distension, patient discomfort, and anatomic distortion of the prostate



Relevant Issues for Interpretation

RELEVANT CLINICAL HISTORY

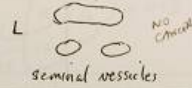



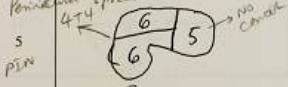


- PSA score
- Prior radiation or hormonal therapy
- Prior TURP or other surgery
- History of prostatitis
- Delay since last biopsy

KEY PATHOLOGIC INFORMATION

- Presence and location of biopsy-proven tumor
- Percent and size of biopsy samples positive for tumor
- Corresponding Gleason score
- Histologic evidence of extra-prostatic spread

PROSTATE SPECIMEN PCA#12 DATE: 3/8/2007

Table 2: slice fixing

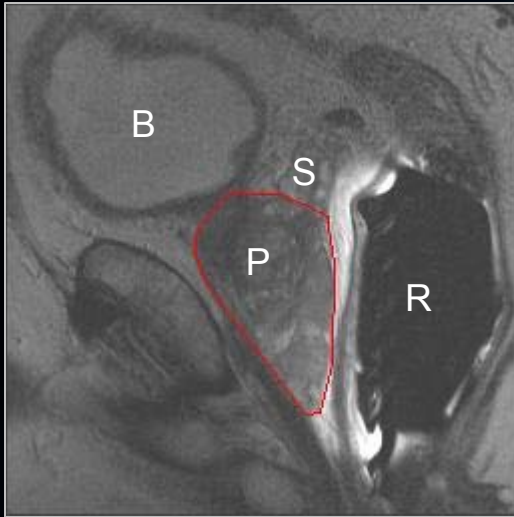
Slice	Figure	Cassette
1		1 Most superior (sem ves)
2		2 (sem ves)
3		3 (sem ves)
4		4 (first slice of prostate)
5		5
6		6
7		7
8		8
9		9

SAMPLE PATHOLOGY REPORT:

When possible, the pathology report should be reviewed in conjunction with interpretation of the imaging.

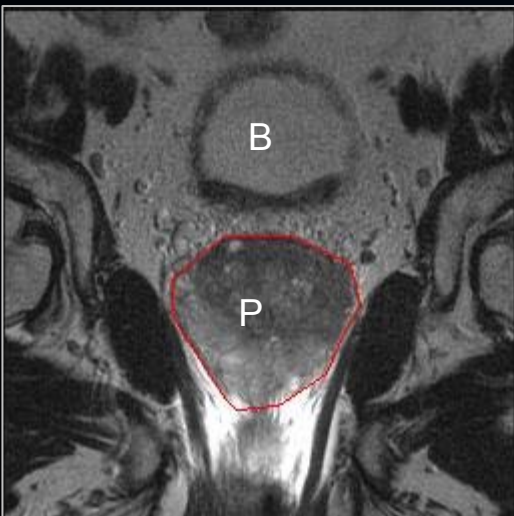


Prostate Anatomy



POSITION WITHIN PELVIS:

- **Prostate (P)** shaped like upside-down cone
 - ❖ Larger superiorly, tapers inferiorly
- **Rectum (R)** is immediately posterior structure
 - ❖ Note artifact/distortion from endorectal coil.
- **Bladder (B)** is superior and directed anteriorly.
- **Seminal vesicles (S)** are superior as well, posterior to the bladder.



DIVISION INTO THIRDS:

- **Base**
 - ❖ From bladder base to level of greatest transverse diameter
- **Mid-gland**
 - ❖ From level of greatest transverse diameter to level of verumontanum
- **Apex**
 - ❖ From level of verumontanum to distal prostatic urethra



Zonal Anatomy of the Prostate

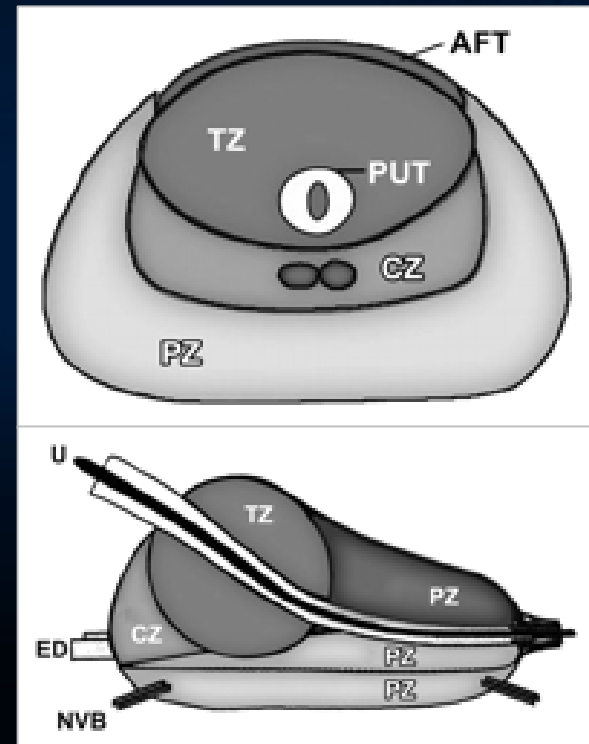
PROSTATE ZONAL ANATOMY

➤ Gland divided into three zones, as described by McNeal et al.:

- ❖ **Peripheral zone**
- ❖ **Central zone**
- ❖ **Transitional Zone**

➤ All three zones contain ducts and acini lined by mucin-containing secretory epithelium.

➤ Each zone has its own unique architecture and histology, predisposing to characteristic local disease processes.



SCHEMATIC OF PROSTATE GLAND ANATOMY IN AXIAL AND SAGITTAL PLANES:

PZ: Peripheral zone. CZ: Central zone.

TZ: Transitional zone. U: Urethra.

AFT: Anterior fibromuscular tissue.

UT: Periurethral tissue. ED: Ejaculatory duct.

NVB: Neurovascular bundle.



Zonal Anatomy of the Prostate

➤ PERIPHERAL ZONE (PZ)

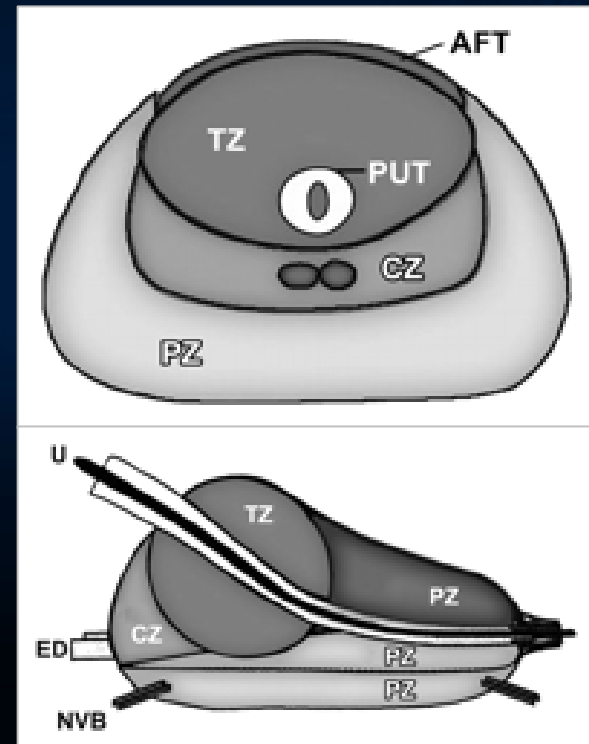
- ❖ 70% of glandular volume
- ❖ Posterior and lateral aspects of gland
- ❖ Occupies greater proportion of gland as proceed from base to apex
- ❖ Contacts the urethra at the level of the apex

➤ TRANSITIONAL ZONE (TZ)

- ❖ 5% of glandular volume in young men, increases in size with age
- ❖ Ball of glandular tissue around prostatic urethra proximal to verumontanum, not found more distally within apex of gland
- ❖ Contains a more compact smooth muscle and fibrous stroma than peripheral zone

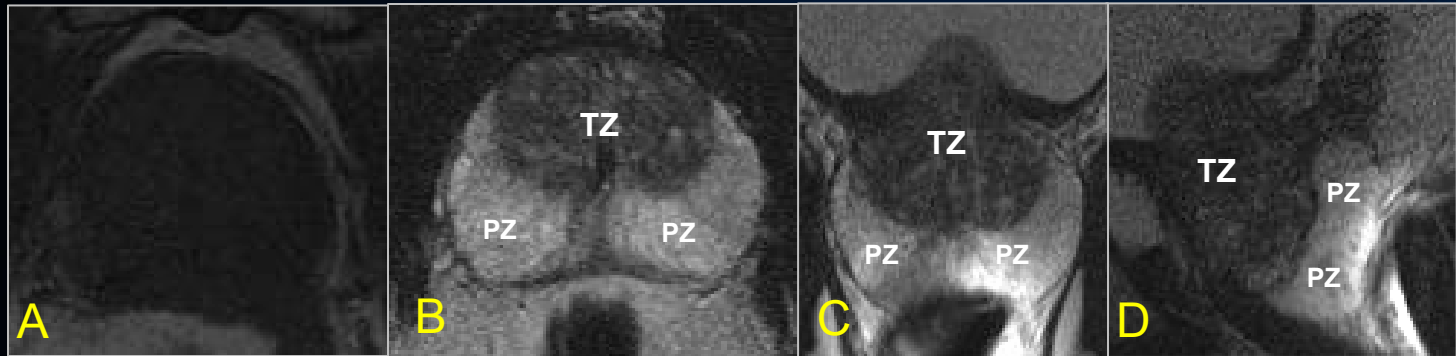
➤ CENTRAL ZONE (CZ)

- ❖ 25% of volume in young men, becomes compressed by transitional zone with age
- ❖ Disk of tissue between transitional and peripheral zones, by prostatic base
- ❖ Contains ejaculatory ducts



SCHEMATIC OF PROSTATE GLAND ANATOMY IN AXIAL AND SAGITTAL PLANES:
PZ: Peripheral zone. CZ: Central zone.
TZ: Transitional zone. U: Urethra.
AFT: Anterior fibromuscular tissue.
UT: Periurethral tissue. ED: Ejaculatory duct.
NVB: Neurovascular bundle.

MRI Appearance of Normal Prostate



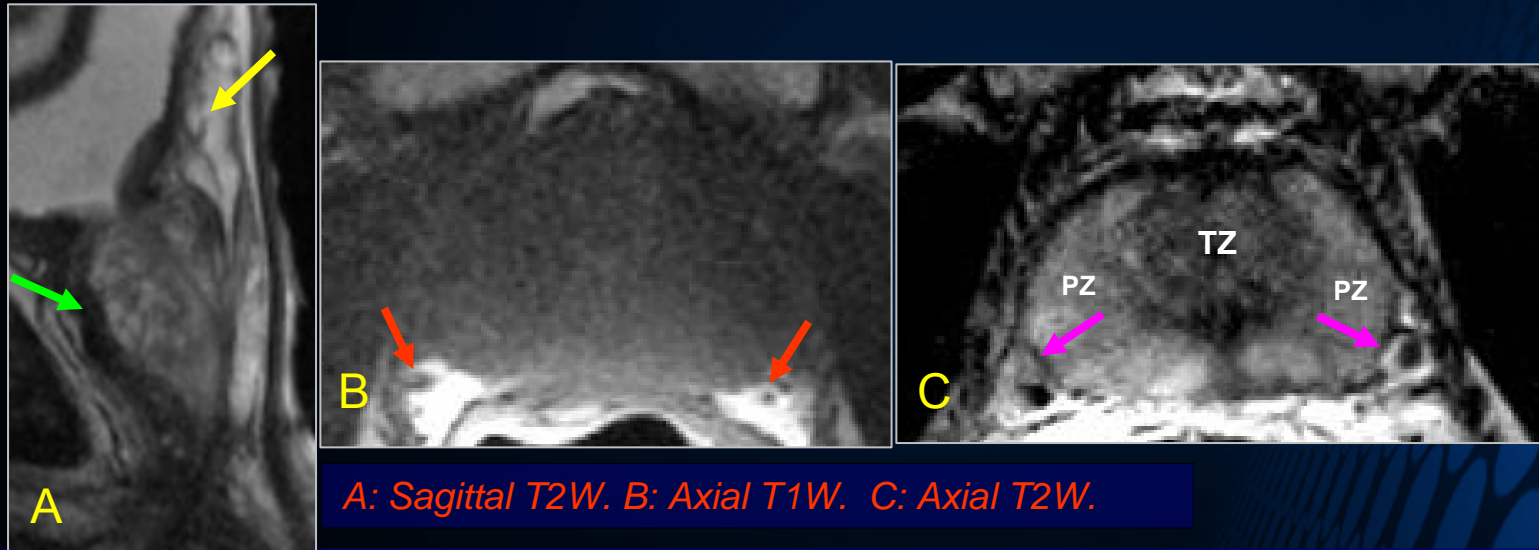
A: Axial T1W. B: Axial T2W. C: Coronal T2W. D: Sagittal T2W.

NORMAL MR SIGNAL CHARACTERISTICS:

- PZ contains abundant mucin-rich glandular tissue and demonstrates homogeneous increased T2 signal when healthy. Thin septations of low T2 signal represent a supporting collagenous network.
- With aging, the TZ enlarges, compressing and effacing the CZ. These two zones can then no longer be visually separated and are collectively referred to as the central gland. The normal TZ demonstrates relatively decreased T2 signal due to compact fibrous stroma.
- On T1W images, all zones have a homogeneous intermediate signal intensity and cannot be reliably distinguished.



Other Structures Seen on MRI



- **SEMINAL VESICLES:** Yellow arrow. Paired structures superior to prostate and posterior to bladder. Contain multiple locules of low-T1 and high-T2 signal.
- **ANTERIOR FIBROMUSCULAR STROMA:** Green arrow. Sheet of low-signal fibrous tissue that extends from bladder neck and drapes over anterior and anterolateral prostate. Contains no glandular tissue.
- **NEUROVASCULAR BUNDLES:** Red arrows. Paired structures posterolateral to the prostate, best seen at the levels of the apex and base. Best evaluated on T1W images as low signal relative to surrounding periprostatic fat.
- **CAPSULE:** Purple arrows. Thin band of low-signal fibrous tissue surrounding peripheral zone, best seen posteriorly and posterolaterally



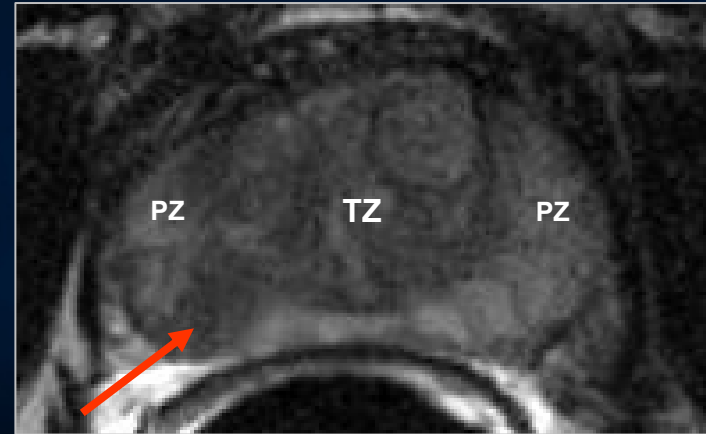
MRI of Prostate Pathology

PROSTATE CANCER

- Arises from prostatic duct acini
- 95% are adenocarcinoma
- 70% occur within PZ and are characterized by decreased T2 signal compared with normal PZ tissue
- 20% occur within TZ and are difficult to detect given normal low T2 signal of TZ
- 10% occur within CZ, which is relatively resistant to pathology

PROSTATIC HYPERPLASIA

- Arises predominantly within TZ
- Causes enlarged, heterogeneous appearance of TZ, with effacement of the CZ
- BPH nodules may be predominantly stromal or predominantly glandular in histology, corresponding with decreased or increased T2 signal respectively



Axial T2W:

Note area of decreased T2 signal (red arrow) within the right PZ, corresponding with foci of prostate cancer. Also note enlarged, heterogeneous TZ, consistent with BPH



Extracapsular Extension

EXTRACAPSULAR EXTENSION (ECE)

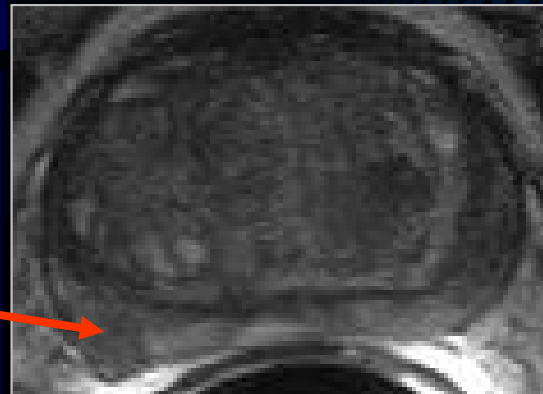
- ECE constitutes one of the most important predictors of prognosis and likelihood of treatment failure
- Directly impacts therapy, as macroscopic ECE often precludes possibly curative prostatectomy.
- While MRI may show macroscopic ECE, microscopic ECE is not detected. However, microscopic ECE is of questionable prognostic and therapeutic significance.
- Direct visualization of gross tumor extension beyond ECE is most reliable finding.
- Other secondary signs are also described.

SECONDARY SIGNS OF ECE

- Asymmetry of the neurovascular bundles
- Obliteration of the rectoprostatic angle
- Capsular retraction or thickening
- Irregular or smooth capsular bulge
- Broad area of tumor contact with capsule



Coronal T2W:
Note gross extracapsular extension of tumor from right prostatic base, contacting the base of the urinary bladder.



Axial T2W:
Note capsular bulge in area of decreased T2 signal within the right mid-gland, a secondary sign of extracapsular extension of tumor.



Seminal Vesicle Invasion

SEMINAL VESICLE INVASION (SVI)

- Occurs from direct extension of tumor from the adjacent prostate base

MOST RELIABLE MR FINDINGS OF SVI

- Decreased T1 and T2 signal within the SV
- Disruption of normal SV histology
- Tumor within the adjacent prostate base

DIFFERENTIAL OF LOW T2 SV SIGNAL

- Extension of tumor
- Post-biopsy hemorrhage
 - ❖ Increased T1 signal
- Post-radiation or hormonal therapy change
- Amyloidosis deposits
- Calculi
- BPH nodule protruding into SV



Axial T2W:

Note decreased T2 signal within the right seminal vesicle, consistent with invasion by tumor.



Other Areas of Tumor Spread

EVALUATION FOR DISTANT METS

- Use large FOV axial T1W sequence
- Spread to bone or nodes outside of the true pelvis constitutes M1 disease, precluding prostatectomy or radiation

LYMPH NODE METASTASES

- Use size criteria (i.e., short axis > 1cm)
- MRI unable to detect micrometastases
- Nodal spread classically proceeds in a stepwise fashion
- Pelvic nodes such as obturator nodes first to be involved
- Unusual to see retroperitoneal or mediastinal nodes without associated pelvic nodes

BONE METASTASES

- MRI more sensitive than bone scan
- Bone mets very unlikely if PSA < 10 ng/mL
- Bone mets expected to show decreased T1 and increased T2 signal, as well as enhancement
- May also see soft tissue component



Axial T1W:

Note right obturator lymph node, enlarged by size criteria, consistent with metastatic nodal disease.



Large FOV axial T1W:

Note focus of decreased T1 signal within right ilium, suspicious for metastasis.



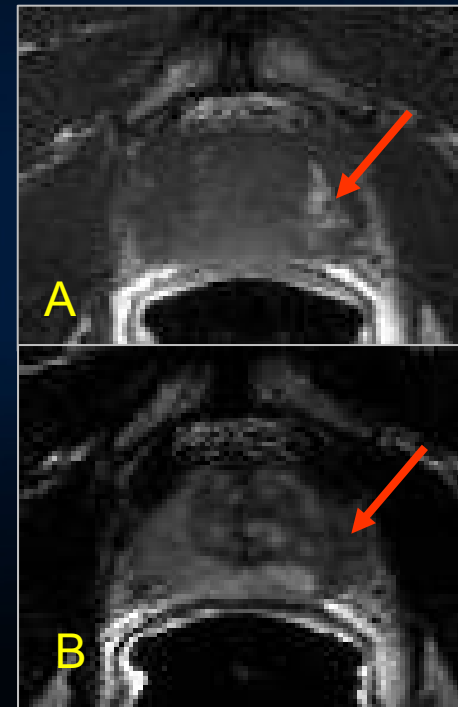
Post-Biopsy Hemorrhage

SIGNIFICANCE OF CITRATE

- The production and secretion of citrate is unique to prostate tissue.
- Citrate is an anticoagulant and will greatly prolong the presence of blood products following biopsy.
- Altered cellular metabolism in the setting of cancer is associated with decreased citrate production.
- Thus, blood products should not persist as long following biopsy of cancer foci.

ROLE IN IMAGING

- Hemorrhage shows low T2 signal, which mimics the appearance of cancer.
- Unlike cancer, hemorrhage shows high T1 signal.
- T1W and T2W images must be assessed together.
- Presence of high T1 signal indicates hemorrhage, which may account for corresponding low T2 signal.
- The co-existence of cancer in such areas of low T2 signal cannot be reliably evaluated.
- For this reason, it is recommended to wait about 6 weeks following biopsy to perform prostate MRI.



A: Axial T1W. B: Axial T2W.

Note area of increased T1 signal within PZ, indicating presence of post-biopsy hemorrhage. This may account for the decreased T2 signal within this area, precluding a reliable evaluation for the presence of prostate cancer.



Need for Advanced MR Applications

CONVENTIONAL T2W MR

- Specificity limited by multitude of processes causing decreased T2 signal within PZ
- Limited sensitivity for tumors within TZ, given normally decreased T2 signal of the TZ and heterogeneous appearance of BPH.
- Limited for small tumors under 1cm
- Limited for local staging of disease
- Does not predict tumor aggressiveness

DIFFERENTIAL OF DECREASED T2 SIGNAL

- Cancer
- Post-biopsy hemorrhage
- BPH
- Radiation change
- Hormonal therapy
- Inflammation/prostatitis
- Atrophy/fibrosis

ADVANCED MR APPLICATIONS

- Advanced MR techniques are being used to assess functional aspects of the prostate.
- MR spectroscopy is most established of these techniques.
- Dynamic contrast-enhanced MR (DCE-MR) and diffusion-weighted imaging (DWI) show promise, but are less well established.
- These techniques are used in conjunction with conventional MR sequences for a comprehensive evaluation.

CONVENTIONAL MRI

<i>T1W, T2W images</i>	Anatomy, tissue characterization
------------------------	----------------------------------

ADVANCED MRI

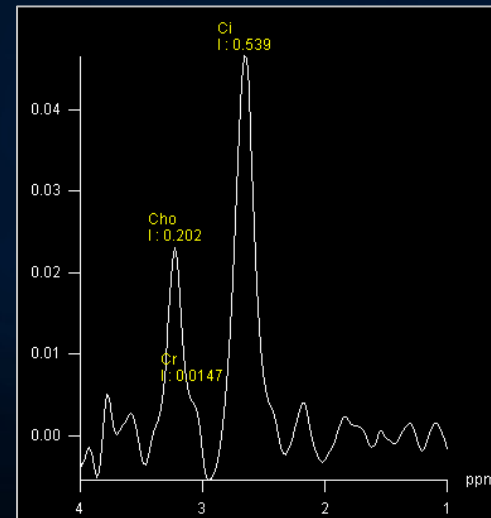
<i>MR Spectroscopy</i>	Metabolism
<i>Dynamic contrast-enhanced MR</i>	Perfusion characteristics
<i>Diffusion-weighted imaging</i>	Cellular density



MR Spectroscopy

CONCEPT

➤ Prostate cancer demonstrates decreased citrate production from altered cellular metabolism and increased choline production from increased cell membrane turnover. Spectroscopy is able to depict the relative concentration of these metabolites within small voxels throughout the prostate gland. Normal PZ is expected to show a large choline peak at a resonance of 2.6 ppm and low peaks for choline and creatine at 3.2 and 3.0 ppm respectively. Given the proximity of the choline and creatine peaks, these two metabolites are difficult to separate at 1.5T and are usually combined. The (choline+creatine)/citrate ratio, termed CC/C, is measured for each voxel for analysis. A mean CC/C ratio within PZ of 0.22 ± 0.13 has been reported. Within PZ, a CC/C ratio that is 2 standard deviations above mean (SDAM) is suggestive of cancer; a ratio that is 3 SDAM is very suggestive. In comparison, benign TZ may show decreased citrate in areas of predominantly stromal BPH, thereby mimicking cancer. A mean CC/C ratio within TZ of 0.61 ± 0.21 has been reported and a more stringent CC/C threshold of 4 SDAM has been applied to evaluate for cancer within TZ.



MR spectrum from a voxel containing normal prostate tissue demonstrates an elevated citrate peak and intermediate choline peak. CC/C ratio of 0.40 is below 2 SDAM and not suspicious for cancer.

BENEFITS

- Increases specificity by differentiating cancer from numerous benign causes of decreased T2 signal.
- Improved localization of tumor within the prostate
- Increased accuracy for predicting ECE.
- CC/C ratio correlates with histologic Gleason score, and therefore, with tumor aggressiveness
- May detect tumor when PZ loses its normal high T2 signal following radiation or hormonal therapy

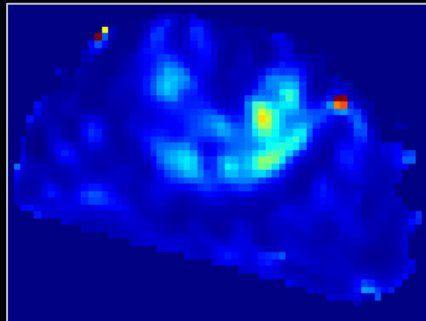


Dynamic Contrast-Enhanced MRI

CONCEPT

- Altered pattern of angiogenesis in cancer:
 - ❖ Increased vascularity
 - ❖ Increased permeability of vessels
 - ❖ Expansion of interstitial space
- Following gadolinium injection and serial rapid volume acquisitions of the prostate, normal PZ shows a homogeneous low level of enhancement. In comparison, PZ cancer shows earlier and stronger wash-in as well as earlier wash-out. This difference can increase the accuracy for tumor detection within PZ compared with T2W MRI. Benign TZ demonstrates heterogeneous and overall increased vascularity due to BPH and is not well assessed with DCE-MR.

K^{trans} map from DCE-MRI of normal prostate shows homogeneous low level of vascularity within the PZ and mild hypervascularity within the TZ, reflective of BPH.



TECHNICAL ISSUES

- Evaluation of perfusion is widely variable and controversial, with two major methods used:
 - **Measure of time-resolved enhancement:**
 - ❖ Direct measures of tissue perfusion
 - ❖ Relatively simple to perform
 - ❖ Includes relative peak enhancement, time-to-peak, wash-in rate, and wash-out rate
 - **Compartmental-based pharmacokinetic models:**
 - ❖ May better estimate vascular permeability
 - ❖ Uses more complex two-compartmental model of the transfer of contrast between the plasma and the extracellular extravascular space
 - ❖ Model provides the volume transfer constant K^{trans} , which is expected to reflect permeability and to be higher in prostate cancer
- **Limited for detection of TZ tumors** due to hypervascularity of BPH.
- Has been applied within peri-prostatic tissue to **more accurately detect ECE**



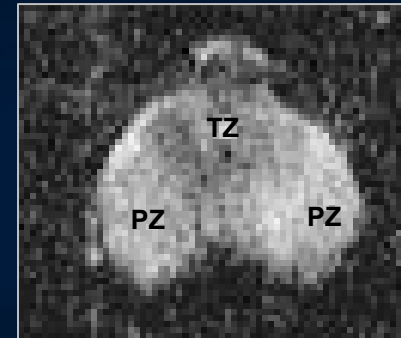
Diffusion Weighted Imaging

CONCEPT

➤ DWI reflects random molecular motion of water molecules, as measured by the apparent diffusion coefficient (ADC). ADC values tend to be decreased in various cancers, attributed to increased tumor cellularity. A decreased ADC value in comparison with benign prostate tissue has also been documented within prostate cancer.

BENEFITS

- May allow detection of visually subtle tumors that are missed on T2W images
 - ❖ Good contrast on ADC map between cancer and benign tissue
 - ❖ Quantitative nature of ADC map
 - ❖ ADC values shown to measure tissue properties not reflected by T2 values
- Tumors within both PZ and TZ tumors observed to have lower ADC compared with benign PZ and TZ tissue respectively
- Various thresholds to distinguish benign and malignant tissue have recently been proposed.
- ADC has been observed to correlate with PSA.



ADC map from DWI of normal prostate demonstrates a bright PZ and comparatively darker TZ.

DIFFICULTIES

- Normal ADC of PZ varies between individuals.
- ADC values within benign and malignant tissues overlap.
- Normal TZ has lower ADC than normal PZ, making analysis within TZ more difficult



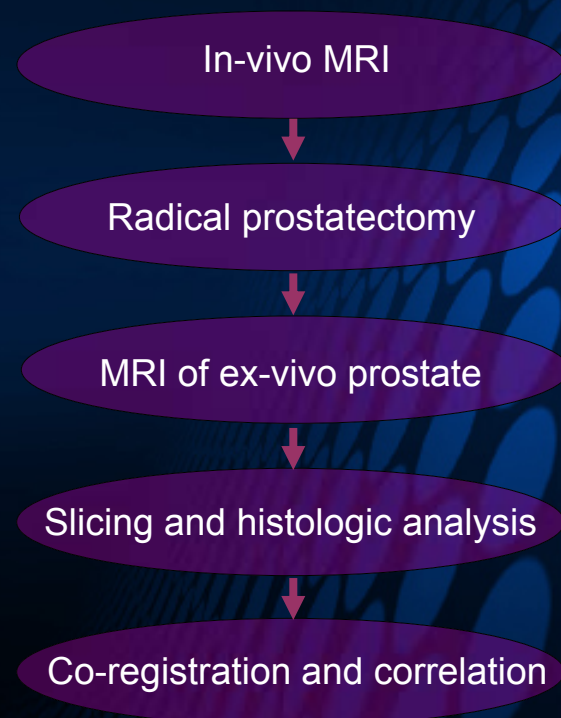
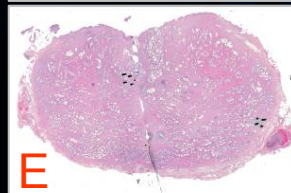
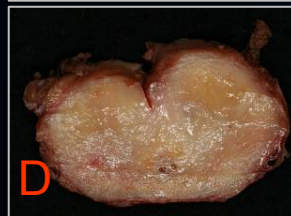
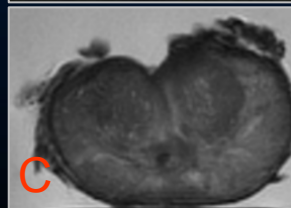
Radiologic-Pathologic Correlation

OUR PROTOCOL

- We present MR imaging from patients with known prostate cancer, awaiting radical prostatectomy.
- The ex-vivo prostate also underwent MRI following prostatectomy, prior to histopathologic analysis.
- The in-vivo images were registered with the ex-vivo images, which were then registered with the pathologic slices. This process allowed for a correlation of the MR findings on the in-vivo images with the pathologic slices.
- Each MRI was obtained on a 1.5T Siemens Magnetom Avanto MRI scanner and included:
 - ❖ Standard T1W and T2W sequences
 - ❖ MR spectroscopy
 - ❖ DCE-MR
 - ❖ DWI
- The advanced sequences were used to obtain CC/C map, K^{trans} map, and ADC map.

SIGNIFICANCE

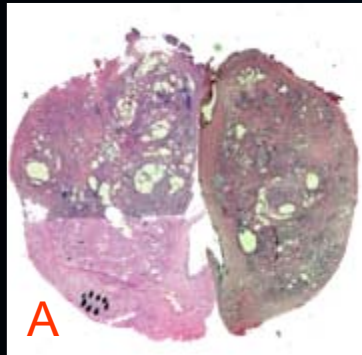
- To our knowledge, the findings on conventional MRI, MR spectroscopy, DCE-MRI, DWI, and histopathology have not all been correlated within individual prostate cancer patients.



- A: In-vivo T2W MRI*
- B: Prostatectomy specimen*
- C: Ex-vivo T2W MRI*
- D: Prostate specimen slice*
- E: Histologic slice using H&E stain*

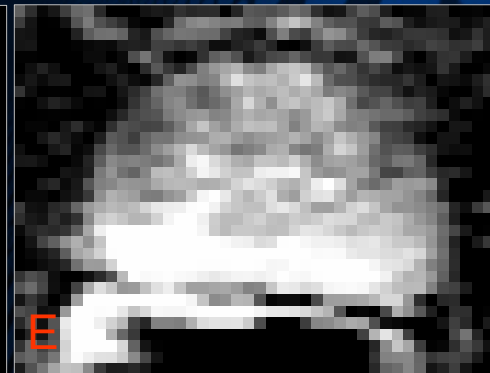
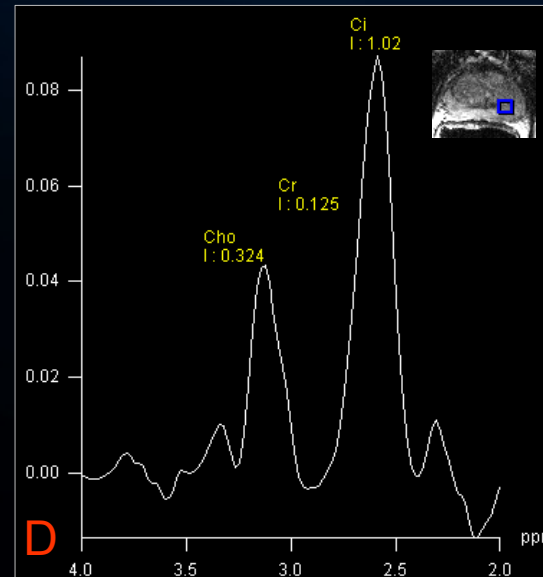
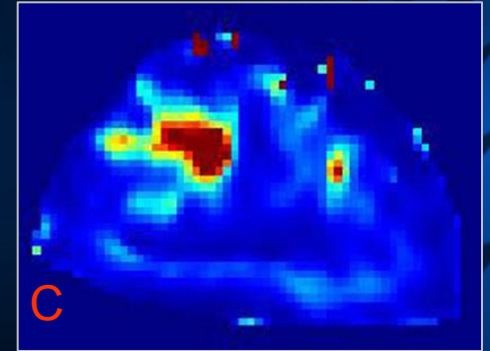
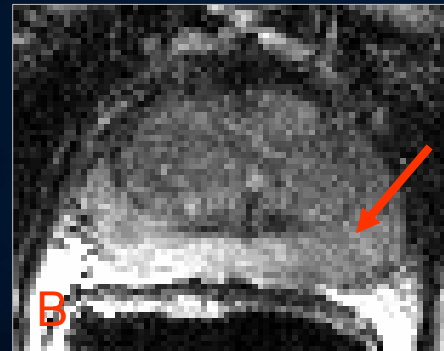


Radiologic-Pathologic Correlation

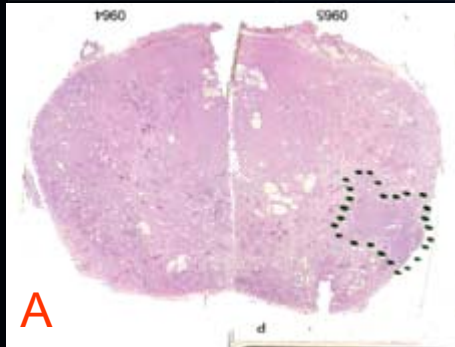


- **Pathology step section (A)** shows prostatitis in left PZ with no evidence of cancer.
- **T2W-image (B)** shows non-specific mild decreased T2 signal in the left PZ.
- **DCE-MRI (C)** shows no hypervascularity in this region.
- **MRS (D)** shows a non-suspicious CC/C ratio of 0.45.
- **ADC map (E)** shows no corresponding restricted diffusion in this region.

PROSTATITIS

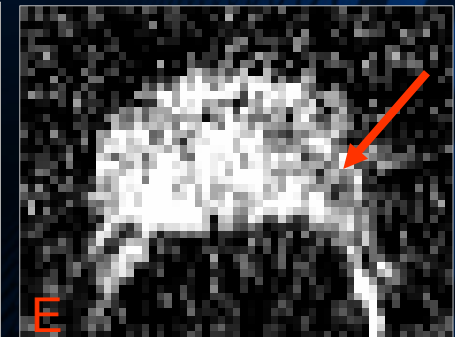
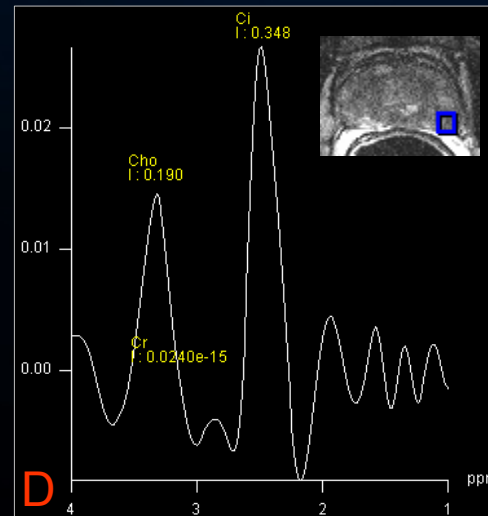
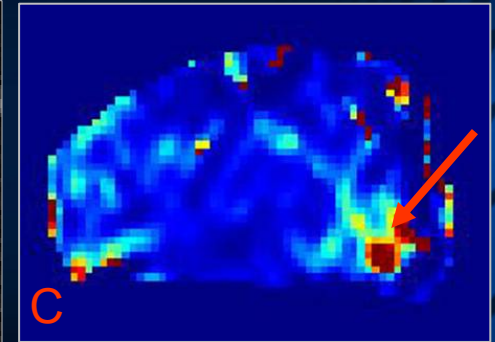


Radiologic-Pathologic Correlation

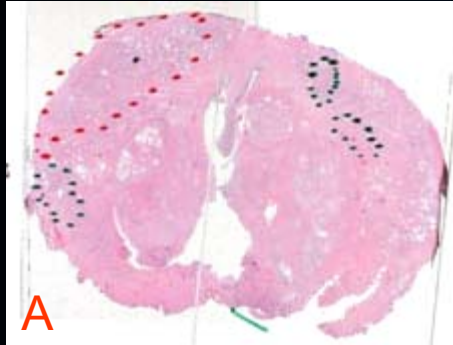


- **Pathology step section (A)** shows left PZ cancer with ECE, marked with dotted green line.
- **T2W-image (B)** shows low signal within the left PZ, with associated asymmetric capsular bulge
- **DCE-MRI (C)** shows a discrete focus of hypervascularity within the left PZ in the region of the capsule.
- **MRS (D)** shows a CC/C ratio of 0.55 in left PZ. This ratio is mildly elevated and may be seen in benign or malignant PZ.
- **ADC map (E)** shows restricted diffusion in the corresponding region of the left PZ.

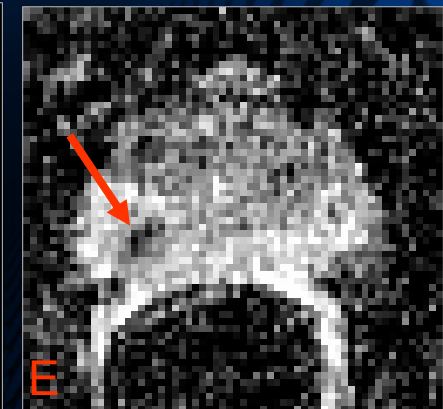
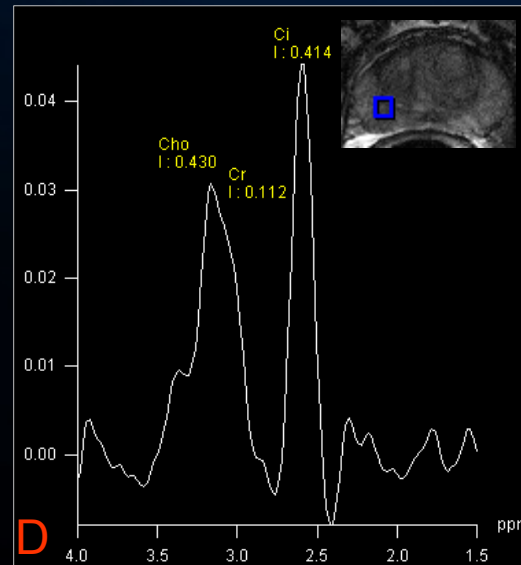
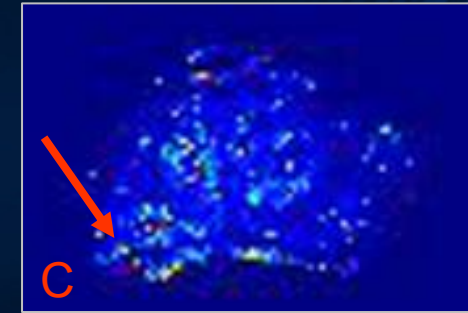
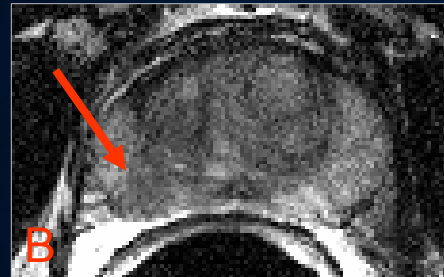
FOCAL TUMOR WITH ECE



Radiologic-Pathologic Correlation



SMALL TUMOR FOCI



➤ **Pathology step section (A)** shows small areas of tumor within the PZ bilaterally, marked by dotted green lines. Dotted red lines mark prostatic intra-epithelial neoplasia.

➤ **T2W-image (B)** shows a focus of low signal within the right PZ.

➤ **DCE-MRI (C)** shows mild asymmetric hypervascularity within the right PZ.

➤ **MRS (D)** shows a CC/C ratio of 1.31 in right PZ, consistent with cancer.

➤ **ADC map (E)** shows restricted diffusion in the right PZ, corresponding with the area of T2 signal abnormality.

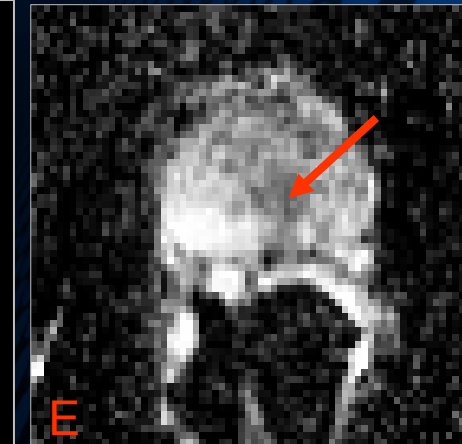
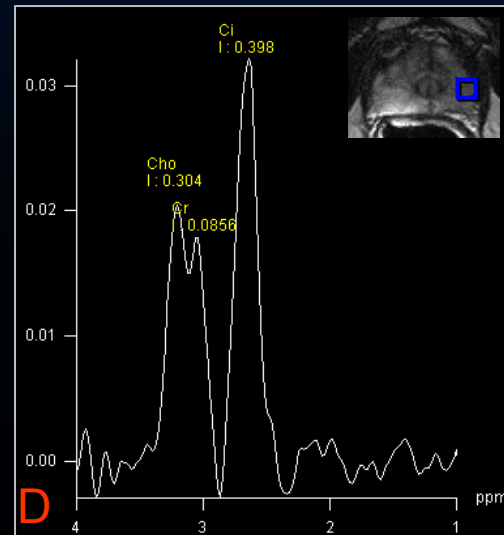
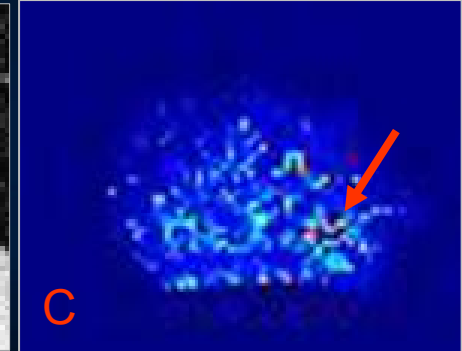
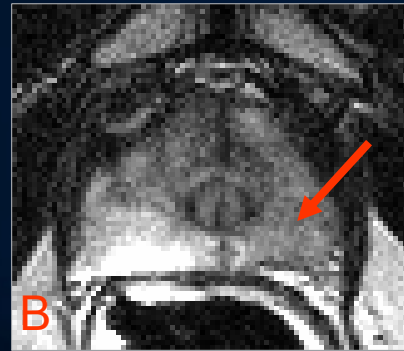


Radiologic-Pathologic Correlation

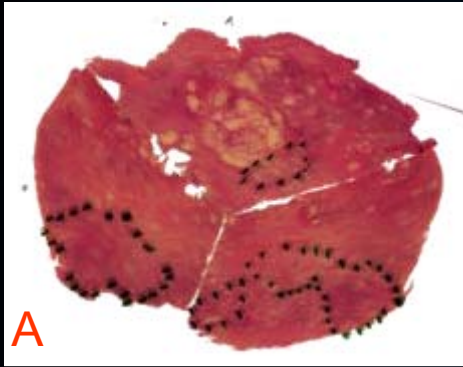


- **Pathology step section (A)** shows areas of tumor within the PZ bilaterally, larger on the left, as marked by continuous green lines. Dotted red lines represent prostatic intra-epithelial neoplasia.
- **T2W-image (B)** shows decreased signal within the PZ bilaterally, more pronounced on the left.
- **DCE-MRI (C)** shows an area of hypervascularity within the left PZ.
- **MRS (D)** shows a CC/C ratio of 0.98 within left PZ, consistent with cancer.
- **ADC map (E)** shows a small area of restricted diffusion within the left PZ.

SMALL TUMOR FOCI

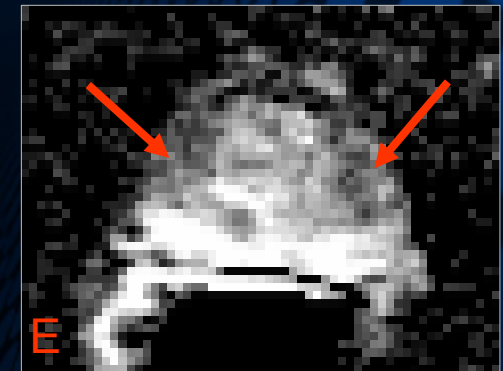
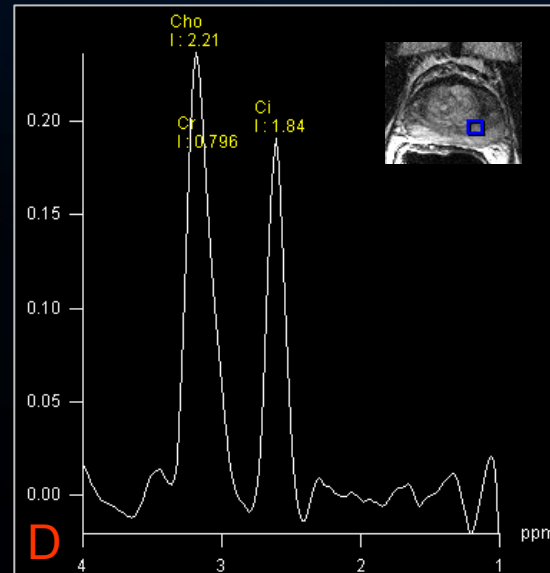
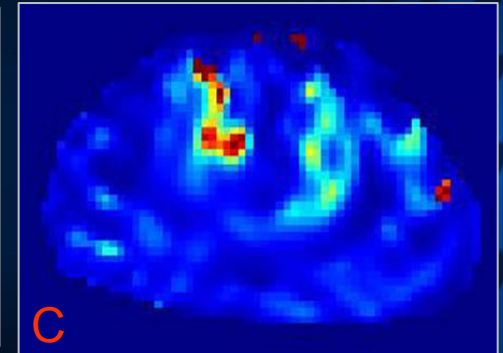
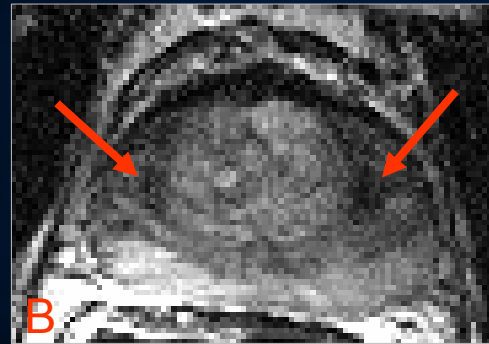


Radiologic-Pathologic Correlation

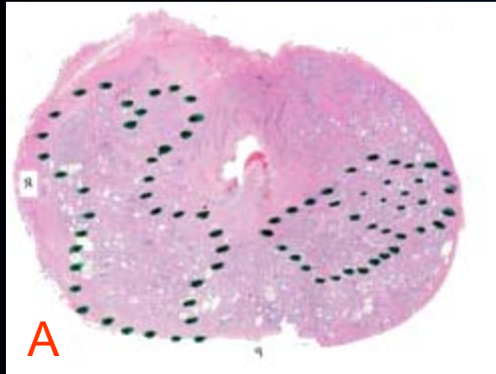


- Pathology step section (A) shows areas of cancer bilaterally, marked with dotted green lines.
- T2W-image (B) shows areas of decreased T2 signal within the lateral aspect of the PZ bilaterally.
- DCE-MRI (C) shows no discrete focus of corresponding PZ hypervascularity.
- MRS (D) shows a CC/C ratio of 1.63 within the left PZ, consistent with cancer.
- ADC map (E) shows corresponding areas of restricted diffusion within the PZ bilaterally.

LARGE TUMOR FOCI



Radiologic-Pathologic Correlation



➤ **Pathology step section (A)** shows large areas of cancer bilaterally, marked with dotted green lines. The inner circle of green dots in the left PZ marks a more ill-defined area of cancer.

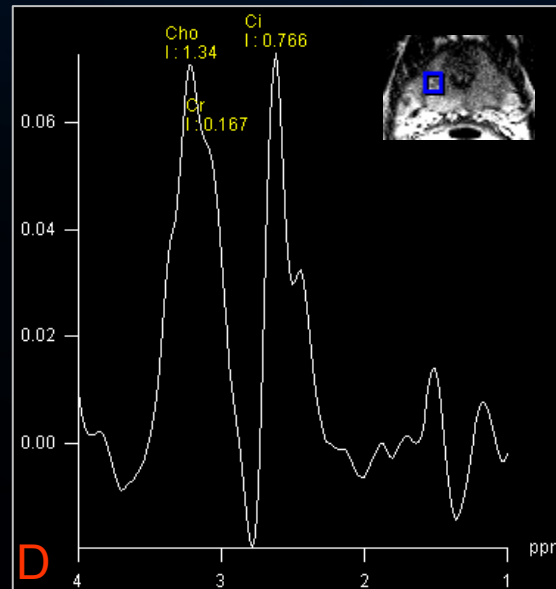
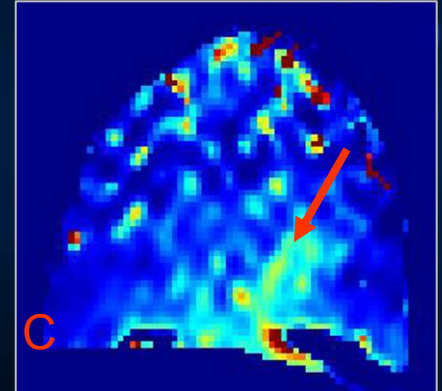
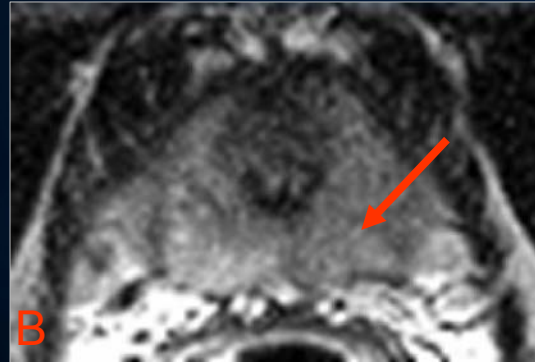
➤ **T2W-image (B)** shows low signal throughout the PZ that is more pronounced on the left.

➤ **DCE-MRI (C)** shows mildly asymmetric hypervascularity within the left PZ.

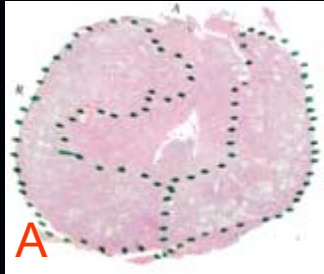
➤ **MRS (D)** shows a CC/C ratio of 1.96 within the right PZ, confirming presence of cancer within this side of the prostate.

➤ **ADC map (E)** shows area within the left PZ that is mildly darker than on the right.

LARGE TUMOR FOCI



Radiologic-Pathologic Correlation



➤ Pathology step section (A) shows diffuse tumor marked by dotted green lines.

➤ T1W-image (B) shows increased T1 signal within the left PZ, consistent with post-biopsy hemorrhage. This finding limits evaluation for cancer in this area.

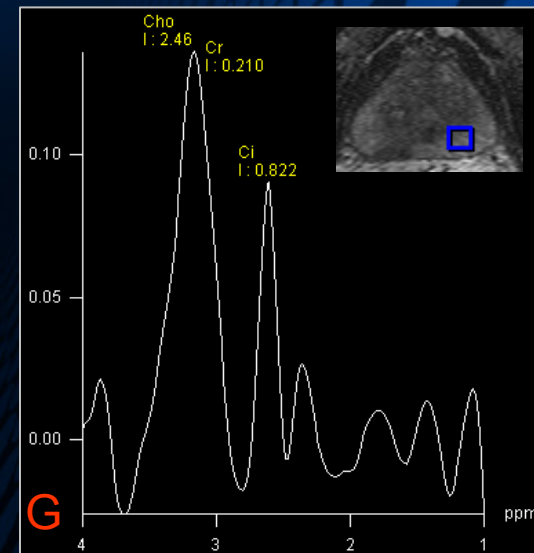
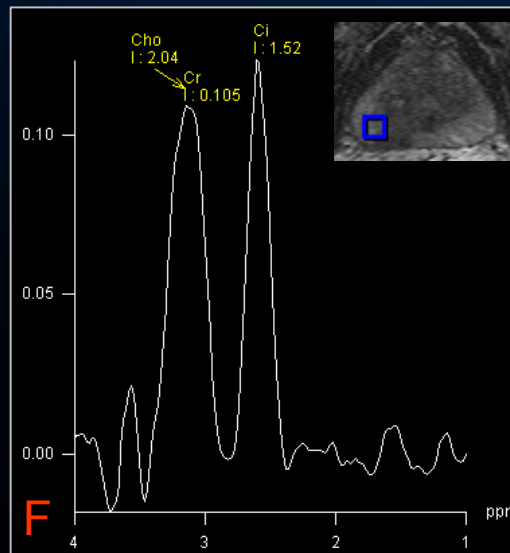
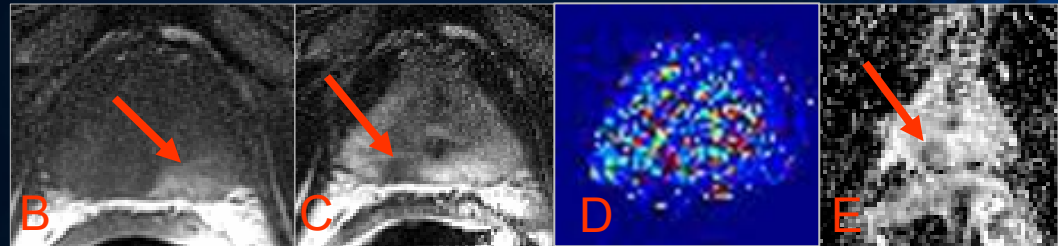
➤ T2W-image (C) shows focal low signal in the right PZ. There is normal signal in the region of abnormal T1 signal within left PZ.

➤ DCE-MRI (D) shows widespread hypervascularity throughout the prostate.

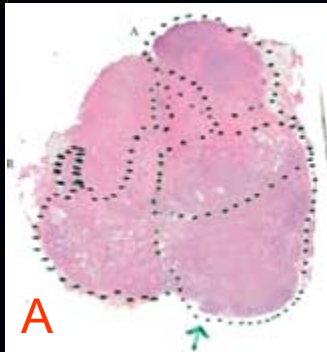
➤ ADC map (E) shows a focus of restricted diffusion within the right PZ, corresponding with the area of T2 signal abnormality.

➤ MRS (F) and (G) from the right and left PZ demonstrate CC/C ratios of 1.41 and 3.2 respectively, consistent with bilateral cancer.

DIFFUSE TUMOR

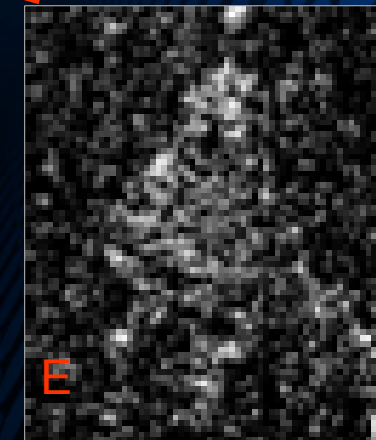
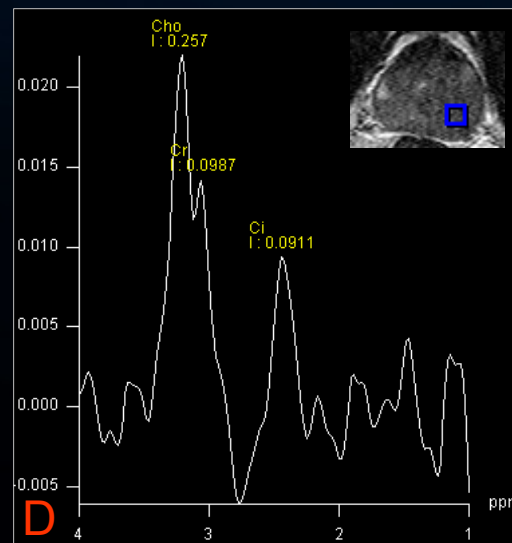
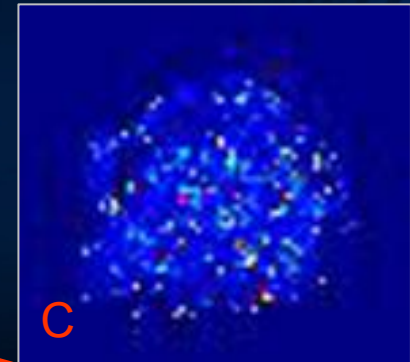
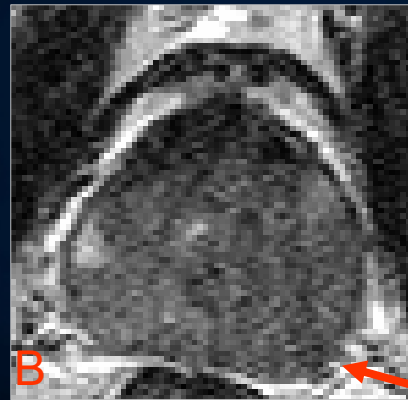


Radiologic-Pathologic Correlation

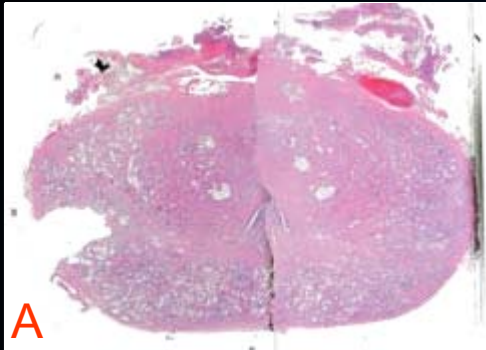


- **Pathology step section (A)** shows diffuse tumor, marked by dotted green lines, with ECE on the left
- **T2W-image (B)** shows widespread decreased signal throughout the PZ and TZ. There is mild irregularity of the capsule on the left.
- **DCE-MRI (C)** shows no discrete focus of hypervascularity.
- **MRS (D)** shows a CC/C ratio of 3.90 in the left PZ, consistent with cancer.
- **ADC map (E)** shows a dark appearance of the entire prostate, corresponding with the diffuse decrease in T2 signal and diffuse cancer observed on pathology.

DIFFUSE TUMOR WITH ECE



Radiologic-Pathologic Correlation



➤ **Pathology step section (A)** shows changes of BPH within the TZ, with no evidence of cancer.

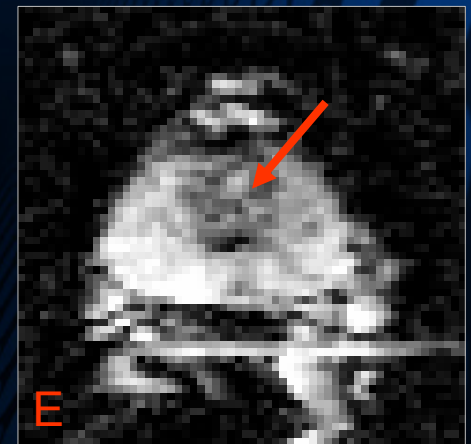
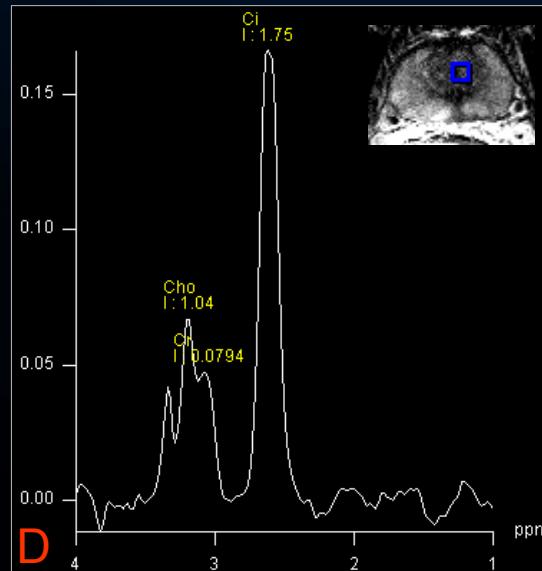
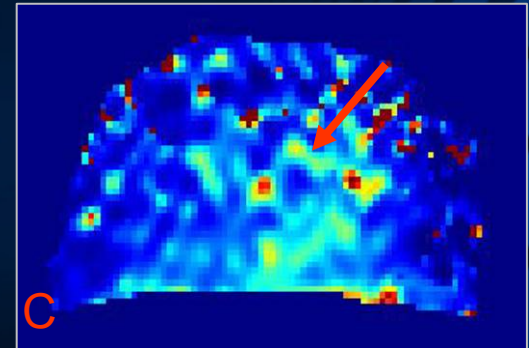
➤ **T2W-image (B)** shows heterogeneous decreased signal throughout the TZ without discrete lesion.

➤ **DCE-MRI (C)** shows mild hypervascularity within the region of the TZ, consistent with the inflammatory nature of BPH.

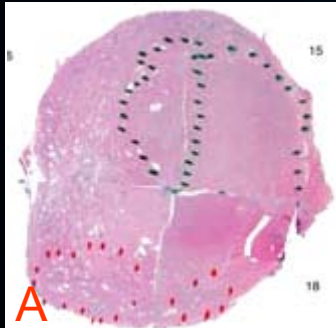
➤ **MRS (D)** shows a CC/C ratio of 0.64. While this ratio in the PZ is concerning for malignancy, this value in the TZ is consistent with non-cancerous BPH.

➤ **ADC map (E)** shows heterogeneously dark appearance of the TZ.

BPH IN BENIGN TZ



Radiologic-Pathologic Correlation



➤ **Pathology step section (A)** shows tumor centered within the left TZ, marked with dotted green lines. Dotted red lines mark prostatic intra-epithelial neoplasia.

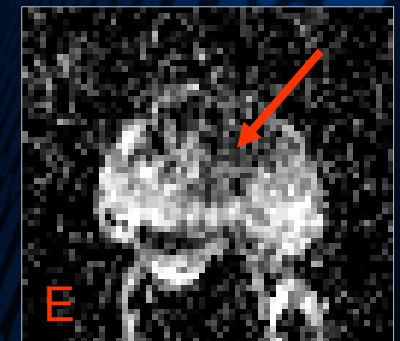
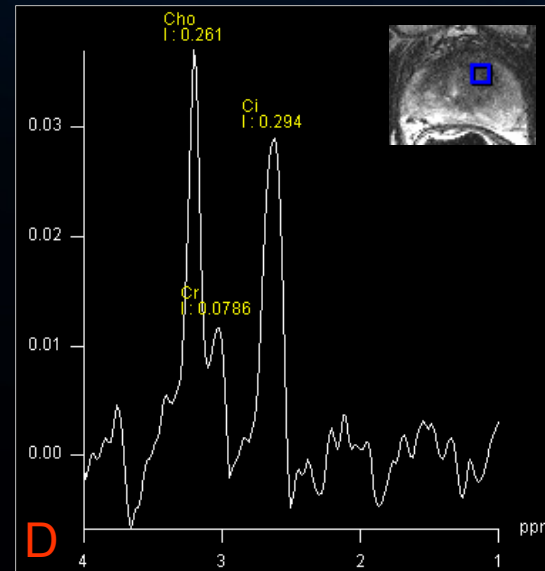
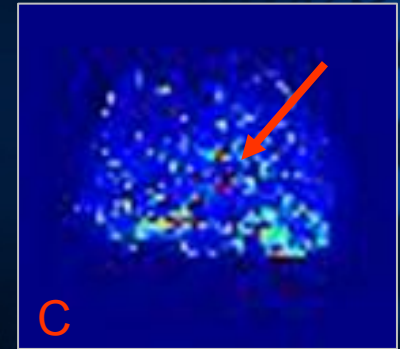
➤ **T2W-image (B)** shows uniformly decreased signal within the left TZ. Homogeneously decreased T2 signal has been suggested as a marker of TZ tumor.

➤ **DCE-MRI (C)** shows mild hypervascularity within this region, which may be a normal finding in the TZ.

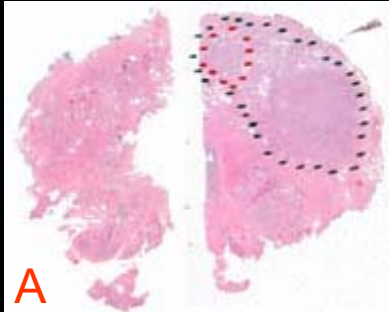
➤ **MRS (D)** shows a CC/C ratio of 1.16. This ratio is greater than the range of values expected for BPH and is suspicious for cancer.

➤ **ADC map (E)** shows restricted diffusion within the TZ, more distinct on the left.

TZ TUMOR



Radiologic-Pathologic Correlation



➤ **Pathology step section (A)** shows tumor within the left TZ, marked with dotted green line. Dotted red line mark prostatic intra-epithelial neoplasia.

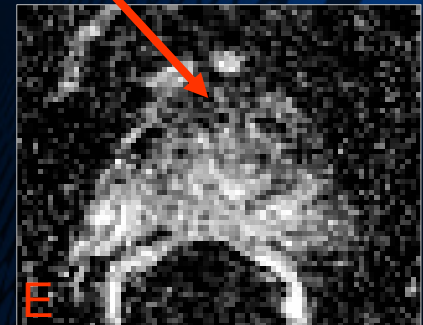
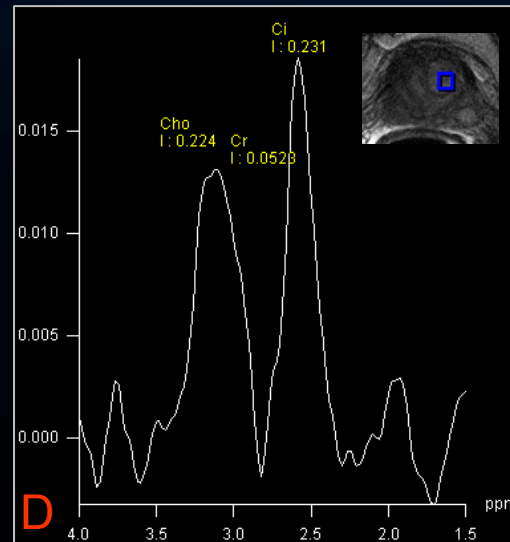
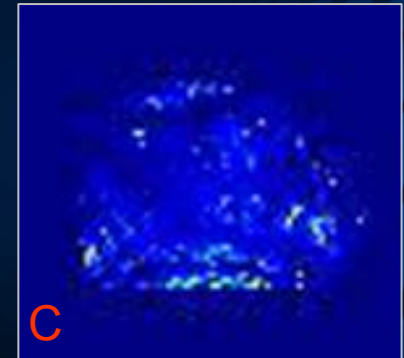
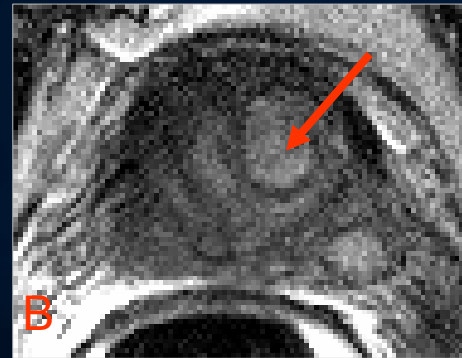
➤ **T2W-image (B)** shows nodular increased signal in the left TZ that could represent a glandular BPH nodule.

➤ **DCE-MRI (C)** shows no hypervascularity within this region.

➤ **MRS (D)** shows a CC/C ratio of 1.20 in left TZ. This ratio is greater than the range of values expected for BPH and is suspicious for cancer.

➤ **ADC map (E)** shows an overall dark appearance of the TZ.

TZ TUMOR



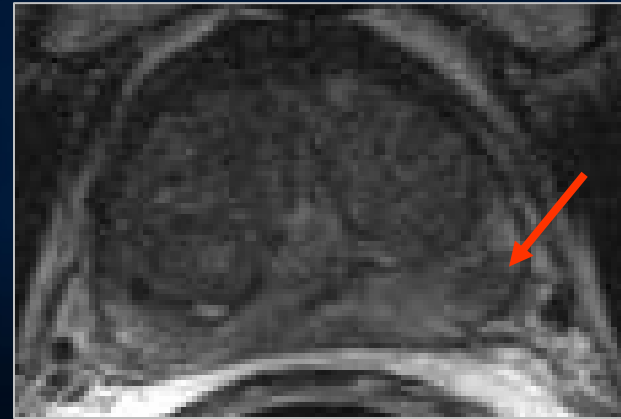
T2W MRI: Summary

ADVANTAGES

- Most widely available and studied MR application in the prostate
- Good sensitivity for detecting tumor
- Routinely applied in extra-prostatic locations (i.e., to evaluate for neurovascular bundle and seminal vesicle invasion)

DISADVANTAGES

- Low specificity
- Poor localization within gland
- Limited by post-biopsy hemorrhage
- Limited for detecting:
 - ❖ TZ tumors
 - ❖ Small tumors under 1cm
 - ❖ Extracapsular extension
 - ❖ Recurrence after therapy



T2W image demonstrates suspicious focus of tumor as area of decreased signal intensity (red arrow).



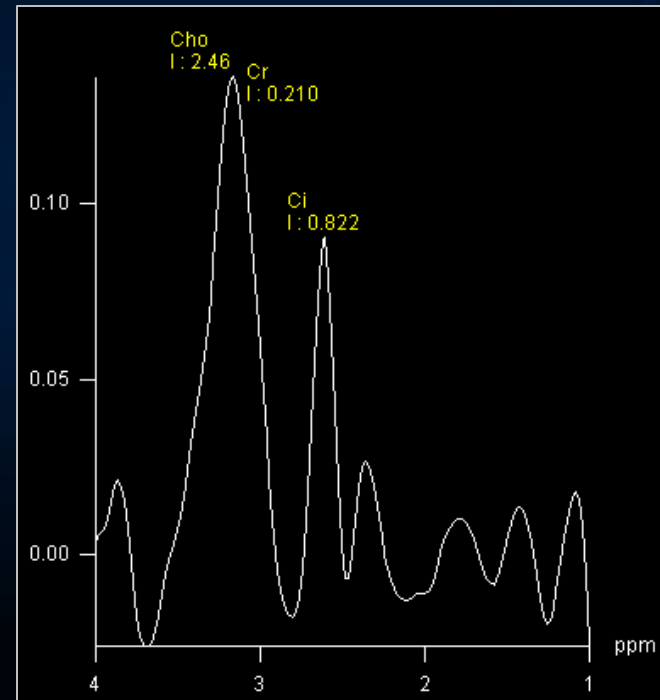
MR Spectroscopy: Summary

ADVANTAGES

- Accuracy well-documented within radiology literature
- May increase sensitivity and specificity combined with T2WI
- Increases ability to localize tumor seen on T2WI and to predict extracapsular extension
- May be applied within TZ
- May be used to detect tumor recurrence after therapy
- Correlates with Gleason score

DISADVANTAGES

- Limited by post-biopsy hemorrhage
- Cannot directly visualize extra-prostatic tissues
- Often obtain larger voxels with limited spatial resolution
- Artifact may result in exclusion of some voxels from analysis
- Long acquisition time (about 10 minutes)



MR spectrum shows a decreased citrate peak and elevated choline peak, giving a CC/C ratio of 3.24, consistent with cancer.



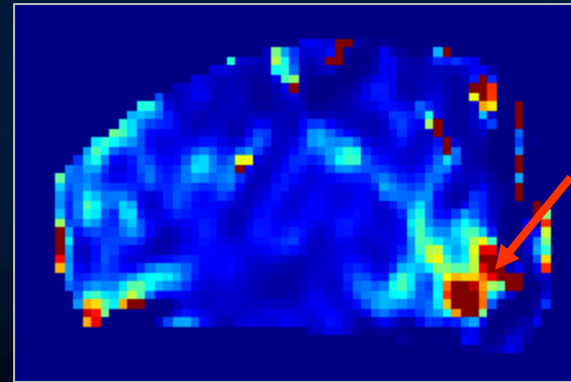
DCE-MRI: Summary

ADVANTAGES

- May increase sensitivity, specificity, and localization combined with T2WI
- May be used to directly image extra-prostatic tissues, allowing visualization of extracapsular extension
- May be used to detect tumor recurrence following therapy
- May be obtained using high spatial-resolution acquisition

DISADVANTAGES

- Limited by post-biopsy hemorrhage
- Limited in TZ due to increased vascularity of BPH
- Currently wide variation in how DCE is performed, without consensus regarding which parameters to use
- Not all cancers demonstrate enough hypervascularity to be detected



Parametric map from DCE-MRI demonstrates suspicious focus of PZ cancer as area of increased K^{trans} .



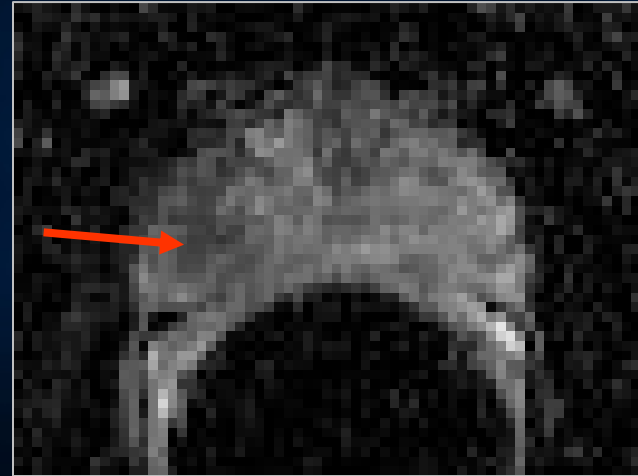
DWI: Summary

ADVANTAGES

- Fast acquisition (as little as under two minutes), with easy post-processing
- May increase sensitivity and specificity combined with T2WI
- Quantitative thresholds to distinguish benign and malignant tissue proposed
- May be applied within TZ
- Correlates with PSA

DISADVANTAGES

- Limited by post-biopsy hemorrhage
- DWI sequence prone to artifacts and image distortion
- Variability between individuals in normal ADC values
- Has not been used to evaluate peri-prostatic tissues
- Data to confirm clinical impact still emerging



ADC map from DWI demonstrates suspicious focus of PZ tumor as area of decreased ADC.



Integrating Advanced MR Techniques

Putting it all together...

Use **conventional T1W and T2W** images to look for cancer within gland itself and within extracapsular tissues; for local invasion of seminal vesicles, bladder, or rectum; and for nodal or osseous metastases

The advanced applications of **spectroscopy, DCE-MR, and DWI** may increase the sensitivity and specificity for tumor detection and localization.

To evaluate transitional zone: **Spectroscopy, DWI**

To increase accuracy for extracapsular spread: **Spectroscopy, DCE**

To correlate with Gleason score/PSA: **Spectroscopy, DWI**



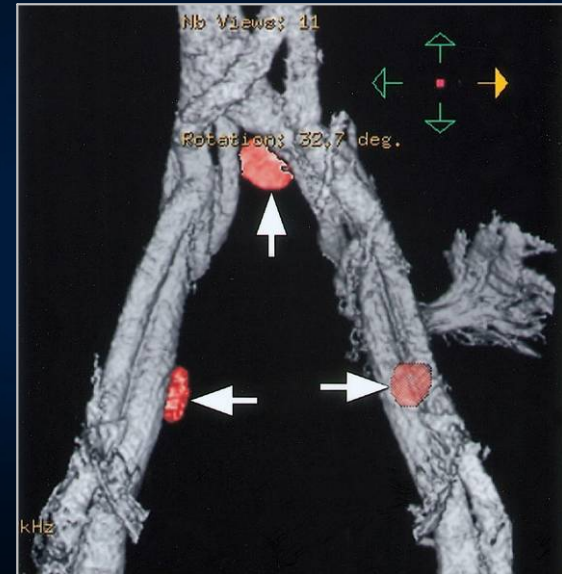
Future Direction of Prostate MR

➤ **3T MRI:** Provides increased SNR which has several potential benefits:

- ❖ May use to increase spatial resolution to detect smaller tumors
- ❖ May use to reduce scanning time to improve DCE-MR and DWI
- ❖ Greater separation of metabolic peaks improves spectroscopy (i.e., routine use of polyamine peak)
- ❖ May not need endorectal coil

➤ **MR LYMPOGRAPHY:** Use of superparamagnetic iron oxide particles may differentiate normal from metastatic nodes.

➤ **MOLECULAR IMAGING:** MR spectroscopy of molecular markers (i.e., markers of cellular proliferation and apoptosis) may better predict tumor cell type and aggressiveness.



MAPPING OF LYMPH NODES IN A PATIENT WITH PROSTATE CANCER:

Surface-rendered 3D MR image shows the iliac vessels, distal aorta, and inferior vena cava, which are enhanced due to the effect of ferumoxtran-10 on T1. Malignant nodes are coded in red (arrows), thus showing their relationships to the major vessels.

Figure courtesy of Harisinghani MG et al. Radiographics 2004;24:867-878. Copyright Radiological Society of North America, 2004. <http://www.rsna.org/>



Conclusions

- We presented the findings on T2-weighted MRI, MR spectroscopy, DCE-MRI, and DWI, with pathologic correlation, in a spectrum of prostate cancer patients.
- These MR applications may improve the detection, localization, and staging of prostate cancer.
- These advances may allow for more individualized treatment regimens that include new targeted therapies that are appropriate for the smaller, lower-grade tumors often detected today.
- Continued research is expected to further refine these techniques and to better delineate their respective advantages and disadvantages.



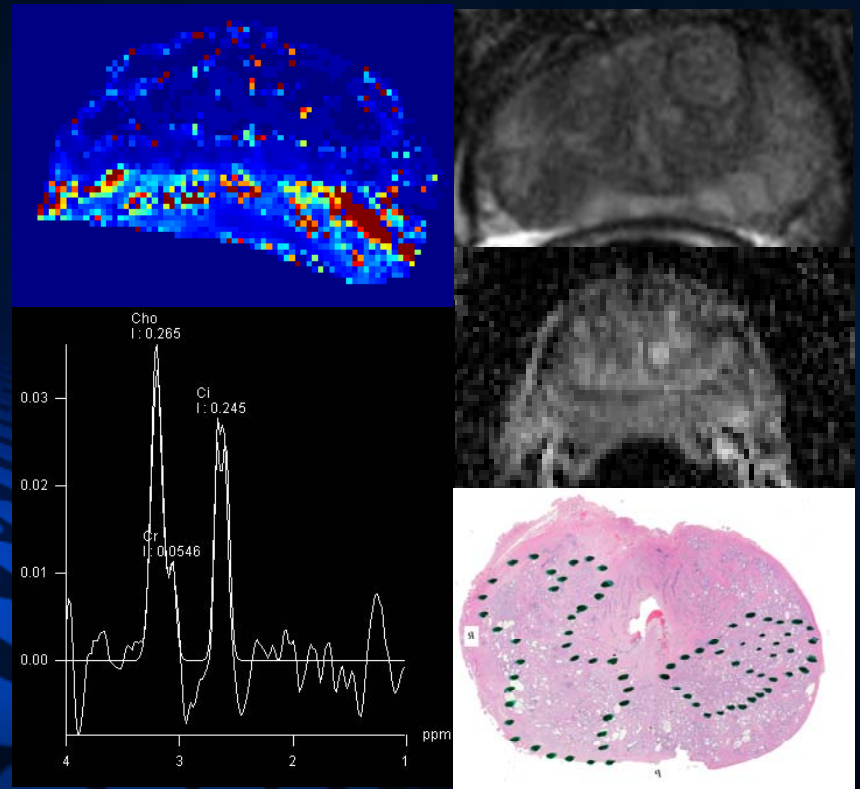
Further Reading

- Hricak H, Choyke PL, Eberhardt SC, Leibel SA, Scardino PT. Imaging Prostate Cancer: A Multidisciplinary Perspective. *Radiology* 2007;243:28-53.
- Choi YJ, Kim JK, Kim N, Kim KW, Choi EK, Cho KS. Functional MR Imaging of Prostate Cancer. *RadioGraphics* 2007;27:63-75.
- Kundra V, Silverman PM, Matin SF, Choi H. Imaging in Oncology from the University of Texas M. D. Anderson Cancer Center: Diagnosis, Staging, and Surveillance of Prostate Cancer. *AJR Am J Roentgenol* 2007;189:830-844.
- Reinsberg SA, Payne GS, Riches SF, et al. Combined Use of Diffusion-Weighted MRI and ¹H MR Spectroscopy to Increase Accuracy in Prostate Cancer Detection. *AJR Am J Roentgenol* 2007;188:91-98.
- Futterer JJ, Heijmink SWTP, Scheenen TWJ, et al. Prostate Cancer Localization with Dynamic Contrast-enhanced MR Imaging and Proton MR Spectroscopic Imaging. *Radiology* 2006;241:449-458.
- Schiebler ML, Schnall MD, Pollack HM, et al. Current Role of MR Imaging in the Staging of Adenocarcinoma of the Prostate. *Radiology* 1993;189:339-352.
- deSouza NM, Reinsberg SA, Scurr ED, Brewster JM, Payne GS. Magnetic resonance imaging in prostate cancer: the value of apparent diffusion coefficients for identifying malignant nodules. *Br J Radiol* 2007;80:90-95.
- Kim CK, Park BK, Han JJ, Kang T, Lee HM. Diffusion-weighted imaging of the prostate at 3T for differentiation of malignant and benign tissue in transition and peripheral zones: preliminary results. *J Comput Assist Tomogr* 2007;31:449-454.
- Bloch BN, Furman-Haran E, Helbich TH, et al. Prostate Cancer: Accurate Determination of Extracapsular Extension with High-Spatial-Resolution Dynamic Contrast-enhanced and T2-weighted MR Imaging-Initial Results. *Radiology* 2007;245:176-185.
- Haider MA, van der Kwast TH, Tanguay J, et al. Combined T2-Weighted and Diffusion-Weighted MRI for Localization of Prostate Cancer. *AJR Am J Roentgenol* 2007;189:323-328.
- Tofts PS, Brix G, Buckley DL. Estimating kinetic parameters from dynamic contrast-enhanced T(1)-weighted MRI of a diffusable tracer: standardized quantities and symbols. *J Magn Reson Imaging* 1999;10:223-232.
- Yu KK, Scheidler JS, Hricak H, et al. Prostate Cancer: Extracapsular Extension with Endorectal MR Imaging and Three-dimensional Proton MR Spectroscopic Imaging. *Radiology* 1999;213:481-488.
- Testa C, Schiavina R, Lodi R, et al. Prostate Cancer: Sextant Localization with MR Imaging, MR Spectroscopy, and ¹¹C-Choline PET/CT. *Radiology* 2007;244:797-806.
- Kurhanewicz J, Vigneron DB, Hricak H, Narayan P, Carroll P, Nelson SJ. Three-dimensional H-1 MR Spectroscopic Imaging of the in Situ Human Prostate with High (0.24-0.7-cm³) Spatial Resolution. *Radiology* 1996;198:795-805.
- Jung JA, Coakley FV, Vigneron DB, et al. Prostate Depiction at Endorectal MR Spectroscopic Imaging: Investigation of a Standardized Evaluation System. *Radiology* 2004;233:701-708.
- Kumar V, Jagannathan NR, Kumar R, et al. Apparent diffusion coefficient of the prostate in men prior to biopsy: determination of a cut-off value to predict malignancy of the peripheral zone. *NMR Biomed* 2007;20:505-511.
- Harisinghani MG, Dixon T, Saksena M, et al. MR Lymphangiography: Imaging Strategies to Optimize the Imaging of Lymph Nodes with Ferumoxtran-10. *Radiographics* 2004;24:867-878.
- Pucar D, Shukla-Dave A, Hricak H, et al. Prostate Cancer: Correlation of MR Imaging and MR Spectroscopy with Pathologic Findings after Radiation Therapy-Initial Experience. *Radiology* 2005;236:545-553.



Advanced MR Imaging of Prostate Cancer: Radiology Pathology Correlation

Andrew Rosenkrantz¹, MD;
Rao Gullapalli¹, PhD;
Khan Siddiqui², MD; Bao Zhang¹ MS;
John Papadimitriou³, MD, PhD;
Danielle Holanda³, MD; Steve Roys¹, MS;
Harris Yfantis³, MD; James Borin⁴, MD;
Michael Naslund⁴, MD; Eliot Siegel^{1,2} MD



¹Department of Radiology, University of Maryland Medical Center

²Department of Radiology, VA Maryland Health Care System

³Department of Pathology, University of Maryland Medical Center

⁴Department of Surgery, University of Maryland Medical Center

Supported by a grant from the Department of Defense,
Proposal No. PC031042, Award No. W81XWH-04-1-0249

Landmark-based Prostate MR Image Matching Using Incompressible Large Deformation Diffeomorphism

X. Liu¹, S. Roys², J. L. Prince^{1,3}, and R. Gullapalli²

¹Computer Science, Johns Hopkins University, Baltimore, MD, United States, ²Radiology, University of Maryland Baltimore, Baltimore, MD, United States, ³Electrical and Computer Engineering, Johns Hopkins University, Baltimore, MD, United States

Introduction: Magnetic resonance (MR) imaging with an endorectal coil is a standard clinical procedure for prostate cancer diagnosis. The balloon used with the endorectal coil is typically inflated to as high as 100 cc for optimal coupling of the coil with the prostate gland, and minimizing movement of the gland during the image or spectral acquisition. However, this method of acquisition deforms the prostate from its native state while images and spectra are obtained. For optimum delivery of radiation dose to the areas of cancer, the information obtained in the deformed state needs to be transformed back to its native state. Registration methods that have been proposed to date [1,2] are either rigid or non-rigid and compressible, neither of which accounts for the true nature of the prostate deformation [3]. In this work we constrained the deformation field to be incompressible, and developed an incompressible landmark-based image matching method using the large deformation diffeomorphism (LDD) framework [4], and applied it to transform the deformed prostate to its native state.

Methods: Our method matches manually specified landmarks on the deformed and non-deformed prostate images using large deformation diffeomorphism (LDD) framework. Given N landmark pairs $((x_n, y_n), n = 1, \dots, N)$, the LDD finds a diffeomorphism $\phi(x, t)$ that maps any point x in the source image to its position y in the target image such that $t \in [0, 1]$ and $\phi(x, 0) = x$, $\phi(x, 1) = y$. The velocity field $v(x, t)$ at time t is defined as the time derivative of $\phi(x, t)$. Unlike the small deformation interpolation, the LDD does not constrain directly the displacement field. Instead, it computes the velocity fields that minimizes the quadratic energy function $E(v) = \int_{\Omega_d} \|Lv(x, t)\|^2 dx dt$ and satisfies $\phi(x_n, 1) = y_n$, $n = 1, \dots, N$, where L is a differential operator. The deformation field is finally computed by integrating v over t . In addition, the velocity field of an incompressible object is divergence free everywhere. A vector spline solution was previously proposed [5] to interpolate a divergence-free vector field. The vector spline minimizes the energy function $J(v) = \int \|\nabla \text{curl}(v(x))\|^2 dx$ with the constraint $\text{div}(v(x)) = 0$, where $\text{div}(\cdot)$ and $\text{curl}(\cdot)$ are the vector divergence and curl respectively. It has been shown that the kernel matrix of this differential operator is $K(x) = \{-\Delta + \nabla \nabla^T\} h(\|x\|)$, where $h(r) = r^4 \log r$ for two dimensions and $h(r) = r^3$ for three dimensions. By incorporating the divergence-free vector spline into the LDD framework we reformulated the problem as: finding the velocity field $\hat{v}(x, t) = \arg \min_v \int_{\Omega_d} \|\nabla \text{curl}(v(x, t))\|^2 dx dt$ that satisfies $\text{div}(v(x)) = 0$ and $\phi(x_n, 1) = y_n$, $n = 1, \dots, N$. The velocity $\hat{v}(x, t)$ and the mapping $\phi(x, t)$ are then solved using discrete time points and iterative gradient descent [4]. We call this the *incompressible LDD* method.

Results: Figure 1 demonstrates the method using a numerical example that has 2 matching points and 4 fixed corner points, as shown in Fig. 1a. In Figs. 1a & d, points A and B move to C and D respectively. Figs. 1a-c show the results of standard LDD, and Figs. 1d-f are the results of the proposed incompressible LDD method respectively. In (a) and (d), the red lines show the trajectories of points using the two different methods. Fig. 1b & e shows the final deformation using deformed grids. Fig. 1c & f are the vector flow of the displacement fields. It is clear that the grid areas are not preserved in the standard LDD solution, while they are preserved in the incompressible LDD solution. The incompressibility of the mesh produces a vortex in the displacement field (shown in Fig. 1f).

We also applied our incompressible LDD method on three T2-weighted prostate datasets (3mm slice thickness, TE/TR 80/3000ms) to transform the deformed prostate images to their native state. For each dataset one image volume was acquired with the coil inserted but with no air in the balloon (Fig. 2a), while the other was acquired when the balloon was inflated with 60cc air. These images were then matched using small deformation registration (thin-plate spline), standard LDD, and incompressible LDD methods, and the results were compared. Fig. 2 shows the results on one of the datasets. The red crosses mark the landmark points chosen. In Fig 2, (a) is the non-deformed image, (b) shows the deformation computed using standard LDD, while (c) shows results of incompressible LDD. We also computed the determinants of Jacobian of the motion field, which is shown in Fig. 3. Figs. 3a-c are the results of incompressible LDD, standard LDD, and thin-plate spline interpolation respectively. The determinant of the Jacobian indicates the local volume change. For an incompressible object, its value remains 1 everywhere. From Fig. 3 we can see the deformation produced by incompressible LDD retains this property, while in the standard LDD and the small deformation registration, the volume change can be as high as 30%.

Conclusion: In this work we developed a landmark-based prostate MR image registration method using incompressible large deformation diffeomorphism. By enforcing the divergence-free condition on the velocity fields the final deformation field is a true reflection of the physical property of prostate. Although the current implementation of this method is limited to 2D images, an extension to 3D is currently under development. In the future we will also include the application of incompressible LDD method to motion estimation and interpolation of incompressible moving tissues, for example, the heart and the tongue.

Acknowledgement: This work is supported by NIH grant R01 HL047405 and grant from DOD Award No. W81XWH-04-1-0249.

References:

1. Fei B, et al., *Comput. Med. Imag.*, 27:267-281, 2003
2. Venugopal N, et al., *Phys. Med. Biol.*, 50:2871-2885, 2005
3. Krouskop TA, et al., *Ultrasonic Imag.*, 20:260-274, 1998
4. Joshi SC, et al., *IEEE Trans. Imag. Proc.*, 9(8):1357-1370, 2000
5. Amodei L, et al., *Journ. Approx. Theo.*, 67(1) :51-79, 1991

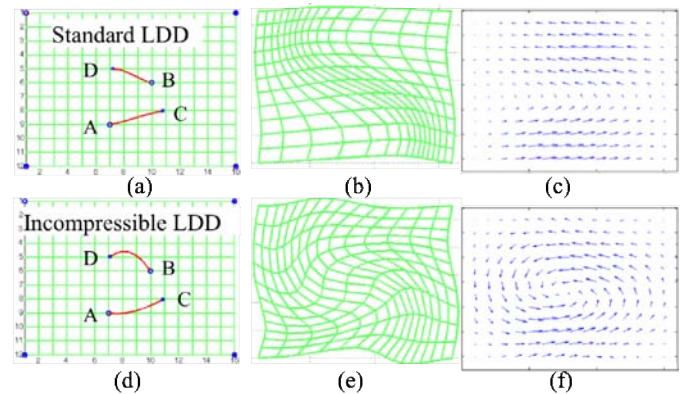


Fig. 1 Numerical example

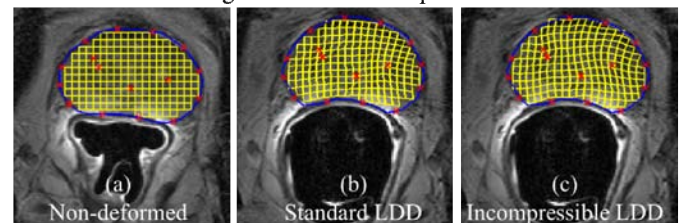


Fig. 2 Results on prostate image matching

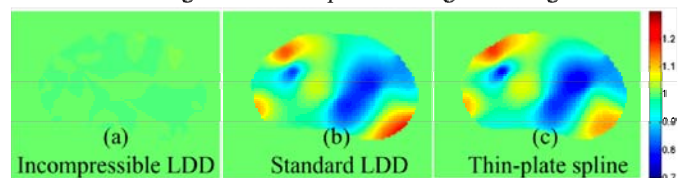


Fig.3 Determinant of Jacobian of deformation field